

An efficient quantum memory in  
 $^{167}\text{Er}^{3+}:\text{Y}_2\text{SiO}_5$ .

James Stuart



A thesis submitted for the degree of  
Doctor of Philosophy of  
The Australian National University

July 2022



# Declaration

This thesis is an account of research undertaken between February 2017 and July 2022 at the Department of Quantum Science & Technology, Research School of Physics, The Australian National University, Canberra, Australia.

Except where acknowledged in the customary manner, all material presented in this thesis including figures and photographs are original and have not been submitted in whole or part for a degree in any university.

James S. Stuart  
July 2022





# Acknowledgements

First and foremost, I would like to thank my head supervisor, Matthew Sellars, whose guidance has helped me grow over these too-many years. If only you weren't right so often. I would also like to thank my secondary supervisors, Rose and Morgan. Morgan, who was always there to bounce experiment ideas off of and who helped shape the experiment into what it is today. Rose, who taught me many of the skills that a scientist needs outside the lab. I also thank Milos, who handed me the reins and taught me how to lead the experiment with them. I hope to be able to offer the same guidance to the new generation of PhD students.

This research would have been nothing if it weren't for all the group members: Rose, David, Lara, Paul, Kieran, Jack, Matt, Matt, and Matt. Along with all of those who were in the group and have since moved on. The many lunchtime conversations about "how many country flags contained the southern cross" or "which vegetables were from the same plant as broccoli" were welcome breaks from experiments. I would also like to thank the entire research group for putting up with my constant barrage of puns, and Matthew Sellars, for encouraging them.

A special thanks goes to the proofreaders: Matt, Rose, Lara, Kieran, and Jack. Rose, your timely and thorough feedback is always impressive. When proofreading, I now ask myself "what would Rose say?", and the answer is usually "comma splice."

A PhD student is more than a researcher. I thank my friends for getting me out of the lab and on to the climbing wall or around the board games. I also thank my family, for always supporting me, even if it meant just smiling and nodding while I explained my work.



# Abstract

This thesis investigates whether a quantum memory suitable for quantum communication applications can be developed using an erbium doped crystal. To assess the potential of the storage material,  $^{167}\text{Er}^{3+}:\text{Y}_2\text{SiO}_5$ , the performance of two quantum memory protocols are characterised, the Atomic Frequency Comb (AFC) and Rephased Amplified Spontaneous Emission (RASE). As such, this work is a spiritual successor to two previous PhD projects, Kate Ferguson’s non-classical demonstration of the RASE protocol using praseodymium, and Milos Rančić’s high resolution spectroscopy and demonstration of long hyperfine coherence times in erbium.

A telecom compatible quantum memory is vital for the DLCZ quantum repeater protocol, a critical device for quantum communications networks. A quantum memory designed for communications networks will need to meet several requirements: operate in the fibre optic telecommunications band, high recall efficiency, long storage time, and high bandwidth. Erbium is of interest as it has an optical transition within the telecommunications C-band (1530 – 1565 nm) and Rančić’s thesis demonstrated the hyperfine coherence time needed for long storage times, 1.3 s. However, efficient quantum memories using erbium have not been demonstrated to date. This thesis will present an efficient quantum memory using erbium and discuss a pathway to demonstrate all the above criteria simultaneously.

Techniques that were developed in Rančić’s thesis are expanded in this thesis to create a new memory preparation process. The preparation process uses the long hyperfine lifetimes and large hyperfine splittings found in  $^{167}\text{Er}^{3+}:\text{Y}_2\text{SiO}_5$ . Using this preparation, two quantum memory protocols were demonstrated, the Atomic Frequency Comb (AFC) and Rephased Amplified Spontaneous Emission (RASE), from Ferguson’s thesis. In the AFC experiments, non-classical storage was demonstrated with a delay time of 0.66  $\mu\text{s}$ , an efficiency of 22%, and a bandwidth of 6 MHz. In the RASE experiments, an efficiency of 47% was demonstrated with a spin-state storage time of 27  $\mu\text{s}$ , and the potential to store 40 temporal modes.

The initial results have shown orders of magnitude increases in storage times and efficiency over previous erbium memories. However, the efficiencies shown are not high enough for a quantum repeater demonstration. Cavity-enhancement offers a way to increase the efficiencies of both the AFC and

RASE demonstrations. In the AFC chapter, cavity enhancement was discussed as a way to increase the efficiency, theoretically, to 96.6% with a 100 MHz bandwidth. These predicted efficiencies and bandwidths, using erbium, would meet three of the requirements needed for applications in a communications network, while Rančić has already demonstrated the remaining requirement in the same material. The next step for this work will be to realise the predicted efficiency and bandwidth, and then implement hyperfine rephasing for long storage times.

In summary, this thesis expands on the works of Ferguson and Rančić to demonstrate quantum memories based in erbium. The demonstrations are promising so far, and proposed improvements to the experiment suggest that a quantum memory fit for quantum networks applications is possible. Furthermore, a pathway to an improved quantum memory is presented. Such a memory could be used in an initial quantum repeater demonstration.

# Contents

<b>Declaration</b>	<b>iii</b>
<b>Acknowledgements</b>	<b>v</b>
<b>Abstract</b>	<b>vii</b>
<b>1 Introduction and Motivation</b>	<b>1</b>
1.1 Entanglement swapping and quantum repeaters . . . . .	2
1.2 Rephased Amplified Spontaneous Emission . . . . .	4
1.3 Rare Earth Ion doped Crystals . . . . .	4
1.3.1 Erbium . . . . .	5
1.4 Summary . . . . .	6
<b>2 Quantum Memories and Rare-Earth Ions</b>	<b>7</b>
2.1 Properties of the rare-earth ions . . . . .	7
2.1.1 Properties of rare-earth dopants in crystals . . . . .	9
2.1.2 Inhomogeneous and homogeneous broadening . . . . .	12
2.2 $^{167}\text{Er}^{3+}:\text{Y}_2\text{SiO}_5$ . . . . .	14
2.2.1 The Kramers ions . . . . .	17
2.2.2 Phonon interactions . . . . .	17
2.3 Spectral holeburning . . . . .	19
2.4 Atom-light interactions . . . . .	21
2.5 Photon echoes and quantum memories . . . . .	23
2.5.1 The Bloch sphere . . . . .	24
2.5.2 Two-level photon echo . . . . .	24
2.5.3 Four-level photon echoes . . . . .	27
2.5.4 Inverted-four-level echo . . . . .	28
2.6 The Atomic Frequency Comb (AFC) . . . . .	31
2.6.1 AFC efficiency . . . . .	32
2.6.2 Noise performance . . . . .	34
2.7 Rephased Amplified Spontaneous Emission . . . . .	35
2.7.1 Optical amplification . . . . .	35
2.7.2 Two-level RASE . . . . .	36
2.7.3 Previous four-level demonstrations . . . . .	37

2.7.4	Four-level RASE . . . . .	37
2.7.5	Correlation and covariance . . . . .	39
2.7.6	Comparing re-preparation of memory protocols . . . . .	41
2.8	Summary . . . . .	42
<b>3</b>	<b>Experimental Setup</b>	<b>45</b>
3.1	Experimental overview . . . . .	45
3.2	Cryostat and sample . . . . .	46
3.3	Laser path . . . . .	47
3.4	Laser frequency stabilisation . . . . .	48
3.4.1	Laser locking setups . . . . .	50
3.5	Electro-optic modulators . . . . .	53
3.5.1	Phase modulators . . . . .	54
3.5.2	Amplitude modulators . . . . .	55
3.5.3	IQ modulators . . . . .	56
3.6	Radio Frequency (RF) sources . . . . .	58
3.7	Heterodyne detection with AM-EOMs . . . . .	60
3.7.1	Balanced heterodyne detection . . . . .	62
3.7.2	Shot-noise-limited detection . . . . .	65
3.7.3	Continuous and discrete variable detection . . . . .	66
3.8	Ensemble preparation . . . . .	67
3.8.1	Absorption spectra at 6,7 T . . . . .	68
3.8.2	Spin polarisation . . . . .	70
3.8.3	Selective anti-polarisation . . . . .	72
3.9	Spectroscopy of selectively anti-polarised features . . . . .	75
3.9.1	Anti-hole lifetime . . . . .	75
3.9.2	Hyperfine broadening . . . . .	78
3.9.3	Excitation induced rethermalisation of hyperfine levels . . . . .	80
3.10	Summary . . . . .	85
<b>4</b>	<b>AFC Experiments</b>	<b>87</b>
4.1	A brief history of the AFC . . . . .	87
4.2	AFC parameters . . . . .	88
4.3	AFC experiment outline . . . . .	89
4.4	Spin pumping background absorption . . . . .	91
4.5	AFC characterisation . . . . .	93
4.5.1	Efficiency . . . . .	93
4.5.2	Spectra and background absorption . . . . .	94
4.5.3	Expected performance . . . . .	95
4.5.4	Characterisation summary . . . . .	96
4.6	Non-classical demonstration . . . . .	96
4.6.1	Phase correction and post processing . . . . .	97
4.6.2	Noise performance . . . . .	99
4.7	Improving the AFC . . . . .	103

4.7.1	Storage level schemes . . . . .	103
4.7.2	Theoretical cavity predictions . . . . .	104
4.7.3	Extending AFC bandwidth and storage time . . . . .	106
4.8	Summary . . . . .	107
<b>5</b>	<b>RASE Prelude</b>	<b>109</b>
5.1	Experiment setup changes . . . . .	109
5.2	Photon echoes . . . . .	110
5.2.1	Two-level echo . . . . .	112
5.2.2	Inverted-four-level echo . . . . .	114
5.2.3	Field gradient . . . . .	121
5.2.4	Transition choice . . . . .	122
5.3	EDFA implementation . . . . .	123
5.4	AWG spurious signals . . . . .	127
5.5	Amplified Spontaneous Emission . . . . .	128
5.5.1	Gain . . . . .	129
5.5.2	ASE measurements . . . . .	130
5.5.3	ASE signal decay . . . . .	132
5.6	Summary . . . . .	134
<b>6</b>	<b>RASE Experiments</b>	<b>135</b>
6.1	RASE experiment outline . . . . .	135
6.2	RASE preparation sequence . . . . .	138
6.2.1	Diagnostic measurements . . . . .	139
6.3	Characterisation of RASE . . . . .	142
6.4	Non-classical RASE measurements . . . . .	147
6.4.1	Characterising the electrical noise . . . . .	147
6.4.2	Correlation measurements . . . . .	149
6.4.3	Inseparability criterion . . . . .	154
6.5	Characterising the classical noise . . . . .	156
6.5.1	Inseparability criterion modelling . . . . .	161
6.6	Summary . . . . .	164
<b>7</b>	<b>Conclusion</b>	<b>167</b>
	<b>Appendices</b>	<b>171</b>
<b>A</b>	<b>EDFA pulsed gain</b>	<b>173</b>
<b>B</b>	<b>AWG spurious signals</b>	<b>177</b>
<b>C</b>	<b>Erbium holeburning simulation</b>	<b>181</b>
C.1	Data used in the simulation . . . . .	181
C.2	Simulating the level structure . . . . .	183
C.3	Other simulations . . . . .	184

<b>D Phase correction accuracy</b>
------------------------------------

<b>189</b>
------------



# Chapter 1

## Introduction and Motivation

The invention of the personal computer and the internet has drastically changed the lives of everyone on the earth. Particularly in developed countries, the fraction of people interacting with the internet daily has gone from only a small percentage to the majority in a matter of decades. Similar to the growth of the personal computer and the internet from the 20<sup>th</sup> century, quantum information is a growing research field with great potential to affect people's lives. One of the technologies from this research field is the quantum computer, analogous to the classical computer. In the same way that classical computers can be networked to form the internet, a quantum network can also be created to network quantum computers. Every communications network needs a memory, this thesis explores one avenue for creating a memory for a quantum network.

There is a growing sentiment that quantum computers and the quantum internet could be extremely useful. Initially, the idea for a quantum computer was presented in 1982 [31], by Feynman. Since then, there has been a lot of research in this field: from algorithms to run on a quantum computer [34, 66] to demonstrations of quantum processors [75, 51]. Yet, quantum computers are still far inferior to classical computers in terms of processing power. Currently, there are a few notable demonstrations that are starting to show promise, including, google [5], IBM [76], and USTC [74]. But, there is still a lot of research needed before these technologies are ready for commercial settings. A reason for this is because both quantum computers and quantum networks require the ability to perform operations on very delicate quantum information and require the entanglement of simultaneous qubits. The preservation of entanglement between particles is difficult as unwanted interactions with the environment can corrupt the delicate quantum states through decoherence. In turn, this limits the scalability of quantum computers.

Quantum networks share many of the same issues quantum computers face, however, the scale of distance is completely different. As a network

grows to the global scale, losses in the network and noise (from decoherence) also increase, but here loss is the biggest issue. For a global quantum network, we could use the current telecommunications infrastructure, in particular the fibre optic cables that form the internet. In this case, we would need to send quantum information (super position states) encoded onto photons over distances of 1000s – 10,000's of kilometers. Thankfully, telecommunications have engineered optical fibres to have extremely low loss at 0.2 dB/km ( $\sim 5\%$ ). While this loss is incredibly small, 5% every kilometer scales very poorly over the circumference of the earth ( $\sim 40,000$  km) and the probability a photon survives a journey of this distance is astronomically low. So loss is still the biggest issue with the network. For classical communications, this technical limitation is solved by periodically amplifying the signal every 50 – 100 km. Unfortunately, by the no cloning theorem [73], amplification is impossible for arbitrary quantum states.

The exponential losses due to attenuation can be mitigated by subdividing the network into links and first establishing entanglement between the links of the network. One proposed protocol to achieve this distributes entanglement throughout the links of the subdivided network through a process called entanglement swapping [42]. Entanglement swapping happens when two unentangled devices exchange entangled particles and, using these entangled particles, the two devices become entangled (explained in more detail below). By using this method, losses in the network grow polynomially with distance [11], instead of exponentially. However, entanglement distribution will only succeed if every link of the network is entangled simultaneously. To simplify this process, we need a way to store entanglement for a prolonged period of time in a device called a quantum memory [71].

In this thesis, I explore the development of a quantum memory using rare-earth ion doped crystals (REIC), explained below. Quantum memories using REIC's have been demonstrated before using a range of different crystal hosts and dopants. This work specifically follows on from Rančić [58] and Ferguson [29] using a rare earth ion, erbium, as a host material to demonstrate a quantum memory protocol, Rephased Amplified Spontaneous Emission (RASE), while being compatible with telecommunications infrastructure.

## 1.1 Entanglement swapping and quantum repeaters

In the above section, we mention that a quantum network will be subdivided into smaller links (or nodes) and entanglement will be distributed across all of these nodes. Here, I will describe one way to achieve entanglement distribution.

At the ends of each node will be a device called a quantum repeater [11]. A quantum repeater is a device or protocol that can generate multiple entangled particles. These entangled particles can either be stored, in a

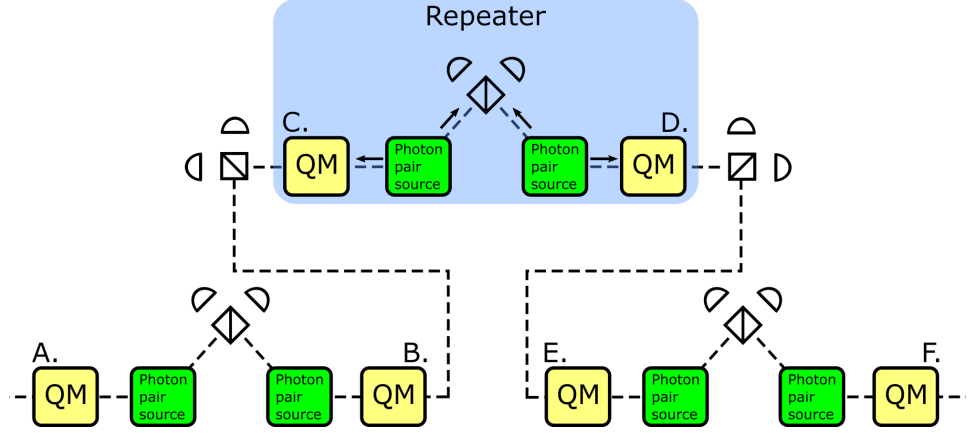


Figure 1.1: A simplified quantum repeater scheme for the DLCZ protocol [24]. This particular quantum repeater comprises two single photon pair sources and two quantum memories. One of the photon pair sources will emit two photons, one towards a quantum memory and another towards a beam splitter. On the output ports of the beamsplitter are two detectors.

quantum memory, or transferred to other repeaters to facilitate the entanglement swapping process. Figure 1.1 shows a simplified schematic for the DLCZ quantum repeater protocol [24]. Entanglement is distributed through the network in the following manner. First, one of the photon pair sources produces a pair of single photons. One of the photons is stored in a quantum memory, the other is sent through a beam splitter and detected on one of the detector pairs. When the detectors measure a single photon, we know that one of the quantum memories must contain a photon. However, which quantum memory contains the photon is unknown, because of the beam splitter before the detectors. In Figure 1.1, quantum memories C and D are now entangled via “entanglement through indistinguishability”. This process is repeated for every repeater node in the quantum network, i.e. quantum memories (A, B) and (E, F) are entangled. In the next stage, the entanglement generated in each node is shared to surrounding nodes through entanglement swapping. The quantum memories B and C are recalled, and a joint measurement is performed between the two repeaters. This process destroys any quantum information in the quantum memories B and C, but in the process quantum memories A and D become entangled. The same process is repeated with quantum memories D and E, now the two quantum memories at the ends of the network are entangled (A and F).

From the description in the previous paragraph, we see that quantum memories must store quantum information for the entire entanglement swapping process. At best, the entanglement swapping process time will be limited by the transmission delays in the network. For a global communications

network, this distance can be up to 40,000 km, which equates to a transmission delay of  $\sim 100$  ms. So the storage time of a quantum memory must be at least 100 ms. Adding to this, the quantum memories must reliably recall the quantum information, any failures from the quantum memories will increase entanglement swapping time. Finally, the pair photon source and quantum memories must also be compatible. The quantum memory's storage time and recall efficiency, along with the compatibility of pair single photon sources, are some of the biggest engineering challenges that need to be solved to implement a global quantum network. The RASE quantum memory protocol is of interest as it offers a way to combine the photon sources and quantum memory into one device.

## 1.2 Rephased Amplified Spontaneous Emission

Here the basic operating principles of RASE are given. More in depth detail of the operating procedure and underlying theory is given in Sections 2.5.2 and 2.7. RASE is a quantum memory protocol that uses an inverted population of atoms to amplify the vacuum state. The amplified spontaneous emission (ASE) can then be recalled on-demand using rephasing  $\pi$ -pulses, similar to techniques found in NMR [35] and photon echoes (Section 2.5.2). The rephased amplified spontaneous emission (RASE) is entangled with ASE. Thus, we have created a photon pair source. Since the quantum state of the ASE is stored on the atomic ensemble, and the RASE can be recalled on-demand, we also have a quantum memory whose storage time is limited by the coherence time of the atomic ensemble that created the ASE photons.

The RASE protocol was initially proposed by Ledingham et al. [49] and simultaneously demonstrated by Ledingham et al. [48] and Beavan et al. [6]. However, both demonstrations were not able to show non-classical storage. The main issue with the RASE protocol is the noise added to the RASE from the FID of the rephasing  $\pi$ -pulse. Ledingham minimised the noise by using uniform  $\pi$ -pulses. Beavan expanded the sequence to four levels, rather than just using two atomic levels, a ground and excited state. By expanding to four levels, two ground hyperfine states and two excited states, ASE and RASE are emitted on different transitions to the rephasing  $\pi$ -pulses and can thus be spectrally filtered. However, ASE and RASE are also emitted on different optical transitions. A non-classical demonstration was also shown by Ferguson et al. [30].

## 1.3 Rare Earth Ion doped Crystals

The rare-earth ions have long been studied for their long optical life (0.1 – 10 ms) and coherence times (0.1 – 4.4 ms) along with their even longer hyperfine

coherence times (1.3 seconds in erbium [59], 6 hours in europium [78]). The three demonstrations mentioned in the previous section all use rare earth ions as the memory material, with the rare earth ions doped into crystal hosts. Ledingham used thulium doped into yttrium aluminium garnet (Tm:YAG) while Beavan and Ferguson used praseodymium doped into yttrium orthosilicate (Pr:YSO). Both of these materials are a part of the REICs of which, there have been many more quantum memory demonstrations using these materials [1, 57, 61, 17, 48, 30]

Doping the rare earth ion into a crystal (YSO, YAG, etc) gives the ion a magnetically quiet environment to occupy, which helps enhance the coherent properties of the dopant ion. Long coherence times allow the REIC to store quantum information while the entanglement swapping process is performed. On top of this, the long storage times allow for temporal multiplexing and the linewidth of the optical transitions allows for spectral multiplexing. Both of these techniques increase the available bandwidth of the quantum memory and thus can increase the bandwidth of a quantum network.

### 1.3.1 Erbium

Some examples of REIC's have been given in the above section (with Pr and Tm as dopants). Both of these materials do not intrinsically operate at the telecommunications band (ranging from at 1260 - 1625 nm, with optimal operation at 1550 nm) and would require frequency conversion. Erbium is another rare-earth ion that operates at the telecommunications wavelength (1532 - 1540 nm depending on host crystal and site). Previous work by Rančić showed that under a large magnetic field  $^{167}\text{Er}^{3+}:\text{Y}_2\text{SiO}_5$  has the appropriate coherence time for a global quantum network [59]. Building on the work of Rančić, the goal of this thesis is to demonstrate that a quantum memory appropriate for a quantum repeater can be made using erbium.

By using  $^{167}\text{Er}^{3+}:\text{Y}_2\text{SiO}_5$  the wavelength requirement for a quantum repeater is met, however there are still several properties that we need to explore. It should also be apparent that the probability of storing entanglement in the memory must be close to unity for the communications network to function. Especially if the communications channel is very long and contains 10s - 100s of repeater nodes. The quantum memory must also be able to store entanglement while the entanglement swapping process is happening, this storage time must be at least the communication time of the channel. For a global scale quantum network, this storage time will be at least 100 ms. Finally, the communications network needs a large bandwidth to pass large amounts of data quickly. Throughout this thesis, we shall see that each of these requirements should be possible using erbium as a storage material.

## 1.4 Summary

Quantum information is a growing research field that could affect people's lives similarly to the growth of the computer and internet from the 20<sup>th</sup>. A quantum network will need a quantum memory. Rare earth ion doped crystals have been used to demonstrate quantum memories previously. Erbium is a rare earth ion that works in the telecommunications band, however, efficient quantum memories using erbium have not been demonstrated to date. This thesis investigates whether a quantum memory suitable for quantum communications applications can be developed using an erbium doped crystal.

## Chapter 2

# Quantum Memories and Rare-Earth Ions

The rare-earth ions have been used in many applications, such as: laser sources, doped fibre laser amplifiers, fluorescence, and phosphors for lighting. The rare-earth ions have also been extensively studied for their sharp spectral lines and coherent properties. However, the structure of these rare-earth ions could not fully be explored until the invention of the laser in the 1960s. In the emerging world of quantum technologies, the coherent properties of rare-earth ions have promising applications in the areas of quantum communications and computation.

This chapter discusses the underlying theory needed to understand the contents of this thesis. This will include an overview of the rare-earth ions and the properties of rare-earth ion doped crystals (REIC) (Section 2.1). Building from here, a subgroup of the rare-earth ions, the Kramers ions are discussed, along with the focus material of this thesis, erbium doped into yttrium orthosilicate,  $^{167}\text{Er}^{3+}:\text{Y}_2\text{SiO}_5$  (Er:YSO) (Section 2.2). Included will be the theory of spectral hole burning (Section 2.3), a technique used in the ensemble preparation of the main experiments. This will lead into atom-light interactions (Section 2.4), photon echoes (Section 2.5), and finally, quantum memories (Sections 2.6 and 2.7).

### 2.1 Properties of the rare-earth ions

The rare-earth ions consist of 17 elements, from lanthanum to lutetium (the lanthanide series, atomic numbers 57–71) along with yttrium and scandium. Although for our purposes we are only concerned with the lanthanide series.

In the lanthanide series, the valence electrons are situated in the  $4f$  electron shell, while the outer  $5s$  and  $5p$  shells are filled. These outer shells act as a small Faraday cage, shielding the optical  $4f - 4f$  transitions from external electric and magnetic fields, electron shells shown in Figure 2.1.

Minimising interactions with the environment is a requirement for coherent experiments. As such, the rare-earth ion doped crystals have recorded very long optical coherence times, 4.4 ms in Er:YSO [9]. Even longer still are the nuclear coherence times, 1.3 seconds demonstrated in Er:YSO [59] and 6 hours demonstrated in Eu:YSO [78].

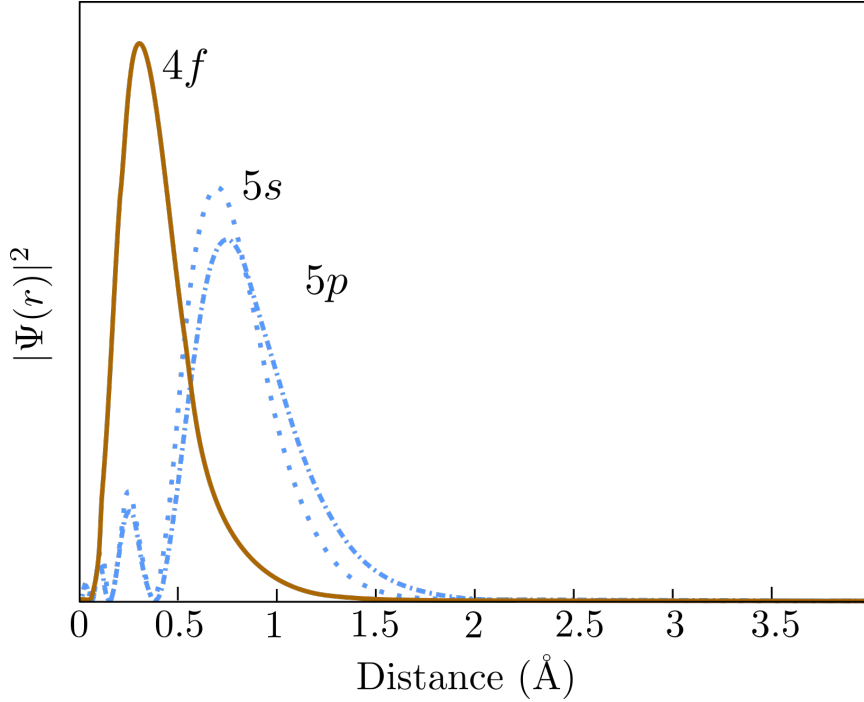


Figure 2.1: Theoretical prediction of the electron orbitals for Gd, based on the data from [32]. The  $4f$  orbital (solid line) is within the  $5s$  and  $5p$  (two dashed lines). This trend remains true for all the lanthanide ions.

While the  $4f$  electrons are shielded from external electric and magnetic fields, the  $4f$  electrons still interact with the nucleus. One physical effect from the nucleus is the reduction in atomic radii across the Lanthanide series. As the atomic number of the lanthanide series increases, the charge of the nucleus increases and attracts the  $4f$  electrons more than the  $4f-4f$  electron repulsion. This trend is known as lanthanide contraction [16], see Table 2.2. Whilst I have stated that minimising interactions with the  $4f$  electrons is necessary for long coherence times, interactions with the nucleus, such as the hyperfine effect (Section 2.1.1), are crucial applications in quantum memories and quantum computation.



Interaction	Frequency shift
Intra-configuration splitting $4f - 4f$	100 - 1000 THz
Non-central electrostatic field	100 THz
Spin-orbit interaction	10 THz
Crystal field	1 THz
Electronic Zeeman splitting	1 - 100 GHz/T
Hyperfine	0.01 - 1 GHz
Nuclear Zeeman splitting	0.01 GHz/T

Table 2.1: The various interactions and the magnitude of their corresponding frequency shift for rare-earth ion doped crystals. [41] The highlighted lines show the interactions that are important for the experiment chapters.

### 2.1.1 Properties of rare-earth dopants in crystals

So far, we have discussed the rare-earth ions as a free ion, unperturbed by external fields. In our experiments, we used rare-earth ions doped into crystals. This section will have a brief overview of the effect a host crystal has on the dopant rare-earth ion. In this thesis, we only concern ourselves with the optical  $4f - 4f$  transitions, as the  $4f$  electrons have the desired coherent properties that we want for quantum memories. The shielding of the  $4f$  electrons by the  $5s$  and  $5p$  means that the effect of a host crystal field on the  $4f$  electrons can be treated as a perturbation from the free-ion.

The degeneracy of a free ion is described by the quantum numbers  $S$ , the total spin,  $L$ , the orbital angular momentum, and  $J = S + L$  the total angular momentum, the free ion  $(2J+1)$ -fold degenerate. The state of these electrons are labelled by Russell-Saunders term symbols  $^{2S+1}L_J$ . Where  $L$  follows the symbol convention:  $L = S, P, D, \dots$  for orbital angular momentum, the ground state of erbium is  $^4I_{15/2}$ .

This energy structure becomes much more complex when the rare-earth ion is doped into a crystal. If the ion occupies a low symmetry site, the crystal field causes the  $2J+1$  degeneracy to lift, for non-Kramers ions (Section 2.2.1). For the Kramers ions, in low symmetry sites, the degeneracy is partially lifted and doublet states are formed. The doublet states remain degenerate if no external magnetic field is applied.

Rare-earth ions with a nuclear spin will also have another level of degeneracy lifted, due to the hyperfine effect. However, as the crystal field is small enough to be treated as a perturbation on the free ion, the hyperfine effect can be treated as a further perturbation on the crystal field. The magnitudes of these interactions are given in Table 2.1 and shown diagrammatically in Figure 2.2.

The effect of the crystal field is  $\mathcal{O}(1\%)$  of the free ion, and the hyperfine effect is  $\mathcal{O}(0.1\%)$  of the crystal field. This means the free ion energy level structure of a rare-earth ion does not shift significantly from crystal host

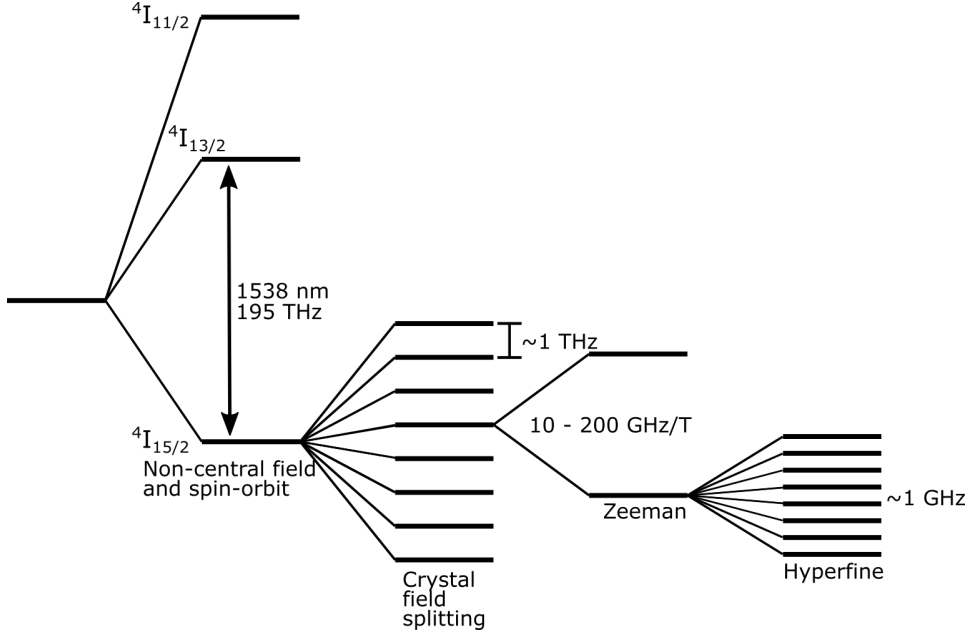


Figure 2.2: Energy level shifts/splittings from several interactions, not to scale, in  $^{167}\text{Er}^{3+}:\text{Y}_2\text{SiO}_5$ .

to crystal host. Figure 2.3 shows the Dieke diagram [20] published in 1968, which shows the energy levels for the lanthanide series doped into  $\text{LaCl}_3$ . Because the general level structure remains so consistent from crystal host to host, this diagram can be used to quickly identify the energy structures for many crystals, even those with low symmetry like YSO.

We can describe the energy structure of a rare-earth ion in a Hamiltonian that is a summation of all the interactions affecting our ion. The Hamiltonian for the  $4f$  electron shell when doped into a crystal can be written as,

$$H = H_{FI} + H_{CF} + H_Z + H_{HF} + H_Q + H_z, \quad (2.1)$$

where  $H_{FI}$  is the free ion Hamiltonian and  $H_{CF}$  is the crystal field Hamiltonian. These two have the largest effect on the ion, however we are more interested in the four smaller terms.  $H_Z$  and  $H_z$  are the electronic Zeeman and nuclear Zeeman Hamiltonians, respectively, which are only non-zero in the presence of a magnetic field.  $H_{HF}$  is the hyperfine,  $H_Q$  is the nuclear quadrupole.

### The Zeeman effect

In the presence of a magnetic field ( $B$ ) the energy levels of rare-earth ion doped crystals are further shifted by the Zeeman effect. In non-Kramers ions doped into low symmetry sites (such as YSO) the energy levels are already

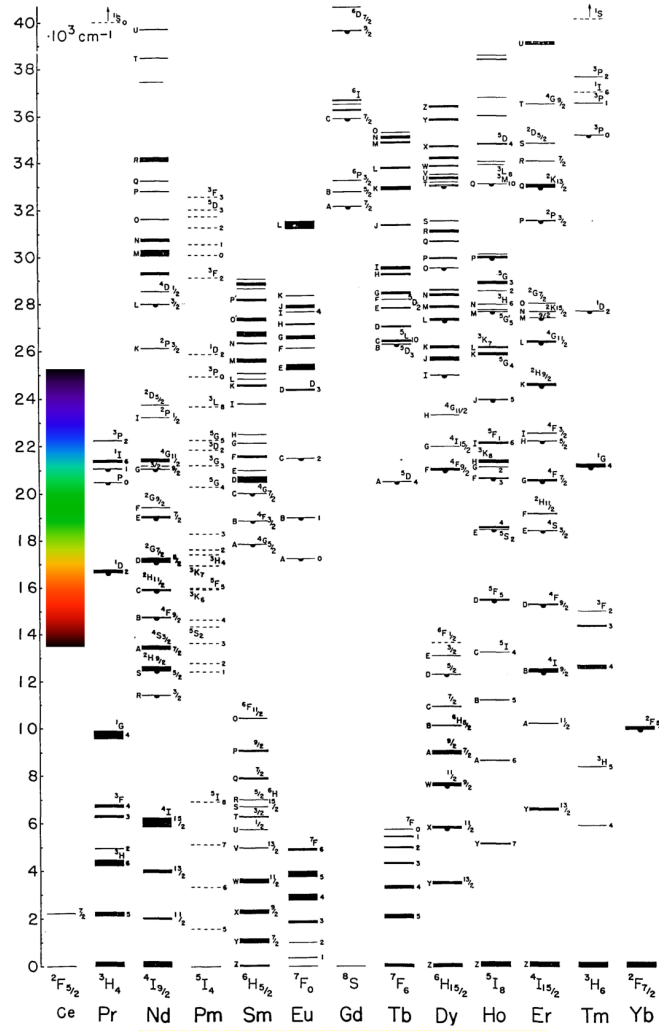


Figure 2.3: The Dieke diagram, published 1968 [20], shows the measured energy level structure for trivalent lanthanide ions doped into LaCl<sub>3</sub>, from mid-IR to ultraviolet. On this figure, the visible spectrum has been shown with a colour inset above cerium

singlets, so the energy is shifted proportional to the total angular momentum ( $J$ ) and the strength magnetic field. In the Kramers ions, the energy levels are all doubly degenerate with  $S = \pm\frac{1}{2}$  electron spin. The Zeeman effect lifts this degeneracy, splitting the energy levels symmetrically about the zero-field frequency. This interaction has the form,

$$H_Z = \mu_B B \cdot g \cdot S, \quad (2.2)$$

where  $\mu_B$  is the Bohr magneton, and  $g$  is the g-tensor, a tensor that describes the coupling strength between the electrons and an external magnetic field. The g-tensor is also non-uniform, due to the surrounding crystal field distorting the electron's coupling to external magnetic fields. The range of this effect can change by over an order of magnitude, as seen in site 2 of Er:YSO in Table 2.3.

The nuclear Zeeman Hamiltonian has a similar form to the electronic Zeeman, however, the g-tensor is replaced with the nuclear g-tensor,  $g_n$ . The effect of the nuclear Zeeman is similar to the electronic Zeeman, i.e. in the presence of a magnetic field the energy levels are split proportional to the ion's nuclear spin. The main difference between the electronic Zeeman and the nuclear Zeeman effect is size, the nuclear Zeeman effect is orders of magnitude weaker. For erbium-167, the only stable erbium isotope with non-zero nuclear spin, the nuclear Zeeman splitting is  $\sim 0.01$  GHz/T compared to the  $10 - 100$  GHz/T of the electronic Zeeman.

### The hyperfine effect

The two remaining terms in Equation (2.1),  $H_{HF}$  and  $H_Q$ , arise from the nuclear spin coupling to internal electric and magnetic fields generated by the surrounding electrons. Clearly, for nuclei with zero nuclear spin, there is no hyperfine effect. Unlike the Zeeman effect, there is a non-zero field effect. In the case of the Kramers ions (or non-Kramers doublets) the magnetic-hyperfine interaction is large,  $\sim$  GHz in zero-field for erbium. Interestingly, this means that the zero-field splitting is orders of magnitude larger than the nuclear Zeeman splitting, for erbium. For the non-Kramers singlet states, this magnetic-hyperfine interaction is quenched to first order. Thus, the hyperfine is a second order effect, and much smaller,  $\sim 0.01$  GHz in praseodymium and europium.

The nuclear spins of nearby host ions will also have an effect on the rare-earth ion, called the super-hyperfine effect, although this is small compared to the hyperfine effect and is not investigated in this thesis.

#### 2.1.2 Inhomogeneous and homogeneous broadening

As the host crystal perturbs the energy levels of the dopant ion, the host crystal will also change the lineshape of the dopant ion's optical transitions.

Atomic number	Element	Radius (pm)
39	Y	101.9
57	La	116.0
58	Ce	114.3
59	Pr	112.6
60	Nd	110.9
61	Pm	109.3
62	Sm	107.9
63	Eu	106.6
64	Gd	105.3
65	Tb	104.0
66	Dy	102.7
67	Ho	101.5
68	Er	100.4
69	Tm	99.4
70	Yb	98.5
71	Lu	97.7

Table 2.2: Atomic radii for the lanthanide series [65]

The lineshape of an ensemble of rare-earth ions doped into a crystal is governed by two types of broadening. The first broadening mechanism affects every ion in a pseudo-random way, and shifts the frequency of an ion from the average center frequency by a pseudo-random magnitude, this is called the inhomogeneous broadening. The second type of broadening mechanisms affects every ion in the same way and by the same magnitude, this is the homogeneous broadening.

The inhomogeneous broadening arises due to irregularities in the local environments around dopant ions. In the case of extremely low doping concentrations ( $< 0.001\%$ ) inhomogeneous broadening is dominated by impurities of the host crystal such as lattice defects, unintended secondary dopants, and local magnetic and electric fields. These effects are a limitation of the crystal host and the quality of the crystal growing process. Inhomogeneous broadening also arises due to mismatches in the ionic radii of the dopant ion and host ion that the dopant replaces. This causes strain on the crystal lattice, and the strain grows as dopant levels are increased. This strain can be minimised if the host ion radii and dopant radii are of similar sizes.

In YSO, dopant rare-earth ions replace yttrium ions in the crystal. Yttrium has an atomic radius of 101.9 pm, thus dopants will apply minimal strain to the host crystal if the dopants radii match yttrium's. From Table 2.2, we can see that Er, Ho, Dy are best matched to yttrium. In fact, 0.005% Er:YSO, which matches yttrium's radius to 1%, has measured inhomogeneous broadening as narrow as 150 MHz [59]. Comparatively, 0.005%

Pr:YSO only matches yttrium's radius to 10%, in similar concentrations Pr:YSO has inhomogeneous broadening on the order of 10 GHz [38].

The homogeneous linewidth is the linewidth of an individual ion within the inhomogeneous ensemble. Homogeneous broadening then affects every ion similarly throughout the crystal. The homogeneous linewidth can be determined by the optical coherence time or dephasing time ( $T_2$ ). The optical coherence time is in turn related to the optical lifetime ( $T_1$ ) and dephasing processes ( $T_2^*$ ) by the equation,

$$\Gamma_h = \frac{1}{\pi T_2} = \frac{1}{2\pi T_1} + \frac{1}{\pi T_2^*}. \quad (2.3)$$

Equation (2.3) tells us the coherence time of a transition is bounded by  $2T_1$  (and thus the homogeneous broadening will be minimal), if all other dephasing processes are minimal,  $T_2^* \gg T_1$ . Where  $T_2^*$  is governed by all the dephasing processes in the crystal environment. Some examples of this are interactions between the dopant ion and the phonon bath, spin-spin interactions with other nearby dopant ions, and spin-flips from host crystal ions which can create a time varying local electric/magnetic field. In these experiments, we operate at cryogenic temperatures where  $\Gamma_h \ll \Gamma_{inh}$ , typically  $\Gamma_{inh} \sim 0.1 - 10$  GHz and  $\Gamma_h \sim 0.1 - 10$  kHz. The linewidth of the optical transition is then dominated by the inhomogeneous broadening but is composed of many, many homogeneous lines (diagrammatically shown in Figure 2.4).

For experiments exploring coherent properties of rare-earth doped crystals, we want long coherence times. Given the coherence time is inversely proportional to the homogeneous linewidth, it is desirable to have a narrow homogeneous linewidth. The dephasing effects mentioned above can all be mitigated. Spin-spin interactions only happens between ions that are spatially very close ( $\sim \text{\AA}$ ) and can be mitigated by using crystals with low doping concentrations. The phonon interactions give the homogeneous linewidth a steep temperature dependence,  $\propto T^7$  [41]. Cooling to cryogenic temperatures suppresses these interactions. Ideally, we would choose a crystal with no nuclear spin. In this regard, YSO is a good choice for a crystal host as both silicon and oxygen only have one stable isotope with nuclear spin ( $^{28}\text{Si}$ , 4% natural abundance and  $^{17}\text{O}$ ,  $\ll 1\%$ ). Yttrium's stable isotope does have a nuclear spin,  $^{89}\text{Y}$ ,  $\frac{1}{2}$ , the nuclear magnetic moment is small ( $-0.13\mu_N$ ) [41].

## 2.2 $^{167}\text{Er}^{3+}:\text{Y}_2\text{SiO}_5$

The material used in the experiments presented throughout this thesis was isotopically purified erbium-167 doped into yttrium orthosilicate ( $^{167}\text{Er}^{3+}:\text{Y}_2\text{SiO}_5$ ) with a concentration of 0.005%, grown by Scientific Materials Corp. Specifically, isotopically pure erbium-167 was used as it is the only stable isotope of

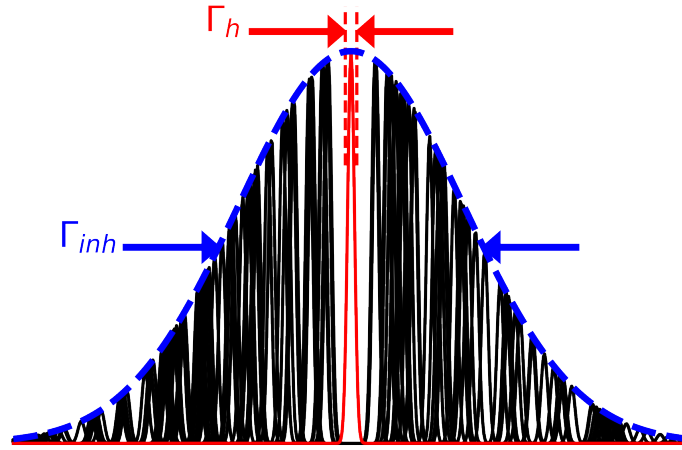


Figure 2.4: A visualisation of inhomogeneous broadening. A group of ions (black) with homogeneous linewidth,  $\Gamma_h$ , and random central frequencies due to inhomogeneous broadening,  $\Gamma_{inh}$ , in blue. The height of the homogeneous peaks corresponds to the probability of an ion having that center frequency.

	Site 1		Site 2	
Direction	g-value	abs. ( $\alpha\Gamma_{inh}$ )	g-value	abs. ( $\alpha\Gamma_{inh}$ )
$D_1$	3.1 (45 GHz/T)	4.8	14.7 (216 GHz/T)	9.6
$D_2$	8.2 (120 GHz/T)	9.0	2.0 (30 GHz/T)	1.2
$b$	5.8 (85 GHz/T)	8.0	0.9 (13 GHz/T)	0.75

Table 2.3: g-values and absorption coefficients along the crystalline axes of the ground states of sites of Er:YSO [67].

erbium with a nuclear spin ( $+7/2$ ). The hyperfine structure generated from the nuclear spin is important for developing quantum memories with long storage times, like the experiments in Chapters 4 & 6. YSO offers favourable coherent properties, and erbium is the only rare-earth ion with a transition in the telecommunications C-band ( $\sim 1538$  nm). However, it was only recently that erbium has demonstrated the coherence times required for quantum information technologies, presented in Rančić’s thesis [58]. Although, the initial optical coherence times and lifetimes were measured by Böttger et al. [9].

YSO is a monoclinic biaxial crystal described by the  $C_{2h}^6$  space group. The principal axes are labelled  $b, D_1, D_2$ , with the  $b$  axis corresponding to a crystal axis with  $C_2$  symmetry. Yttrium ions within YSO occupy two distinct crystallographic sites, labelled as ‘site 1’ and ‘site 2’, each with  $C_1$  symmetry. Eight units of  $Y_2SiO_5$  are arranged to form a single crystal unit cell. The  $C_2$  symmetry axis means that 4 of these  $Y_2SiO_5$  units are a mirror of the other 4. This creates two subgroups within a YSO unit cell, referred to as the magnetic inequivalent subgroups. At zero magnetic field, or any applied field parallel to the principal axes, the magnetic inequivalent subgroups are degenerate. Applying a magnetic field in any other direction causes this degeneracy to lift, as the effective g-value for each subgroup will be different, resulting in a different Zeeman splitting.

Erbium ions will replace yttrium ions at both crystallographic sites, with the wavelength of the  $^4I_{15/2} - ^4I_{13/2}$  optical transitions as 1536.1 nm and 1538.6 nm, for site 1 and site 2 respectively. Site 2 is studied in this thesis. Historically, site 1 has been studied the most, because of the longer lifetime ( $T_1$ ) and optical coherence time ( $T_2$ ) of 11.44 ms and 4.38 ms, respectively [9]. This is compared to the 9.2 ms lifetime [10] and 1.35 ms coherence time [58] measured in site 2. However, site 2 has much larger g-values, as shown in Table 2.3. The importance of large g values and large electronic Zeeman splitting will be explained in Section 2.2.1.

To utilise the large Zeeman splitting of site 2 a magnetic field is applied along the  $D_1$  axis. However, due to the geometry of our cryostat, this means the light is also propagating parallel to the  $D_1$  axis. From Table, 2.3, the axis



with the largest g-value corresponds to the axis with the largest oscillator strength. Unfortunately, this means that we cannot align our light with the strongest absorption axis, which means the atom-light interactions are weaker.

### 2.2.1 The Kramers ions

Erbium is a Kramers ion, the Kramers ions are ions with an odd amount of electrons in their valence shells. When doped into a low symmetry crystal, like YSO, the energy levels of the Kramers ions remain doubly degenerate. Whereas the energy levels of the non-Kramers ions (such as Pr and Eu) form singlet states. The Kramers doublets, historically, have limited the coherence times of the Kramers ions, and the non-Kramers ions have shown the best quantum memory demonstrations [78, 1, 57].

In the presence of any magnetic field (for example, the earth's magnetic field) the Kramers doublets are split by a small frequency,  $\sim\text{GHz}$ . There is a large population of thermal phonons that can cause electron spin flips between the doublet levels, even at cryogenic temperatures. Electron spin flips limit the lifetime of electron spin to 130 ms in erbium [36]. More importantly, the flipping electron spins coupled with erbium's large ground state orbital angular momentum creates an oscillating field that limits coherence times in the ground state levels to  $\sim 50$  ns [47]. Rančić et al. were able to demonstrate a much longer 1.3 second hyperfine coherence time in  $^{167}\text{Er}^{3+}:\text{Y}_2\text{SiO}_5$  [59] by using a large magnetic field (7 T) and cooling to 1.4 K. In doing so, the Zeeman splitting between the ground state Zeeman levels becomes much larger than the peak frequency of the phonon bath. This depopulates the upper Zeeman level, suppressing the electron spin flipping, shown in Figure 2.5.

The Kramers ions also have larger hyperfine splittings. This is because the non-Kramers ions magnetic-hyperfine effect is quenched to first order. We will see later, the hyperfine splitting becomes the limiting factor for the bandwidths of certain quantum memory demonstrations, Section 4.7.3.

### 2.2.2 Phonon interactions

Rare-earth ion doped crystals are lattices of charged ions. As such, vibrational modes can be excited in the lattice, which causes the charged ions to oscillate. These oscillations, in turn, create oscillating electric and magnetic fields in the form of phonons. Spin-lattice coupling is the interaction that couples phonons to the energy levels of our ions. Kramers ions, in particular, can be susceptible to the effects of phonons because of their doublet electron states. The spectrum of phonons that can interact with the crystal,

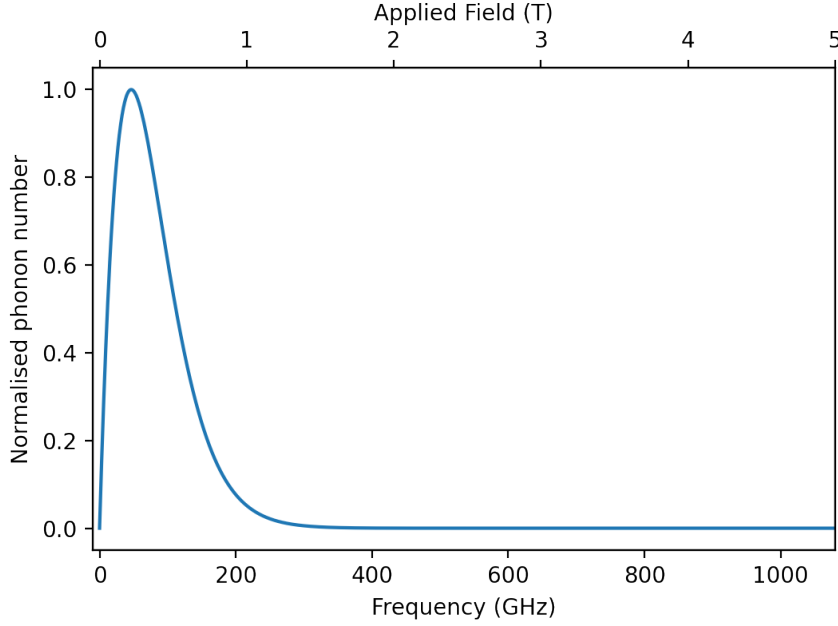


Figure 2.5: Theoretical phonon number distribution for a given phonon frequency at a temperature of 1.4 K. The top  $x$ -axis shows the field applied to the  $D_1$  axis of site 2 needed to get the corresponding Zeeman splitting, in  $^{167}\text{Er}^{3+}:\text{Y}_2\text{SiO}_5$ .

the phonon bath, is described by the black body radiation curve.

$$\rho_{en} = \frac{2h\omega^3}{v^2} \frac{1}{e^{\frac{h\omega}{kT}} - 1} \quad (2.4)$$

For a given phonon frequency ( $\omega$ ), speed of sound ( $v \sim 2000$  m/s), temperature (T), and  $h$ ,  $k$  are the Planck and Stefan Boltzmann constants, respectively. Equation (2.4) describes the energy density of the phonons, the number of discrete phonons is then proportional to  $\rho_{en}/\omega$ .

At cryogenic temperatures, the phonon number peaks around 100 GHz. This gives a relatively narrow range of transitions where phonons will directly interact with the ions of our crystal. However, along with the direct relaxation process, there are two more methods in which phonons couple to our ions. The two other methods: Orbach and Raman are referred to as ‘multi-phonon’ processes. In multi-phonon processes, several phonons can combine, sometimes through the aid of a virtual level, to interact with a transition far outside their individual frequencies. These processes are shown in Figure 2.6.

The Raman process, or virtual phonon process, uses two or more phonons to combine and create a virtual phonon at the beat frequency of the phonons. For example, two phonons with frequencies  $\omega_1$  and  $\omega_2$  can combine to form

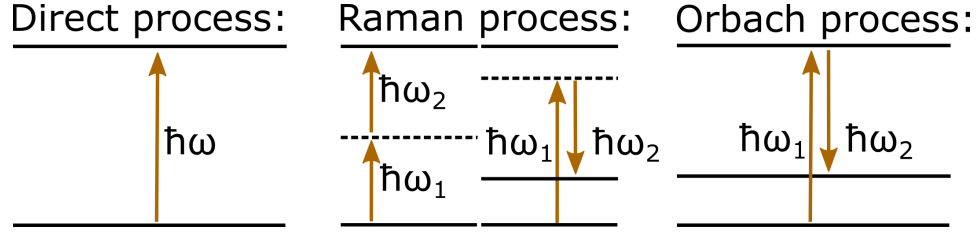


Figure 2.6: Phonon processes diagram. The dashed lines indicate a virtual level, while the solid lines are real energy levels.

a virtual phonon with frequency  $\omega_v = |\omega_1 \pm \omega_2|$ . The Raman process can allow phonons to interact with higher frequency transitions more commonly than the black body distribution would allow. More importantly, interacting with low frequency transitions becomes much more probable. Two phonons produced near the peak of the distribution, which might be 10s of GHz, can create a beat in the MHz frequency regime.

The Orbach process uses an intermediary energy level that two phonons interact with. The intermediate level could be an electron spin with an energy level near the peak of the phonon spectrum. The lower energy levels could be much smaller than the peak, such as a hyperfine level. The main difference between the Orbach and Raman processes is that the Orbach process uses phonons with discrete energy levels, while the Raman process creates a broadband spectrum of phonons.

## 2.3 Spectral holeburning

The previous sections of this chapter have discussed the theory of the rare-earth ions and the energy level structure from doping the rare-earth ions into a crystal. Sections 2.3 and 2.4 explore how atoms interact with light.

Spectral holeburning, also referred to as holeburning, is a technique that creates narrow spectral features from within an inhomogeneously broadened optical transition. Holeburning is often used for high resolution spectroscopy, to probe the optical structures hidden within inhomogeneously broadened lines, and to prepare ensembles for quantum technologies, such as, quantum memories and quantum computation.

In essence, holeburning involves sending a monochromatic light source, such as a laser, through a medium to drive resonant atoms to an excited state ( $e_0$ ). The excited atoms will then decay to some other long-lived ground state(s) ( $g_{1-n}$ ), or to their original ground state ( $g_0$ ) to be re-excited. If the ground state lifetimes were infinitely longer than the excited state lifetimes, then all the atoms resonant with the light source will, eventually, be pumped out of their original ground state. This will leave behind a hole in the absorption spectrum at the frequency of the light source. However, other

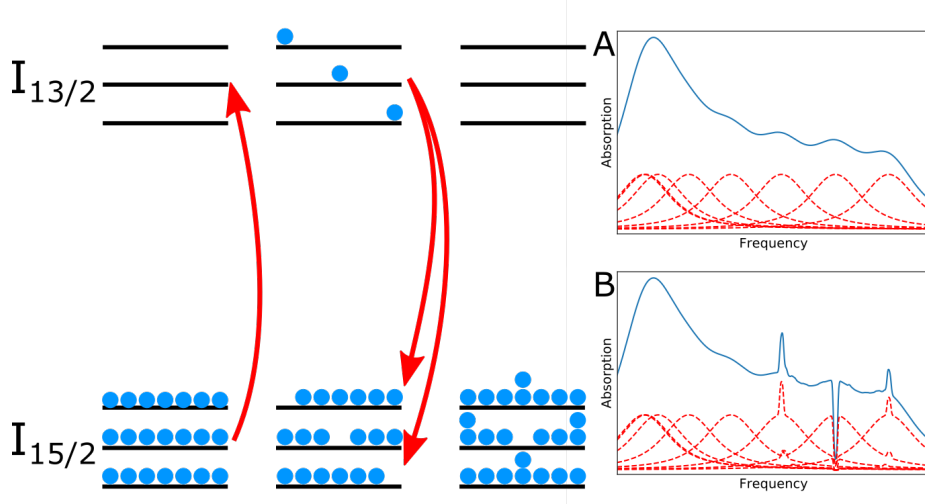


Figure 2.7: Holeburning example using theoretical Er:YSO spectra. The right side shows a model of the spectra of Er:YSO, zoomed in on the main ( $\Delta m_I = 0$ ) line. The red dotted lines show individual inhomogeneously broadened optical transitions, the blue line is a summation of all of these absorption lines, the absorption line of the erbium ions. A. shows the initial state of the ions, all in the ground state. B. shows the final state of the ions after spectral holeburning. The left side of the figure shows the energy level diagram of the three highest optical transitions (corresponding to the three right most dotted red lines in A and B). The left-most level diagram shows atomic populations of A, with all the ground state hyperfine levels equally populated. The right-most level diagram shows the atomic populations of B. The middle level diagram shows the atomic populations during the holeburning.

holes will appear in any other transition resonant with the ions' burnt out of  $g_0$ .

Once a hole has been burnt into an inhomogeneously broadened ensemble, corresponding anti-hole(s) will be created in all the transitions resonant with the other ground state(s) ( $g_{1-n}$ ). To complicate matters, in many systems the inhomogeneous broadening is large enough that multiple optical transitions can spectrally overlap. This means that any one frequency in the inhomogeneous line can contain multiple groups of ions in different ground states. Thus, burning a hole in a single frequency can excite multiple optical transitions and create anti-holes in multiple ground states.

Figure 2.7 shows an example of spectral hole burning using an Er:YSO holeburning model, Appendix C. The right side of the figure shows the spectra of the like-to-like optical-hyperfine transitions of the  $I_{15/2} - I_{13/2}$  optical transition in site 2. The ensemble of erbium ions starts with each hyperfine

ground level equally populated, Figure 2.7 A. For simplicity, we only concern ourselves with the three highest frequency transitions. A laser burns at the peak of the second-highest frequency transition. Ions resonant with this frequency are driven to the excited state, this includes ions in the inhomogeneous tails of the highest and third-highest frequency transition. Figure 2.7 B shows a hole burnt in the ensemble after with many anti-holes.

In rare-earth ions, the long-lived ground states are either the other electronic Zeeman level (in an applied magnetic field) or ground state hyperfine levels. The ground state lifetimes can be orders of magnitude (minutes to days) longer than the excited state lifetimes (100s of  $\mu\text{s}$  to 10s of ms). These long lifetimes allow for deep holes to be burnt in the inhomogeneous line (>99% depth). We will see, in the experimental chapters, that the long lifetimes can be used to create complicated spectral holeburning sequences. These sequences are used to tailor the absorption profile and hyperfine populations of a crystal for quantum experiments.

## 2.4 Atom-light interactions

The previous section discussed one of the results of a classical light field interacting with a classical ensemble of atoms. To explain the mechanisms of the quantum experiments, specifically experiments relating to coherence, we need to shift our theory to a semi-classical one. This section will introduce the atom-light interactions that we are concerned with for photon echoes and quantum memories, laying the foundations for the following sections.

We begin, as with the hole burning, with a monochromatic light source at a frequency  $\omega_0$ ,

$$E = E_0 \cos(\omega_0 t) \quad (2.5)$$

$$= \frac{E_0}{2} (e^{i\omega_0 t} + e^{-i\omega_0 t}). \quad (2.6)$$

We are ignoring the spatial and polarisation components of the light. The spatial component can be ignored as the wavelengths of light we are using (1.5  $\mu\text{m}$ ) are orders of magnitude larger than the size of the atoms. For simplicity, we will assume the polarisation is aligned with the dipole of the atoms.

We will assume the atoms are a perfect two level system with a ground state  $|g\rangle$  and an excited state  $|e\rangle$  with energy  $\hbar\omega$ . The Hamiltonian that describes this system is a sum of the free atom Hamiltonian ( $H_A$ ) and the atom-light interaction ( $H_{AL}$ ),

$$H = H_A + H_{AL} \quad (2.7)$$

$$= \hbar\omega |e\rangle \langle e| - \left( d \cdot e^{-i\omega t} |g\rangle \langle e| + d \cdot e^{i\omega t} |e\rangle \langle g| \right) \cdot E. \quad (2.8)$$

The first term accounts for  $H_A$  and the bracketed term accounts for  $H_{AL}$ , and  $d$  is the dipole moment of this optical transition. We can also assign  $\sigma = |g\rangle\langle e|$ ,

$$H = \hbar\omega\sigma^\dagger\sigma - d \cdot \frac{E_0}{2}(e^{-i\omega t}\sigma + e^{-i\omega t}\sigma^\dagger)(e^{i\omega_0 t} + e^{-i\omega_0 t}). \quad (2.9)$$

If we expand the brackets in Equation (2.9) we will see that  $H_{AL}$  will have two frequencies, rapid oscillations at optical frequencies  $\omega + \omega_0$  and slower oscillations at  $\omega - \omega_0$ . We are only interested in the behaviour of the atoms in experimental time scales (sub-optical oscillation timescale). We can apply the Rotating-Wave Approximation (RWA) if we assume that  $\omega + \omega_0 \gg |\omega - \omega_0|$ , and that any effects due to the oscillations at optical frequencies will average to zero over experimental timescales. Thus  $H_{AL}$  is reduced to,

$$H_{AL} = d \cdot \frac{E_0}{2}(e^{-i\Delta t}\sigma + e^{-i\Delta t}\sigma^\dagger) \quad (2.10)$$

$$= 2\hbar\Omega(e^{-i\Delta t}\sigma + e^{-i\Delta t}\sigma^\dagger), \quad (2.11)$$

where  $\Delta = \omega - \omega_0$ , and we have defined a new constant  $\Omega = \frac{d \cdot E_0}{\hbar}$ , the Rabi frequency. The Rabi frequency tells us the strength of the atom-light coupling. We describe the state of the atoms with the following simple wavefunction,

$$|\Psi\rangle = c_g |g\rangle + c_e |e\rangle, \quad (2.12)$$

where  $|c_g|^2$  and  $|c_e|^2$  are the probabilities of finding the atom in the respective ground and excited states. Then, substituting  $H_A + H_{AL}$  into the Schrödinger equation ( $i\hbar\frac{\partial}{\partial t}|\psi\rangle = H|\psi\rangle$ ),

$$\frac{\partial c_g}{\partial t}|g\rangle + \frac{\partial c_e}{\partial t}|e\rangle = -i\omega c_e |e\rangle - i\frac{\Omega}{2}e^{i\omega_0 t}c_e |g\rangle - i\frac{\Omega}{2}e^{i\omega_0 t}c_g |e\rangle, \quad (2.13)$$

which can be separated out into two coupled differential equations:

$$\frac{\partial c_g}{\partial t} = -i\frac{\Omega}{2}e^{i\omega_0 t}c_e, \quad (2.14)$$

$$\frac{\partial c_e}{\partial t} = -i\omega c_e - i\frac{\Omega}{2}e^{i\omega_0 t}c_g. \quad (2.15)$$

Currently, we are in the reference frame of the laboratory, where we observe the atoms oscillate at the resonant frequency,  $\omega_0$ . We can apply the rotating frame transformation,  $c'_e = c_e e^{i\omega_0 t}$ , to change to the atom's reference frame. This way, we only observe changes to the atoms outside their resonant frequency. This transforms Equations (2.14) and (2.15) to,

$$\frac{\partial c_g}{\partial t} = -i\frac{\Omega}{2}c'_e, \quad (2.16)$$

$$\frac{\partial c'_e}{\partial t} = i\Delta c'_e - i\frac{\Omega}{2}c_g. \quad (2.17)$$

If we are on resonance,  $\Delta = 0$ , and we start in the ground state,  $c_g = 1, c_e = 0$ , then these partial differential equations have the solution,

$$c_g = \cos\left(\frac{\Omega}{2}t\right), \quad (2.18)$$

$$c_e = -i\sin\left(\frac{\Omega}{2}t\right). \quad (2.19)$$

Thus, atoms being driven by a resonant light field will flip sinusoidally at the Rabi frequency ( $\Omega$ ), as shown in Figure 2.8. Also, if we apply a resonant field for a time  $t$  such that  $\Omega t = \pi$  then our atoms will all been driven coherently into the excited state. A pulse like this is referred to as a  $\pi$ -pulse. A pulse of half this duration ( $\pi/2$ -pulse) brings our atoms in a 50:50 superposition state.  $\pi$ -pulses are important for coherent experiments as they manipulate atoms between two energy levels, while still maintaining (or generating) coherence between the two energy levels. Because of this,  $\pi$ -pulses are the building blocks of many quantum memory and quantum computational experiments.

Recall that the above derivation made the assumption that the driving field is on resonance,  $\Delta = |\omega - \omega_0| = 0$ . In reality this is never completely true, instead there is some non-zero detuning that shifts the Rabi frequency. In this case, we use the generalised Rabi frequency ( $\Omega$ ),

$$\Omega = \sqrt{\Omega^2 + \Delta^2} \quad (2.20)$$

and the solutions to equations 2.16 change slightly with the non-zero  $\Delta$  term. The result is an oscillation at the generalised Rabi frequency with an amplitude less than one ( $\frac{\Omega^2}{\Omega^2 + \Delta^2}$ ). Thus, a perfect, off-resonant  $\pi$ -pulse will never fully invert an ensemble of ions.

## 2.5 Photon echoes and quantum memories

In the remaining sections, I will introduce photons echoes and common quantum memory protocols. The two main quantum memory protocols studied in this thesis will also be introduced in more detail, including the non-classical tests used with these protocols. All of these quantum memory protocols store light in an ensemble of atoms and behave similarly to the photon echo. More specifically, a pulse of light is sent into (or produced by) a quantum

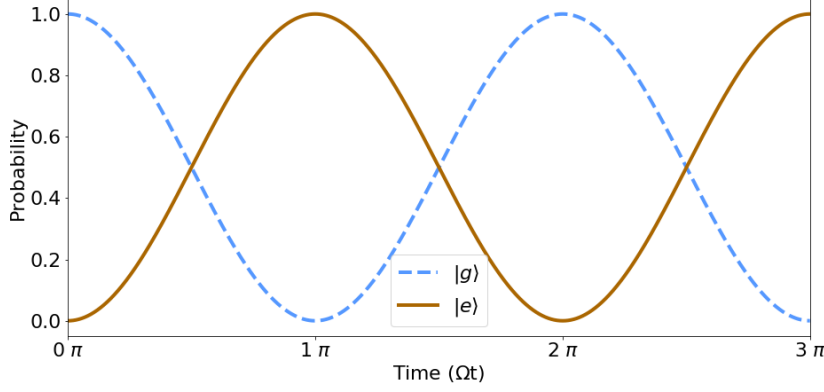


Figure 2.8: Rabi flopping, given a two level atom driven by a resonant electric field, the atoms will flip between the ground and excited state  $|g\rangle$  &  $|e\rangle$  sinusoidally. The rate of this oscillation depends on the electric field strength and the electric field-atom coupling strength.

memory and after some delay (and some pulse sequence), an echo of the original input pulse is produced.

Over this section I will explain the simplest photon echo, the two-level photon echo and why it is not suitable as a quantum memory. Then I will expand on the two-level echo to more complicated echo sequences like the four-level photon echo, the Atomic Frequency Comb (AFC), and the Rephased Amplified Spontaneous Emission protocol (RASE).

### 2.5.1 The Bloch sphere

To visualise two-level systems in the context of photon echoes and coherent measurements, a Bloch sphere representation is used (Figure 2.9). The Bloch sphere maps the state of a two level system to the surface of a sphere. The southern and northern poles,  $\pm 1\hat{z}$ , corresponds to the ground state,  $|g\rangle$ , and the excited state,  $|e\rangle$ , respectively. Any superposition state is mapped linearly on the  $\hat{z}$  axis, i.e. a 50:50 superposition state is mapped on the equator. The  $\hat{x}$  and  $\hat{y}$  axes then refer to the phase of the two level system,  $\frac{1}{\sqrt{2}}(|g\rangle + |e\rangle)$  and  $\frac{1}{\sqrt{2}}(|g\rangle + i|e\rangle)$ , respectively. A  $\pi$ -pulse will also cause a state to rotate about the  $y - z$  plane by  $\pi$  radians.

### 2.5.2 Two-level photon echo

The two-level echo sequence is simple, but does introduce new ideas and concepts that are shared with quantum memory protocols. Two-level echoes were first developed for nuclear magnetic resonance in the 1950s [35] and are used today for MRI. Optical two-level echoes were demonstrated shortly



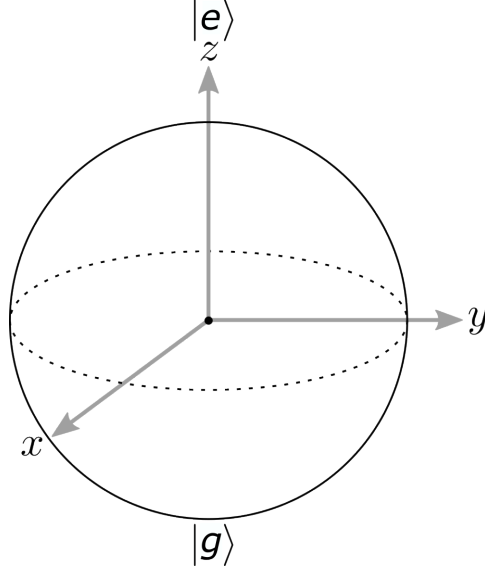


Figure 2.9: A two level system can be represented using the Bloch sphere. The poles relate to the ground and excited state of the two levels, while an angle about the  $x - y$  plane represents the phase of the system.

after the invention of the laser in the early 1960s [46]. The optical version of a photon echo is identical to the nuclear magnetic resonance echoes in all but the pulse frequencies.

A visualisation of the two-level echo is shown in Figure 2.10. Initially all the atoms are in the ground state, a  $\frac{\pi}{2}$ -pulse is sent a time  $t = 0$ . This pulse brings the atoms into a superposition state,  $\frac{1}{\sqrt{2}}(|g\rangle + |e\rangle)$ , and all the atom's Bloch vectors align with the  $y$ -axis of the Bloch sphere. At this point, the atoms begin to dephase relative to each other. The dephasing happens because the atoms have some linewidth governed by the frequency bandwidth of the  $\frac{\pi}{2}$ -pulse. This dephasing process causes the atoms to 'fan-out' along the Bloch sphere equator. As the atoms dephase the collective ensemble will emit a decaying signal called the Free Induction Decay (FID). The physical interpretation of the FID comes from the atomic ensemble's response to the  $\frac{\pi}{2}$ -pulse. When the  $\frac{\pi}{2}$ -pulse is sent to the ensemble, the ensemble absorbs the pulse. Absorption is analogous to the atoms emitting light  $180^\circ$  out of phase with the  $\frac{\pi}{2}$ -pulse, which results in destructive interference. However, when the  $\frac{\pi}{2}$ -pulse ends, the ensemble will continue to emit light (FID). As the atoms dephase destructive interference causes this signal to decay, with a lifetime that is the inverse of the  $\frac{\pi}{2}$ -pulse's bandwidth. The FID is shown as the tails of the blue trace after the two pulses at the bottom of Figure 2.10. Some time,  $t = \tau$ , after the  $\frac{\pi}{2}$ -pulse, a  $\pi$ -pulse is sent to the ensemble. The  $\pi$ -pulse causes all the Bloch vectors to flip around the  $x - y$  plane and reverses their dephasing. The Bloch vectors continue to evolve until time

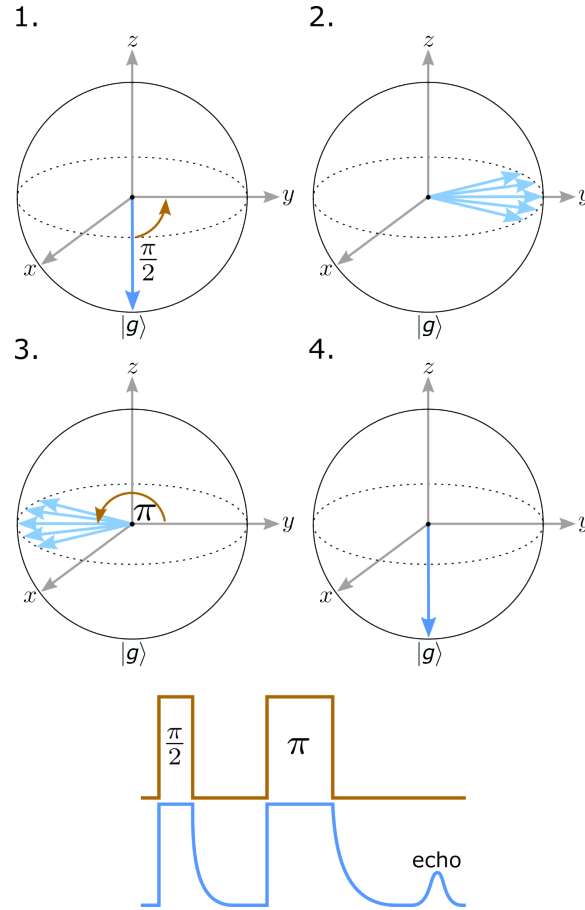


Figure 2.10: Pulse sequence of a two-level echo. The top section of the figure shows the atoms as they evolve on the Bloch sphere. The bottom section shows the light incident on the ensemble (red) and the atom's response to the incident light (blue).

$t = 2\tau$  where all the Bloch vectors re-align at the  $-y$ -axis. A pulse of light is emitted coherently as all the Bloch vectors align. In this sequence, the  $\pi$ -pulse can be considered as a time reversal event. The pulse of light emitted at  $t = 2\tau$  is a time reversal of the FID emitted after the  $\pi/2$ -pulse.

The time delay between the  $\pi/2$ -pulse and the echo can be lengthened or shortened by changing  $\tau$ . However, the echo amplitude will decrease for longer time delays. The upper bound on the time delay is limited by the homogeneous linewidth,  $\Gamma = 1/(\pi T_2)$ , of the atomic ensemble. The amplitude of the echo will exponentially decrease,  $A = e^{-\frac{\tau}{T_2}}$ . The two-level echo can be used as a way to directly measure the homogeneous linewidth of the atoms, by repeating the two-level echo multiple times with different time delays. The coherence time is defined as the time when the echo amplitude has decreased by  $e^{-1}$  of the zero time-delay echo amplitude.

We also define the rephasing efficiency of the photon echo as the ratio of the  $\pi/2$ -pulse FID intensity to the echo intensity. Remember that the FID is the response of the atomic ensemble to a coherent pulse of light, and the echo is the rephasing of this FID. Thus, the rephasing efficiency is a measure of how well we can rephase the FID using a  $\pi$ -pulse. This means that when we calculate the rephasing efficiency, the  $\pi/2$ -pulse intensity must be discarded from our calculations. This point will be important in the later experiment chapters.

The two-level echo presents a way to coherently store a pulse of light with a controllable time delay. However, a two-level echo is not capable of quantum storage. The FID created by the inversion  $\pi$ -pulse adds noise to the echo, since the inversion pulse and echo are on the same transitions the FID and the echo are at the same frequency and cannot be distinguished from each other. Theoretically a perfect  $\pi$ -pulse should not produce an FID and therefore the FID should not be a fundamental limitation. However, the rephasing  $\pi$ -pulse drives atoms to the excited state. These atoms driven to the excited state can spontaneously decay on the same transition as the photon echo. This spontaneous decay acts as a further noise source in the echo and is unavoidable. To remove the noise from the FID and spontaneous decay, the echo and rephasing  $\pi$ -pulse need to be distinguishable, a way to achieve this is to move the inversion pulse and the echo to different optical transitions. This can be achieved by extending the photon echo to four levels.

### 2.5.3 Four-level photon echoes

The four-level echo [7], as the name suggests, is an extension of the two-level echo to operate using four energy levels: two ground and two excited state levels, shown in Figure 2.11. Let us start, like the two-level echo, with an initial  $\pi/2$ -pulse on the  $|g_1\rangle \rightarrow |e_1\rangle$  transition. However, we wish for the echo to radiate on the  $|g_2\rangle \rightarrow |e_2\rangle$  transition. To achieve the same rephasing as the two-level echo, we now require two inversion pulses. One inversion pulse is

resonant with the  $|g_2\rangle \rightarrow |e_1\rangle$  and the other is resonant with the  $|g_1\rangle \rightarrow |e_2\rangle$  transitions. In pulse order, the following coherence is generated:

1. the  $\frac{\pi}{2}$ -pulse generates coherence between the  $|g_1\rangle$  and  $|e_1\rangle$  levels,
2. after a time,  $t_1$ , the first inversion pulse shifts this coherence to the  $|g_2\rangle$  and  $|g_1\rangle$  levels,
3. after a time,  $t_2$ , the second inversion pulse shifts this coherence to the  $|g_2\rangle$  and  $|e_2\rangle$  levels.

The echo is radiated time symmetric about the inversion pulses, similar to the two-level echo, however, we must also add the time between the two inversion pulses,  $t_{echo} = 2t_1 + t_2$ . With this pulse sequence, the echo and all subsequent pulses occur on different transitions, thus with frequency filtering, the FID from the inversion pulses can be completely decoupled from the echo.

The first inversion pulse shifts the coherence to the two ground levels. As explained in Section 2.2, for quantum memory experiments the ground states are hyperfine levels with long coherence times. Thus, if  $|g_1\rangle$  and  $|g_2\rangle$  are ground hyperfine levels, then we can make use of the long ground state coherence times. However, long hyperfine storage cannot, typically, be achieved with this particular pulse sequence. This is because the two ground states might have different hyperfine inhomogeneous broadenings. If this is true, then the two atomic populations will dephase at slightly different rates, given by the difference in hyperfine inhomogeneous broadening. The different dephasing rates will appear as an extra source of decoherence. We refer to this dephasing rate as the four-level echo coherence time.

The four-level echo coherence time can be extended to the hyperfine coherence time by applying a rephasing pulse on the  $|g_1\rangle \rightarrow |g_2\rangle$  transition [78]. The hyperfine transition frequencies are  $\sim$ GHz and require RF coils to drive them, adding to experiment complexity. However, when this is achieved the delay between the two inversion pulses,  $t_2$ , can be very long, up to 1.3 seconds in the case of Er:YSO [59] and hours in Eu:YSO [78]. The process of transferring optical storage to RF levels such as the hyperfine levels is referred to as spin-wave (or spin-state) storage, and is the key to quantum memories with long storage times.

#### 2.5.4 Inverted-four-level echo

In our experiments, we will use a variant of the four-level echo called the inverted-four-level echo. We use the inverted-four-level echo because it closely resembles the RASE sequence (described in a later section, Section 2.7). The inverted-four-level echo was initially demonstrated in Duda's thesis [25] as a way to predict the performance of the RASE sequence for different operating parameters.

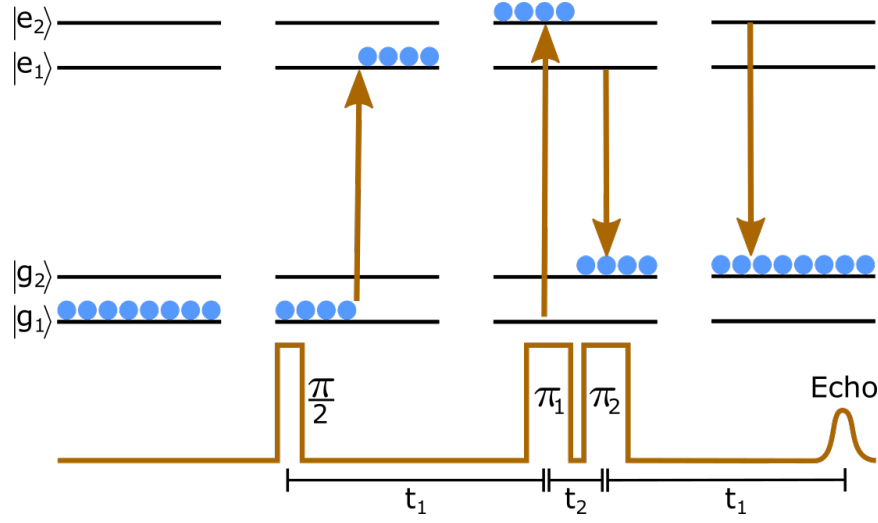


Figure 2.11: Four-level echo level diagram (top) with corresponding pulse sequence (bottom).

The inverted-four-level echo is almost identical to the four-level echo. The main difference is that all the atoms in the ensemble start in some initialisation state  $|g_i\rangle$ . From here, the population is inverted to the excited level  $|e_1\rangle$ . Now, the remainder of the inverted-four-level echo pulse sequence is identical to the four-level echo. The main experimental difference between the four-level echo and the inverted-four-level echo is that the  $\pi/2$ -pulse is applied to a transition with gain rather than absorption. The pulse is amplified as it travels through the crystal and, depending on the gain, the  $\pi/2$ -pulse may need to be heavily attenuated. Thus, this pulse will not be a  $\pi/2$ -pulse, and we will refer to this pulse as the input pulse.

Next I will discuss some of the more common quantum memory protocols, particular detail is given to the AFC and RASE protocol as they are the focus of the main experiment chapters, Chapters 4 and 6.

### Revival Of Silenced Echo (ROSE)

ROSE [19] is a quantum memory protocol very similar to the two-level echo. The difference is the rephasing  $\pi$ -pulse is instead two  $\pi$ -pulses that are spatially phase mismatched. This spatial phase mismatching stops the Bloch vectors from rephasing at the exact same time, resulting in the initial echo being suppressed or silenced. The second  $\pi$ -pulse acts to reverse the spatial phase mismatching and again rephase the Bloch vectors, which causes a revival of the silenced echo. Unfortunately, to date, ROSE has suffered from noise issues and has not yet demonstrated non-classical storage.

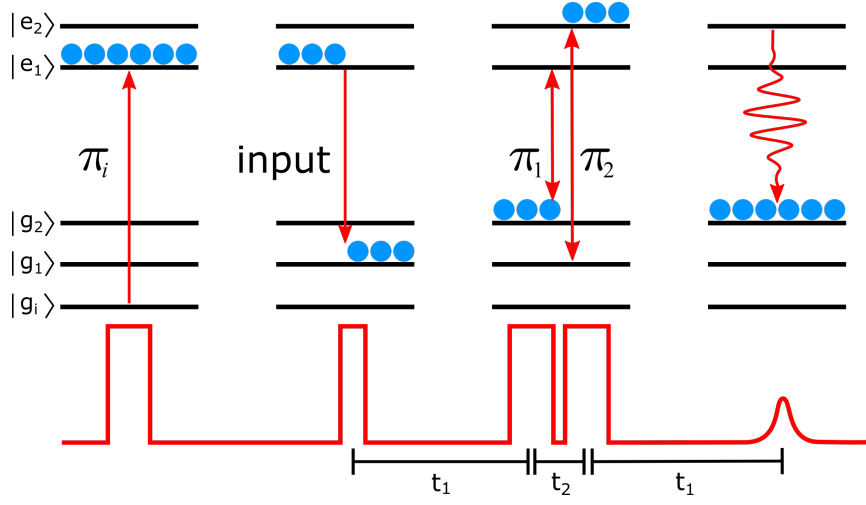


Figure 2.12: Inverted-four-level echo diagram (top) with corresponding pulse sequence (bottom).

### CRIB and GEM

Controlled Reversible Inhomogeneous Broadening (CRIB) [62] and the Gradient Echo Memory (GEM) [57] are two similar quantum memory protocols. Neither rely on inversion pulses to rephase atoms, but instead use an electric/magnetic field gradient. Recall that when a magnetic field is applied to atoms, the energy levels of the atoms shift, due to the Zeeman effect (Section 2.1.1). By preparing a narrow, optically thick ensemble, a magnetic field gradient can drastically broaden the bandwidth of the ensemble. Then a pulse of light excites the ensemble, like the two-level echo, and the atoms will begin dephasing. Reversing the field will then invert the Zeeman broadening and begin the rephasing process. The echo is then emitted time symmetric about the field reversal. GEM has been used to demonstrate some of the most efficient quantum memories to date. Achieving an efficiency of 69% in rare-earth doped solids [57] and 87% in Rubidium vapour [40]. CRIB uses the same technique, but instead applies an electric field gradient, rather than a magnetic field gradient.

### HYPER

HYbrid Photon Echo Rephasing (HYPER) [53] is a hybrid technique that combines CRIB and the two-level echo. With the goal to use the broadening from the Stark effect to reduce the noise associated with the inversion pulse in the two-level echo. An input pulse is applied at time  $t = 0$ , which is absorbed by an ensemble of atoms, like in the two-level echo. Following this input pulse, an electric field broadens the ensemble. This has the effect of reducing the absorption of the ensemble, by spreading the ensemble over a

larger frequency range. When the  $\pi$ -pulse is applied, at time  $t = t_1$ , the ensemble is then inverted, but the FID generated from the inversion pulse is diminished. The dephasing from the electric field also prevents the primary echo from forming, this silenced echo would have occurred at time  $t = 2t_1$ . The electric field is then reversed and a second  $\pi$ -pulse is then applied at a time  $t_2$ , after the initial  $\pi$  pulse. The result is an echo without FID noise from the inversion pulses.

## 2.6 The Atomic Frequency Comb (AFC)

The Atomic Frequency Comb (AFC) [2] is a quantum memory protocol that does not rely on  $\pi$ -pulses to invert or rephase atoms in order to produce an echo. In fact, the AFC can be thought of as a more passive memory protocol. As such, there is no pulse sequence or any precise timings or pulse shapes that need to be optimised for the AFC to work efficiently. The difficulty of implementing the AFC is then front loaded onto a preparation sequence. The storage time of the two-level AFC is also determined during the preparation sequence and is then fixed, making the AFC a delay line rather than a memory. Extending the AFC to hyperfine storage allows for more flexible storage times, and is needed to create a true quantum memory.

An AFC is a spectrally shaped absorption feature consisting of a series of narrow, highly absorbing spectral peaks separated by areas of low, ideally no, absorption. The frequency splitting between the teeth is referred to as  $\Delta$  and the width of the teeth,  $\gamma$ . The absorption feature, as the name implies, resembles a comb as shown in Figure 2.13. If a single photon is absorbed into the AFC then the ensemble can be described by the following Dicke state,

$$|\Psi\rangle = \sum_{j=0}^N c_j e^{i\delta_j t} |g_1 \dots e_j \dots g_N\rangle, \quad (2.21)$$

$$\delta_j = \omega + \Delta n, \text{ for some integer } n. \quad (2.22)$$

For simplicity we are ignoring spatial dependence and assuming that the teeth have 0 width and infinite absorption.  $\delta_j$  is the resonant frequency of the  $j$ th atom in the ensemble, with the corresponding probability of absorption  $|c_j|^2$ . The Dicke state tells us that a single atom has absorbed the photon, but because that absorber is unknown, we must assume the ensemble is a superposition state of every atom in the comb absorbing the photon. Alternatively, we can also conceptualise that every atom has absorbed a small fraction of the photon.

As with the photon echo, we can use the Bloch sphere to describe the state of the ensemble throughout the storage sequence, shown diagrammatically in Figure 2.14. The Bloch vectors start pointing in the  $-\hat{z}$  axis. At time

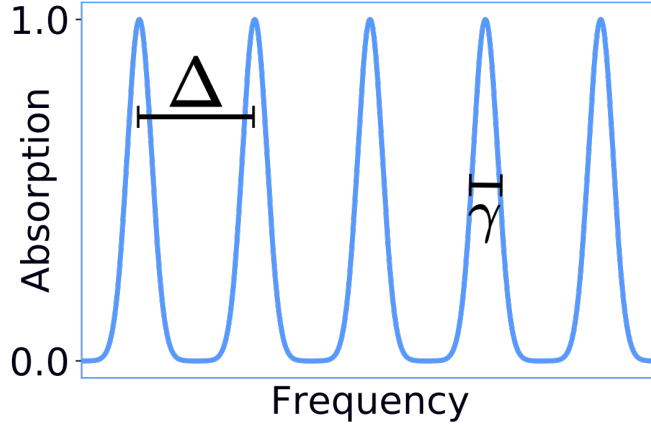


Figure 2.13: Example of an AFC absorption spectrum, showing the spacing between the teeth,  $\Delta$  and the tooth width,  $\gamma$ .

$t = 0$  a pulse, much weaker than a  $\pi$ -pulse, is absorbed by the AFC. The Bloch vectors are rotated about the  $y$ -axis and initially are all in-phase. Immediately after the pulse is absorbed, the Bloch vectors start to dephase. In the example of the photon echo, the Bloch vectors dephase according to the inhomogeneous broadening of the ensemble, which looks like the Bloch vectors are ‘fanning out’. Here, the atoms in the ensemble are all at discrete frequencies  $\omega + \Delta n$ . Thus, the Bloch vectors spread out in groups with an even spacing. After some time,  $t = \frac{1}{\Delta}$ , the Bloch vectors realign and coherently emit a pulse of light. The realigning time of the Bloch vectors is given by the inverse of the AFC tooth frequency spacing,  $\Delta$ . Thus, the time that the echo is emitted is predetermined at a time  $t = \frac{1}{\Delta}$ .

### 2.6.1 AFC efficiency

Ultimately, the free space two-level AFC is limited to  $\approx 54\%$  efficiency [62], the forward recall limit. The full mathematical derivation for the 54% limit is explained in great detail in Sangouard et al. [62]. In brief, an AFC with high optical depth will fully absorb the input pulse. However, when the echo is emitted it has to travel through the crystal where it can be reabsorbed. The efficiency of the memory grows with the optical depth ( $d$ ) by  $d^2$ , while the re-absorption grows with the Beer-Lambert law,  $e^{-d}$ . This gives an optimal efficiency when the optical depth is 2. The forward recall limit can be surpassed by using an impedance matched cavity [33].

The efficiency of the free-space two-level AFC can be determined purely by the spectra of the AFC. An ideal AFC, as was assumed in Equation (2.21), would have infinitely narrow absorption peaks with infinite absorption. However, this is not feasible in reality. The teeth of an AFC will have



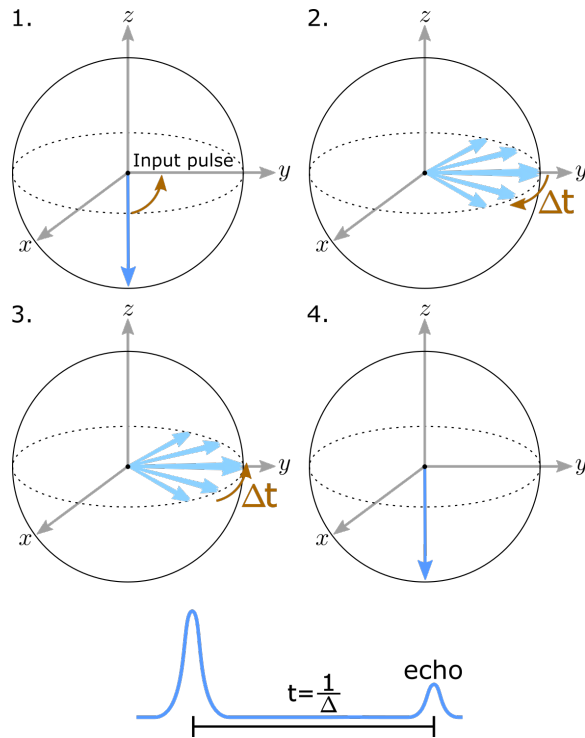


Figure 2.14: Bloch sphere representation of an AFC echo. The input pulse has been shown as a  $\frac{\pi}{2}$ -pulse for visual clarity. This evolution works for any weaker pulses, the strength of the pulse simply changes where the Bloch vectors are on the  $z$ -axis. Below the Bloch sphere is the very simple pulse sequence. An input pulse is applied at some time  $t$  and the echo is emitted at time  $t + \frac{1}{\Delta}$ .

some finite absorption. The AFC teeth must have a non-zero width in order to absorb the input pulse. If the teeth are too wide, comparable to  $\Delta$ , then not all the Bloch vectors will align at  $t = \frac{1}{\Delta}$ , resulting in a weaker echo. The efficiency then depends on the ratio between  $\Delta$  and  $\gamma$ . This ratio is called the finesse of the AFC and is defined as  $F = \Delta/\gamma$ . The optimal finesse also depends on the shape of the teeth. Where the shape of the AFC teeth will add a dephasing term to the overall efficiency. The efficiency of the AFC is then,

$$\eta = \tilde{d}^2 e^{-\tilde{d}} \eta_{\text{dephase}}, \quad (2.23)$$

where  $\tilde{d}$  is the effective absorption of the AFC. If we assume the teeth are Gaussian-shaped, the effective absorption is simply  $\tilde{d} = \frac{d}{F} \cdot \sqrt{\frac{\pi}{4 \ln 2}} \approx \frac{d}{F}$  [2]. In Equation (2.23), the first two terms are common to all forward recall memories. The last term,  $\eta_{\text{dephase}}$ , is specific to AFC's and accounts for the dephasing due to the non-zero width of the teeth. For Gaussian-shaped teeth,  $\eta_{\text{dephase}} = \exp^{-\frac{1}{F^2} \frac{\pi^2}{4 \ln 2}}$  [1]. Thus, the efficiency of an AFC is determined by the peak absorption of the teeth and the finesse of the AFC. The fact that the two-level AFC's performance is only dependent on the preparation sequence makes the AFC a good benchmarking memory.

### 2.6.2 Noise performance

In theory, an AFC is capable of storing quantum information (an arbitrary super-position state). However, in experiments, noise can affect this quantum information storage and cause a memory to become classical. It is important to have metrics to test for non-classicality in a quantum memory. One non-classicality test examines the noise performance of the memory. In the AFC experiments, we will use the noise performance test to demonstrate non-classical storage.

Noise performance is a measurement of how much noise is added to a given quantum state stored in a memory, by the memory. Where the noise added to the quantum state is defined as the variance of the echo minus the variance of the input state. Any measured added noise to the echo is assumed to be a result of storing the quantum state in the memory. We compare the noise performance of the memory to a perfect classical memory to determine if our memory is non-classical. If our memory performs better than a perfectly classical memory, then the memory is considered non-classical. The appendix of Hedges et al. [57] shows that the variance added to each quadrature of a quantum state stored in a classical memory is at least  $2\eta$ , with a storage efficiency of  $\eta$ , in units of shot noise.

## 2.7 Rephased Amplified Spontaneous Emission

The RASE [49] quantum memory protocol provides a way of creating two weak, entangled fields of light. As a memory protocol, RASE operates very similarly to the photon echo. In a previous section, we saw that a photon echo is not suitable for quantum information storage due to amplified spontaneous emission following the rephasing  $\pi$ -pulse. By initially inverting a population of atoms, RASE essentially uses this Amplified Spontaneous Emission (ASE) in place of the  $\pi/2$ -pulse in the photon echo. The amplified vacuum is entangled with the initial population of inverted atoms. By applying a  $\pi$ -pulse, the state of the atoms is recalled in the same manner as the photon echo. This creates an entangled, time reversed echo of the ASE called the Rephased Amplified Spontaneous Emission (RASE).

To understand the mechanisms of RASE we must first look at the concept of optical amplification. Then both the two level and four level variants of RASE will be explained, along with the benefits of switching to a four-level system. From here I will explain how the entanglement between ASE and RASE is quantified through correlation/covariance, which will lead into the inseparability criterion, a metric used to show non-classicality.

### 2.7.1 Optical amplification

In a classical sense, optical amplification is the process where the intensity of a light field  $I$  is amplified by a gain level  $g$ . The concept of optical gain (referred to from here simply as gain) is not intuitive. Instead, it is easier to start from a more familiar concept, absorption. We will look at the concept of gain in the context of absorption and the Bloch Sphere, introduced in Section 2.5.1. When a light field is resonant with an ensemble of atoms in the ground state ( $g$ ), the atoms absorb some photons from the light field and are promoted to the excited state ( $e$ ). The Bloch vector for this ensemble of atoms, initially pointing to  $-\hat{z}$ , has now been rotated about the  $y$ -axis, with the angle of rotation dependent on how many atoms were excited. We also know that if the light field is a  $\pi$ -pulse then all the atoms will have been driven to the excited state, Bloch vector  $+\hat{z}$ . The light field must be attenuated for energy to be conserved. If the light field was a  $2\pi$ -pulse, then the Bloch vector will have been driven around the Bloch sphere from  $-\hat{z}$  to  $+\hat{z}$  and back to  $-\hat{z}$  again. This time, for energy conservation, the  $2\pi$ -pulse must not have been attenuated as the atoms finish in the same state that they started in. Thus, as the atoms absorbed light to be promoted into the excited state, they must also have emitted light when they were driven back to the ground state.

Now consider a weak pulse of light, with much less energy than a  $\pi$ -pulse. The atomic ensemble attenuates the pulse by a factor of  $e^{-\alpha L}$  for an absorption coefficient ( $\alpha$ ) and medium length ( $L$ ). Instead, if the ensemble

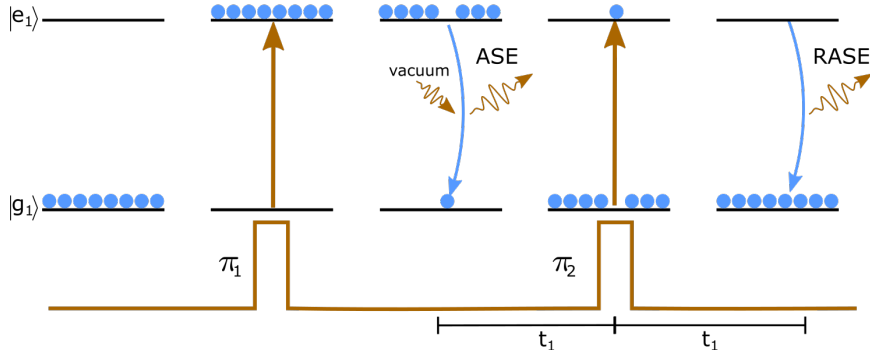


Figure 2.15: The pulse sequence and atomic levels for the two-level RASE sequence.

is driven to the excited state by a  $\pi$ -pulse a weak pulse of light is then amplified by a factor of  $e^{+\alpha L}$ , where the gain ( $g$ ) is simply the inverse of the absorption,  $\alpha L$ . If the same  $\pi$ -pulse is applied, but no weak pulse is sent, then the atoms will begin to spontaneously decay as the vacuum state interacts with the atoms. The spontaneous decay is, in turn, amplified by the ensemble of atoms creating Amplified Spontaneous Emission (ASE).

### 2.7.2 Two-level RASE

The RASE pulse sequence starts with an inversion pulse. This pulse creates a population of atoms in the excited state. As explained above, the vacuum state is then amplified by the inverted population by a factor of  $\alpha L$ . The amplification of the vacuum state is referred to as the ASE. As a consequence of producing ASE, a few atoms will decay back to the ground state. For simplicity, we will assume that only one atom has decayed to the ground state, the ensemble can be described by the following Dicke state,

$$|\Psi\rangle = \sum_{j=0}^N c_j e^{i\omega_j t} |e_1 \dots g_j \dots e_N\rangle, \quad (2.24)$$

where  $\omega_j$  is the resonant frequency of the  $j$ th atom, with the corresponding probability  $|c_j|^2$ . All the atoms are in the excited state, except for a single atom that produced the ASE signal, shown in Figure 2.15. As there is no way to determine which atom has decayed to the ground state, we have entanglement through indistinguishability. The ensemble is in a superposition state, where any of the atoms in the ensemble may have decayed to the ground state. After ASE is emitted, the Bloch vector for this ensemble is no longer aligned with the poles of the Bloch sphere. The atoms begin to dephase because of the inhomogeneity of the ensemble, just like the photon echo. This dephasing can be reversed by a  $\pi$ -pulse after a delay time of  $t_1$ .

We now have a single atom in the excited state and all other atoms were driven to the ground state, the Bloch vectors begin to rephase. At time  $t = 2t_1$  after ASE was emitted, the ensemble produces a second photon, the Rephased Amplified Spontaneous Emission (RASE). Here we have created two time separated photons that are entangled.

The two-level RASE sequence also suffers from the same drawbacks of the two-level echo. In theory, a perfect rephasing  $\pi$ -pulse will also generate no free induction decay (FID) or excess noise as all the atoms are driven to the ground state. In practice, however,  $\pi$ -pulses are not perfect and rephasing pulses produce an FID. This FID is produced at the same frequency as the RASE signal, and the RASE signal can not be discriminated from the large FID. An imperfect rephasing  $\pi$ -pulse will also leave some atoms in the excited state. These atoms will continue to spontaneously decay, which will add more noise to the RASE signal. The delay time,  $t_1$ , is also limited by the optical coherence time of the atoms. For longer delay times hyperfine rephasing is required (Section 2.5.3), thus at least three levels are needed, however there is a benefit to using a total of four levels.

### 2.7.3 Previous four-level demonstrations

There have been two previous four-level RASE demonstrations to date. Both demonstrations used the REIC, Pr:YSO, as a storage material. The first four-level demonstration was performed by Beavan et al. [6]. In this demonstration, a pulse sequence similar to the previously discussed four-level echo was used. Correlations between the ASE and RASE fields were clearly shown using single photon detection. However, these results were not non-classical. The second four-level RASE demonstration was performed by Ferguson et al. [30]. These experiments were a continuation of Beavan's work, but heterodyne detection was used instead of single photon detectors. The improved spectral filtering from heterodyne detection, along with experimental stability improvements, allowed a non-classical demonstration with 98% certainty [30].

### 2.7.4 Four-level RASE

We can extend the RASE protocol to four levels, using two ground states and two excited states and a fifth initialisation level. The benefit of this configuration is that the  $\pi$ -pulses, ASE, and RASE are produced at different frequencies. This removes the noise issues found with 2 level RASE because the  $\pi$ -pulse FIDs can be spectrally filtered from the RASE signal. On top of this, the long coherence times of the hyperfine levels can be used to extend the storage time of the RASE protocol. This spectral filtering and long coherence times can be achieved by using three levels, in a  $\Lambda$ -system. However, a three-level system would only use one excited state. This means that both ASE

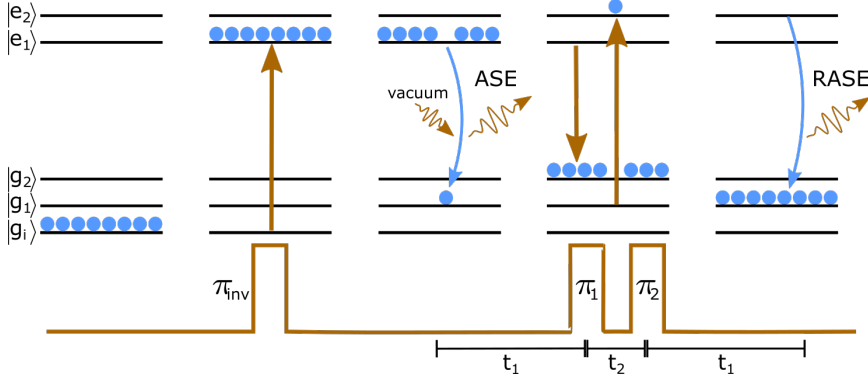


Figure 2.16: Four-level RASE pulse sequence and atomic level diagram.

and RASE use the same excited state level, and an imperfect rephasing  $\pi$ -pulse would leave atoms in the excited state where they can spontaneously emit. Using four levels resolves this problem by introducing a secondary excited state level at a different frequency.

Figure 2.16 shows the pulse sequence for the four-level RASE scheme. However, before performing the RASE sequence, we first need to prepare the ensemble. The four-level RASE sequence, unlike the two-level RASE, uses multiple ground state levels ( $g_i, g_1, g_2$ ) and we require that  $g_1$  and  $g_2$  are completely empty of atoms. If  $g_1$  and  $g_2$  are not empty, then the ASE and RASE signals will be attenuated, leading to extra loss. Furthermore, these atoms can be driven to the excited state levels by the rephasing  $\pi$ -pulses ( $\pi_1$  and  $\pi_2$ ) where they can spontaneously decay, potentially adding more noise to the sequence. The exact preparation sequence will be explained in Chapter 3, for now we shall assume that only  $g_i$  contain atoms.

The ensemble of atoms is driven to the excited state  $e_1$  by an inversion  $\pi$ -pulse,  $\pi_{inv}$ . These inverted atoms will amplify the vacuum state, creating ASE on all three possible optical paths ( $e_1 \rightarrow g_i, e_1 \rightarrow g_1, e_1 \rightarrow g_2$ ). However, we're only interested in the ASE produced between  $g_1 \rightarrow e_1$  and the other ASE signals can be spectrally filtered. After some time window of length  $t_1$  the first rephasing  $\pi$ -pulse drives the atoms in the excited state from  $e_1 \rightarrow g_2$ . This stops the production of ASE photons and transfers the coherence to the ground hyperfine levels. Hyperfine rephasing pulses can be added here to facilitate long storage times. After a storage time  $t_2$  the second rephasing  $\pi$ -pulse drives the decayed atoms to the excited state  $g_1 \rightarrow e_2$ . RASE is then emitted over the duration of  $t_1$ , time symmetric about the rephasing  $\pi$ -pulses.

As can be seen from Figure 2.16, all the signals are resonant with distinct optical transitions, ASE ( $g_1 \rightarrow e_1$ ), RASE ( $g_2 \rightarrow e_2$ ) and the  $\pi$ -pulses ( $g_2 \rightarrow e_1$ ) and ( $g_1 \rightarrow e_2$ ). Also, hyperfine storage is built into the sequence, extending the storage time further only requires a hyperfine rephasing RF

pulse.

### 2.7.5 Correlation and covariance

To quantify the entanglement between the ASE and RASE fields, and eventually demonstrate non-classicality, we must quantify the strength of the correlation between the two (R)ASE fields. In statistics, correlation and covariance are defined as:

$$\text{corr} = \rho_{AB} = \frac{\langle (A - \mu_A)(B - \mu_B) \rangle}{\sigma_A \sigma_B}, \quad (2.25)$$

$$\text{cov} = \sigma_{AB} = \langle (A - \mu_A)(B - \mu_B) \rangle, \quad (2.26)$$

where  $\mu_x$  is the mean of the variable  $x$ ,  $\langle x \rangle$  is the expectation value of  $x$  and  $\sigma_x$  is the standard deviation of  $x$ . I will refer to the variance of a variable  $x$  as  $\sigma_x^2$ . The expectation value for a discretised variable is,

$$\langle X \rangle = \frac{1}{n} \sum_{i=0}^{i=n} x_i, \quad (2.27)$$

where  $x_i$  is a measurement of the variable  $X$ , assuming all measurements are weighted equally. In our experiments, we are also interested in the time-varying cross-correlation between the ASE and RASE fields, rather than a static correlation defined above. We can instead write the correlation as a function of a temporal offset between the two variables,

$$\rho_{AB}(t) = \langle (A(\tau) - \mu_A)(B(\tau - t) - \mu_B) \rangle \cdot \frac{1}{\sigma_A \sigma_B} \quad (2.28)$$

$$\propto \sum_{\tau=t-}^{\tau=t+} (A(\tau) - \mu_A)(B(\tau - t) - \mu_B) \cdot \frac{1}{\sigma_A \sigma_B}, \quad (2.29)$$

where  $\rho_{AB}(t)$  gives a discrete series of correlation values between the two variables A and B for some temporal offset,  $t$ , between the two variables. We can make this equation continuous by integrating instead,

$$\rho_{AB}(t) = \frac{1}{\sigma_A \sigma_B} \int_{\tau=t-}^{\tau=t+} \bar{A}(\tau) \cdot \bar{B}(\tau - t) d\tau \quad (2.30)$$

$$\propto \bar{A}(\tau) * \bar{B}(\tau - t). \quad (2.31)$$

Note, that I have defined  $\bar{X}(\tau) = X(\tau) - \mu_X$ . Equation (2.30) is simply the definition of the convolution between the two variables A and B. This means that we can calculate the correlation between our ASE and RASE

time windows by finding the convolution between the two time windows. The physical interpretation of this is that if the two fields are perfectly aligned ( $t = 2t_1 + t_2$  from Figure 2.16) then the overlapped ASE and RASE windows will coherently add, giving a non-zero magnitude. As the two windows misalign ( $t \neq 2t_1 + t_2$ ) the ASE and RASE windows should appear to be completely random variables, since the two fields are derived from the vacuum state. In reality, our (R)ASE will have some spectral bandwidth in which the (R)ASE fields will stay correlated for a time inversely proportional to that bandwidth.

The correlation metric is doubly useful for the RASE sequence. Since the ASE and RASE signals are derived from the vacuum state, an ASE window will only be correlated with the corresponding RASE window. Unlike the AFC, ROSE, or photon echoes whose inputs are derived from a laser. Because of this, we can ensure that the ASE is truly spontaneous (and not stimulated) by looking at the correlation between the ASE window and a phase correcting reference pulse, or between two separate ASE shots. Both of these cases should give no correlation.

### Inseparability

We can quantify the strength of the entanglement between ASE and RASE windows by looking at their correlations. This is a useful metric for an initial demonstration, but we still require a way to show that the correlation is non-classical. To show this, we will also show that the ASE and RASE fields form a squeezed state [23] and thus the covariance of the two fields exhibits noise smaller than the shot noise. We will use the inseparability criterion to quantify the noise of the squeezed state and demonstrate that the two fields are inseparable, a necessary condition for quantum entanglement. The inseparability criterion was proposed by Duan et al. [23].

To measure the separability of a quantum state, we must measure two independent quadratures of the state. By using heterodyne detection, we can measure the in-phase (I) and out-of-phase (Q) quadratures of our ASE(1) and RASE(2) fields. We then construct a maximally entangled state from our two quadratures:

$$\hat{u} = \sqrt{b}I_1 + \sqrt{1-b}I_2, \quad (2.32)$$

$$\hat{v} = \sqrt{b}Q_1 - \sqrt{1-b}Q_2, \quad (2.33)$$

where  $b$  is a unitless weighting parameter between 0 and 1. When  $b = 0$  the operators  $\hat{u}, \hat{v}$  are just the RASE quadratures, and similarly when  $b = 1$  they are the ASE quadratures. The inseparability criterion then states that, for a separable quantum state, the summed variances for the operators



follows the inequality,

$$\sigma_u^2 + \sigma_v^2 \geq 2 \text{ (shot noise units)}. \quad (2.34)$$

For a maximally entangled state, this equation is bounded by 0, instead of 2. The variance of the operator is given by  $\sigma_x^2 = \langle x^2 \rangle - \langle x \rangle^2$ . Again, our states are derived from an amplified vacuum state, which has an expectation value of 0,  $\langle x \rangle = 0$ . Thus, the variance is simply  $\langle x^2 \rangle$ . We can write the variance of our two operators  $\hat{u}, \hat{v}$  as,

$$\langle u^2 \rangle = b \langle I_1^2 \rangle + (1 - b) \langle I_2^2 \rangle + 2\sqrt{b(1 - b)} \langle I_1 I_2 \rangle, \quad (2.35)$$

$$\langle v^2 \rangle = b \langle Q_1^2 \rangle + (1 - b) \langle Q_2^2 \rangle + 2\sqrt{b(1 - b)} \langle -Q_1 Q_2 \rangle. \quad (2.36)$$

Equations (2.35) and (2.36) are composed of the variances of ASE, RASE and the covariance between ASE and RASE along with the weighting parameter,  $b$ . The variances and covariances are all elements of the covariance matrix. The extrema of the inseparability criterion will be variances of the ASE and RASE fields. If the ASE and RASE have no correlation, then the inseparability criterion will be a straight line between the two ASE and RASE variances ( $\langle I_1 I_2 \rangle = 0$ ). If the two windows are vacuum, then the inseparability criterion will be a flat line at 2. Finally, if the ASE and RASE windows are correlated (negatively) then the inseparability line will dip with minima at some value of  $b$  between 0 – 0.5 depending on the rephasing efficiency of the RASE sequence.

### 2.7.6 Comparing re-preparation of memory protocols

When experimentally realising quantum memory protocols for quantum networks, a very important factor is quantum key distribution rate. This distribution rate is limited by the repetition rate of the experiment and the mode storage capacity of the memory. First, I will discuss the repetition rates of memory protocols. Repetition rate is limited by how quickly a protocol can be re-prepared between storage events. The need for re-preparation can be greatly reduced if the ensemble returns to pre-storage state. The AFC and GEM protocols are good examples of protocols that require minimal re-preparation. The four-level protocols, such as: RASE, four-level echo, and inverted-four-level echo, use several  $\pi$ -pulses that transfer the initial population to another energy level (from  $g_i$  to  $g_2$  in RASE). For RASE, re-preparing the ensemble involves pumping atoms back from  $g_2$  to  $g_i$  for every storage event. The need for constant re-preparation can slow down data collection times and is discussed in the RASE chapter, Section 6.2.

At first glance, the need for re-preparation is a limitation of protocols with multiple  $\pi$ -pulses, such as RASE. However, this is only true for memory demonstrations without hyperfine rephasing. Hyperfine rephasing requires

transferring the prepared ensemble into a different spin level, using a  $\pi$ -pulse, destroying the initially prepared feature. The ensemble would need to be transferred back to the initialisation level, just like the four-level protocols as explained in the above paragraph. re-preparation is then a problem inherent to any protocol that will use hyperfine rephasing, which will be needed to achieve the long storage times needed for a global quantum repeater network. In the work presented in this thesis, re-preparation time is limited by erbium's exceptionally long optical lifetime, long even for the lanthanides. For example, Pr:YSO and Eu:YSO, two other commonly used materials for memory demonstrations, have optical lifetimes of 160  $\mu$ s [27] and 1.5 ms [28] respectively. Furthermore, vapour-based memories, such as Rubidium, have much shorter optical lifetimes and would have much faster re-preparation times. Erbium's lifetime can be reduced using Purcell enhancement via an optical cavity [14, 54], this technique is relatively new for erbium.

Quantum key distribution rates are also limited by the mode storage capacity of the memory. In this example, I will compare the mode storage capacity of the two memory protocols presented in this thesis, AFC and RASE. In terms of mode storage capacity, the AFC protocol is heavily limited, the number of modes stored in an AFC is limited by the number of teeth in the AFC. This essentially removes a form of multiplexing; the temporal mode storage capacity of the AFC is also set by the number of teeth (spectral multiplexing). Essentially, this means that frequency and temporal multiplexing are one and the same in the AFC. However, in the RASE protocol, a single RASE feature can store  $n$  temporal modes. Spectrally multiplexing RASE increases the mode storage capacity to  $m \times n$ , where  $m$  is the number of frequency modes, compared to the  $m$  modes available to the AFC.

In conclusion, the re-preparation step needed between each RASE shot is a limitation of all memory protocols once hyperfine rephasing is considered. However, the slow ensemble preparation shown in this thesis is a limitation of the memory material due to erbium's long optical lifetime. The optical lifetime can be reduced using Purcell enhancement at the cost of adding experimental complexity.

## 2.8 Summary

The rare-earth ions offer a lot of useful coherent properties due to their shielded valence  $4f$  electrons. Most importantly, the rare-earth ions offer very long hyperfine coherence times, useful for storing quantum information over long timescales. Particularly, we looked at the properties of the Kramers ions and erbium-167.

Following this, the theory of atom-light interactions and spectral hole-burning was discussed. The theory in these sections lays the foundation of

the experimental techniques used, and developed, in the following experimental chapters. This is also built on in the photon echoes section, which briefly explains several of the quantum memory protocols. Of these protocols, the Atomic Frequency Comb (AFC) and Rephased Amplified Spontaneous Emission (RASE) are explained in greater detail as they are the focus of the two main experimental results chapters.



## Chapter 3

# Experimental Setup

Quantum memory protocols typically have simple pulse sequences, with only a few steps. The main experimental complexity in running quantum memory experiments comes from the atom ensemble preparation that takes place before the protocol's pulse sequence, and the frequency control needed to run the pulse sequence on the atomic ensemble. Quantum memory protocols, at a minimum, require absorption features with high absorption for any ions participating in the memory, and low absorption for any spectator ions. To tailor these optical features from a broadband optical ensemble, a laser with precise frequency and amplitude control is needed. This chapter explains the experimental setup used in this thesis and the ensemble preparation techniques developed for the main experiment chapters. Finally, some spectroscopy experiments, related to the ensemble preparation, are also presented.

This chapter contains the information needed to understand the main experiment chapters, Chapters 4, 5, and 6. The experiment overview (Section 3.1) introduces the experiment and Sections 3.2 – 3.7 explain sections of the experiment in greater detail. Then, ensemble preparation techniques used in the main experiment chapters are explained (Section 3.8): the spin polarisation, and selective anti-polarisation sequences. Finally, some basic spectroscopy experiments, related to the preparation processes, are discussed (Section 3.9).

### 3.1 Experimental overview

Figure 3.1 shows the experiment setup used for all the experiments performed in this thesis. The stable laser controlled all the pulse sequences and readout described in the experiments. An amplitude modulating electro-optic modulator (AM-EOM) was used to precisely control the frequency and power of the stable laser. The components in the grey rectangle were added during the RASE experiments, Chapter 5, an erbium doped fibre amplifier (EDFA) am-

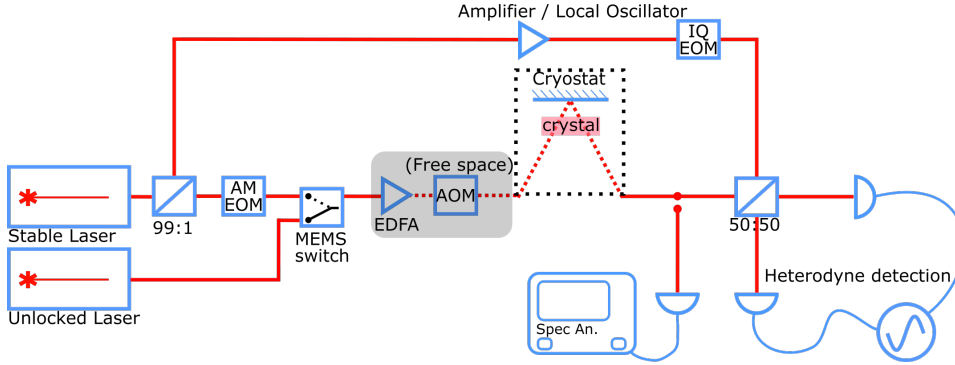


Figure 3.1: The general diagram of the experimental setup in all experiments. Light propagated through fibre optics and fibre optic elements, except when coupling into and out of the cryostat, which was coupled in free space. The solid red line indicates optical fibres, the dashed red lines indicate a free space beam. The greyed region was only added in the RASE experiments, Chapter 5.

plified light going to the cryostat, and an acousto-optic modulator (AOM) switched between low and high intensity, by controllably attenuating the laser. The unlocked laser was a sweepable laser source that performed part of the ensemble preparation process. A switch was used to control which laser accessed the sample. Light coupled out of the cryostat was then sent to data acquisition. Data was acquired either by a pair of heterodyne detectors or sent to a fast detector to record spectra using a spectrum analyser (Spec An.). Finally, a small pick-off of the stable laser was amplified and modulated to act as the local oscillator for heterodyne detection.

### 3.2 Cryostat and sample

All the experiments conducted in this thesis used an isotopically purified (0.005%)  $^{167}\text{Er}:\text{YSO}$  crystal with  $91.77 \pm 0.04\%$  isotopic purity. The crystal's dimensions were  $3 \times 4 \times 5$  mm in the  $D_1, D_2, b$  axes, respectively.

With light propagating, and magnetic field applied in the  $D_1$  direction.

Experiments investigating coherent properties in rare-earth ion doped crystals (REIC) require cryogenic temperatures. In erbium, a large magnetic field is needed to achieve the long coherence times needed for quantum communications [59]. These experiments were conducted in an Oxford helium bath cryostat with a superconducting magnet capable of generating magnetic fields up to 15 T. In these experiments, a magnetic field of 6 – 7 T was applied along the crystal's  $D_1$  axis, laser light also propagated along this direction. The crystal was cooled by letting liquid helium flow from a helium reservoir into the sample space. Once the crystal was immersed,

the helium flow was stopped, then the temperature was lowered to 1.4 K by using a scroll pump to lower the pressure in the sample space. The crystal was optically accessible through a series of three windows at the bottom of the cryostat. A mirror directly above the crystal reflected light back through the crystal and out the windows. This reflected light was then coupled into a single-mode fibre for detection.

Vibrations were an issue in the experiment because the superconducting magnet's magnetic field was not entirely homogeneous. Any change in the position of the crystal in the magnetic field caused the atoms' optical transitions frequency to change. Initially, two sources of vibrations were from the scroll pump pumping on the sample space coupling to the cryostat via the pumping line and the vibrations in the lab floor coupling to the base of the cryostat. The pump was moved to another room with an extended pumping line to reduce the effects of the vibrations coming through the pumping line, and the cryostat was moved onto a small vibration isolation table.

### 3.3 Laser path

In the experiment setup shown in Figure 3.1, the stabilised laser used differed between the AFC experiment and the RASE experiment. In the AFC experiments, the stabilised laser was a Thorlabs TLK-1150R diode laser stabilised to a home-built fibre reference cavity. For the RASE experiments, the stabilised laser was replaced with a Koheras E15 BASIK fibre laser with a linewidth of 0.1 kHz. In the non-classical RASE experiments, Section 6.4 onwards, the Koheras laser was locked to a reference cavity.

The stabilised laser light was passed through an amplitude modulating electro-optic modulator (AM-EOM), explained in Section 3.5. This allows for agile frequency control whilst still benefiting from the stability of cavity-locked feedback. This laser was used to probe or burn small sections of the inhomogeneous line or sweep the entire 2 GHz optical line. A micro electromechanical systems (MEMS) was used to control which laser accessed the sample. The MEMS switch had a switching time of 300  $\mu$ s with an extinction ratio of at least 60 dB. At the cryostat, the laser was coupled to free space and then focused onto a mirror directly above the crystal, with a beam waist of  $40 \pm 1$   $\mu$ m. The mirror above the crystal reflected light back through the crystal in a double-pass configuration. This double-pass configuration gave the crystal an effective thickness of 6 mm. The laser beam focus was optimised such that the beam intensity was maximum in the crystal. For a single pass configuration, this is when the beam focus is in the centre of the crystal. However, for a double pass configuration, the maximum laser energy density was when the two beams spatially overlap, i.e. when the laser was focused on the mirror above the crystal. The beam focus was optimised by maximising the Rabi frequency, Section 2.4: the laser

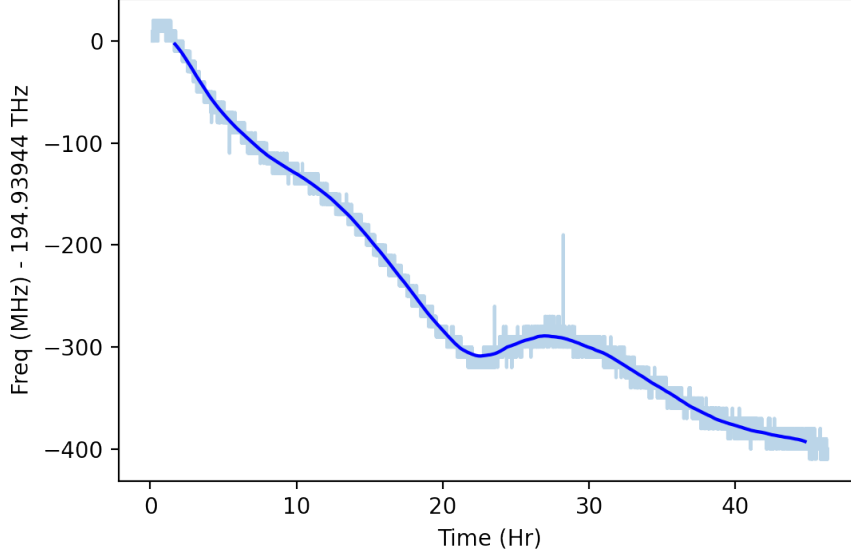


Figure 3.2: Free-running fibre laser drift, recorded on a wavemeter. The raw wavemeter data is shown in grey. Because the frequency resolution was only 10 MHz, the data has been averaged, shown in blue.

was swept over the optical line and attenuated until Rabi oscillations were weak, but noticeable. Then, the focus of the beam was adjusted to increase the Rabi oscillations, attenuating the laser further and repeating as needed.

Light exiting the cryostat was then coupled back into a single-mode fibre for detection, either by a fast 5 GHz InGaAs detector or to a pair of balanced heterodyne detectors. The 5 GHz detector output was recorded with a 2.9 GHz HP-8560 spectrum analyser (Spec An. in Figure 3.1). The heterodyne detectors (Section 3.7.1) had a bandwidth of 30 MHz bandwidth and the output was recorded on a 5000 series Picoscope (oscilloscope).

### 3.4 Laser frequency stabilisation

This section describes the laser frequency stabilisation and explains the two laser frequency stabilisation setups used throughout this thesis. The Koheras E15 BASIK fibre laser used in Chapters 5 and 6 had a linewidth of 100 Hz, however, this was the instantaneous linewidth which was only true over  $\sim 10$  ms timescales. Pressure and temperature fluctuations could cause the laser's frequency to drift by  $> 100$  MHz/day, Figure 3.2. In the RASE experiments, Chapter 6, data recording would take place over hours, and over this timescale the laser must not drift relative to the erbium inhomogeneous



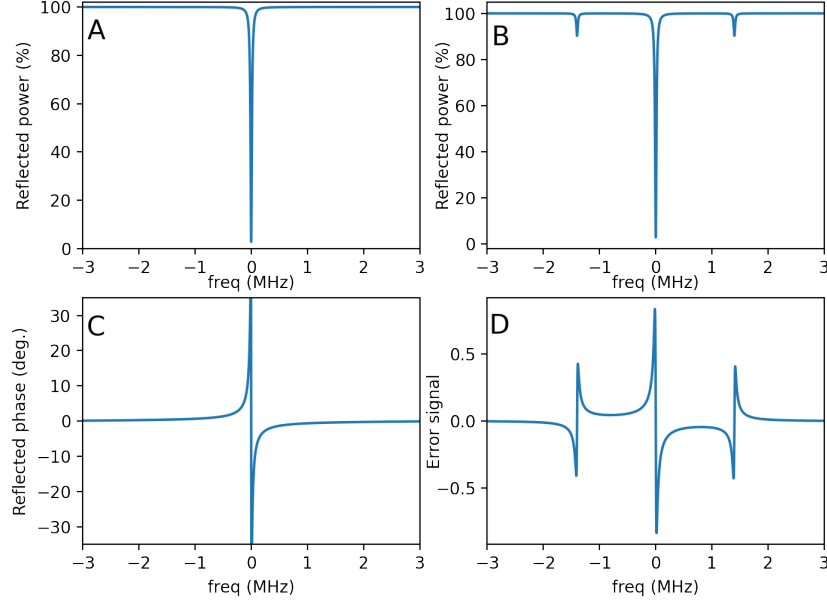


Figure 3.3: Modelled cavity transmission and error signal. A shows the reflection spectrum of a Fabry-Perot cavity. B shows the reflection spectrum if the laser is phase modulated at a constant frequency. C shows the phase of the reflection signal from A. D shows the error signal, which can be generated from the reflection signal shown in B.

linewidth, 150 MHz. Drifts as small as 10 MHz had noticeable effects on the data. Thus, the laser had to be frequency locked to a stable frequency reference, such as a Fabry-Perot cavity [22]. Frequency locking a laser to a reference cavity can also decrease the instantaneous linewidth of the free-running laser, sub-Hz linewidths have been demonstrated [77].

I briefly describe the laser frequency stabilisation, more information can be found in references [22, 64, 8]. Both stabilised lasers had their frequencies locked to a Fabry-Perot cavity. The Pound-Drever-Hall (PDH) technique was used to lock the lasers to the dip of the cavity reflection. The PDH technique uses a phase modulator to apply sidebands to a laser. The reference cavity was used as a frequency discriminator, such that a beat signal was produced when one of the bands was resonant with the reference cavity. The beat signal can be demodulated to produce the characteristic error signal, Figure 3.3 D.

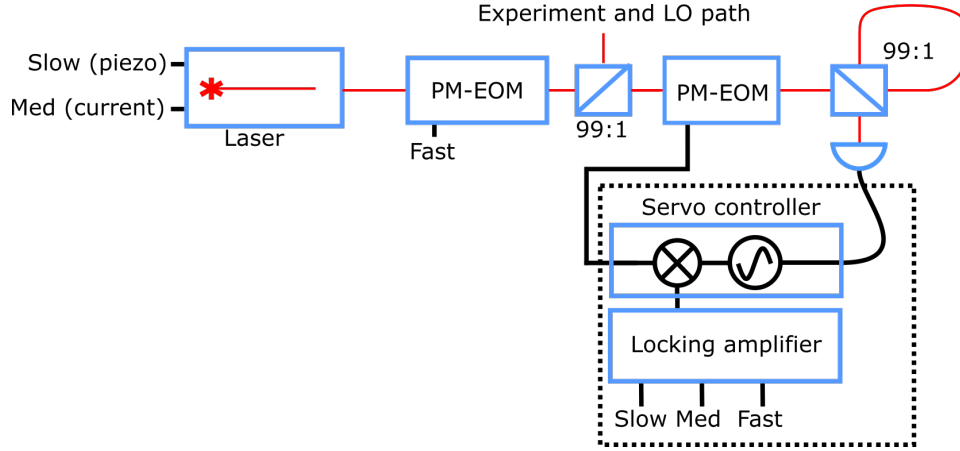


Figure 3.4: Diode laser locking experiment setup. ‘Laser’ refers to the Thorlabs TLK-1150R diode. The black box indicates the locking electronics.

### 3.4.1 Laser locking setups

A small pick-off of the laser was sent to the laser locking path. First, the light was sent through a phase modulator, which applied the locking sidebands. From here the laser was coupled into the reference cavity, the cavity’s reflection was sent to a fast detector. The signal from the detector was demodulated by the servo controller to create the error signal. The locking amplifier filtered and amplified the error signal before sending it back to the laser to apply feedback.

#### Diode laser

This laser locking setup was used in this chapter as well as in Chapter 4. All the components in this setup were fibre based, so no alignment was needed. Figure 3.4 shows the experimental diagram of the diode laser locking setup. Light from the diode laser passed through a PM-EOM before splitting off to the laser locking path.

The reference cavity was designed in-house by a previous PhD student, Milos Rančić. The cavity was a 99:1 fibre beamsplitter where two of the ports were spliced together, creating a fibre reference cavity. Light off-resonant to the cavity would be 99% reflected by the beamsplitter. Light on resonance with the cavity would circulate in the spliced optical fibres. The loss of the cavity was 1% plus the loss of the fibre splice. This cavity had a finesse of 130, with a cavity linewidth of 800 kHz. The reference cavity had thermal stabilisation, but still had a thermal drift of 10 MHz/hr.

The feedback electronics had several frequency ranges: a low frequency range (DC - 10 Hz), which applied feedback via a piezo on the grating arm of the laser cavity. A medium frequency range (10 – 10,000 Hz), which

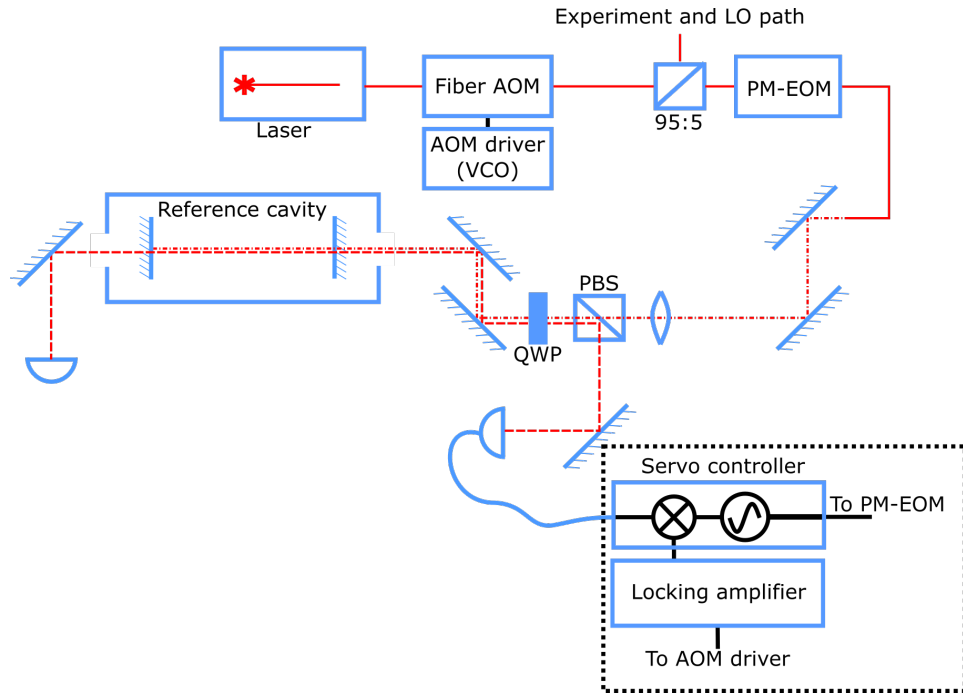


Figure 3.5: Fibre laser locking experiment setup. ‘Laser’ refers to the Koheras E15 BASIK fibre laser. The solid red line indicates optical fibres, the dashed and dash-dotted lines indicate a free space beam. The black dashed box indicates the locking electronics.

applied feedback by modulating the current powering the laser. Finally, a high frequency range (10 – 2,000 kHz), which applied feedback via the first PM-EOM.

The Thorlabs laser diode was locked with a 20 kHz linewidth. However, this was only true when there was minimal audio noise around the laser. The motor controlling the position of the diffraction grating in the laser cavity had a mechanical resonance at 525 Hz. This means that any audio from the lab at this frequency, such as people talking or nearby vacuum pumps, could cause instabilities in the laser which corresponded to frequency jumps of hundreds of kilohertz. This limitation was removed in the RASE experiments when the Thorlabs diode laser was replaced with the fibre laser, in Chapters 5 and 6.

### Fibre laser

This laser locking setup was used in the non-classical RASE experiments, Section 6.4. Figure 3.5 shows the fibre laser locking experimental diagram. First, the output of the laser was sent through a fibre coupled AOM. This AOM applied the laser locking feedback. After splitting into the laser locking

path, the laser beam was coupled into free space and sent through the cavity alignment optics. The laser beam was focused by a 500 mm focal length lens to match the divergence of the reference cavity. A polarising beamsplitter and a quarter waveplate were used to allow light reflected off the cavity to be sent to the locking detector. The locking detector then sent the locking signal to the feedback electronics. The feedback electronics had a single frequency range (0 – 2 MHz) which applied feedback to the laser by the AOM

The reference cavity was a Stable Laser Systems notched Fabry-Perot cavity inside a vacuum cavity housing by the same company. The cavity had a linewidth of 30 kHz and a large finesse, 50,000, so precise alignment was needed to couple light into the cavity. The cavity was pumped to  $< 10^{-6}$  mbar and had active thermal stabilisation to keep the cavity drift rate as low as  $< 5$  kHz/day. However, the cavity housing had a leak of 0.04 mbar/day, which equated to a frequency drift of 2 MHz/day. This drift rate was acceptable for the measurements in this thesis.

To keep the fibre laser locked to the reference cavity, the AOM had to counteract the thermal drift of the laser. The AOMs bandwidth was only 20 MHz, which meant that the laser would fall out of lock if the laser drifted beyond this frequency range. From Figure 3.2, we can see that the laser will stay locked for a few hours at most, before drifting too far. Like the diode laser, the fibre laser also had a piezo in its laser cavity. One solution to the thermal drift problem would be to use the piezo in the lasing cavity to counteract the long term thermal drifts, similar to the slow frequency feedback stage in the diode laser locking. However, the piezo driver injected high frequency (100 kHz) phase noise onto the laser, which would throw the laser out of lock. Instead, a python script was developed to change the laser’s wavelength setting, counteracting the long term thermal drifts. The laser’s wavelength was controlled thermally, however the software provided to interface with the laser did not allow access to the laser’s temperature settings. Instead, the laser’s temperature could be controlled, by proxy, through the laser’s wavelength setting. The wavelength tuning resolution was 0.1 pm, which is a frequency resolution of  $\sim 12$  MHz. A 12 MHz resolution is too large, given the 20 MHz bandwidth of the AOM. Smaller wavelength steps were achieved by applying pulse width modulation to the laser wavelength setting.

Pulse width modulation was achieved using the following algorithm. The laser wavelength setting was rounded down to the nearest 0.1 pm ( $\lambda_r$ ) with the remainder,  $\lambda_e$ . Let  $s$  be the fraction of a laser wavelength step,  $s = \frac{\lambda_e}{0.1}$ , in picometers. The python script would send the following commands, on loop.

```
Set wavelength to  $\lambda_r$ 
Wait  $2 \cdot (1 - s)$  seconds
Set wavelength to  $\lambda_r + 0.1$ 
```

Wait  $2 \cdot s$  seconds

The thermal response time of the laser was long, 1 – 10 seconds. By switching the laser wavelength every second, the actual wavelength of the laser ( $\lambda$ ) averaged between the two set wavelengths. The laser wavelength will approach the following value, assuming a sufficiently long thermal time constant,

$$\lambda = \lambda_r \cdot (1 - \text{step}) + (\lambda_r + 0.1) \cdot \text{step}.$$

This method was used to control the wavelength of the laser to  $<0.01$  pm ( $\sim$ MHz) steps.

In Section 6.5, 30 kHz phase noise was discovered on the frequency locked fibre laser. The phase noise was being injected onto the laser by an oscillation in the frequency feedback loop. There was no one point of failure that caused this oscillation, but the combined effects of two issues: the AOM modulation time delay, and the locking electronics bandwidth. AOMs have an intrinsic time delay before modulation is applied to the light. This time delay is limited by the speed of sound in the AOM. In effect, this time delay adds a phase shift to the laser and limits the bandwidth of the laser locking. The locking electronics had a specified bandwidth of 2 MHz, however, the pre-amplifier was damaged, in effect, this limited the locking electronics bandwidth to 100 kHz.

A solution to these problems is to build customised locking electronics with a higher bandwidth and to have two stages of frequency feedback,  $< 10$  kHz feedback and higher frequency feedback applied to the laser by the AOM and a PM-EOM, respectively. This solution is similar to the diode laser's locking electronics, but the high frequency feedback will be limited to  $\sim 100$  kHz rather than  $\sim$  MHz. However, this solution was not implemented in time for these experiments.

### 3.5 Electro-optic modulators

The experimental techniques that will be discussed in the following chapters required a broad range of laser frequency control. From GHz wide, high power laser sweeps to narrow sub-MHz pulses near the single-photon level. Also, due to the large hyperfine splittings of Er:YSO, the locations of the optical transitions targeted by these sweeps and pulses can be GHz apart. In more complicated experiments, we needed to switch between these transitions in the microsecond timescale. We required a laser source(s) with extremely narrow linewidth but the flexibility to jump and sweep large frequency ranges. Unfortunately, a laser cannot be highly stable and tunable simultaneously.

By incorporating an EOM to the setup, a stabilised laser can remain locked to a reference cavity while the light from the laser can be modulated,

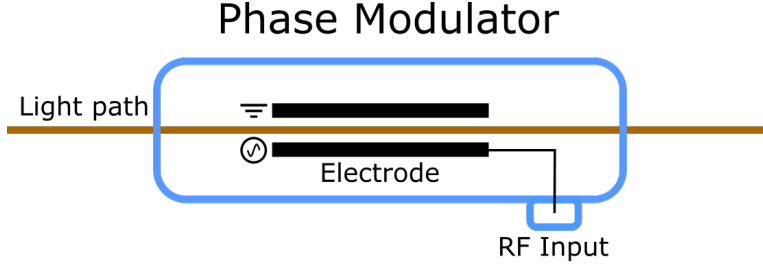


Figure 3.6: Internal diagram of a Phase Modulating (PM)-EOM. Between the two electrodes is a LiNbO<sub>3</sub> waveguide. Due to the Pockels effect, the refractive index of the waveguide can be changed by applying a voltage to the electrodes. The top electrode is grounded, while the bottom electrode is connected to an RF port, typically with  $> 10$  GHz bandwidth.

maintaining agile frequency control. Here, I explain the different types of EOMs used in the experiment. One of the benefits of working in the telecommunications band is the availability of GHz-bandwidth EOMs.

Over the next few sections, I will describe the three types of EOMs in detail. This level of detail is needed to understand how to operate the EOMs. In particular, IQ modulators are not common in this research field and running the IQ modulator in carrier-suppressed single-sideband mode with  $>20$  dB sideband suppression was required to run the experiments in this thesis.

### 3.5.1 Phase modulators

The simplest EOM is a phase modulator, diagram shown in Figure 3.6. It is the basis of the other modulator types used in the experiment. The EOMs used in this experiment all contain lithium niobate waveguides, LiNbO<sub>3</sub>. Light is coupled into the waveguide via optical fibres. Applying an electric field to the waveguide changes the output laser beam's phase, due to the Pockels effect. Sinusoidally modulating this electric field results in a sinusoidally changing phase (to first order) described by the following equation,

$$E_{PM} = Ae^{i\omega_0 t} \cdot e^{i\beta \sin(\omega t)}, \quad (3.1)$$

for some input light with amplitude,  $A$ , frequency,  $\omega_0$ , modulation amplitude,  $\beta$ , and modulation frequency,  $\omega$ . We make a first order expansion of  $e^{i\beta \sin(\omega t)}$ ,

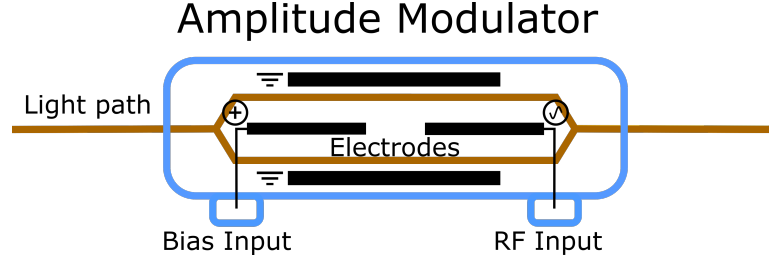


Figure 3.7: Internal diagram of an Amplitude Modulating EOM, as with the PM-EOM, contains a  $\text{LiNbO}_3$  waveguide. Initially, the light path is split by a beamsplitter. The refractive index of each path can be modulated by applying RF to the RF port, changing the phase of each path relative to each other. At the second beamsplitter the two light paths interfere with each other which results in amplitude modulation. The bias input is used to apply a DC phase shift between each path.

$$E_{PM} = Ae^{i\omega_0 t}(1 + i\beta \sin(\omega t)) \quad (3.2)$$

$$= A \left( e^{i\omega_0 t} + \frac{\beta}{2} e^{i(\omega_0 + \omega)t} - \frac{\beta}{2} e^{i(\omega_0 - \omega)t} \right). \quad (3.3)$$

This is assuming some small modulation amplitude ( $\beta$ ), the output has three frequency components: the original frequency at  $\omega_0$  (referred to as the carrier) and two sidebands frequency-symmetric about  $\omega_0$  at  $\omega_0 \pm \omega$ . However, there are an infinite amount of harmonic sidebands at  $\omega_0 \pm n\omega$  if the full Taylor expansion is used in Equation (3.1). If the modulation amplitude remains small,  $\beta < 1$ , then the higher order harmonics are considerably weaker than the first harmonic (the amplitude scales with  $\beta^n$ ) and are ignored.

### 3.5.2 Amplitude modulators

In an amplitude modulating EOM, the input light is split by a beamsplitter and each path is then phase modulated with opposite phase shifts, diagram shown in Figure 3.7. When the two paths recombine, the interference between the paths results in amplitude modulation rather than phase modulation. The phase of the two beam paths is controlled by the bias electrode. Following the same logic as Equation (3.2),

$$\begin{aligned}
E_{AM} &= Ae^{i\omega_0 t} \left( \frac{1}{2} e^{i\beta \sin(\omega t)} - \frac{1}{2} e^{-i\beta \sin(\omega t)} \cdot e^{i\theta} \right) \\
&= \frac{A}{2} \left( e^{i\omega_0 t} + \frac{\beta}{2} e^{i(\omega_0 + \omega)t} - \frac{\beta}{2} e^{i(\omega_0 - \omega)t} \right. \\
&\quad \left. - e^{i\theta} \left[ e^{i\omega_0 t} - \frac{\beta}{2} e^{i(\omega_0 + \omega)t} + \frac{\beta}{2} e^{i(\omega_0 - \omega)t} \right] \right),
\end{aligned} \tag{3.4}$$

where  $\theta$  is the DC phase shift on each light path due to the bias voltage. Note that there is a factor of  $-1$  between each light path as the beamsplitter transmits one light path and reflects the other, creating a  $\pi$  phase shift between the two beam paths. We will consider two cases: firstly, the bias voltage causes the two laser carriers ( $e^{i\omega_0 t}$ ) to be out of phase with respect to each other  $\theta = \pi$ . Secondly, the bias voltage causes the two laser carriers to be in phase with respect to each other  $\theta = 0$ ,

$$E_{AM} = A \left( \frac{\beta}{2} e^{i(\omega_0 + \omega)t} - \frac{\beta}{2} e^{i(\omega_0 - \omega)t} \right) \quad \theta = \pi \tag{3.5}$$

$$E_{AM} = Ae^{i\omega_0 t}. \quad \theta = 0 \tag{3.6}$$

Equations (3.5) and (3.6) tell us that we can use the bias voltage to shift power between the carrier and the sidebands. In case where  $\theta = \pi$ , the carrier term has completely vanished, and the sidebands have maximum laser power. In the case where  $\theta = 0$ , the sideband terms have vanished, and the carrier has maximum laser power.

In the following experiments, amplitude modulators were used to create agile frequency sidebands on a frequency locked laser. Most of the experiments in this thesis used high laser power to excite atoms and manipulate their energy levels. To maximise the sideband power, the bias voltage was set to suppress the carrier, with  $>20$  dB carrier suppression over hours. Experiments where the 5 GHz detector and spectrum analyser were used operated with 50% laser power in the carrier and 25% laser power in each sideband. So that a beat between the carrier and sidebands could be measured by the detector and spectrum analyser.

### 3.5.3 IQ modulators

An IQ modulator is composed of two AM-EOMs whose outputs are recombined, with one output passing through an PM-EOM. This combination allows for arbitrary modulation of phase and amplitude. There are many applications for IQ modulation, however, we focus on the application of single sideband modulation.



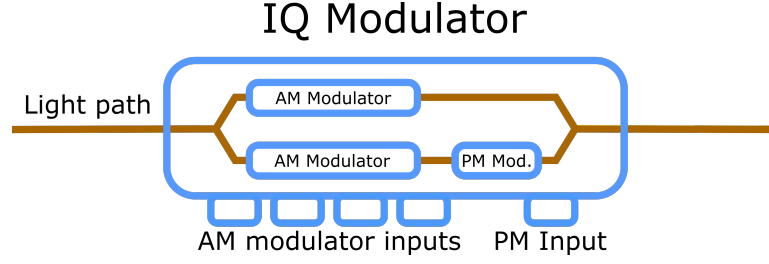


Figure 3.8: Internal diagram of an IQ modulating EOM, this modulator is the sum of two AM modulators, with one of the AM modulators passing through a phase modulator. In total, there are 5 inputs. Three RF inputs, one for each modulator, and two bias inputs for each amplitude modulator.

The mathematics of an IQ modulator can become quite unwieldy when accounting for all three modulators. We will, instead, consider a special case where both amplitude modulators have suppressed carriers and the RF of each modulator has the same frequency but are phase shifted by  $\frac{\pi}{2}$  with respect to each other. Finally, the phase modulator will have a DC input rather than an AC input. The equation to describe the output of this modulator is as follows,

$$E_{IQ} = A \frac{\beta}{2} \left[ \left( e^{i(\omega_0+\omega)t} - e^{i(\omega_0-\omega)t} \right) - \left( e^{i(\omega_0+\omega)t+i\frac{\pi}{2}} - e^{i(\omega_0-\omega)t-i\frac{\pi}{2}} \right) e^{i\theta} \right]. \quad (3.7)$$

If we set  $\theta$  to  $\pi/2$ ,

$$E_{IQ} = A\beta e^{i(\omega_0+\omega)t}. \quad (3.8)$$

The first bracketed term in line 1 of Equation (3.7) refers to the top amplitude modulator of Figure 3.8, while the second bracketed term refers to the lower amplitude modulator. There is also an additional  $-1$  factor due to the reflection in the IQ modulator's beamsplitter and an  $e^{i\theta}$  term due to the phase modulator. By applying the RF and biases described in the previous paragraph, we have both single-sideband modulation and carrier suppression. Note, if  $\theta$  is instead chosen to be  $-\frac{\pi}{2}$  then the higher frequency sideband ( $\omega_0 + \omega$ ) is suppressed, and we have  $E_{IQ} = A\beta e^{i(\omega_0-\omega)t}$ .

Amplitude and IQ modulators both have bias voltages to control the suppression of at least one of the three output frequencies (bands). The bias voltages can drift over an hour timescale, which will affect the suppression of these bands. In the experiments in this thesis, we only want one band to interact with the ions at a time. In the case of heterodyne detection,

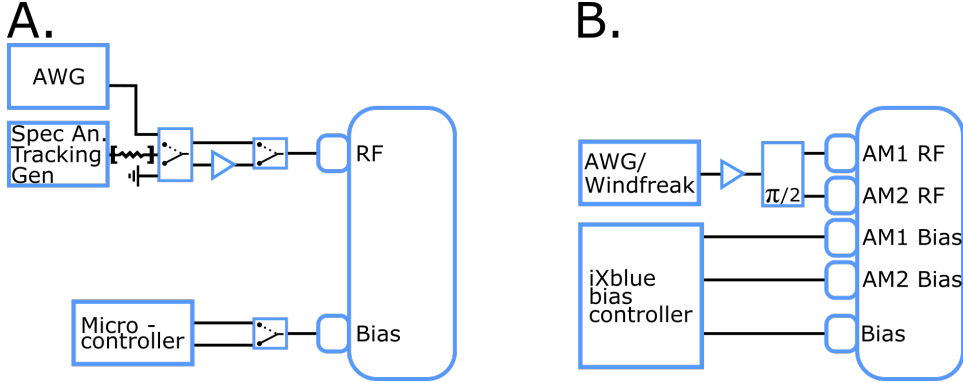


Figure 3.9: RF circuit diagram. **A.** The RF sources that drove the AM - EOM. AWG was an ADS7-V2 during the AFC experiments and a Tabor P9082D during the RASE experiments. Spec An. Tracking Gen was the tracking generator output of an HP8560E with a sweep range of 0 – 2.9 GHz, attenuated by 20 dB. A Teensy 3.6 microcontroller was used to control the bias.

**B.** The RF sources that drove the IQ - EOM. The RF source was a Windfreak SynthNV during the AFC experiments and a Tabor AWG during the RASE experiments. The phase shifter was a Minicircuits ZAPDQ-2. A Mini-circuits iXblue bias controller (MBC-DG-LAB) controlled the biases for the IQ modulator. The amplifiers were Mini-circuits ZHL-42W+s and the switches were ZASWA-2-50DR+s.

detecting more than one sideband leads to unwanted signals and excess noise at the heterodyne beat frequency. An iXblue bias controller (MBC-DG-LAB) was used to maintain >25 dB sideband and carrier suppression for the IQ modulator.

### 3.6 Radio Frequency (RF) sources

The inhomogeneous line of our  $^{167}\text{Er}:\text{YSO}$  crystal is only 150 MHz, but due to the  $\sim$  GHz hyperfine splittings, the optical transitions we investigated are spread over a 2.5 GHz range. The experiments in this thesis required large dynamic power ranges, from  $\pi$ -pulses to single photon levels, with a large frequency bandwidth to cover the entire 2.5 GHz erbium line. The RF driving the EOMs needs to be flexible, high bandwidth, low noise, and have a large dynamic power range to meet these requirements. As a result, several RF sources were combined with a series of switches and amplifiers to supply RF to the two EOMs. A simplified circuit diagram is given in Figure 3.9 and the RF sources for each EOM are explained in the two follow sections.

### RF circuit, AM-EOM

An ADS7-V2 evaluation board was used to drive the AM-EOM as an Arbitrary Waveform Generator (AWG) for frequencies up to 6 GHz (replaced with a Tabor Proteus P9082D in the RASE experiments). These waveforms were amplified by a Mini-circuits ZHL-42W+ 1W amplifier to drive the AM-EOM at the optimal power to efficiently transfer laser power to the sidebands. However, for quantum measurements, pulses with intensities near the single-photon level were required. For such weak pulses, the RF needed to be attenuated by up to 100 dB. The 1 W amplifier was bypassed using another RF switch. Not only would this attenuate the RF power, but it would also avoid the broad band noise that the amplifier would introduce. The AWG could be digitally attenuated on demand to attenuate the RF to desired levels.

The spectrum analyser's tracking generator was used to sweep one optical sideband across the entire inhomogeneous line. A 30 dB RF attenuator was used to keep this signal weak and avoid unnecessary holeburning. A series of fast 5 GHz ZASWA-2-50DR+ switches from Mini-circuits were used to switch between the RF devices and amplifiers.

The relative powers of the laser carrier and sidebands were controlled by changing the DC bias into the AM-EOM. The DAC output of a Teensy microcontroller was used as the DC source for the AM-EOM bias, and a TTL on the Teensy could be used to switch between carrier suppression and non-carrier suppression. For non-carrier suppression, the DC bias was set such that the laser-carrier-to-sideband power ratio was 2:1, as this gave the strongest beat signal between the carrier and sidebands without driving too much power into the second harmonic sidebands.

### RF circuit, IQ-EOM

A WindFreak SynthNV 2.4 RF signal generator controlled the AM sidebands of the IQ-EOM. This signal was amplified with another Mini-circuits ZHL-42W+ 1W amplifier. The amplified signal was then split into two paths. One path phase-shifted by  $\frac{\pi}{2}$  with a Mini-circuits ZAPDQ-2-N hybrid splitter and phase-shifter, from 0.8 – 2 GHz the phase shift between the two outputs was  $90 \pm 1$  degrees. This allowed  $>20$  dB sideband suppression.

An IX-Blue IQ modulator bias controller was used to control and supply DC voltage to the three RF biases of the IQ modulator. Carrier-suppressed single-sideband modulation (CS SSB) requires the biases of the IQ modulator to be set to  $\pi$  for AM biases and  $\pi/2$  for the PM bias. EOM biases tend to drift slowly over time (a few percent over 10 minutes). To maintain CS SSB, the biases had to be constantly optimised. The modulator bias controller achieves this by applying a low-frequency modulation feedback ( $\sim 1$  kHz). However, this feedback is only accurate if the higher harmonic

sidebands are weak. To achieve consistent CS SSB with suppression  $> 20$  dB, the RF into the IQ modulator had to be attenuated by 8 dB from optimal power. Combined with the intrinsic losses of the IQ modulator (6 dB) and experimental losses, the IQ modulator had a total loss of almost 98%. Thus, an EDFA was needed to amplify the single sideband and mitigate these losses.

### 3.7 Heterodyne detection with AM-EOMs

As briefly mentioned in Section 3.1, the experiment had two ways to detect optical signals. One way involved using the 2.9 GHz spectrum analyser to sweep sidebands of the laser created by the AM-EOM. The other way used the balanced heterodyne detectors. When using the spectrum analyser, a heterodyne beat was created between the carrier and sidebands of the AM-EOM, which was then demodulated by a spectrum analyser. This technique was useful when recording GHz wide spectra, but had some severe limitations, discussed below. These wide spectras were used during the spectroscopy experiments, Section 3.9.3, but for all other experiments the balanced heterodyne detectors were used.

A limitation of the AM-EOM detection technique arises because a standard EOM produces two sidebands frequency-symmetric about the laser carrier ( $\pm\omega_{RF}$ ). When the fast detector measures the beat signal between these two sidebands and the carrier, the beat from each sideband is indistinguishable. To avoid confusion when interpreting spectra, we only want one sideband to interact with the atoms. To achieve this, we set the laser carrier to either frequency extremum of the absorption spectra, either below the  $\Delta m_I = -1$  or above the  $\Delta m_I = +1$  optical transitions (Section 3.8.1). The oscillator strengths of the  $\Delta m_I > |2|$  are too weak to have noticeable absorption ( $\ll 1$  dB). This way, we can assume only one sideband is absorbed by the ions.

We still have the issue that we always detect the beat signal from both sidebands. Even when one sideband is completely absorbed, the total beat signal amplitude only decreases by a factor of 2. This means that the beat intensity drops by a factor of 4 (6 dB). Thus, this measurement technique becomes inaccurate at high absorption. Unfortunately, there is another level of complexity. Because we measure the combined beats between the carrier and the two sidebands, we are also sensitive to the phase of the sidebands relative to each other.

As the sidebands sweep over highly absorbing regions of the spectrum, they are not only attenuated, but also phase-shifted, by the Kramers-Kronig relation [43]. Around highly absorbing features, this phase shift can be more than  $\frac{\pi}{2}$ . The beat between the two sidebands now destructively interferes, giving an apparent decrease of signal of more than 6 dB. Then as the sideband

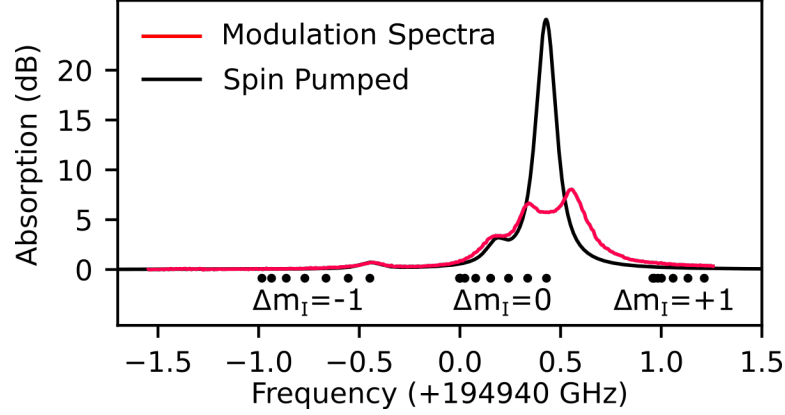


Figure 3.10: This figure shows the difference between a spectrum recorded using an AM-EOM (red) and absorption spectra (black) generated from the erbium absorption model in Appendix C. The modulation spectrum was quite accurate for optical depths  $< 3$  dB. However, the absorption measurements near an absorbing feature become inaccurate because of both the high optical depth of the feature and the frequency dependent phase shift.

is attenuated further, and the phase shift approaches  $2\pi$ , the constructive interference decreases. The effect this has is that for optically thick regions of the spectrum we end up with the absorption at the peak appearing as 6 dB, but around the absorption peak there are regions of absorption from 8 – 10 dB, shown in Figure 3.10. It is a non-trivial task to reverse this effect and obtain the absorption spectrum from this modulation response spectrum.

A solution to this problem is to use an IQ modulator to produce a single sideband. However, running the IQ modulator in single sideband mode requires two phase coherence RF sources that are  $\pi/2$  phase shifted relative to each other, Section 3.5.3. During these experiments, we did not have access to such a frequency sources. Instead, the IQ-EOM used a  $\pi/2$  phase-shifter that worked between 0.8 – 2 GHz. Our experiments require that the experimental beam can operate over a large bandwidth (3 GHz). Thus, the IQ-EOM could not cover the experiment frequency range and an AM-EOM was used instead.

The IQ-EOM was used to control the local oscillator in the balanced heterodyne detection. As long as the suppression of the other sideband is more than the peak absorption of the crystal, then there is no noticeable signal from the second sideband. For this crystal, the peak absorption is between 20 – 25 dB, depending on the preparation sequence used. The single-sideband suppression was always at least 25 – 30 dB.

### 3.7.1 Balanced heterodyne detection

In quantum optics, signals need to be very weak to minimise the contributions of classical noise. In the non-classical experiments of the AFC and RASE chapters, our signals needed to be near, or even less than, the single photon level, on average. Thus, we must be able to record such weak signals.

For continuous variable measurements, one method of detection involves interfering a weak experiment signal with a strong local oscillator. This method is referred to as homodyne if the signal and local oscillator are the same frequency, and heterodyne if they are not.

The experiment signal is composed of two orthogonal quadratures, the “in-phase” quadrature (I) which has the same phase as the local oscillator ( $\theta = 0$ ), in other works this is sometimes referred to as the amplitude quadrature,  $\hat{x}$ . The other quadrature is the “out-of-phase” quadrature (Q) which has the phase  $\theta = \frac{\pi}{2}$ , sometimes referred to as the phase quadrature,  $\hat{p}$ . With homodyne measurement, you choose which quadrature you measure by setting the phase of the local oscillator, which also means that only one quadrature can be measured at a time. Homodyne detection measures the phase of the weak experiment signal.

In the case of heterodyne detection, the local oscillator and the weak signal are at different frequencies. The interfered signal is a beat between the two input signals, at a frequency  $\Delta\omega = \omega_{LO} - \omega_S$ . This can be conceptualised as the output heterodyne signal is continuously oscillating between measuring the in-phase quadrature and out-of-phase quadrature, measuring both simultaneously. The trade-off between these two methods is that, while homodyne can only measure one signal at a time, it does so with a higher signal-to-noise ratio than heterodyne. Experimentally, however, homodyne is more sensitive to phase drift between the two input signals and to  $\frac{1}{f}$  noise from the local oscillator. In these experiments, heterodyne detection was used to avoid the low frequency noise from homodyne.

In the experiment, there are two examples of heterodyne detection. The first is when using the fast 5 GHz detector and the 2.9 GHz spectrum analyser. Here, the local oscillator is the carrier of the AM-EOM and the signal is the sidebands of the AM-EOM. The other example of heterodyne detection is in the form of balanced heterodyne detection. For our balanced heterodyne detection, a beam splitter is used to interfere a weak signal,  $E_s$ , with a much stronger local oscillator,  $E_{LO}$ . When two sources of light are sent through a beamsplitter, the outputs of the beamsplitter are the sum of the two inputs. Balanced heterodyne detection compares both output ports of the beamsplitter, using two detectors. The reasoning and mathematics of why this is advantageous is described below.

The inputs and outputs of a 50:50 beamsplitter, Figure 3.11, are described by the following equations:

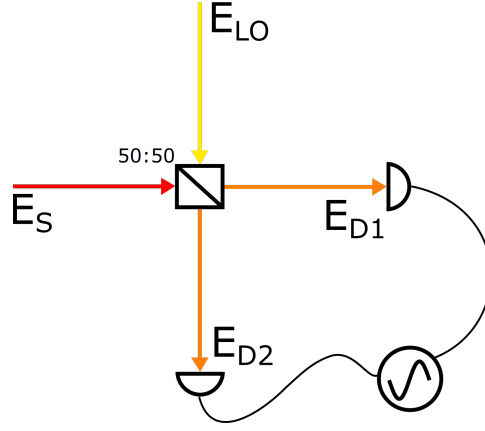


Figure 3.11: Balanced heterodyne detection, using a 50:50 beamsplitter. Two signals  $E_S$  and  $E_{LO}$  are combined using a beamsplitter. There is a detector on the output of each beamsplitter port. The balanced heterodyne signal is found by subtracting D1 from D2.

$$E_S = E'_S e^{-i\omega_S t}, \quad (3.9)$$

$$E_{LO} = E'_{LO} e^{-i\omega_{LO} t}, \quad (3.10)$$

$$E_{D1} = \frac{1}{\sqrt{2}} (E'_S e^{-i\omega_S t} + E'_{LO} e^{-i\omega_{LO} t}), \quad (3.11)$$

$$E_{D2} = \frac{1}{\sqrt{2}} (E'_S e^{-i\omega_S t} - E'_{LO} e^{-i\omega_{LO} t}). \quad (3.12)$$

The two inputs of the beamsplitter are our probe ( $E_S$ ), which contains a weak signal that we wish to measure, and the local oscillator ( $E_{LO}$ ). For now, we will consider that the signal and local oscillator are CW with amplitudes  $E'_S$  and  $E'_{LO}$  and frequencies  $\omega_S$  and  $\omega_{LO}$ , respectively. The electric field detected by the two detectors in Figure 3.11 is given by equations (3.11) and (3.12). The  $(-)$  sign in equation (3.12) arises from the reflection in the beamsplitter. The intensity at each detector is then equal to the square of the electric field,

$$I_{D1} = \frac{1}{2} (|E'_S|^2 + |E'_{LO}|^2 + 2E'_S E'_{LO} \cos([\omega_S - \omega_{LO}]t)), \quad (3.13)$$

$$I_{D2} = \frac{1}{2} (|E'_S|^2 + |E'_{LO}|^2 - 2E'_S E'_{LO} \cos([\omega_S - \omega_{LO}]t)), \quad (3.14)$$

where the first two terms are both DC, thus, when we subtract the signals of the detectors only the  $2E'_S E'_{LO}$  terms remain,

$$I_{D1} - I_{D2} \propto E'_S E'_{LO} \cos(\Delta\omega t). \quad (3.15)$$

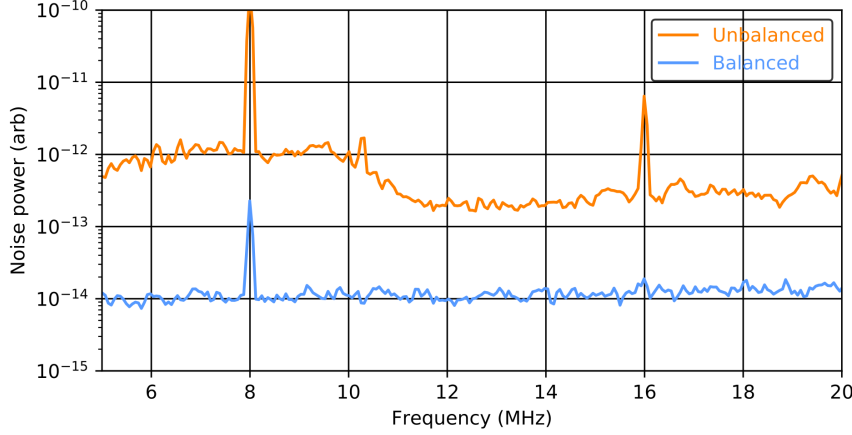


Figure 3.12: Comparing the noise levels of the balanced heterodyne signals (blue) to the non-balanced heterodyne (orange) signal, which is the direct output of one of the detectors. We can see that the broad band background noise is removed. Also, electrical noise spikes (8, 16 MHz) are suppressed by  $\sim 30$  dB, showing the two detectors are balanced close to 0.1% of each other. The balanced trace is not completely flat due to the frequency response of the detectors.

With  $\Delta\omega = |\omega_S - \omega_{LO}|$ , we measure a signal at the beat frequency between the two signals,  $\Delta\omega$ , with the measured signal proportional to both the amplitude of the weak signal and local oscillator. There are several important outcomes from measuring our signals in this way:

1. Although our detectors measure intensity, the balanced heterodyne signal here is proportional to the amplitude of the electric fields of the signal and local oscillator, which is the square root of the intensity.
2. The detected signal is proportional to the amplitude of the local oscillator, which is much stronger than the weak signal ( $E_S$ ).
3. The strong intensity of the local oscillator has been completely cancelled (the  $|E_{LO}|^2$  term), thus, the local oscillator can be arbitrarily large (as long as the detectors do not saturate), amplifying the heterodyne beat signal.

As we can see in Equation (3.15), when we subtract the signals from our two detectors, our two heterodyne beats coherently sum. However, any noise not correlated with the weak signal or local oscillator will be subtracted out. Figure 3.12 shows the difference between noise levels in the subtracted and non-subtracted heterodyne signals.

In the next section, I will describe how balanced heterodyne detection is used to measure signals down to the quantum noise limit.



### 3.7.2 Shot-noise-limited detection

In the previous section, the intensity of the local oscillator was treated as a constant CW signal. In reality, this is not true, as the stochastic process of generating photons leads to intensity fluctuations in the local oscillator in the form of Poissonian noise. Considering Figure 3.11, if the  $E_S$  port is completely blocked then the signals on detectors  $E_{D1}$  and  $E_{D2}$  will fluctuate proportional to the square root of the incident photons,  $\sqrt{N}$ . Classically, this is considered a result of a stochastic process. However, using another line of thought, we can still treat the local oscillator as a perfect CW signal and find that the fluctuations arise from the vacuum state entering the empty beam splitter port ( $E_S$  port). Which interpretation we use does not change the end effect, but it is easier to conceptualise the shot noise as fluctuations in the vacuum state. This also becomes important when discussing non-classical quantum memory demonstrations, sections 4.6 and 6.4.

The noise floor is referred to as shot noise or quantum noise. From the result of the previous section, we know that our probe signal (and thus the shot noise) can be made arbitrarily large by increasing the intensity of the local oscillator. The goal of shot-noise-limited detection is achieved when the local oscillator is strong enough that the shot noise becomes the dominant source of noise in the detection (as opposed to electrical noise from the detectors, digitisation noise from the digital oscilloscope, or ‘classical noise’ from the weak signal). Demonstrating shot-noise-limited detection is then an exercise in showing that the noise of the detection scales with the square root of the local oscillator intensity. As any other noise source will be constant (electrical, digitisation noise) or scale linearly (classical noise) with local oscillator power.

Figure 3.13 shows the local oscillator noise, with the weak probe blocked, averaged between 10 – 20 MHz (the flat region of Figure 3.12) for varying local oscillator powers. At  $< 0.5$  mW the noise scales faster than the square root of the local oscillator power (indicated by the orange line) indicating we are still in the classical noise dominated regime. Above 1.5 mW, the noise scales with the square root of the local oscillator power (1.5 dB/ 3 dB LO power), indicating that we are in the shot-noise-limited regime. While the detectors were shot-noise-limited up to 4 mW, in these experiments the local oscillator was set to 2 mW.

Ideally, the local oscillator would be set to 4 mW, to give the best clearance over the classical / electrical noise from the detectors. However, there were experimental issues running the single-sideband modulation at high power. As mentioned in Section 3.6, a feedback loop was used to keep the single-sideband suppression above 20 dB. The feedback system for the single-sideband suppression became unstable when strong RF was used to drive the IQ modulator. Even with the EDFA running at full power, 100 mW, the output of the IQ modulator was only 2 mW. Further optimisation of the

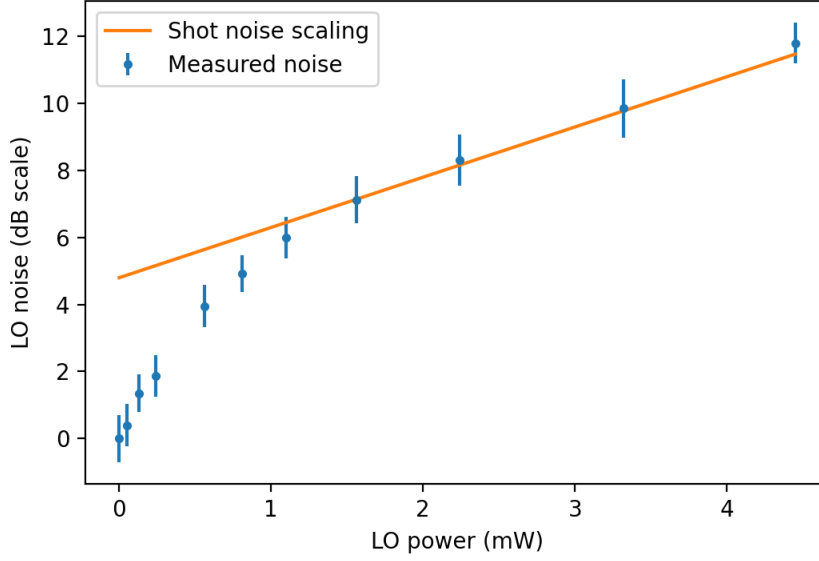


Figure 3.13: Scaling of the heterodyne local oscillator noise, showing that heterodyne noise is shot-noise-limited above 1.5 mW. The shot-noise-limited regime is indicated when the noise scales with the square root of the local oscillator power (a gradient of 0.5 on a log scale).

IQ modulator bias feedback may increase this power slightly, but for these experiments, 2 mW is sufficient.

### 3.7.3 Continuous and discrete variable detection

The experiments presented in this thesis use continuous variable (CV) detection in the form of balanced heterodyne detection, discrete variable (DV) detection is also very common in quantum optics. The decision on whether to use CV or DV detection is commonly discussed, as both techniques have clear advantages and disadvantages.

CV detection records a time-varying voltage produced via a light field incident on a detector, while DV detection records individual photons using single photon detectors, such as: avalanche photo-diodes (APDs) or superconducting nanowire single-photon detectors (SNSPDs).

DV detection has the advantage that a recorded single photon will result in a ‘click’ from the detector. Because there is no local oscillator in this detection method, we do not have to consider the effects of shot noise from such a local oscillator, and a click on the detector will, ideally, correspond to a photon arriving from the experiment. However, single photon detectors suffer from dark counts, detection events that do not correspond to photons interacting with the detector. Dark count rates are proportional to temperature, thus, cooling the detector can reduce dark counts. Some APDs are

cooled with liquid nitrogen, for example. SNSPDs need to operate in the  $\sim 1$  Kelvin regime, both to reach superconductivity and reduce dark counts. DV detectors also have an associated dead-time; if multiple photons arrive during the dead-time, only one single photon will be counted. Dead-times of  $<100$  ns are common, with corresponding count rates in the 10s of MHz, however, count rates as high as 1 GHz have been shown [21]. Single photon detectors can only count one photon at a time. Photon-number resolving single-photon detectors are able to get around this limitation. Single photon detectors also do not inherently record any phase or frequency information about the photons. In quantum memory experiments, we are usually interested in recording photons from one or a few optical transitions. Frequency filters are needed to remove background signals, such as, free induction decays from pi-pulses or spontaneous decay from other optical transitions.

CV, particularly heterodyne and homodyne detection, has the advantage that frequency discrimination and phase detection is built into the technique, thus no extra frequency filters are needed. This also limits the bandwidth of the detection to a narrow frequency region about the frequency of the local oscillator. Section 6.4 used an agile local oscillator to overcome the bandwidth limitation by switching the local oscillator frequency in the sub-microsecond timescale, recording two time-separated signals produced on two optical transitions split by  $\sim 100$  MHz. As mentioned in Section 3.7.1, heterodyne detection requires a phase-locked local oscillator. This adds experimental complexity and laser-atom phase stability was, ultimately, a limitation of experiments in this thesis, Section 6.5. Also, heterodyne detectors are limited by shot noise generated from the local oscillator, rather than dark counts. Typically, this means that many averaged measurements are needed to confirm if a single photon level signal has been recorded, Sections 4.6 and 6.4.2 show examples of this.

For context in this thesis, RASE demonstrations have been shown with both DV [6] and CV [48, 30]. The DV demonstration was limited by spontaneous emission from other optical non-RASE transitions during the RASE window. This issue was solved by using CV and shifting to a four-level configuration [30], thus, distinguishing ASE photons from RASE photons and filtering FIDs from  $\pi$ -pulses. CV detection is also used in this thesis for this reason. Although, as we will see in Section 6.5, the phase stability of the local oscillator, relative to the atoms, was a huge experimental challenge and ultimately was not overcome by the end of this thesis.

### 3.8 Ensemble preparation

In this section, I will explain the techniques that were developed and used when preparing the ensemble of erbium ions for both the AFC and the RASE protocols. However, these preparation techniques are fairly general and can

be applied to any quantum memory protocol in any material with a resolved hyperfine structure.

The experiments in the AFC section used a magnetic field of 7 T, while the RASE experiments used 6 T. Using 6 or 7 T does not change the experiment in any meaningful way because the nuclear Zeeman splittings are small  $\mathcal{O}(10\text{MHz/T})$  compared to the zero field hyperfine splittings  $\mathcal{O}(\text{GHz})$ . This means that the general shape of the absorption line does not change much with magnetic field, even though some optical transitions will cross. Thus, the preparation process does not change, except for changes in the exact frequencies driven.

### 3.8.1 Absorption spectra at 6,7 T

All experiments in the following chapters were performed on site 2, for the  $^4I_{15/2} Z_1 - ^4I_{13/2} Y_1$  transition, on the like-like transition of the lower electric Zeeman arm. The magnetic field was applied  $\sim 1$  degree off-axis to the  $D_1$  crystal's axis. The off-axis field splits the two magnetically inequivalent subgroups, the experiments were performed on the lower frequency subgroup. The spectrum of both subgroups is shown in Figure 3.14.

The absorption spectrum of the lower subgroup shows three defined peaks centered approximately at  $-0.8$ ,  $0.2$ ,  $1.0$  GHz. These peaks correspond to groups of optical transitions that change the nuclear spin projection,  $m_I$ , of an erbium ion. We refer to them as  $\Delta m_I = x \equiv (m_I(g) - m_I(e))$ , where  $x$  is an integer, for example  $\Delta m_I = -1$  transitions will lower the hyperfine levels of the erbium ions by 1. In Figure 3.14, the three peaks are the  $\Delta m_I = -1, 0$ , and  $+1$  transitions, respectively. Each peak contains 7 to 8 optical transitions for each hyperfine level, with the transitions indicated by a black dot. The  $\Delta m_I = -2$  transitions are also indicated, around  $-1.5$  GHz, but the oscillator strengths of these transitions are too weak to see any absorption at this scale. The oscillator strengths of the optical transitions decrease rapidly with increasing  $|\Delta m_I|$ , for example, the oscillator strengths of the  $\Delta m_I = 1$  are between 2 and 30% of the  $\Delta m_I = 0$ .

In Figure 3.14 transitions are grouped according to their  $\Delta m_I$ , because the hyperfine splittings of the ground and excited states are fairly similar, ranging between  $800 - 1,000$  MHz, as shown in Table 3.1. This leads to the optical transitions with the same  $\Delta m_I$  clustering within  $200 - 400$  MHz of each other, while different  $\Delta m_I$  transitions are split by almost a gigahertz. The table also shows that the hyperfine splittings decrease monotonically with hyperfine level. This means that the lower  $\Delta m_I$  transitions are more spread out, but also means that the optical transitions within clusters of  $\Delta m_I$  are almost, but not always, ordered by their hyperfine level, in frequency. There are some important exceptions to this rule, as we will see in later sections. Along with the clustering of  $\Delta m_I$  transitions, the narrow (150 MHz) linewidth of the crystal leads to a resolved hyperfine structure, which

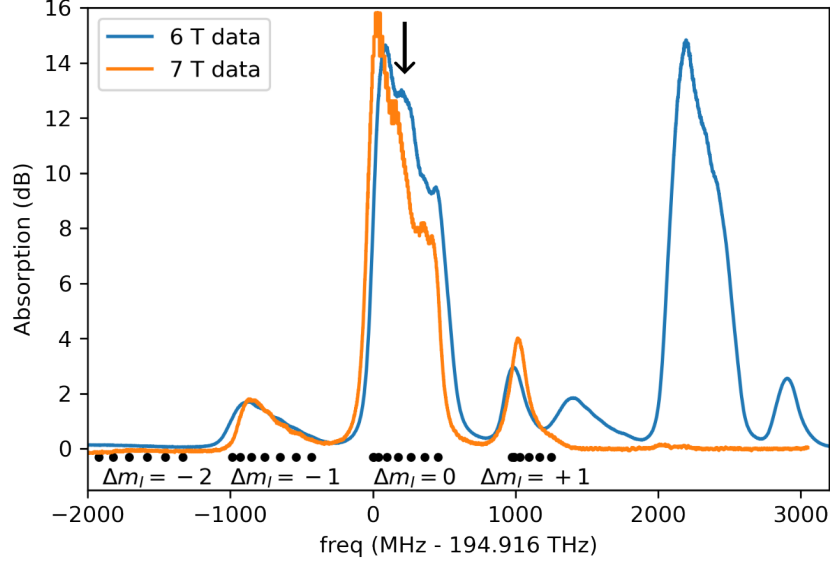


Figure 3.14: Absorption spectra of  $^{167}\text{Er}^{3+}:\text{Y}_2\text{SiO}_5$  at 1.4 K with an applied field of 6 and 7 T. The 7 T absorption data was taken from data presented in Rančić's thesis [58] and is used to show the similarities between the two spectra. The 7 T data has been shifted by 20 GHz to overlap with the 6 T data. The black dots show the locations of the optical transitions for the  $\Delta m_I = -2 \rightarrow +1$  transitions on the 6 T data. The black arrow indicated the location of the isotopic impurities in the 6 T data. The other magnetic inequivalent subgroup can be seen, beyond 1200 MHz. The 7 T data does not have the other subgroup as the magnetic field was applied further off the  $D1$  axis than the 6 T data.

MHz ( $\pm 0.05$ )		6 T		7 T	
hyperfine splitting		ground	excited	ground	excited
$-\frac{7}{2} \rangle \rightarrow -\frac{5}{2} \rangle$		985.16	989.94	997.06	993.10
$-\frac{5}{2} \rangle \rightarrow -\frac{3}{2} \rangle$		935.39	969.51	945.15	972.08
$-\frac{3}{2} \rangle \rightarrow -\frac{1}{2} \rangle$		891.67	950.42	899.09	952.71
$-\frac{1}{2} \rangle \rightarrow +\frac{1}{2} \rangle$		854.76	932.95	860.35	934.61
$+\frac{1}{2} \rangle \rightarrow +\frac{3}{2} \rangle$		825.97	916.76	829.43	918.23
$+\frac{3}{2} \rangle \rightarrow +\frac{5}{2} \rangle$		805.73	901.54	807.83	903.06
$+\frac{5}{2} \rangle \rightarrow +\frac{7}{2} \rangle$		794.36	887.80	795.46	888.86

Table 3.1: Hyperfine splittings for the ground and excited states of  $^{167}\text{Er}^{3+}:\text{Y}_2\text{SiO}_5$  with an applied field of 6 and 7 T.

is key to the preparation techniques used in this thesis.

In the spectrum of  $^{167}\text{Er}:\text{YSO}$ , there are also isotopic impurities, 180 MHz in Figure 3.14. Erbium ions in the crystal are 92%  $^{167}\text{Er}$ . The remaining 8% are a mixture of  $^{166}\text{Er}$ ,  $^{168}\text{Er}$ ,  $^{170}\text{Er}$ , and trace amounts of  $^{164}\text{Er}$ . The optical frequencies of these isotopes changes by 50 MHz per nucleon [68, 52]. The natural abundance of these isotopes is 3:10:8:5, by atomic weight [58]. The abundance in our crystal is not known, but in the isotopic purification process the impurities are more likely to be from isotopes with similar atomic mass. We assume that most of the impurities are  $^{166}\text{Er}$  and  $^{168}\text{Er}$ , which will be split by 100 MHz. For simplicity, it is assumed that they are one single impurity with a 150 MHz linewidth at 180 MHz in Figure 3.14.

Finally, YSO has two magnetically inequivalent subgroups whose properties are related by a rotation about the crystalline C2 axis. Fields that are not applied along or perpendicular to the C2 axis will give different Zeeman shifts on the two sites, splitting the optical line. Here, we exploited this effect to enable us to work with a single magnetic subgroup. We applied a field approximately 1 degree off the D1 direction, which gives a Zeeman splitting between the two subgroups of 2.5 GHz at 6 T, Figure 3.14. The 7 T data from Rančić's thesis does not have the other subgroup, as the magnetic field was applied further off of the D1 axis, in Rančić's experiments the splitting between the two subgroups was roughly 5 GHz.

### 3.8.2 Spin polarisation

From here, I will detail the preparation process used in spectrally preparing an ensemble for quantum memory demonstrations and photon echo measurements. The preparation is broken into two steps: spin pumping (or spin polarisation), and selective anti-polarisation. The first step was initially demonstrated by Rančić [58] where the ensemble of  $^{167}\text{Er}$  ions were pumped into a single hyperfine level (either of the  $|\pm\frac{7}{2}\rangle_g$ ). The second step, developed during this thesis, takes a narrow 0.1 – 3 MHz sub-ensemble from within the spin polarised ensemble and ‘anti-polarises’ it into another hyperfine level. In most experiments, the sub-ensemble is anti-polarised into the other extremum hyperfine level,  $|\mp\frac{7}{2}\rangle_g$ .

Spin polarisation is the process of manipulating an ensemble from a thermal distribution of energy levels into a single spin level. For these experiments, erbium ions will be manipulated into a single ground state hyperfine level. Spin polarising is achieved here using the resolved hyperfine structure. Because of the clearly resolved  $\Delta m_I = \pm 1$  transitions, Figure 3.14, we can selectively interact with the optical transitions that will either increase or decrease the hyperfine levels of erbium ion in the ensemble. By sweeping a laser continuously over the  $\Delta m_I = +1(-1)$  optical transitions, the  $^{167}\text{Er}$  ions will be pumped into the excited state with their nuclear spins changed by  $+1(-1)$ , except for ions already in the  $|\pm\frac{7}{2}\rangle_g$  ground state, which

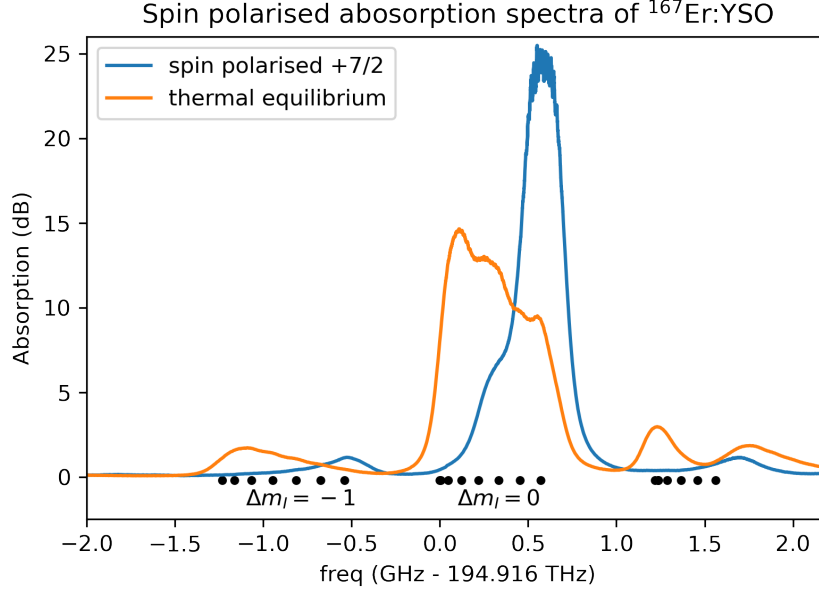


Figure 3.15: Comparison of the spin polarised ensemble compared to the non-spin polarised (thermal equilibrium) ensemble, at 6 T.

have no further hyperfine level to be pumped into. As the ions decay back to the ground state, they do so preferentially via the  $\Delta m_I = 0$  transition (given by the relative oscillator strengths, Table 3.2). Thus, the average hyperfine level of our ensemble has increased (decreased). By repeatedly sweeping the laser over the  $\Delta m_I = +1(-1)$  feature for many optical lifetimes, the ensemble of erbium ions is driven into a single hyperfine state,  $|+\frac{7}{2}\rangle_g$  ( $|-\frac{7}{2}\rangle_g$ ). Rančić demonstrated spin polarisation with at least 95% of the  $^{167}\text{Er}$  ions driven into the  $|+\frac{7}{2}\rangle_g$  [59]. In this thesis, I achieve the same level of spin polarisation, although using an altered experiment set up.

In the experimental setup, Figure 3.1, the ‘unlocked laser’ was dedicated to the spin polarisation process. The laser was attenuated to a power of 3 mW and swept via current modulation using a 25 Hz, 1.5 V triangle wave, corresponding to a  $\sim 1.5$  GHz sweep. The laser power was set to 3 mW and the frequency was set such that the sweep covered the entire  $\Delta m_I = +1$  transition and overlapped slightly with the  $\Delta m_I = +2$  (as this gave the best performance). I took particular care to make sure that the sweep did not overlap with the  $\Delta m_I = 0$  as this would immediately undo the spin polarisation. The laser frequency was set to 194.9412 THz and 194.9206 THz for 7, 6 T respectively when spin polarising into the  $|+\frac{7}{2}\rangle_g$  hyperfine level and 194.9180 THz for 6 T spin polarising into the  $|-\frac{7}{2}\rangle_g$  hyperfine level.

Figure 3.15 shows the spin polarised spectrum for an ensemble polarised

state:	$ \frac{7}{2}\rangle_e$	$ \frac{5}{2}\rangle_e$	$ \frac{3}{2}\rangle_e$	$ \frac{1}{2}\rangle_e$	$ \frac{1}{2}\rangle_e$	$ \frac{3}{2}\rangle_e$	$ \frac{5}{2}\rangle_e$	$ \frac{7}{2}\rangle_e$
$ \frac{7}{2}\rangle_g$	0.763	0.237						
$ \frac{5}{2}\rangle_g$	0.160	0.668	0.172					
$ \frac{3}{2}\rangle_g$		0.145	0.710	0.145				
$ \frac{1}{2}\rangle_g$			0.127	0.758	0.115			
$ \frac{1}{2}\rangle_g$				0.107	0.812	0.080		
$ \frac{3}{2}\rangle_g$					0.084	0.875	0.040	
$ \frac{5}{2}\rangle_g$						0.055	0.917	0.028
$ \frac{7}{2}\rangle_g$							0.023	0.977

Table 3.2: Table of normalised oscillator strengths, calculated from Rančić's thesis [58]. The oscillator strengths for the  $\Delta m_I = 0$  optical transitions are the main diagonal, with the  $\Delta m_I = \pm 1$  on either side. Rančić measured the oscillator strengths of the  $\Delta m_I = \pm 1$  relative to the  $\Delta m_I = 0$  optical transitions and assumed that the oscillator strengths of the  $\Delta m_I = 0$  were constant. Logically, it would follow that the sum of the optical transitions for each hyperfine level should be constant. To account for this, Rančić's oscillator strength numbers have been normalised according to the row of the above table. The oscillator strengths of the  $\Delta m_I > |1|$  have not been measured, but it is assumed that they are  $< 1\%$  because they cannot be seen in the spectra of Figure 3.15.

into the  $|\frac{7}{2}\rangle_g$  hyperfine level. From looking at the optical transitions (black dots) we can see that the population has moved into the  $|\frac{7}{2}\rangle_g$  hyperfine level, the high frequency transition of the  $\Delta m_I = -1, 0$ . As a result, the  $\Delta m_I = +1$  feature has almost disappeared. However, it is hard to distinguish the  $\Delta m_I = +1$  in the spin polarised ensemble from the other magnetic inequivalent subgroup. This is because spin polarising to the  $|\frac{7}{2}\rangle_g$  hyperfine level has also partially spin polarised the magnetic inequivalent subgroup towards the  $|\frac{7}{2}\rangle_g$  hyperfine level. As a result, the  $\Delta m_I = -1$  and  $\Delta m_I = +1$  for both subgroups have merged. The spectrum of both subgroups can be seen in Figure 3.14.

The optical depth of the  $\Delta m_I = 0$  has also increased to 24.6 dB. Another notable feature in the spin polarised spectrum is the bump from the isotopic impurities at 180 MHz.

### 3.8.3 Selective anti-polarisation

The second step in the preparation is referred to as selective anti-polarisation and uses the spin polarised ensemble explained in the Section 3.8.2. This technique takes a small sub-ensembles of ions from within a spin polarised ensemble and transfers them into another hyperfine level. Here, I describe



the process for the example of ions spin polarised into the  $|+\frac{7}{2}\rangle_g$  hyperfine level and then a narrow anti-hole is transferred into the  $|-\frac{7}{2}\rangle_g$  hyperfine level.

Selective anti-polarisation is achieved by, first, burning a spectral hole in the peak of the spin polarised feature. This creates anti-holes in the nearby hyperfine levels. We burn on the  $\Delta m_I = -1$  optical to transfer ions into the lower  $|+\frac{5}{2}\rangle_g$  hyperfine level, to facilitate efficient population transfer. Thus, we have created a hole in the  $|+\frac{7}{2}\rangle_g$  feature and an anti-hole in the  $|+\frac{5}{2}\rangle_g$  hyperfine level. This anti-hole can then be transferred into the  $|+\frac{3}{2}\rangle_g$  hyperfine level by burning directly on the  $|+\frac{5}{2}\rangle_g$  anti-hole in the  $\Delta m_I = -1$  transition. We can repeat this process sequentially, burning on the remaining 5 hyperfine levels until there is an anti-hole in the  $|-\frac{7}{2}\rangle_g$  hyperfine level.

In reality, when burning a spectral hole, anti-holes can be created in any of the hyperfine levels, as the ions can decay by any  $\Delta m_I$  transition, even back to a hyperfine level from a previous step (although decaying via the  $\Delta m_I = 0$  is most likely because of the branching ratios). To account for this, each holeburning step is only 100  $\mu\text{s}$  long and the entire process is continuously repeated for 150 ms. By repeating the process for many lifetimes ( $> 15$ ) we can ensure that the majority of the ions (over 90%) of the narrow sub-ensemble end up in the  $|-\frac{7}{2}\rangle_g$  hyperfine level.

To perform the anti-polarisation technique, the hyperfine splittings need to be measured to a higher accuracy than the width of the anti-hole we wish to create. That is why the hyperfine splittings were measured to such a high accuracy (50 kHz) as shown in Table 3.1. The hyperfine splittings were measured by spin polarising the ensemble and preparing anti-holes in different hyperfine levels. Then, the frequency of the anti-holes were recorded.

Figure 3.16 B shows the spectrum of a 1.5 MHz wide anti-hole that was anti-polarised into the  $|-\frac{7}{2}\rangle_g$  hyperfine level. Figure 3.16 A models the absorption profile of the  $\Delta m_I = 0$  absorption feature after the anti-polarisation process, using the Er:YSO absorption model, Appendix C. The anti-hole has a very high optical depth, 21 dB (Figure 3.16 B). It has a lower optical depth than the spin polarised feature because of the difference in oscillator strength for these two transitions, see Table 3.2. We expect that more than 95% of the erbium ions have been transferred from the  $|+\frac{7}{2}\rangle_g$  to the  $|-\frac{7}{2}\rangle_g$ . However, it is difficult to accurately measure optical features with more than 20 dB absorption. Finally, in the modelled spectrum, we can see the hole burnt into the spin polarised  $|+\frac{7}{2}\rangle_g$  ions at 428 MHz and the corresponding anti-hole at 0 MHz along with many other holes and anti-holes. The holes are due to the anti-polarisation processing burning into different points in the  $|+\frac{7}{2}\rangle_g$  line, due to overlap between optical transitions.

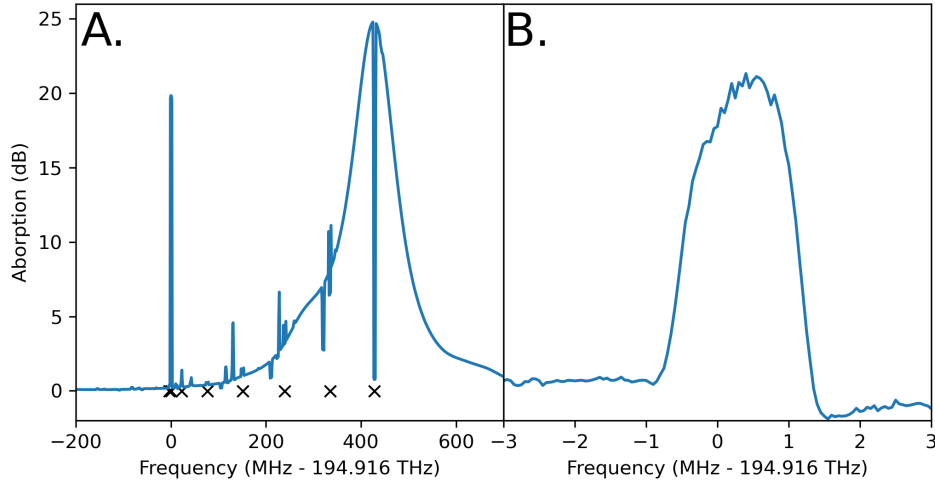


Figure 3.16: A. Modelled spectrum of the  $\Delta m_I = 0$  peak when spin polarised into the  $|+\frac{7}{2}\rangle_g$  hyperfine level with a narrow feature anti-polarised into the  $|-\frac{7}{2}\rangle_g$  hyperfine level (the model explained in Appendix C). Extra holes and anti-holes (between 0–350 MHz) are due to the overlap of optical transitions. The crosses mark the different  $\Delta m_I = 0$  transitions. B. Recorded spectrum of a 1.5 MHz anti-hole prepared in the same way as A. The background level changes between the two sides of the anti-hole due to dispersion from the optically thick anti-hole causing a phase shift between the weak signal and local oscillator.

### 3.9 Spectroscopy of selectively anti-polarised features

This section details several spectroscopy experiments on anti-polarised features. The experiments here investigated the lifetime of prepared anti-holes, the broadening between ground state hyperfine levels, and a mechanism that can undo spectral preparation.

The experiments are discussed here because the results of the experiments are unrelated to the experimental chapters, Chapter 4, 5 and 6. However, the results here are still very much related to ensemble preparation and are still very relevant to the thesis as a whole.

#### 3.9.1 Anti-hole lifetime

When looking to create specially tailored spectral features for the purposes of storing quantum information, an important property of these features is their lifetime. The coherence time for a given transition is bounded by two times the optical lifetime ( $T_2 \leq 2T_1$ ). Quantum communications require quantum memories with an efficiency of at least 90% and storage times of at least 100's of milliseconds. For such a system to be realised, we need our optical preparation to have a lifetime much longer than the intended storage time. Previously Rančić measured the spectral hole lifetime with the ensemble in thermal equilibrium to be 60 seconds [59]. In his thesis, he explains that the main cause of hyperfine relaxation above 3 T is due to hyperfine cross relaxation, as erbium ions can exchange spin with nearby erbium ions. The upper bound for this lifetime is given by the spin-lattice lifetime, predicted to be around 10 minutes [59].

The selective anti-polarisation process creates narrow optical features from a spin polarised ensemble. This also removes ions from adjacent hyperfine levels that will couple strongly and cause nuclear spin flips. Thus, we expect an anti-polarised feature to have a lifetime longer than the unpolarised ensemble. We measure the lifetime of an anti-polarised feature by preparing the feature and then regularly probing the feature with weak pulses. We also probe the other hyperfine levels to observe where the ions decay to, along with the anti-hole lifetime.

First, the ensemble was spin polarised into the  $|-7/2\rangle_g$  hyperfine level. From there, a 1 MHz wide anti-hole was selectively anti-polarised into one of the other hyperfine levels  $[-5/2 \rightarrow +7/2]$ . Periodically, every hyperfine level was probed with a series of weak pulses for delay times up to several minutes. This process was repeated until every hyperfine level had been tested.

Figure 3.17 shows the results for the anti-hole prepared into the  $|+7/2\rangle_g$  hyperfine level. Each vertical line corresponds to the population in a hyperfine level. For each hyperfine level, the absorption was measured and scaled to show the percentage population in each hyperfine level.  $|-7/2\rangle_g$  starts at

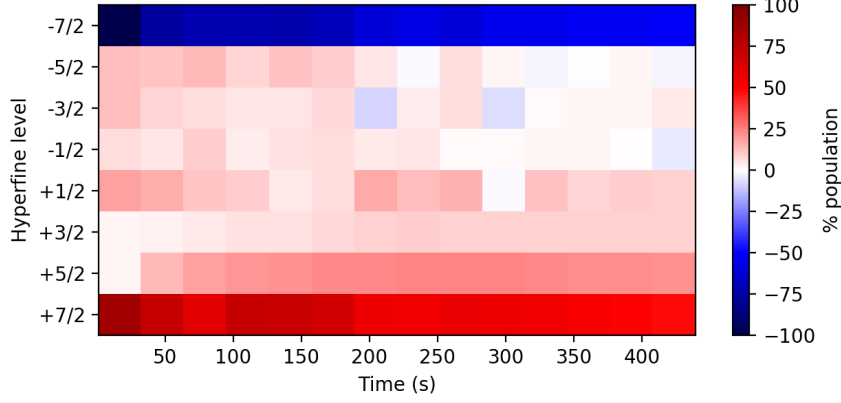


Figure 3.17: Lifetime and decay pathways of an anti-hole prepared into the  $|+\frac{7}{2}\rangle_g$  hyperfine level. The population of each hyperfine level is shown in vertical bands. The  $|-\frac{7}{2}\rangle_g$  hyperfine level starts at  $-100\%$  as the ions have been removed from this level to create the anti-hole.

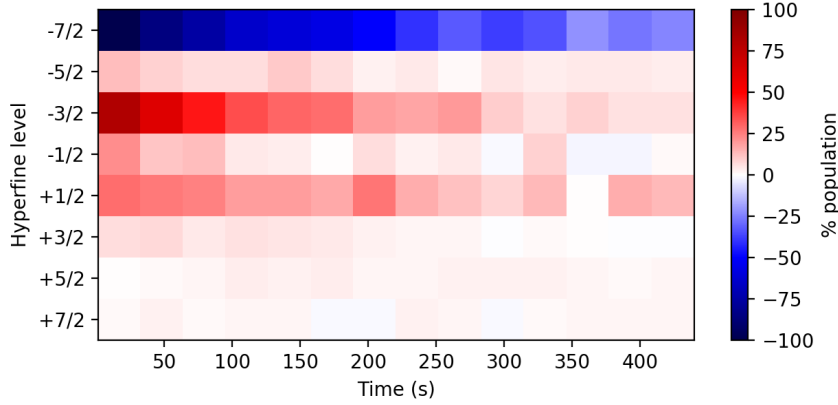


Figure 3.18: Lifetime and decay pathways of an anti-hole prepared into the  $|-\frac{3}{2}\rangle_g$  hyperfine level. The population of each hyperfine level is shown in vertical bands. The  $|-\frac{7}{2}\rangle_g$  hyperfine level starts at  $-100\%$  as the ions have been removed from this level to create the anti-hole.

hyperfine level	lifetime (s)
$ \frac{5}{2}\rangle_g$	$147 \pm 17$
$ \frac{3}{2}\rangle_g$	$152 \pm 9$
$ \frac{1}{2}\rangle_g$	$167 \pm 14$
$ \frac{1}{2}\rangle_g$	$156 \pm 17$
$ \frac{3}{2}\rangle_g$	$188 \pm 4$
$ \frac{5}{2}\rangle_g$	$180 \pm 37$
$ \frac{7}{2}\rangle_g$	$821 \pm 96$

Table 3.3: lifetime of each hyperfine level when the ensemble is spin polarised into the  $|\frac{7}{2}\rangle_g$  hyperfine level (at 6 T).

–100% as ions have been anti-polarised from this level into the  $|\frac{7}{2}\rangle_g$ . From looking at this graph, we can see that the  $|\frac{5}{2}\rangle_g$  and  $|\frac{7}{2}\rangle_g$  hyperfine levels are slowly repopulated, and the other hyperfine levels remain relatively empty. Figure 3.18 shows the results for the anti-hole prepared into the  $|\frac{3}{2}\rangle_g$  hyperfine level. In this data set, the anti-hole only decays directly back to the  $|\frac{7}{2}\rangle_g$  hyperfine level, and does not decay to the surrounding hyperfine levels ( $|\frac{5}{2}\rangle_g$  and  $|\frac{1}{2}\rangle_g$ ).

The results from the  $|\frac{7}{2}\rangle_g$  data shows two main decay pathways, a direct relaxation path back to the highly populated  $|\frac{7}{2}\rangle_g$  hyperfine level, and a second relaxation method where the anti-hole decays into the surrounding hyperfine levels  $\Delta m_I = \pm 1$ . The  $|\frac{3}{2}\rangle_g$  data, however, only shows one decay pathway. The anti-hole decays directly back to the  $|\frac{7}{2}\rangle_g$  hyperfine level. This data indicates a general trend. Relaxing directly back to the  $|\frac{7}{2}\rangle_g$  hyperfine level is the dominant decay path when the anti-polarised feature is prepared in a hyperfine level close to the spin polarised feature, i.e. the negative hyperfine levels. This is also indicated by the shorter lifetimes of the hyperfine levels close to the  $|\frac{7}{2}\rangle_g$  hyperfine level, Table 3.3.

The results in Table 3.3 show that the lifetime of the anti-polarised features increases for anti-holes prepared into hyperfine levels further away from the bulk spin polarised feature, as expected. Interestingly, the increase in lifetime does not seem to be significant between the extrema of the hyperfine levels ( $|\frac{5}{2}\rangle_g$  to  $|\frac{5}{2}\rangle_g$ ). I have ignored the  $|\frac{7}{2}\rangle_g$  which shows an extraordinarily long lifetime, which is on the order of the spin-lattice lifetime, the upper bound for anti-hole lifetimes. The reason for this long lifetime is not yet understood. I speculate that this particular magnetic field and crystal orientation creates a particular hyperfine splitting that suppresses the hyperfine cross relaxation between the two  $|\pm\frac{7}{2}\rangle_g$  levels. Another interesting result is the  $|\frac{5}{2}\rangle_g$  hyperfine level (the level adjacent to the spin polarised

feature) has a much longer lifetime than the spectral hole lifetime recorded by Rančić [59], where the only key differences between these measurements and Rančić's was that the ensemble was not spin polarised in Rančić's experiment and the magnetic field orientation was different, by  $\sim 1$  degree. A possible reason for this could be that the laser we have used to probe the ions has better frequency stabilisation than the laser Rančić used. Rančić's laser might have accidentally unburnt the anti-hole. Or Rančić's probe pulses may have been too strong and may have directly unburnt the probed feature.

### 3.9.2 Hyperfine broadening

In the RASE chapters, Chapters 5 and 6, the properties of four-level echos are examined (Sections 5.2.2 and 6.3). Without hyperfine rephasing, the storage time of these multi-level echoes is limited by the broadening between the different ground state levels used as shelving levels. Here, I describe an experiment to measure the broadening between different hyperfine levels. This broadening also affects the widths of anti-holes prepared using the anti-polarisation sequence, this was seen in Section 4.5.

To measure this hyperfine broadening, first a MHz-wide anti-hole was prepared into a given hyperfine level. Then, a narrow hole was burnt in the MHz-wide feature. Corresponding anti-holes would appear in the adjacent hyperfine levels. The broadening between the hyperfine levels was determined by comparing the width of the narrow hole to the narrow anti-holes. Raw data and the corresponding fit to a hole and anti-hole are shown in Figure 3.19.

The anti-hole spectrum will be a convolution between the narrow hole's spectrum and the hyperfine broadening. We assume that the narrow hole's spectrum and the hyperfine broadening are both Gaussian. The width of the anti-hole is the width of the hole and the broadening mechanism added in quadrature. The broadening between hyperfine levels is shown in Table 3.4, under the broadening column.

The width of the narrow hole varied depending on the hyperfine level, and decreased with hyperfine level. The width of the narrow holes ranged from  $\sim 100$  kHz in the  $|-7/2\rangle_g$  hyperfine level to  $\sim 30$  kHz in the  $|+5/2\rangle_g$  hyperfine level, shown in Table 3.4.

Table 3.4 shows that the broadening and the width of the narrow holes decreases with hyperfine level. The range of hyperfine broadening is quite extreme. An order of magnitude over the different hyperfine levels. This would suggest that if we want to create narrow spectral features, less than 100 kHz wide, we would want to use the higher hyperfine levels. Section 5.2.2 shows that the four-level echo coherence times are also longer for the higher hyperfine levels.

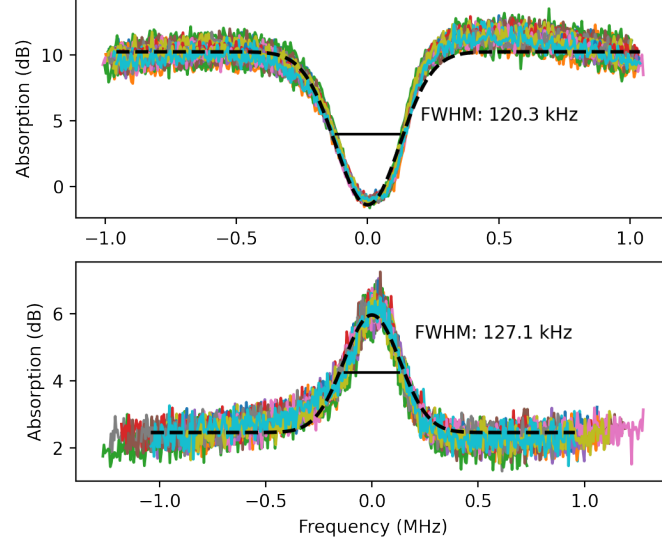


Figure 3.19: Raw data and fit for a series of holes and anti-holes. A feature was prepared in the  $|-5/2\rangle_g$  hyperfine level and a hole was burnt on the  $|-5/2\rangle_g \rightarrow |-5/2\rangle_e$  optical transition. The top graph shows 20 spectra of a 120 kHz hole burnt into a broad feature, a Gaussian (black dashed line) was fit to the average of the 20 holes. The bottom graph shows the anti-holes that on the  $|-3/2\rangle_g \rightarrow |-3/2\rangle_e$  transition, with the corresponding Gaussian fit.

hyperfine transitions	hole width (kHz)	broadening (kHz)
$ +5/2\rangle_g \rightarrow  +7/2\rangle_g$	$28 \pm 5$	$9 \pm 5$
$ +3/2\rangle_g \rightarrow  +5/2\rangle_g$	$36 \pm 6$	$16 \pm 6$
$ +1/2\rangle_g \rightarrow  +3/2\rangle_g$	$37 \pm 4$	$9 \pm 5$
$ -1/2\rangle_g \rightarrow  +1/2\rangle_g$	$57 \pm 6$	$11 \pm 5$
$ -3/2\rangle_g \rightarrow  -1/2\rangle_g$	$98 \pm 3$	$36 \pm 7$
$ -5/2\rangle_g \rightarrow  -3/2\rangle_g$	$120 \pm 3$	$42 \pm 3$
$ -7/2\rangle_g \rightarrow  -5/2\rangle_g$	$78 \pm 2$	$76 \pm 5$

Table 3.4: Broadening between hyperfine levels in  $^{167}\text{Er}^{3+}:\text{Y}_2\text{SiO}_5$  at 6 T. The broadening column refers to the inhomogeneous broadening between two hyperfine levels.

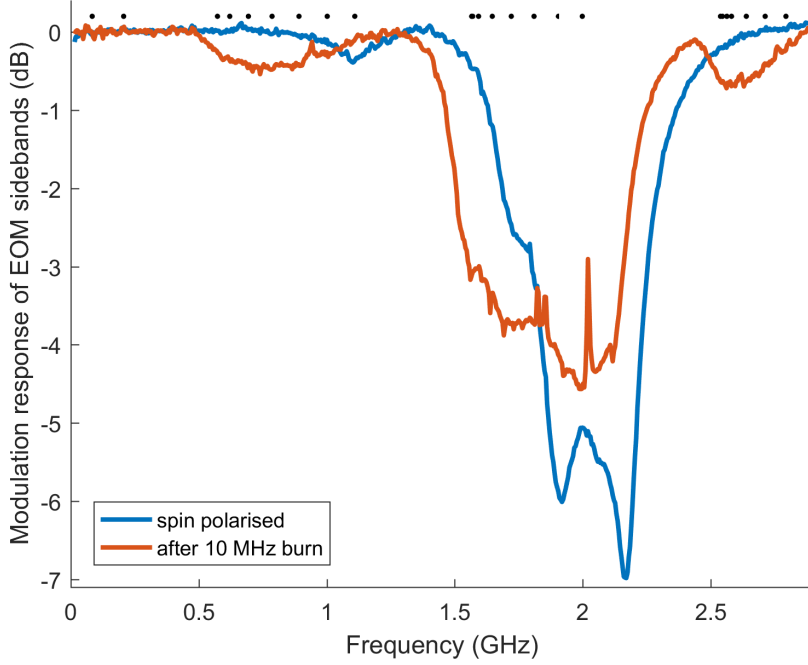


Figure 3.20: Initial evidence of ensemble rethermalisation. The blue trace shows the spectrum of the spin polarised ensemble. The red trace shows the spectrum after a 100 ms, 10 MHz trench burn. The spectrum was taken using an EOM, (explained in Section 3.7), and has an inverted peak around the  $\Delta m_I = 0$  (at 2 GHz).

### 3.9.3 Excitation induced rethermalisation of hyperfine levels

When developing the ensemble preparation process, Section 3.8, the ensemble was first spin polarised and then a narrow ensemble was anti-polarised into a different hyperfine level. We noticed that when anti-polarising a large ensemble of ions,  $\sim 10$  MHz, the spin polarised ensemble would revert to the unpolarised state. Figure 3.20 shows a 10 MHz trench burnt into a spin polarised ensemble, with a burn time of 100 ms. The ensemble, in a short timescale (100s of milliseconds), rethermalises back to the thermal distribution where all hyperfine levels are equally populated, much quicker than the  $\mathcal{O}(100)$  second hyperfine lifetime, Section 3.9.1. The rethermalisation shows that an interaction is affecting ions not directly driven by the laser.

In Figure 3.20 we compared the spin polarised spectrum before and after perturbation. Recording the spectrum with this method was useful for demonstrating the effect. It showed that the ensemble has indeed returned to the thermal state and that all hyperfine levels have been repopulated. However, using this method was difficult to quantify the effect, because the



modulation response of the EOM is non-linear for high ( $> 6$  dB) optical depths. Instead, spectral holes were probed to measure the rethermalisation effect. First, a spectral hole was burnt into the ensemble. Then, a 10 MHz wide trench was burnt into the ensemble (at a different frequency), referred to as the perturbation beam. The hole was probed before and after perturbation, to measure how much the hole fills in as a result of perturbation. we refer to this measurement technique as hole filling.

The data collected in this section was taken with assistance from an Honours student, Adrian Schmidt. Parts of the data analysis and graphs were performed and created by Adrian and are referenced as such. Figures 3.21 and 3.22 were generated from data presented in Chapters 4 and 5 of Adrian's thesis [63]. The following experiments were performed, with Adrian, to measure the spectral and spatial properties of the rethermalisation effect. First, we tested the spectral bandwidth of the rethermalisation effect. For these tests, we prepared a hole in the ensemble and then perturbed the other magnetic inequivalent subgroup, shown in Figure 3.14. Recall, from Section 2.2, that the magnetic inequivalent subgroup will be degenerate when no magnetic field is applied to the crystal, or with an applied magnetic field aligned with, or perpendicular to, the  $C_2$  axis. This means if we can rotate the crystal in the magnetic field, then we can control the frequency splitting between these two groups. The rotation of the crystal was controlled using a set of Attocube nanopositioning goniometers.

The attocubes were used to align the  $D_1$  crystal axis with the magnetic field, such that the two magnetic subgroups overlapped in frequency. The hole filling technique was used to measure the rethermalisation effect while the attocubes rotated the crystal to spectrally separate the two magnetic subgroups. The probe beam continued to probe the lower frequency subgroup, whilst the perturbation beam burnt the higher frequency subgroup.

Figure 3.21 shows the filling of a spectral hole as the two magnetic inequivalent subgroups were spectrally separated. The data shows that the effect of the perturbing beam decreases with frequency separation, with the hole filling reducing by  $e^{-1}$  after the two subgroups were separated by 3.1 GHz.

Next, the spatial range of the rethermalisation effect was tested by separating the spectral hole and the perturbing beam spatially. The perturbing laser was mounted on a translation stage so that the perturbing beam could be spatially separated from the probe beam. As with the spectral separation measurement, the hole filling technique was used to measure the effect of the perturbing beam as the two beams were spatially separated. The experiment was run two times. Firstly, a standard circular lens was used to focus the perturbing beam on the sample, producing a line of excitation through the crystal. Secondly, a cylindrical lens to change the perturbing beam into a  $3 \times 0.1$  mm ellipse, producing a plane of excitation through the crystal.

Figure 3.22 shows the rethermalisation was still present even when the

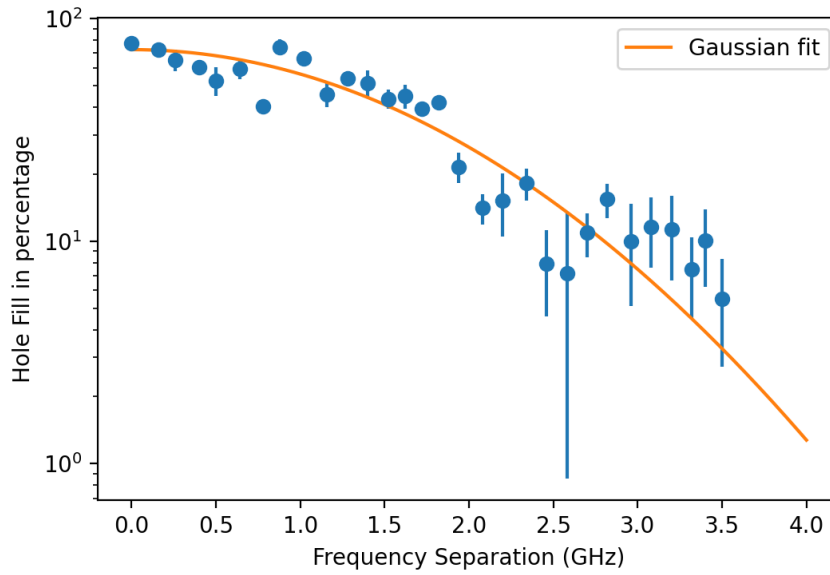


Figure 3.21: Hole filling from the perturbation beam as the crystal was rotated in the magnetic field. The perturbation beam was incident on the higher frequency magnetic inequivalent subgroup. The  $x$ -axis shows the frequency splitting between the magnetic subgroups as the crystal was rotated.

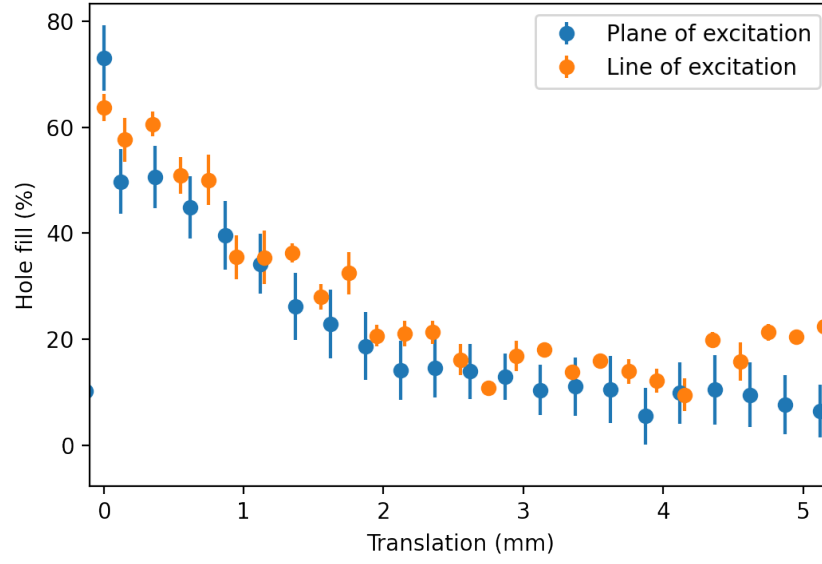


Figure 3.22: Hole filling as the perturbation beam was spatially separated from the probe beam. Line of excitation refers to a focused perturbation beam with a  $40\text{ }\mu\text{m}$  beam width, plane of excitation refers to the perturbation beam focused using a cylindrical lens, focusing to a  $3\text{ mm} \times 100\text{ }\mu\text{m}$  ellipse on the crystal.

spectral hole and perturbing beam are separated by millimeters. This hole filling reduced by  $e^{-1}$  after a separation of 1.5 mm. The data also shows that the two excitation methods have similar effects on the ensemble. This tells us that the phonons are scattering throughout the crystal, rather than travelling ballistically [12]. Also, In the line of excitation data, the hole filling increases at 4.5 – 5 mm. This was because the laser beam intersected with the edge of the crystal, causing laser backscatter throughout the crystal.

The rethermalisation effect's 1.5 mm range discounts any short range ion-ion effects, such as spin-spin interactions. The only likely long range effect between ions in these crystals are from phonons. Phonons can either be created from by a resonant process, such as the relaxation between Zeeman levels, or non-resonantly by locally heating the crystal with the laser. For the laser to heat the crystal, some portion of the ions excited by the laser must decay to a crystal field level or the upper Zeeman level. The ions then decay, non-radiatively, to the ground state and then scatter into the thermal distribution. Heating the crystal will only depend on the number of ions excited, and not the optical or hyperfine frequencies of those ions. The results shown in Figure 3.21 discounts thermal phonons as the rethermalisation effect has a narrow frequency bandwidth. This means that rethermalisation effect is from resonant phonons.

From Figure 3.21, we might assume that the bandwidth of these phonons is 3.1 GHz. However, 3.1 GHz was only the optical splitting between the two magnetic subgroups. The bandwidth of the phonons will depend on the transitions that produced the phonons. For example, if the phonons are produced between the two Zeeman levels of the ground state, then the phonon bandwidth is much larger than 3.1 GHz. This is because the Zeeman levels split by 200 GHz/T, whereas the optical transitions only split by 20 GHz/T. Thus, the bandwidth of the phonons could be 31 GHz. Alternatively, if the phonons are produced between two of the crystal field levels then the bandwidth will depend on the splitting of the crystal field levels. Currently, the exact transition(s) that produce that phonons are not known, more measurements are needed to fully characterise the frequency and lifetime of the phonons.

To summarise, we have found that spectral rethermalisation is caused by resonant phonons. While the resonant phonons are an issue for spectral preparation, the rethermalisation effect requires a large bandwidth of ions to be perturbed. In the examples shown here, trench widths of 10 MHz were used. In the next few chapters, we will prepare features using selective anti-polarisation technique. To avoid spectral rethermalisation the bandwidth of these anti-holes will be limited to 2 MHz, and usually kept to 1 MHz.

### 3.10 Summary

This chapter explained many of the details of the erbium quantum memory experiment. The later parts of the chapter described the general ensemble preparation techniques that were developed in this thesis for the main experiment chapters, Chapters 4, 5, and 6. Finally, the end of this chapter shows some spectroscopy experiments related to the preparation techniques, including the measurements of the: anti-hole lifetime, hyperfine broadening, and spectral rethermalisation.

The experiment is designed so that the user could interact with any of the optical-hyperfine transitions, with high spectral accuracy. The ensemble preparation shows the level of control we have over our atomic ensemble. We have the ability to spin polarise into a given extremum hyperfine level and then prepare sub-ensembles into any of the other hyperfine ground levels.



## Chapter 4

# AFC Experiments

This chapter discusses a series of experiments that demonstrate an Atomic Frequency Comb (AFC) [2] using  $^{167}\text{Er}^{3+}:\text{Y}_2\text{SiO}_5$ . The overarching goal of demonstrating an AFC was to both test the preparation techniques discussed in Section 3.8.2 and to show that  $^{167}\text{Er}^{3+}:\text{Y}_2\text{SiO}_5$  is capable of non-classical storage. The AFC protocol was chosen because the performance of the memory protocol depends entirely on the preparation of a spectral comb. This is different to memory protocols like RASE [49] or Revival Of a Silenced Echo (ROSE) [19], which require high efficiency  $\pi$ -pulses to operate efficiently, or to protocols like the Gradient Echo Memory (GEM) [3] which requires external electric or magnetic field gradients.

This chapter will focus, mainly, on two AFC results. The first result is a classical memory demonstration which characterises the preparation and efficiency of the AFC. The second result is the demonstration of non-classical storage using the AFC, then the limitations of the current AFC experiment are discussed. Finally, the theoretical performance of a cavity-enhanced AFC using spin-state storage is calculated using the limitations of the preparation sequence, found from the classical memory demonstration.

### 4.1 A brief history of the AFC

As discussed in Section 2.6, an AFC is a spectral comb, a series of highly absorbing teeth, of width  $\gamma$ , separated by regions of minimal absorption, of width  $\Delta$  [2], Figure 4.1. The AFC was first proposed as a quantum memory protocol in 2009 by Afzelius et al. [2] and was then demonstrated by the same group in 2010 [4]. The initial demonstrations of AFCs used non-Kramers ions doped into  $\text{Y}_2\text{SiO}_5$ , such as praseodymium [4], europium [69], and thulium [15]. More recent demonstrations using Kramers ions, such as neodymium [17], and ytterbium [13] have shown efficiencies comparable to their non-Kramers counterparts (35% in praseodymium compared to 33% in neodymium).

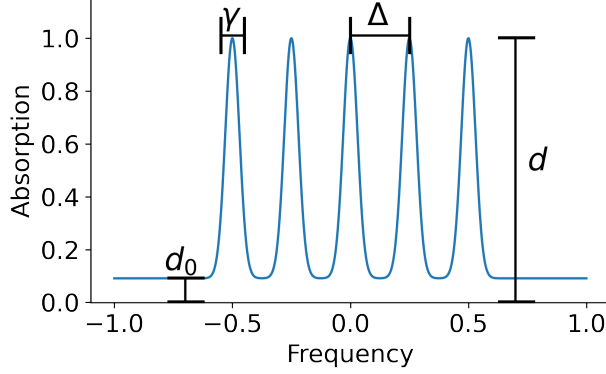


Figure 4.1: Example showing the four parameters of an AFC: the tooth width and spacing ( $\gamma$ ,  $\Delta$ ), the tooth absorption ( $d$ ), and the AFC background absorption ( $d_0$ ).

To date, there have been no such memory demonstration, AFC or otherwise, in erbium that match the performance of the non-Kramers ions. Erbium-based memory demonstrations have shown  $<1\%$  efficiencies and  $<1 \mu\text{s}$  storage times [61, 47]. In these demonstrations, the storage time was limited by short optical coherence times, while the efficiency was limited by the preparation of the memory. Ultimately, the memory preparation was limited because of the short ground state lifetimes in erbium [47, 37]. Rančić et al. showed that both the ground state hyperfine lifetime and coherence time can be extended by applying a large magnetic field [59]. The main goal of this chapter is to expand on Rančić’s work to show that an efficient AFC can be created using erbium.

## 4.2 AFC parameters

There are several important parameters to consider when making an AFC: the tooth width and spacing ( $\gamma$ ,  $\Delta$ ), the tooth absorption ( $d$ ), and the AFC background absorption ( $d_0$ ) (Figure 4.1). These parameters will also determine the efficiency, bandwidth, and optical storage time of the AFC, which are the three memory parameters we are interested in when characterising the performance of a quantum memory.

Three of the four AFC parameters ( $\gamma$ ,  $\Delta$ , and  $d$ ) can be directly measured by recording the spectra of the AFC. The background absorption, however, is more difficult to measure due to limitations in the AFC preparation process. The next section, Section 4.3, will explain the AFC preparation process. Ideally, spin pumping will remove all background absorption from the optical storage transition ( $|-7/2\rangle_g \rightarrow |-7/2\rangle_e$ ). However, due to the 150 MHz inho-



ogeneous linewidth of our crystal and imperfect spin polarisation, this is not true. This spin pumping background absorption will attenuate the input pulse and the resultant echo, lowering the AFC efficiency. But, this attenuation will not be detectable in the AFC storage experiments since both the input pulse and echo are attenuated. Instead, spectral holeburning is used to probe and measure the spin pumping background absorption.

### 4.3 AFC experiment outline

The experiments detailed in this chapter use the experimental setup outlined in Section 3.1. To create an AFC, we make use of the preparation techniques explained in Section 3.8. The first step is spin pumping, which prepares the bulk ensemble into one hyperfine level, either of the  $|\pm\frac{7}{2}\rangle_g$  (ground state) hyperfine levels. Then the next step is selective anti-polarisation, which creates an anti-hole resolved from the broader spin polarised ensemble, Section 3.8.3. This is the first tooth of the comb. The remaining teeth of the AFC are created by repeating the selective anti-polarisation technique. Each subsequent time the technique is repeated, the initial burn frequency is changed by the AFC tooth gap,  $\Delta$ . For the following experiments, the ensemble was spin pumped into the  $|\pm\frac{7}{2}\rangle_g$  hyperfine level. The AFC was prepared in the other extremum hyperfine level,  $|\mp\frac{7}{2}\rangle_g$ , as indicated by Figure 4.2. The AFC was prepared with 5 teeth,  $\gamma = 380$  kHz, and  $\Delta = 1.5$  MHz.

Once the AFC is prepared, any light pulse resonant with the AFC will be stored. After a time delay,  $t = 1/\Delta$ , an echo is coherently re-emitted from the AFC, more detail in Section 2.6. In these experiments, the input pulses stored in the AFC were  $0.2 \mu\text{s}$  Gaussian pulses, with a corresponding 5 MHz bandwidth. The intensity of the pulse depended on the particular experiment. Strong,  $\langle N \rangle > 10^6$ , photon pulses were used in the classical experiments, while weak,  $\langle N \rangle = 0.8$ , photon pulses were used in the non-classical experiments. Preceding and following the stored pulses were a pair of non-resonant phase correcting pulses, discussed later in Section 4.6.1. Figure 4.3 shows a simplified pulse diagram for an AFC experiment. The light transmitted through the AFC was detected on a pair of balanced heterodyne detectors. The local oscillator frequency was 15 MHz detuned from the central frequency of the AFC.

The results will be presented in the following order. First, the spin pumping background absorption is determined using spectral holeburning to probe the absorption at the frequency of the AFC. Next will be the classical AFC measurements. The strong input pulses were used to determine the efficiency of the AFC and accurately measure the four AFC parameters:  $\gamma$ ,  $\Delta$ ,  $d$ , and  $d_0$ . Finally, the non-classical measurements will be presented, using weak input pulses. Then coherence between the input and echo is shown. The noise performance of the AFC is measured and, by using a

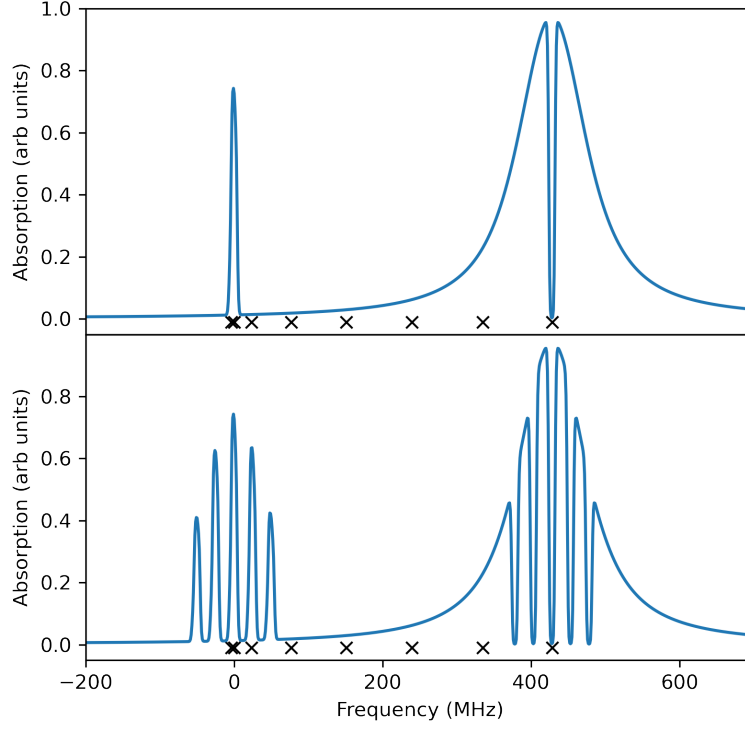


Figure 4.2: Visual demonstration of the end point of the anti-polarisation process and how the process is repeated to create an AFC. This figure shows the modelled spectrum of the  $\Delta m_I = 0$  optical transition in our crystal, with the ensemble spin polarised to the  $|+\frac{7}{2}\rangle_g$  hyperfine level (model explained in Appendix C). The top figure shows the end point of the selective anti-polarising sequence for a single 10 MHz wide feature, the arrow shows the initial burn frequency (428 MHz). The bottom figure shows an AFC made by sequentially burning at 5 different initial frequencies. For visualisation purposes, the teeth are much wider and more spaced out ( $\gamma = 10$  MHz,  $\Delta = 25$  MHz) than in the actual AFC demonstration ( $\gamma = 380$  kHz,  $\Delta = 1.5$  MHz). The x's indicate the center of the different optical transition frequencies. They start at  $|-\frac{7}{2}\rangle_g$  (0 MHz) and increase to  $|+\frac{7}{2}\rangle_g$  (428 MHz).

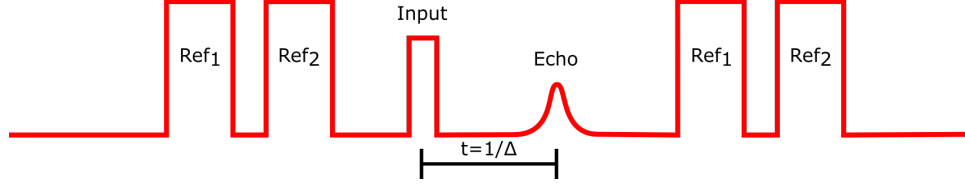


Figure 4.3: AFC pulse diagram. Ref<sub>1</sub> and Ref<sub>2</sub> are phase reference pulses that are not resonant with the AFC.

non-classicality test, described in Section 2.6.2, non-classical storage will be shown.

## 4.4 Spin pumping background absorption

To determine the spin pumping background absorption, we spin-polarise the ensemble and measure the transmission of two  $0.5 \mu\text{s}$  Gaussian pulses at the frequency of the AFC (0 MHz in Figure 4.2). The first pulse was sent through directly after spin pumping the ensemble, and the second pulse was sent after burning a narrow (250 kHz) spectral hole at the frequency of the AFC.

The pulse intensity was weak (0.1% burn power) to minimise holeburning from the pulses themselves, and the experiment was repeated 1,000 times at a repetition rate of 1 kHz. The background absorption was determined by dividing the averaged Fourier transforms of the two pulses. Figure 4.4 shows the spectra of the two Gaussian pulses. In the top graph, evidence of a small hole can be seen at the peak of the after burn pulse, at 18.1 MHz. The bottom graph shows the after burn probe pulse divided by the before burn probe pulse, converted to dB. This is the relative transmission of the after burn probe pulse. A Lorentzian fit to the transmission data gives a hole depth of  $0.48 \pm 0.06$  dB.

We can estimate how much the absorption of various optical transitions contributed to the spin polarisation background absorption using the erbium holeburning model described in Appendix C. If we assume perfect spin polarisation into the  $|+\frac{7}{2}\rangle_g$  hyperfine level, then we have two populations of ions that contribute to the background absorption around the AFC. The first is the tails of the spin polarised  $^{167}\text{Er}$  ions absorption line which, from the model, contribute a background absorption of 0.3 dB. The second population is the isotopic impurities  $^{166}\text{Er}$ ,  $^{168}\text{Er}$ , and  $^{170}\text{Er}$  with an abundance ratio of 10:8:5 [58], respectively, in naturally abundant erbium. However, in our isotopically purified sample, the abundance ratios are not known. For simplicity, we will treat of all these impurities as a single population with the same transition frequency and the same linewidth as the  $^{167}\text{Er}$  ions. In reality, the transition frequencies of the different isotopes will shift based on

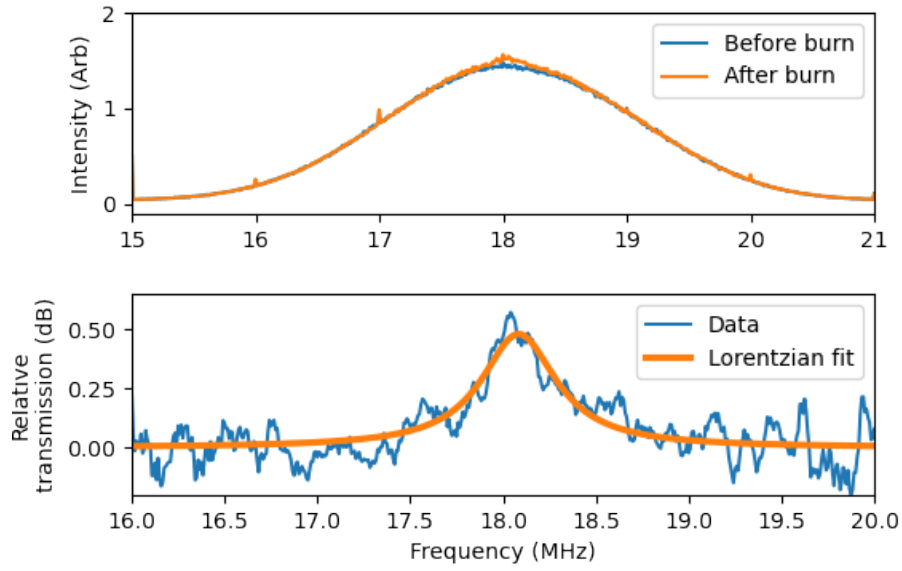


Figure 4.4: Background absorption measurements at the AFC frequency, after spin polarisation. The top graph shows the averaged spectra of the 1000 Gaussian probe pulses burning a spectral hole. The bottom graph shows the transmission of the after burn pulse relative divided by the before burn pulse. The probe pulses and hole burn were both centered at 18.1 MHz.

atomic mass [52]. From the model we expect a background absorption contribution of 0.08 dB from the isotopic impurities, giving a total background absorption of 0.38 dB (4% absorption).

From the measured 0.48 dB spin polarisation background absorption, 0.08 dB is attributed to the isotopic impurities, 0.3 dB to the wings of the  $|+\frac{7}{2}\rangle_g$  feature, and the remaining 0.1 dB is assumed to be from imperfect spin pumping (other  $^{167}\text{Er}$  ions). From these values, we see that  $>80\%$  of the background absorption can be attributed to  $^{167}\text{Er}$  ions, with the remainder due to isotopic impurities. The background absorption due to  $^{167}\text{Er}$  ions is removable. A quick ( $\sim 100$  ms) ‘clean-up’ trench burn around the AFC location will hole-burn any  $^{167}\text{Er}$  ions into a different hyperfine level and to a different region in the spectra. The isotopic impurities, however, have no hyperfine structure to be hole-burned into. Thus, the only way to reduce the background absorption due to the isotopic impurities is to grow a higher quality crystal with either narrower inhomogeneous linewidths or with lower concentrations of isotopic impurities. For our current crystal, the isotopic impurities give us a baseline for the lowest spin polarisation background absorption we can achieve, 0.08 dB. The 0.08 dB spin polarised background absorption is a baseline level of background absorption if the clean-up trench burn is implemented into the experiment. For the follow experiments, the ‘clean-up’ trench burn was not used. So 0.48 dB will be assumed for the spin polarised background absorption.

## 4.5 AFC characterisation

### 4.5.1 Efficiency

In this section, the results of a series of classical AFC experiments are presented. A strong input pulse was stored in the AFC. Figure 4.5 shows a time trace of the input pulse (blue) and the echo (orange). The first-order echo was emitted at a time  $t = \frac{1}{\Delta} = 0.66 \mu\text{s}$ . We can see that about 30% of the input pulse is transmitted through the AFC as the zeroth-order echo at time  $t \approx 0$ . Interestingly, the zeroth-order echo leads the input pulse by 24 ns. This is a consequence of phase-dispersion from the AFC. Finally, in the echo time trace, there are also smaller pulses in between the zeroth and first-order echoes. These smaller pulses are a consequence of the finite width of the AFC and that the input pulse is wider than the AFC. As a consequence, there is a longer, albeit weak, ring down from the input pulse.

The efficiency of the AFC is the ratio of the input pulse and first order echo intensities, the input pulse was digitally amplified by 0.48 dB to account for the spin pumping background absorption. The intensity of the input pulse was calculated by taking the area of the input pulse windowed about  $t = 0$  and the intensity of the first echo was calculated with the window centered

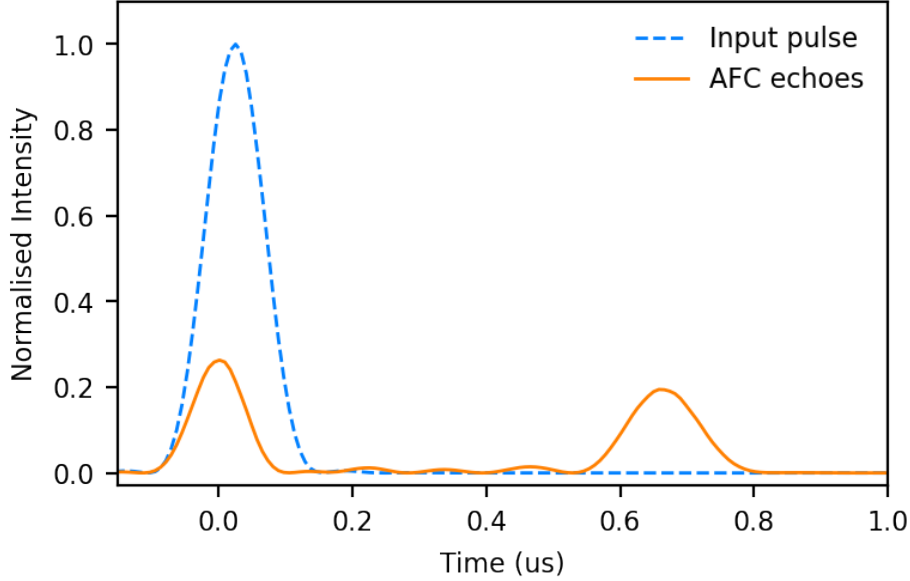


Figure 4.5: Time trace of a  $0.2 \mu\text{s}$  pulse stored in the AFC. The first echo can be seen at a time  $t = 0.66 \mu\text{s}$ . The data shown here was digitally beaten down to DC from the original heterodyne data (beat frequency at 15 MHz).

on  $t = 0.66 \mu\text{s}$ . Comparing these two time windows gives an efficiency of  $22.4 \pm 0.7\%$ .

#### 4.5.2 Spectra and background absorption

We can also measure the spectrum of the AFC by dividing the Fourier transform of the input pulse by the Fourier transform of the echo. Figure 4.6 shows the spectrum of the AFC. There are several important attributes in this spectrum: high optical depth, low background absorption, and remnants of the  $|-5/2\rangle_g$  hyperfine level from the anti-polarisation process.

In the AFC spectrum, we can see the remnants of the  $|-5/2\rangle_g$  hyperfine level, below  $-4 \text{ MHz}$ . The gaps between the AFC teeth ( $\Delta$ ) were chosen such that the  $|-7/2\rangle_g$  teeth and  $|-5/2\rangle_g$  remnants would overlap. This way the presence of ions in the  $|-5/2\rangle_g$  hyperfine level does not negatively affect the AFC performance.

The optical depth of the comb averaged at  $18 \pm 4 \text{ dB}$  and peaked at  $20 \text{ dB}$ . This high optical depth is very close to the maximum absorption of this transition,  $21 \text{ dB}$ , as explained in Section 3.8.3. Thus, demonstrating that the anti-polarisation process can move most of the erbium ions across 8 hyperfine levels, while still creating specific spectral shapes, like a comb. Here we have shown optical depths as high as 85 – 95% of the peak optical

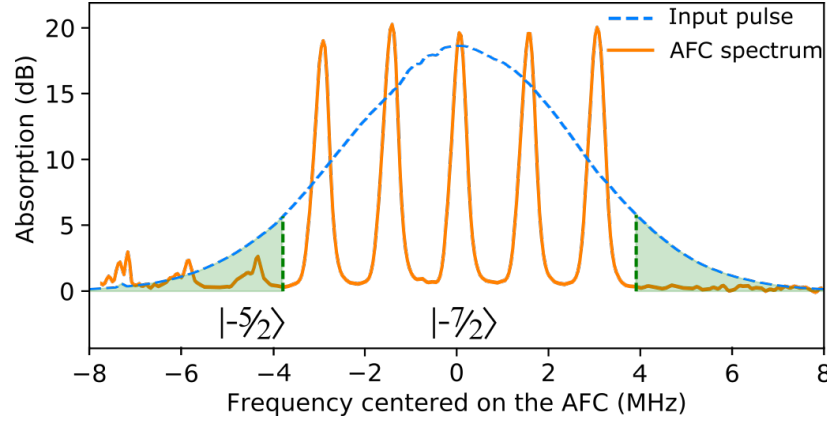


Figure 4.6: Spectrum of a five-tooth AFC with tooth width,  $\gamma = 380$  kHz, tooth gap,  $\Delta = 1.5$  MHz. The bandwidth of the input pulse is indicated by the blue dashed line. The green highlighted area shows the section of the input pulse that was not absorbed by the comb.

depth. The high peak optical depth is also important for obtaining high storage efficiencies.

The AFC has a low background absorption, averaging at  $0.51 \pm 0.05$  dB. This gives the AFC an absorption contrast relative to the average absorption peak of 40:1. This high contrast is promising, as low absorption contrast limited the efficiency of Saglamyurek et al.’s erbium memory demonstration [61]. The 0.51 dB background absorption is separate from the spin pumping background absorption. This is the background absorption added to the AFC during the anti-polarisation process. The total background absorption for the AFC is the sum of the two backgrounds, 0.99 dB.

Finally, the AFC teeth can be described by a 380 kHz Gaussian. In the selective anti-polarisation process, the tooth width was set to 300 kHz. There are two main mechanisms that would affect the width of the anti-hole: the hyperfine broadening, Section 3.9.2, and the laser linewidth. The combined broadening from all the hyperfine levels would only account for 20 kHz of the broadening. The remaining 60 kHz is assumed to be from laser frequency instabilities. Due to the mechanical instabilities in the laser, the laser frequency can jump by 100 kHz, as explained in Section 3.4.1. This is more than enough to account for the broadening measured here.

### 4.5.3 Expected performance

From the measuring the AFC’s spectrum, we have the variables required to predict the efficiency of the AFC. The efficiency of an AFC is given by Equation (2.23), we can substitute the effective optical depth,  $\tilde{d}$ , for  $\frac{d}{F}$  and  $\eta_{dephase} = e^{-\frac{1}{F^2} \frac{\pi^2}{4 \ln 2}}$  for an AFC with Gaussian-shaped teeth. A new term

was also added to account for the spin polarised background absorption and the AFC background absorption. Both sources of background absorption will attenuate our echo and will be described by  $\exp(-d_0)$ .

$$\eta = \frac{d^2}{F^2} \exp\left(-\frac{d}{F}\right) \exp\left(-\frac{1}{F^2} \frac{\pi^2}{4 \ln 2}\right) \exp(-d_0) \quad (4.1)$$

In the above equation,  $d$  is the peak optical depth, 18 dB, the finesse,  $F = \Delta/\gamma = 3.9$ , and the background absorption,  $d_0 = 1$  dB. From these values, we calculate an expected efficiency of 24.5%, which is higher than the experimentally determined efficiency, 22.4%. There are a few possible reasons for the lower measured efficiency: the teeth are not perfect Gaussians, the comb does not contain an infinite number of teeth, and the input pulse is wider than the AFC.

We assume that the first two points will negligibly contribute to the drop in efficiency. The main reason for the discrepancy comes from the wide input pulse. In Figure 4.6, the green shaded region shows the area of the pulse that is off-resonant with the AFC. This shaded region accounts for 9% of the input pulse power. Taking this overfilling into account, the experimental efficiency would be  $24.6 \pm 0.1\%$ , matching the predicted efficiency within uncertainty.

#### 4.5.4 Characterisation summary

To summarise, a  $0.2 \mu\text{s}$  pulse was stored in an AFC for  $0.66 \mu\text{s}$  with an efficiency of  $22.4 \pm 0.7\%$ , which corresponds to an efficiency of 24.6% when adjusted for the overfilling input pulse. The storage time is longer than the few previous erbium demonstrations: 200 ns [47], and 5 ns [61]. The increase in efficiency is over an order of magnitude better than the previous demonstrations: 0.2% [47], and  $\sim 1\%$  [61]. The key reason for the increase in storage time and efficiency comes from the longer ground state hyperfine lifetime and optical coherence times from operating at our temperature (1.4 K) and magnetic field (7 T). From the long ground state hyperfine lifetimes, we can achieve deeper holeburning, which allows for more absorbing features on much lower backgrounds. Along with high optical depth, we can still maintain low background absorption with a contrast ratio of 40:1 between the peaks and troughs of the AFC. Overall, this result is promising and there are methods that can be employed to improve it. These improvements are a topic of later sections, Sections 4.7.2 and 4.7.3.

### 4.6 Non-classical demonstration

In this section, we will see that the input pulse and AFC echoes are coherent with each other. Using this result, we will see that the memory is behaving non-classically. To demonstrate this coherence, we will show that the



quantum information stored in the AFC was not corrupted. One method to demonstrate non-classicality is to show that no significant noise has been added to the input pulse by storing it in the AFC. What constitutes ‘significant noise’ is explained in Section 4.6.2. However, to measure the AFC noise we will first remove any phase noise added to our AFC measurement by experimental equipment.

#### 4.6.1 Phase correction and post processing

There are two main sources of phase noise to consider in the experimental setup. The first source is from changes in the refractive index of the optical fibres and the second noise source is caused by unsynchronised RF clocks in the experimental equipment.

The experimental setup has 16 meters of optical fibre, Figure 3.1. The local oscillator and signal beam are split and pass through different optical fibres. The air conditioning in the lab jostles these fibres, and these small movements generate strain in the fibre resulting in changes in the refractive index. In turn, the effective path length of the optical fibres is changed. This change in path length creates a phase shift between the signal beam and local oscillator. The phase drift would be  $>2\pi$  radians over the data recording time frame.

The second source of phase noise comes from the unsynchronised RF clocks in the experiment, most notably the AWG and the oscilloscope. The AWG clock affects the phase of the side bands of our laser, while the oscilloscope clock controls the phase of the detection system. Throughout data collection, these two clocks drift relative to each other and give a random shot-to-shot phase drift in our heterodyne signals. The oscilloscope, upon receiving a trigger, would begin to record data at the start of its next 8 ns clock cycle. Given our heterodyne beat is 15 MHz, a random delay of up to 8 ns results in a phase shift of up to  $\pi/4$ . At the time of the experiment, the AWG did not support external clocking, nor was there an easy way to synchronise the oscilloscope clock with the AWG clock.

Phase reference pulses can be used to correct for these noise sources. The second source of phase noise acts as a random time delay ( $t_0$ ) between the starting time of the data shot, which results in a frequency-dependant phase delay. The first noise source acts as a global phase delay, constant across all frequencies ( $\phi_0$ ). Thus, to correct for the two unknown variables,  $t_0$  and  $\phi_0$ , we require two phase references at different frequencies.

The phase correcting reference pulses were both 10  $\mu$ s long Gaussian-shaped pulses, their frequencies were within 20 MHz of the storage pulse (within the 30 MHz bandwidth of the heterodyne detectors). Two pairs of reference pulses were sent through the crystal, before and after the AFC shots, as shown in Figure 4.7. These pulses were very strong compared to the storage pulse,  $10^3 - 10^5$  times the intensity and 50 times longer, giving

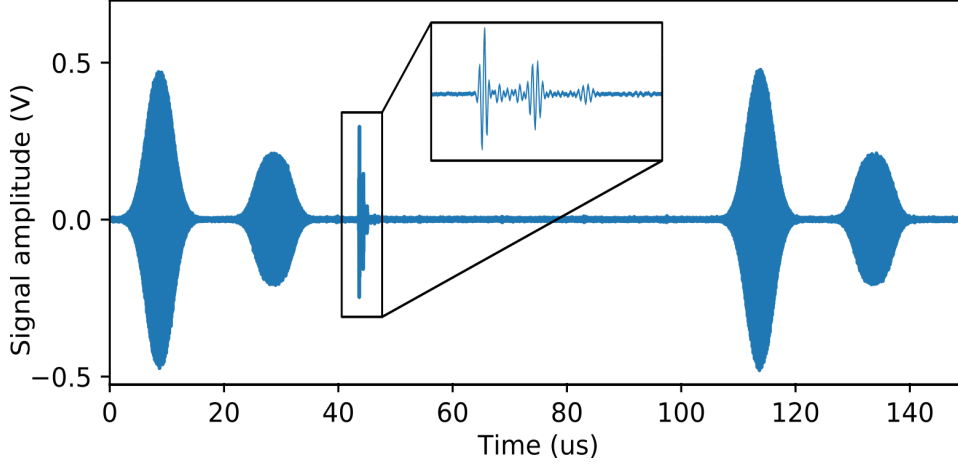


Figure 4.7: A raw shot of an AFC storage event showing reference pulses, reference pulse 1 (13 MHz relative to the local oscillator) at 8 and 113  $\mu\text{s}$ , reference pulse 2 (-19 MHz relative to the local oscillator) at 28 and 133  $\mu\text{s}$ . The AFC echoes start at 42  $\mu\text{s}$  at a frequency of 15 MHz relative to the local oscillator. This graph uses a strong storage pulse ( $> 10^6$  photons). The inset zooms in on the input pulse and echoes.

a strong signal to measure the phase of a shot.

A reference pulse can be described by the function  $\sin(\omega t + \phi) \cdot G(t)$ , for some frequency,  $\omega$ , (13 MHz and -19 MHz for reference pulses 1 and 2 respectively), a Gaussian envelope,  $G(t)$ , and unknown phase offset,  $\phi = \omega t_0 + \phi_0$ . The phase of a reference pulse was calculated by measuring the in-phase (I) and out-of-phase (Q) quadratures (Section 3.7.1) for the reference pulse.

We arbitrarily define that our reference pulse is in-phase if  $\phi = 0$  and out-of-phase if  $\phi = \pi/2$ . The amplitude of the I(Q) quadrature can then be calculated by beating the reference pulse to DC using  $\sin(\omega t)[\cos(\omega t)]$  and integrating over the time window of the reference pulse. For the I quadrature,

$$I \propto \int G(t) \sin(\omega t + \phi) \cdot \sin(\omega t) dt \quad (4.2)$$

$$= \int G(t) \left( \sin^2(\omega t) \cos(\phi) + \frac{1}{2} \sin(2\omega t) \sin(\phi) \right) dt. \quad (4.3)$$

In equation (4.3), the second term can be ignored because the integral of  $\sin(2\omega t)$  will oscillate about 0. Thus,

$$I = \cos(\phi) \int G(t) \sin^2(\omega t) dt. \quad (4.4)$$

We can use the same logic when finding the Q quadrature,

$$Q = \sin(\phi) \int G(t) \sin^2(\omega t + \pi/2) dt. \quad (4.5)$$

As we expect, the I and Q quadratures are proportional to the cosine and the sine of the phase, respectively. The phase of the reference pulse is simply then,

$$\phi = \tan^{-1} \left( \frac{Q}{I} \right). \quad (4.6)$$

Given two reference pulses at distinct frequencies,  $\omega_1$  and  $\omega_2$ , we can solve for  $t_0$  and  $\phi_0$  and finally find a correction phase,  $\phi_c$ , for the AFC echo.

$$t_0 = \frac{\phi_2 - \phi_1}{\omega_2 - \omega_1} \quad (4.7)$$

$$\phi_0 = \phi_1 - \omega_1 t_0 \quad (4.8)$$

$$\phi_c = \omega_{\text{echo}} t_0 + \phi_0 \quad (4.9)$$

Finally, we can phase correct the AFC echoes and calculate the quadratures of the AFC echoes in one step.

$$I_{\text{echo}} \propto \int \psi(t) \cdot \sin(\omega_{\text{echo}} t + \phi_c) dt \quad (4.10)$$

$$Q_{\text{echo}} \propto \int \psi(t) \cdot \cos(\omega_{\text{echo}} t + \phi_c) dt \quad (4.11)$$

Where  $\psi(t)$  is the AFC echo signal. In a given data set, each shot was phase corrected such that all shots were in-phase with the first shot of the data set. Thus, for each shot of data, the phase of each reference pulse was measured and a unique  $\phi_c$  was calculated.

Figure 4.8 shows the I and Q quadratures of the input of an AFC and the echo, using a ball and stick diagram. Each point on a diagram shows the amplitude (in arbitrary units) of a single AFC shot, with the total diagram showing 2500 shots. The data set used in Figure 4.8 was relatively strong ( $\langle N \rangle = 250$  photons). A 250-photon input is strong enough to have classical noise dominate the shot noise. On the figure, the classical noise appears as phase noise, which elongates the ball of the ball and stick diagram, giving a slight elliptical shape. To suppress classical noise in the non-classical demonstration, a much weaker input pulse was used.

#### 4.6.2 Noise performance

As with the classical demonstration, a series of storage events were recorded without the AFC to act as a reference to the input pulse before storage.

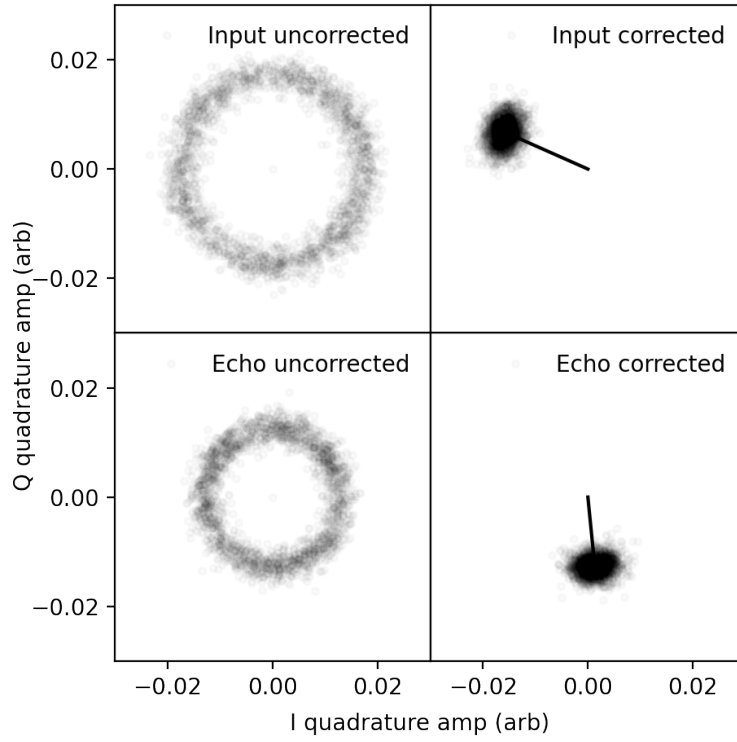


Figure 4.8: Experiment results showing the phase correction of an AFC input and echo. The top graphs show the amplitudes of the I and Q quadratures for an input pulse of  $\langle N \rangle = 250$  photons. The left graphs show the uncorrected data, where the phase is effectively random. The right graphs show the phase corrected data.

Given the weak signal strength of the non-classical storage, input pulse  $\langle N \rangle = 0.8$  photons, many shots were recorded. The particular data set analysed in this section contained  $10^5$  shots.

To test for non-classicality we will use the noise performance metric introduced in Section 2.6.2. The memory is non-classical if the variance added to the input pulse by the AFC is less than  $2\eta$  units of shot noise. The variance added to the input pulse is measured by subtracting the input pulse variance from the AFC echo variance. However, we must also reference our signal to the shot noise. In Section 3.7.2 we saw that the measurement system was shot-noise limited. Thus, we can choose any time window of our storage shots with no light recorded to act as a reference to shot-noise.

The variance added to the echo by the AFC is then,

$$V_{added} = \frac{V_{echo} - V_{input}}{a}, \quad (4.12)$$

where  $a$  is the attenuation of the signal from the crystal to the heterodyne detectors. Accounting for the attenuation between the crystal and detector is crucial. This is because any classical noise will be attenuated by any losses in the detection system. The shot noise, however, can never be attenuated. The losses can be thought of as the signal being passed through a beamsplitter with the second port mixing in shot noise. Thus, attenuation in the detection system will make the classical noise smaller, which would make a classical memory appear non-classical if the variance of the classical noise was less than  $2\eta/a$ , in shot noise units.

Figure 4.9 A and B show the amplitude of the input pulse and echo, respectively, for an angle  $\theta$ , where  $\theta = 0$  shows the amplitude of the I quadrature and  $\theta = \pi/2$  shows the amplitude of the Q quadrature. Figure 4.9 (A) shows the amplitude of an  $\langle N \rangle = 0.8$  photon pulse stored, Figure 4.9 (B) shows the corresponding echo. In each graph the shaded region represents the uncertainty ( $1\sigma$ ) in the amplitude and in (B) the classical boundary is shown. Finally, Figure 4.9 (C) shows the variance added to the input pulse (A) by the AFC ( $\frac{V_{echo} - V_{input}}{a}$ ), and the shaded region represents the  $2\sigma$  uncertainty in the added variance. This uncertainty was found using the bootstrapping method [72] to randomly sample the data sets  $10^4$  times. From Figure 4.9 (C) we can see that the variance added to the input pulse by the AFC is well below the classical boundary, indicating a clear non-classical result. The results here show that the AFC storage is non-classical with a certainty of  $5.8\sigma$ .

The results of this section show that phase noise in the experiment can be corrected and removed from the data by using two phase correcting reference pulses. Applying this correction to our data analysis allows us to see that the storage in the AFC is indeed non-classical.

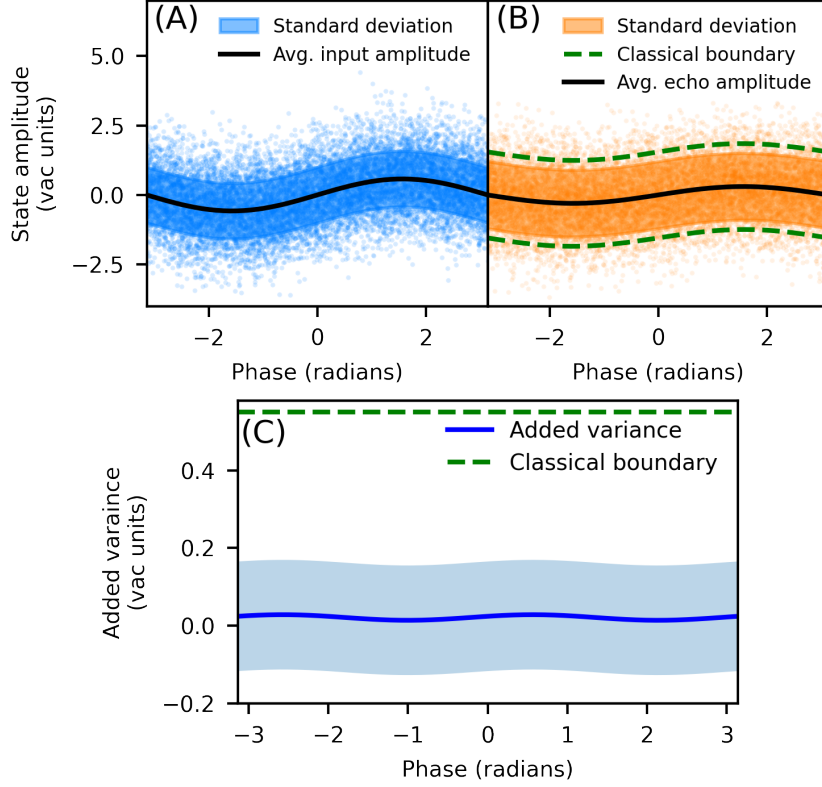


Figure 4.9: A, B show the amplitude of a weak  $\langle N \rangle = 0.8$  photon state stored in the AFC. A shows the input state and B shows the output state. The  $y$  axis corresponds to the amplitude of the state for the I ( $x = 0$ ) and Q ( $x = \pi/2$ ) quadrature when the state has been phased corrected to align with the Q quadrature. B also shows the classical boundary for the variance in the state amplitude. C shows the variance added to the output of the AFC, with the highlighted region showing  $2\sigma$  certainty.

## 4.7 Improving the AFC

Here we will examine the performance of the AFC and discuss several ways to improve the efficiency, storage time, and bandwidth. First, we will look at the efficiency of the current AFC. Recall that the efficiency for a free-space AFC is given by equation (4.1).

Equation (4.1) assumes an AFC with Gaussian shaped teeth. Ultimately, our free space AFC was limited by the optical depth of the host crystal. For example, using the current  $^{167}\text{Er}^{3+}:\text{Y}_2\text{SiO}_5$  crystal and the  $|- \frac{7}{2}\rangle_g \rightarrow |- \frac{7}{2}\rangle_e$  optical transitions for storage, with a peak absorption of 21 dB, we are limited to a maximum efficiency of 35%. Even with arbitrarily large optical depth the free space storage efficiency is limited to 54%, by the forward recall limit [62].

This forward recall limit can be surpassed by enhancing the AFC storage using an impedance-matched cavity. By impedance-matching a cavity and meeting the phase-matching conditions for backwards recall [56], the echo from the AFC can be produced in the opposite direction with unitary efficiency, theoretically [2]. However, to approach unitary efficiency there must be no background absorption in our AFC,  $d_0 = 0$ . From Section 4.4 we saw that our AFC's background absorption is, ultimately, limited to 0.08 dB from absorption due to isotopic impurities. The 0.08 dB is specific to the particular storage level shown in these experiments,  $|- \frac{7}{2}\rangle_g \rightarrow |- \frac{7}{2}\rangle_e$ . Theoretically, any transition  $|- \frac{7}{2}\rangle_g \rightarrow |\pm \frac{x}{2}\rangle_e$  can be used for optical storage. Each of those transitions will have a different background absorption from the isotopic impurities, the  $|- \frac{7}{2}\rangle_g \rightarrow |- \frac{5}{2}\rangle_e$  transition is discussed below.

### 4.7.1 Storage level schemes

The  $|- \frac{7}{2}\rangle_g \rightarrow |- \frac{7}{2}\rangle_e$  transition was used in these experiments because it had the highest optical depth, and thus, had the highest free-space storage efficiency. However, to extend the storage efficiency further, we will want to use an impedance-matched cavity. Importantly, in cavity-enhanced memories, the efficiency of the memory is not limited by the peak optical depth of the storage transition. Instead, the efficiency is limited by the ratio between peak absorption ( $d$ ) and background absorption ( $d_0$ ). This reason gives cavity implementations more options for storage transitions. We shall compare the level scheme used in these experiments to another more suited for cavity-enhanced storage. Consider two level schemes for both optical and spin-state storage, shown in Figure 4.10.

Option 1, denoted by the blue arrows in Figure 4.10, is the optimal solution for a free-space AFC and is the level scheme used in this chapter ( $|- \frac{7}{2}\rangle_g \rightarrow |- \frac{7}{2}\rangle_e$ ). Spin-state storage can then be achieved by applying control pulses to a  $\Delta m_I = -1$  transition ( $|- \frac{5}{2}\rangle_g \rightarrow |- \frac{7}{2}\rangle_e$ ) explained in more detail in Section 4.7.3.

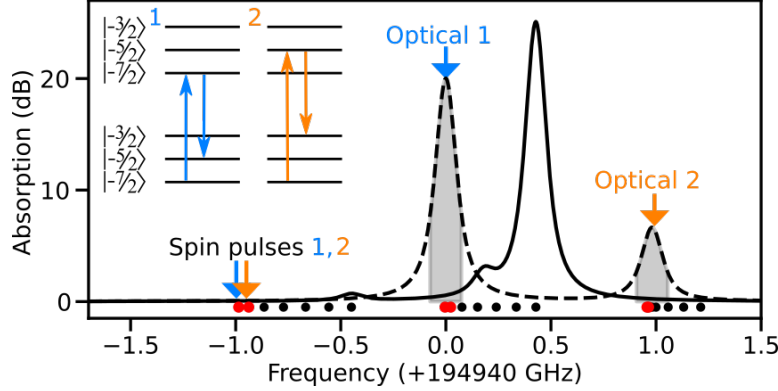


Figure 4.10: Visualisation of the two proposed storage options for our AFC. The solid black line shows the spectra of our spin pumped ensemble. The dashed black line shows the spectra of only the  $|-7/2\rangle_g$  ions. When we prepare an AFC into the  $|-7/2\rangle_g$ , the peak optical depth of the AFC teeth will be bounded by the black line. The grey shaded regions indicate a 100 MHz bandwidth, which is the largest bandwidth the AFC can have before the lineshape of the ions significantly affects the performance of the AFC. Finally, the two coloured arrows and level diagrams show the two storage options discussed below.

Option 2, denoted by the orange arrows in Figure 4.10, uses a  $\Delta m_I = +1$  transition for optical storage ( $|-7/2\rangle_g \rightarrow |-5/2\rangle_e$ ). Spin-state storage can also be achieved by applying control pulses to another  $\Delta m_I = -1$  transition ( $|-3/2\rangle_g \rightarrow |-5/2\rangle_e$ ). The oscillator strength of this optical transition is only 30% of option 1. However, the isotope background absorption is 6% of option 1, which leads to a higher cavity-enhanced efficiency. This is because the  $\Delta m_I = +1$  transitions are further detuned from the isotopic impurities than the  $\Delta m_I = 0$ , by more than a GHz.

We expect that the  $\Delta m_I = 2$  should have an even higher  $\frac{d}{d_0}$ , although we do not know the relative oscillator strength of this transition. It is likely that the oscillator strength is  $<1\%$ , which is quite weakly absorbing,  $<0.2$  dB. Reaching the impedance matching condition with a weaker oscillator strength will require a higher Q cavity. A higher Q implies a narrower the linewidth for the cavity, or a larger free spectral range (smaller cavity). This can potentially limit the bandwidth of the memory.

#### 4.7.2 Theoretical cavity predictions

We can predict the efficiency of our AFC, from Section 4.5, in an impedance-matched cavity. Consider a simple Fabry-Perot cavity comprising two mirrors with reflectivity  $R_1$  and  $R_2$  with our crystal in between them. Let the reflectivity of the end mirror  $R_2$  be 1. If  $R_1$  is chosen such that the losses of



the cavity are equal to the absorption of the crystal ( $R_1 = e^{-2\tilde{d}}$ ), then the impedance matching condition is met. Any transmission out of the cavity is perfectly cancelled by reflections off of the input mirror, giving no net output signal. When impedance matching is achieved, all the incident light is absorbed by the crystal. As a consequence, there is no re-absorption of the echo and the echo is emitted backwards [1]. Thus, it can be shown that the memory efficiency is bounded by the dephasing term of Equation (4.1) [1]. Jobez et al. [45] derived an equation to show that we can approach an efficiency of  $0.99\eta_{\text{dephase}}$  with an effective optical depth of  $\alpha L = 0.2$  (or 0.87 dB),

$$\eta_{\text{cavity}} = \frac{1}{\left(1 + \frac{\epsilon}{4\tilde{d}}\right)^4} \cdot \eta_{\text{dephase}}, \quad (4.13)$$

where  $\epsilon$  is the round trip loss of the cavity (not including the AFC absorption). Equation (4.13) holds under the assumption that both  $\epsilon$  and  $\tilde{d}$  are smaller than 1 and that  $\epsilon \ll \tilde{d}$ .

With Equation (4.13), we can predict the efficiency of our AFC in an impedance-matched cavity. Using the parameters of our current AFC, peak absorption of 18 dB and background absorption of 1 dB, gives an AFC efficiency of 57.9% with an AFC and cavity finesse of 4.4 and 2.8 respectively. The AFC finesse is not too different from our current AFC ( $F = 3.9$ ). Thus, cavity-enhancing our current AFC should lead to efficiencies above the forward recall limit.

In Section 4.4, an AFC clean-up sequence was discussed as a way to remove background absorption from the AFC. If this clean-up sequence is implemented, then the background absorption ( $d_0$ ) is limited by the isotopic impurities. Using option 1 as our level scheme, this background is 0.08 dB. Using this value as our background absorption, we calculate AFC efficiencies of 88.8% for an AFC and cavity finesse of 9.2 and 11 respectively. With these AFC parameters, the effective optical depth,  $\tilde{d}$ , of the AFC is  $\alpha L = 0.45$  (1.96 dB) and  $\epsilon$  is simply  $e^{-2d_0} = 3.7\%$ . Therefore, the assumptions of Equation (4.13) are still satisfied. The requirements for the cavity are also reasonable; an impedance-matched cavity with a cavity linewidth of 100 MHz can be achieved with a 27 cm long cavity. This fact is important because as the peak optical depth of the AFC is reduced the cavity finesse will need to increase to keep a constant effective optical depth for the AFC. If we increase the finesse of the cavity but keep the linewidth constant then we must increase the free spectral range, decreasing the length of the cavity. The length of the cavity is bounded by the length of the crystal. Also, high finesse cavities require precise alignment, which increases the complexity of the experiment.

Using the current level scheme, efficiencies of 88.8% are theoretically possible. Recall that option 2 stores optically using the  $\Delta m_I = +1$  transitions. This gives a lower peak optical depth (30% of the  $\Delta m_I = 0$ ) but also lower

background absorption due to the increased frequency detuning from the isotopic impurities (6%). Thus, we can expect a peak absorption of 6 dB with a background absorption of 0.005 dB. This gives an efficiency of 96.6% for an AFC finesse of 16.9 and a cavity finesse of 38. As with the previous level scheme, the finesse of the proposed cavity is still quite low and could be achieved with a 10 cm long cavity.

### 4.7.3 Extending AFC bandwidth and storage time

To expand to spin-state storage in the future, both level schemes will make use of a  $\Delta m_I = -1$  optical transition. The reason for choosing this particular subset of transitions is subtle, but allows wide bandwidth AFCs and maximises the Rabi frequency of the control pulses. The control pulses can limit the bandwidth of the AFC if the storage transition and control pulses overlap in frequency. This is another way of saying that the control pulses cannot interact with the AFC. This poses a problem as optical transitions in the same  $\Delta m_I$  feature overlap. Recall that the AFC is prepared in the  $|-7/2\rangle_g$  hyperfine level, we do not want to apply control pulses to optical transitions that will overlap with the  $|-7/2\rangle_g$  hyperfine level. The  $\Delta m_I < 0$  transitions do not interact with the  $|-7/2\rangle_g$  ions. Thus, as long as the control pulses use a  $\Delta m_I < 0$  transition, then the control pulses will not interact with the AFC. This lack of overlap is shown in Figure 4.10 as the control pulses are detuned from the optical storage transition by over a GHz. Thus, the upper bound for the AFC bandwidth is still the linewidth of our crystal, 150 MHz. Finally, we have specifically chosen the  $\Delta m_I = -1$  transitions because they have the largest oscillator strengths of the  $\Delta m_I < 0$  transitions.

Spin-state storage can then be achieved by applying the appropriate control pulses for a given level scheme. The requirement is that the control pulses can be applied faster than the optical storage time of the AFC (0.66  $\mu$ s in our current implementation). The current Rabi frequency is 500 kHz, Section 5.2, which is too low to apply control pulses. The Rabi frequency can be increased by two methods, the spot size on the crystal can be reduced or the power of the laser can be increased. The current 40  $\mu$ m spot size can be reduced to 10  $\mu$ m by changing the optics on the input to the cryostat. The laser power can be increased using an erbium doped fibre amplifier (EDFA) to amplify the laser. Amplifying the laser to 50 mW and reducing the spot size to 10  $\mu$ m would increase the Rabi frequency to 100 MHz. This Rabi frequency would allow spin state storage on a larger bandwidth AFC. Implementing these control pulses would then increase the storage time of the AFC to the hyperfine coherence time, 1.3 seconds [59].

Increasing the bandwidth of the AFC is then an exercise in preparing more AFC teeth. Ultimately, we are limited by the 150 MHz inhomogeneous broadening of the erbium atoms, however, we do need to consider the extra time required to prepare a larger AFC. The selective anti-polarisation

process for the current five-tooth AFC took 150 ms. However, the speed of the preparation process is limited by 10 ms excited state lifetime of erbium, rather than the power of the preparation laser. Recall that the Rabi frequency is 500 kHz. This means that 100 MHz of ions can be driven into the excited state in 400  $\mu$ s, which is still an order of magnitude shorter than the excited state lifetime. So a 100 MHz bandwidth AFC could be prepared in 150 ms. However, resonant phonons, discussed in Section 3.9.3, may affect the preparation of a large bandwidth AFC, because preparing more AFC teeth means anti-polarising more erbium ions. An AFC with a finesse of 9.2 and a bandwidth of 100 MHz would require preparing  $\frac{100\text{MHz}}{9.2} \approx 10$  MHz of erbium ions to make the AFC.

Increasing the bandwidth of the AFC will also change the background absorption due to isotopes and the average peak optical depth of the comb teeth. The background absorption decreases on one side of the comb and increases on the other. These two changes almost cancel each other out. For option 1 the average background absorption due to the isotopes only increases to 0.095 dB for a 100 MHz wide AFC. However, the peak optical depth does reduce to 16.5 dB, which reduces the maximum efficiency to 86.7%, from 88.8%, a small change. The clean-up process does become more complicated as the AFC would overlap with both the  $|-5/2\rangle_g$  and the  $|-3/2\rangle_g$  hyperfine levels, so the clean-up process would need to clean both of these levels in conjunction with the  $|-7/2\rangle_g$  hyperfine level. Ultimately this is not a fundamental limitation, but does increase experiment complexity. Currently, there are no fundamental limitations that would stop us from creating a cavity-enhanced AFC with a bandwidth of 100 MHz and spin-state storage with a storage time of 1.3 seconds.

## 4.8 Summary

In this chapter, an AFC was characterised and has shown non-classical storage. The AFC protocol proved itself to be a good benchmarking test for our preparation sequence. To estimate the limits of the preparation sequence, the background absorption and of the preparation process was modelled. A free space AFC demonstration was performed with optical storage only, although the extension to spin-state storage is relatively simple. The demonstration showed an efficiency of 22% and an optical storage time of 0.66  $\mu$ s with non-classical storage. At the time of writing, this is the best quantum delay line at the telecommunications wavelength. Also discussed was the process needed to extend the storage time, bandwidth, and efficiency (through cavity enhancement). If all of these improvements can be implemented, the AFC would meet the requirements needed for quantum repeater demonstrations. The techniques and processes developed in this chapter are used in the following chapters, where the RASE protocol is demonstrated.



## Chapter 5

# RASE Prelude

This chapter details a series of experiments that were performed in preparation for the RASE experiments in the following chapter. The primary aim of these experiments was to characterise the RASE sequence, by proxy, using the inverted-four-level echo. From these experiments we determined the optimal level scheme for the RASE experiments along with the expected efficiency, coherence time, and hyperfine storage time for the RASE protocol. ASE was also characterised, estimating the intensity and bandwidth of the RASE experiments.

The experimental setup used in this chapter differs slightly from the setup used in chapter 4. Section 5.1 details these changes. Section 5.2 details a series of echo measurements, from which the coherence time, hyperfine storage time (without hyperfine rephasing), and rephasing efficiencies are measured. From the echo measurements, we will compare two different level schemes and discuss the limitations of each scheme, and then choose which scheme is optimal for the RASE experiments. Finally, the performance of ASE is characterised in Section 5.5

### 5.1 Experiment setup changes

Section 3.1 details the experimental setup and ensemble preparation used in this chapter. In later sections of this chapter, the greyed region of Figure 5.1 was added, containing an Erbium Doped Fibre Amplifier (EDFA) and a free space Acousto-Optic Modulator (AOM). In addition to this change, all experiments performed in this chapter used a magnetic field of 6 T, rather than 7 T used in Chapters 3 and 4. This was to accommodate the limited frequency range of the fibre laser which replaced the frequency locked Thorlabs diode laser as the stable laser in Figure 5.1.

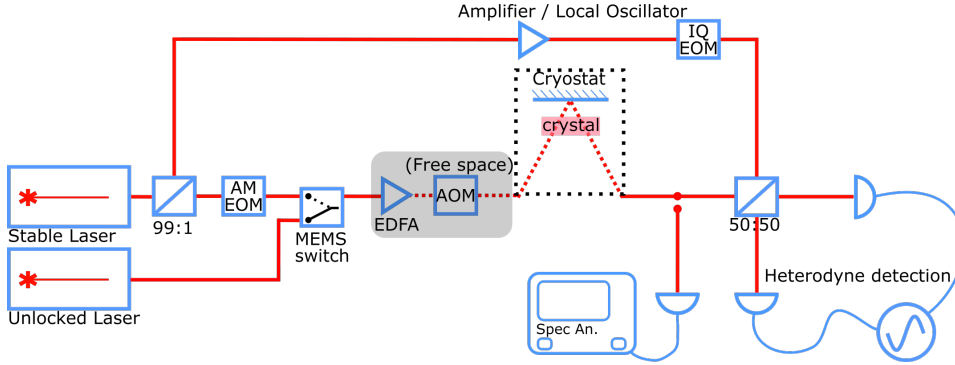


Figure 5.1: Experimental setup used in this chapter. The frequency locked Thorlabs diode laser was replaced with a Koheras E15 BASIK fibre laser and the greyed area shows the EDFA and AOM which were added part way through the experiment. The solid red line indicates optical fibres, the dashed red lines indicate a free space beam.

## 5.2 Photon echoes

This section explores the coherent properties of high field  $^{167}\text{Er}^{3+}:\text{Y}_2\text{SiO}_5$ . There are three lifetimes that we are interested in for the RASE experiments. The optical coherence time, initially measured by Böttger et al. [9] in site 1 and Rančić’s thesis [58] in site 2 (both at 7 T). The hyperfine coherence time, also measured by Rančić et al. [59] at 7 T. The four-level echo coherence time, which is a measure of how quickly the four-level echo amplitude changes as a function of delay time, Section 2.5.3. To date, the four-level echo coherence time has not been measured in  $^{167}\text{Er}^{3+}:\text{Y}_2\text{SiO}_5$ . However, along with the coherent properties of  $^{167}\text{Er}^{3+}:\text{Y}_2\text{SiO}_5$ , we are also interested in characterising the performance of RASE. Specifically, the window time, efficiency, and spin-state storage time.

Photon echoes offer a way to measure the coherent properties of  $^{167}\text{Er}^{3+}:\text{Y}_2\text{SiO}_5$ . We have used the two-level echo and inverted-four-level echo, introduced in Sections 2.5.2 and 2.5.4, to measure the optical and four-level echo coherence times. We have investigated the inverted-four-level echo, rather than the four-level echo, because the inverted-four-level echo pulse sequence is almost identical to the RASE pulse sequence. As a result, we expect that the inverted-four-level echo performance will approximate the RASE performance. Thus, the efficiency, storage time, and coherence time of the inverted-four-level echo should be similar to RASE, while the strong signals from the inverted-four-level echo made data collection and analysis easier.

Rančić’s thesis did report the optical coherence time for  $^{167}\text{Er}^{3+}:\text{Y}_2\text{SiO}_5$  in site 2, however, these measurements were retaken as we were operating at a different magnetic field, 6 T. However, the hyperfine coherence time

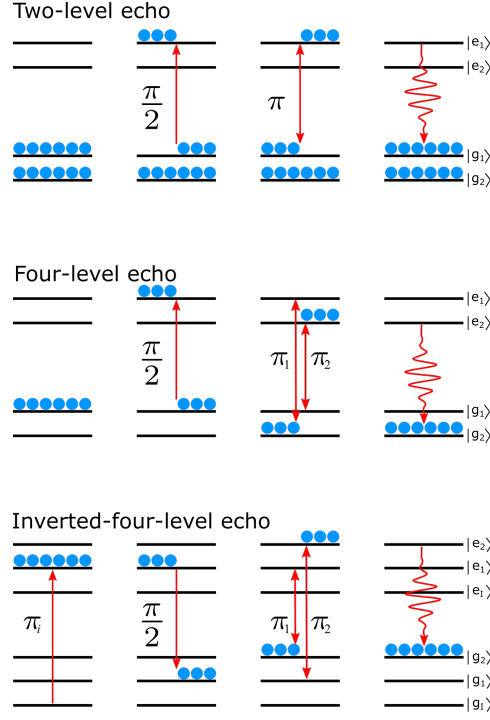


Figure 5.2: Level diagram and pulse sequence for the different photon echoes.

measurement were not retaken. The RASE experiments presented in this thesis did not use hyperfine rephasing. Since hyperfine rephasing was not used, the RASE storage time was limited by dephasing due to broadening between the storage hyperfine levels. Thus, to characterise RASE we needed to measure the four-level echo spin-state storage time too.

Figure 5.2 shows the level diagram and pulses used in each photon echo. Table 5.1 shows the two inverted-four-level echo level schemes investigated in this section. These particular level schemes were chosen for the following reasons, the hyperfine broadening (Section 3.9.2) and relative oscillator strengths (Appendix C) for the  $\Delta m_I = \pm 1$  are both minimal for the  $|+\frac{7}{2}\rangle_g$  and maximal for the  $|-\frac{7}{2}\rangle_g$  hyperfine level. Thus, an inverted-four-level echo sequence on these levels should show the extremes of the inverted-four-level echo performance. This is because hyperfine broadening limits the four-level echo coherence time, while the oscillator strengths of the  $\pi$ -pulse transitions will affect the Rabi frequency of the  $\pi$ -pulses and absorption. The Rabi frequency limits how quickly the atoms can be rephased, and the absorption on the  $\pi$ -pulse transition distorts the  $\pi$ -pulses, which ultimately limits rephasing efficiency.

Each level scheme starts with a 1 MHz ensemble of erbium ions initialised into one of the extremum hyperfine levels ( $|\pm\frac{7}{2}\rangle_g$ ) using the preparation

	$ - \frac{7}{2} \rangle$ scheme	$ + \frac{7}{2} \rangle$ scheme
$\pi_{inv}$	$ - \frac{7}{2} \rangle_g \rightarrow  - \frac{5}{2} \rangle_e$	$ + \frac{7}{2} \rangle_g \rightarrow  + \frac{5}{2} \rangle_e$
$\pi/2$ (ASE)	$ - \frac{5}{2} \rangle_g \rightarrow  - \frac{5}{2} \rangle_e$	$ + \frac{5}{2} \rangle_g \rightarrow  + \frac{5}{2} \rangle_e$
$\pi_1$	$ - \frac{3}{2} \rangle_g \rightarrow  - \frac{5}{2} \rangle_e$	$ + \frac{3}{2} \rangle_g \rightarrow  + \frac{5}{2} \rangle_e$
$\pi_2$	$ - \frac{5}{2} \rangle_g \rightarrow  - \frac{3}{2} \rangle_e$	$ + \frac{5}{2} \rangle_g \rightarrow  + \frac{3}{2} \rangle_e$
echo (RASE)	$ - \frac{3}{2} \rangle_g \rightarrow  - \frac{3}{2} \rangle_e$	$ + \frac{3}{2} \rangle_g \rightarrow  + \frac{3}{2} \rangle_e$

Table 5.1: Energy levels used in the two different inverted-four-level echo level schemes. These two level schemes are mirrors of each other, performed on the extremum of the hyperfine levels.

sequence outlined in Section 3.8. The echo sequence is then performed using the inverted-four-level echo sequence shown in Figure 5.2 where each pulse is performed on the optical transitions in Table 5.1. The sequence ends with the echo produced on the  $|\pm \frac{3}{2} \rangle_e \rightarrow |\pm \frac{3}{2} \rangle_g$  transition.

To measure the four-level echo coherence time, we vary the time delay between the input pulse and the rephasing  $\pi$ -pulses. To measure the efficiency of the inverted-four-level echo, we need to compare the FID of the input pulse to the echo, as discussed in Section 2.5.2. Since the FID and the input pulse overlap, I have measured the input pulse without the atoms (with the magnet turned off) to measure the intensity of the input pulse. Then the intensity of the FID is simply the input pulse (with atoms) intensity minus the input pulse (without atoms). The intensity of the echo will depend on the time delay between the input pulse and rephasing  $\pi$ -pulses, due to dephasing from hyperfine broadening. To maximise the efficiency, we use the shortest reasonable time delay. The time delay must be longer than the two rephasing  $\pi$ -pulses plus the echo time; any shorter and the echo will overlap with the  $\pi$ -pulses, leading to inefficient rephasing. In the efficiency experiments, a time delay of 20  $\mu$ s was used.

### 5.2.1 Two-level echo

The optical coherence time was measured using a two-level echo, explained in Section 2.5.2. A time trace of the heterodyne beat signal from a two-level echo can be seen in Figure 5.3. The two-level echo was performed in the center of the  $|+ \frac{7}{2} \rangle_g$  hyperfine level in the  $\Delta m_I = 0$ , on an unpolarised ensemble with a 4  $\mu$ s long  $\pi$ -pulse. The two-level echo was repeated for varying time delays ( $\tau$ ) between the input ( $\pi/2$ -pulse) and rephasing  $\pi$ -pulse.

Figure 5.4 shows the two-level echo coherence time measurements. The data presented looks noisy, particularly for delays beyond 3 ms. We attribute this noise to laser-atom frequency instabilities. To create a photon echo, we need to use a  $\pi$ -pulse to rephase the same ensemble of atoms that was initially excited by the  $\pi/2$ -pulse. If the frequency of our laser drifts relative to the



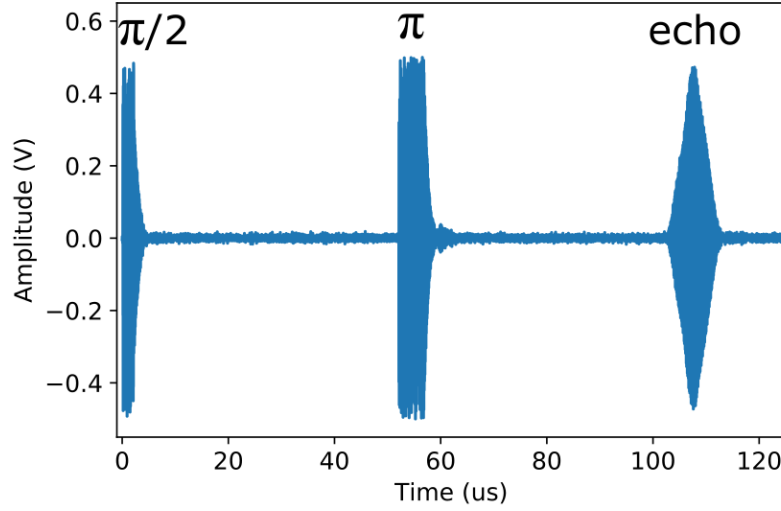


Figure 5.3: Heterodyne beat signal from a two-level echo with a delay,  $\tau = 52.5 \mu\text{s}$ . Heterodyne beat frequency was 15 MHz, the 15 MHz signal is not resolvable on this timescale, thus, the pulses appear as a solid block. The  $\pi/2$ -pulse and the  $\pi$ -pulse can both be seen at time  $t=0$  and  $t=52.5 \mu\text{s}$ , respectively. The echo is at time  $t=105 \mu\text{s}$ .

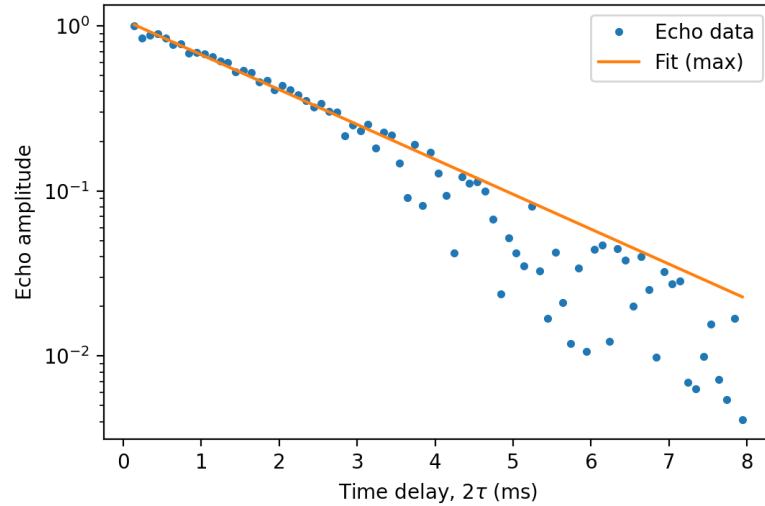


Figure 5.4: Coherence time measurement for the two-level echo. The  $\pi$ -pulse was a  $4 \mu\text{s}$  square pulse. The coherence time was found by fitting a line to the maximum values of the log echo intensity. A linear fit is matched to the log of the echo amplitude,  $T_2 = 2.24 \pm 0.07 \text{ ms}$ .

atoms in the time between the  $\pi/2$ -pulse and  $\pi$ -pulse, then the laser may only rephase a small percentage of the ensemble, resulting in a weaker echo. Thus, it will appear as though more atoms have decohered, however, the atoms were never rephased by the  $\pi$ -pulse. For this experiment the  $\pi$ -pulse was 4  $\mu\text{s}$  long which means that laser-atom instabilities of 100 kHz would affect the echo amplitude.

There are two likely sources of frequency instability in the experiment. The first and most obvious is the laser frequency can be drifting on the 3 ms timescale by 100 kHz. The second is that our crystal is moving in the magnetic field. Given the optical transition shifts by 20 GHz/T, and we have an 11.4 mT field gradient across our 3 mm crystal, Section 5.2.2, a movement of 1.3  $\mu\text{m}$  would shift the optical frequency of the atoms by 100 kHz.

Regardless of the source of laser-atom instability, this instability does not decrease the coherence time of our atoms, but only makes it appear as if the coherence time is less than reality. For this reason, in Figure 5.4 we discard any data points that do not fit the trend of the first 2 ms of data, as is shown by the linear fit in Figure 5.4. From the linear fit, we measure the optical coherence time as  $2.24 \pm 0.07$  ms.

Böttger et al. measured the optical lifetime ( $T_1$ ) of site 2 as 9.2 ms [9], albeit with the magnetic field oriented off the  $D_1$  axis. The  $T_1$  measurement gives an upper bound for the optical coherence at 18.4 ms, or a homogeneous linewidth of 17 Hz. The shorter coherence time shown here indicates some unaccounted dephasing processes, which may include local magnetic field fluctuations. The large g-values in site 2 (tabulated in Section 2.1.1) indicates a high sensitivity to magnetic field fluctuations.

We can also compare this result to Rančić et al.'s optical coherence time measurements, 1.35 ms, in site 2. We see that our coherence time measurement (2.24 ms) is much longer than Rančić's. There are a few small differences between Rančić's measurements and these measurements. Firstly, Rančić performed the echo on the  $|-7/2\rangle_g \rightarrow |-7/2\rangle_e$  transition, whereas here the echo was performed on the  $|+7/2\rangle_g \rightarrow |+7/2\rangle_e$  transition. Secondly, Rančić used higher optical power, with a  $\pi$ -pulse time of 1.5  $\mu\text{s}$ , here the  $\pi$ -pulse time was 4  $\mu\text{s}$ . The increased optical power might lead to instantaneous spectral diffusion, which decreases the coherence time. Thirdly, Rančić's measurements were taken at 7 T, whereas these were taken at 6 T.

### 5.2.2 Inverted-four-level echo

Figure 5.5 shows a heterodyne beat time trace of the inverted-four-level echo, using the  $|+7/2\rangle_g$  level configuration. Only the input and echo pulses can be seen in the time trace. The  $\pi$ -pulses were detuned by over a GHz, which is well beyond the heterodyne detector's 30 MHz bandwidth. However, the  $\pi$ -pulses were strong enough to saturate the detector, thus, the only evidence of the  $\pi$ -pulses is the noiseless regions of the time trace. In Figure 5.5, the

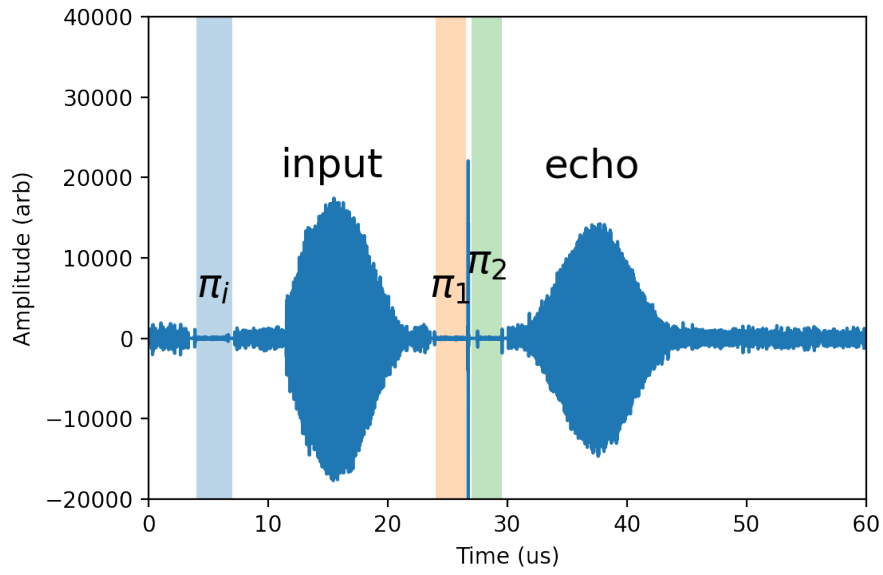


Figure 5.5: Heterodyne beat time trace of an inverted-four-level echo. The input and echo can be clearly seen, centered at  $16\text{ }\mu\text{s}$  and  $38\text{ }\mu\text{s}$ , respectively. Like the two-level echo, the heterodyne beat frequency is so high that the signals appear as solid blocks. The  $\pi$ -pulses are detuned by a GHz and were well beyond the bandwidth of the heterodyne detectors. The  $\pi$ -pulses have been highlighted and labelled.

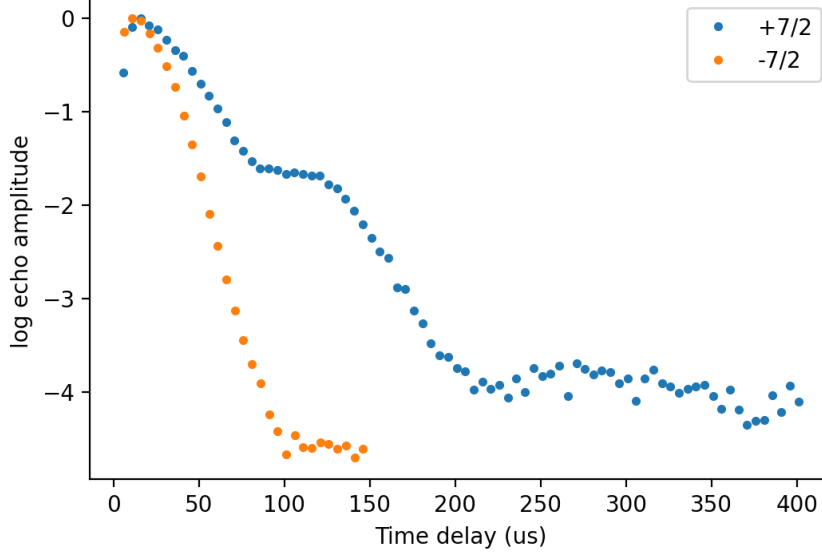


Figure 5.6: Coherence time measurements of the inverted-four-level for both level configurations,  $|-7/2\rangle_g$  (20  $\mu\text{s}$ ) and  $|+7/2\rangle_g$  (46  $\mu\text{s}$ ).

$\pi$ -pulse regions have been highlighted and annotated.

Figure 5.6 shows the inverted-four-level echo coherence time measurements for both level configurations. Immediately, we see that the coherence time for the  $|-7/2\rangle_g$  configuration (20  $\mu\text{s}$ ) is substantially shorter than the  $|+7/2\rangle_g$  (46  $\mu\text{s}$ ). There are two other interesting features in Figure 5.6.

The first is the ‘turn-on’ period at the start of the decay curve. This is where the time delay of the echo is comparable to the duration of both rephasing  $\pi$ -pulses ( $\sim 4, 9 \mu\text{s}$  for the  $|-7/2\rangle_g$  and,  $|+7/2\rangle_g$  respectively). Here, the start of the echo overlaps with the rephasing  $\pi$ -pulses, resulting in a weaker echo. In these data sets, the turn-on period was  $\sim 16 \mu\text{s}$  long. The second other interesting feature of Figure 5.6 is the plateau regions between 80–150  $\mu\text{s}$  and 225–350  $\mu\text{s}$  in the  $|+7/2\rangle_g$  decay curve. These plateau regions are evidence of a magnetic field gradient, discussed in Section 5.2.3.

Figure 5.7 shows a time trace of an inverted-four-level echo for both level schemes. The measurement was repeated with and without the applied magnetic field. To calculate the intensity of the inverted-four-level signals: input, echo, and input with no magnet, the data has been digitally beaten down to DC at the frequencies of the input and the echo. The intensity for each pulse is then the area of the graph within the shaded regions. Each echo was recorded with a time delay of 20  $\mu\text{s}$ . The left sub-figure shows the inverted-four-level echo using the  $|-7/2\rangle_g$  configuration, and the right shows

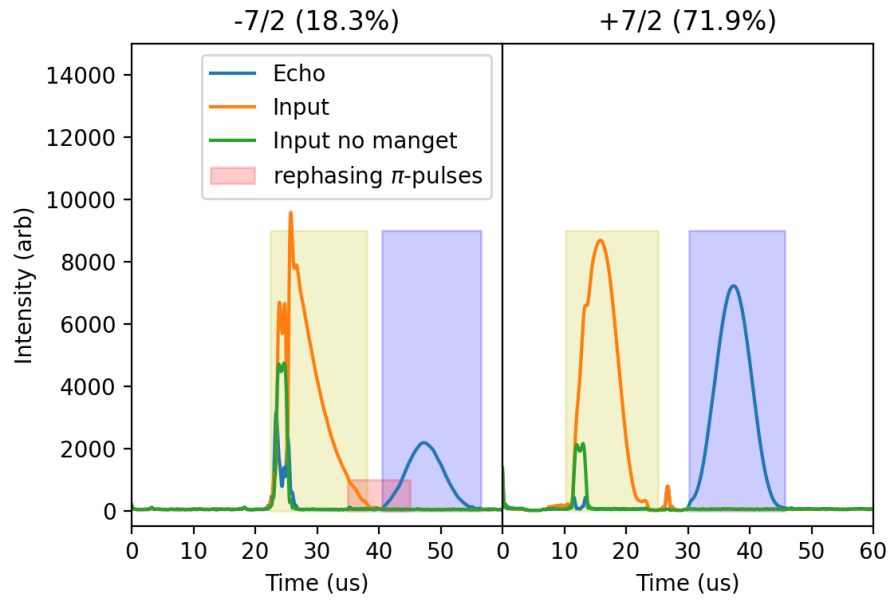


Figure 5.7: Two inverted-four-level echo time traces, using the two level schemes. Each time trace shows a heterodyne signal that has been digitally beaten to homodyne at both the input pulse and echo frequency. The left graph shows the time trace of the  $|-7/2\rangle_g$  configuration and the right graph shows the  $|+7/2\rangle_g$ . Each data set was taken with and without the magnet turned on. When the magnet is turned off, the laser does not interact with the erbium ions, thus there is no echo or FID from the input pulse.

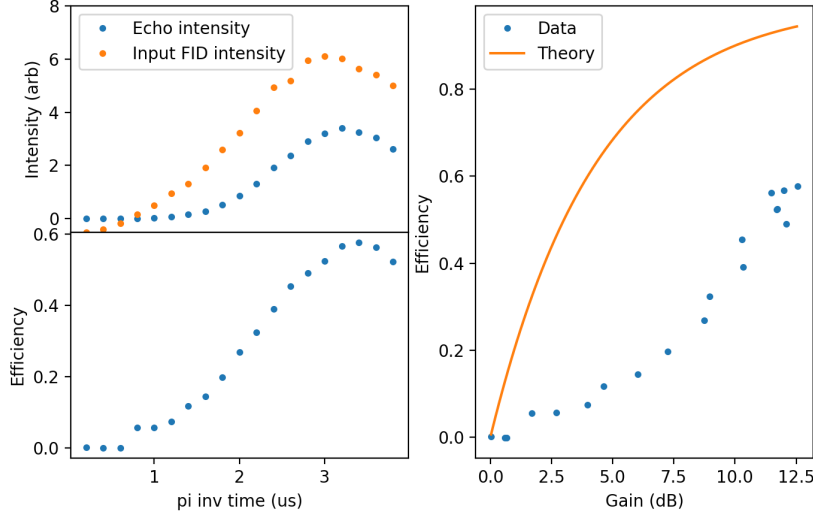


Figure 5.8: Efficiency of the inverted-four-level echo as a function of the gain from  $\pi_{inv}$  for the  $|+\frac{7}{2}\rangle_g$  level configuration.

the  $|+\frac{7}{2}\rangle_g$ , with efficiencies of 18.3% and 71.9%, respectively.

The efficiency measurement for the  $|+\frac{7}{2}\rangle_g$  level configuration were repeated using different  $\pi_{inv}$ -pulse times. Figure 5.8 shows the relative intensities in the input FID and echo (top left). This is converted into efficiency (bottom left), and the  $\pi_{inv}$  times are converted into optical gain (right).

Finally, the spin-state storage was demonstrated by increasing the time delay between the two rephasing  $\pi$ -pulses, shown in Figure 5.9. The Mims model [55] was used to fit the decay curve, giving a storage time of 20  $\mu\text{s}$ .

#### Four-level coherence time

The results from the coherence time measurements, Figure 5.6, show that the  $|+\frac{7}{2}\rangle_g$  coherence time is much longer than the  $|-\frac{7}{2}\rangle_g$ . In Section 3.9.2, the broadening between the ground state hyperfine levels was measured. If the four-level-echo coherence time is limited by dephasing from the broadened hyperfine lines, then the results from Section 3.9.2 would suggest that the coherence time of the inverted-four-level echoes should improve as higher hyperfine levels are used. The inverted-four-level echo coherence times shown here support the hyperfine broadening measurements. However, more coherence time measurements at different hyperfine level schemes would be needed to make any conclusive statements.

The turn-on period in the two decay curves is a large fraction of both configuration's coherence times, particularly for the  $|-\frac{7}{2}\rangle_g$ . The duration of

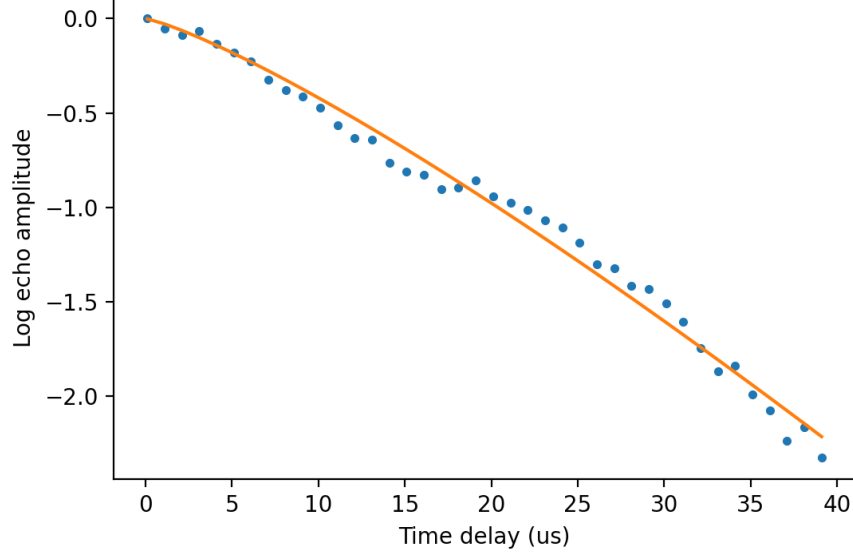


Figure 5.9: Spin-state using the inverted-four-level echo without hyperfine rephasing. Time delay refers to the time between rephasing  $\pi$ -pulses 1 & 2. Storage time: 20  $\mu$ s.

the turn-on period is an issue of Rabi frequency, which is determined by laser power and the transition's oscillator strength. Since the rephasing  $\pi$ -pulses are applied to  $\Delta m_I = \pm 1$  transitions, with lower oscillator strengths, the Rabi frequency is relatively low, sub-megahertz. The only solution is then to increase the laser power, which is achievable using an EDFA to amplify our laser light. For the RASE experiments, an EDFA was used to increase laser power and subsequently reduce  $\pi$ -pulse duration.

There is also a modulation on the decay curve. The regions where the echo plateaus, 80 – 150  $\mu$ s, and where the echo intensity increases, 225 – 350  $\mu$ s, suggests that there are multiple populations of ions that are interfering with each other. The echo modulation is further discussed below in Section 5.2.3 where a magnetic field gradient across the crystal was measured.

### Efficiency

It is immediately clear from Figure 5.7 that the  $|+\frac{7}{2}\rangle_g$  configuration is much more efficient than  $|-\frac{7}{2}\rangle_g$ . The  $|-\frac{7}{2}\rangle_g$  efficiency is only 25% of the  $|+\frac{7}{2}\rangle_g$  configuration. There are several reasons for this: differences in coherence time, gain, and rephasing efficiency.

Firstly, the coherence time for the  $|-\frac{7}{2}\rangle_g$  is only 20  $\mu$ s, compared to the 46  $\mu$ s from the  $|+\frac{7}{2}\rangle_g$ . Given that the inverted-four-level echo time delay

was 20  $\mu\text{s}$ , the  $|\frac{7}{2}\rangle_g$  and  $|\frac{7}{2}\rangle_g$  echo amplitude would decrease by a factor of  $e^{-1}$  and  $e^{-0.5}$ , respectively. Thus, the  $|\frac{7}{2}\rangle_g$  echo amplitude would drop by a factor of  $e^{-0.5}$ , compared to the  $|\frac{7}{2}\rangle_g$  echo. Then the echo intensity will drop by a factor of  $e^{-1}$ . Thus, if the recall efficiencies of the two echo sequences were identical then, due to decoherence, we would expect the efficiency of the  $|\frac{7}{2}\rangle_g$  echo to drop by 63% relative to the efficiency of the  $|\frac{7}{2}\rangle_g$  echo.

Secondly, the gain for the  $|\frac{7}{2}\rangle_g$  is much lower than the  $|\frac{7}{2}\rangle_g$  gain. Ledingham et al.'s model [49, 29] shows that the efficiency of an echo sequence increases with higher optical depth. In Figure 5.7 we can clearly see that there is more gain on the  $|\frac{7}{2}\rangle_g$  input pulse than the  $|\frac{7}{2}\rangle_g$  input pulse. This is evident because the “input pulse no magnet” is relatively smaller than the “input” for the  $|\frac{7}{2}\rangle_g$  data, compared to the  $|\frac{7}{2}\rangle_g$ . Thus, the  $|\frac{7}{2}\rangle_g$  input has been amplified more. The input pulse gain was 16.9 dB for the  $|\frac{7}{2}\rangle_g$  compared to 7.7 dB for the  $|\frac{7}{2}\rangle_g$ . From Ledingham et al.'s model [49, 29] we predict a relative efficiency drop of 15%.

The reason for this difference in gain between the two level schemes stems from the relative oscillator strengths of the  $\pi_{inv}$  transitions. The  $|\frac{7}{2}\rangle_g$   $\pi_{inv}$  optical transition has an oscillator strength 10 times less than the  $|\frac{7}{2}\rangle_g$   $\pi_{inv}$  optical transition (2.5% relative to 33%, Appendix C). The absorption of the  $|\frac{7}{2}\rangle_g$   $\pi_{inv}$  transition is 0.6 dB relative to the  $|\frac{7}{2}\rangle_g$   $\pi_{inv}$  transition's 2.7 dB. Such a large absorption for the  $|\frac{7}{2}\rangle_g$  level scheme will mean that  $\pi_{inv}$  will be distorted as it traverses the crystal. This leads to less efficient population inversion and lower gain on the input pulse transition.

Finally, I also expect the rephasing efficiency of both level schemes to be different. This is for the same reason as the above paragraph. The relative oscillator strengths for the rephasing  $\pi$ -pulses are lower for the  $|\frac{7}{2}\rangle_g$  level scheme (7% and 6% compared to 18% and 15%). The drop in rephasing efficiency that this would cause is difficult to quantify. However, given the 60% efficiency drop from the difference in coherence time and the 17% from the difference in optical gain. A further 20% reduction of efficiency would satisfy the difference in inverted-four-level echo efficiencies. Since the  $\pi_{inv}$  pulse accounts for a 15% reduction in efficiency, 20% for both rephasing  $\pi$ -pulses is reasonable.

From Figure 5.8 two important points are revealed about the inverted-four-level echo. First, the efficiency is superlinear with gain, while Ledingham et al.'s model predicts a sublinear relationship. One explanation for this is that the  $\pi$ -pulses for all the echo sequences are optimised for maximum gain. Less gain will mean that the  $\pi$ -pulses experience less distortion as they traverse the crystal. There is also a large difference between the theoretical and measured efficiency. Ledingham et al.'s model assume that the rephasing



$\pi$ -pulses are perfect. The model predicts a maximum efficiency of 94%, and we observed a maximum of 60% (in this particular data set), this suggests that the rephasing  $\pi$ -pulses have a rephasing efficiency of 78% each, which is a reasonable efficiency for a  $\pi$ -pulse.

The second important piece of information is shown by the input FID intensity (top left of Figure 5.8) dropping below zero. Recall that the input FID intensity is calculated as the intensity of the input pulse with gain from the inverted ions minus the input pulse without the presence of ions. The fact that this value dips below zero suggests that there is some background absorption on the input pulse transition ( $|+\frac{5}{2}\rangle_g \rightarrow |+\frac{5}{2}\rangle_e$ ). The background absorption is most likely residue ions from the selective anti-polarisation sequence, Section 3.8.3. Most of the ions are anti-polarised from the  $|-\frac{7}{2}\rangle_g$  hyperfine level to the  $|+\frac{7}{2}\rangle_g$  hyperfine level. However, inefficient pumping can leave ions in the other hyperfine levels. In the RASE experiments, the preparation process was further optimised to remove any background absorption.

### Spin-state storage

Finally, the last useful metric we can obtain from the inverted-four-level echo is the spin-state storage time. In a fully realised implementation of Erbium-RASE RF rephasing  $\pi$ -pulses will be used to extend the spin-state storage time to the full hyperfine coherence time of 1.3 seconds [59]. However, before this is implemented the storage time is limited by the hyperfine broadening, Figure 5.9, shows the amplitude of the inverted-four-level echo as the time between the rephasing pulses is extended. This data shows a storage time of 20  $\mu$ s.

#### 5.2.3 Field gradient

After the completion of the RASE experiments, Chapter 6, we found that the crystal was not centered in the magnetic field during experiments. This poses an issue as the magnetic field inhomogeneity was smallest at the center of the superconducting magnet. Moving the crystal from the center of the field lead to a magnetic field gradient across the crystal. Given our large 6 T magnetic field, a small relative field gradient can cause a large effect on our atoms. The crystal was centered in the magnetic field at room temperature. However, at experimental temperatures, thermal contraction of the sample stick caused the crystal to move out of the center of the magnetic field. In total, the crystal was displaced 3 mm, axially, from the center of the magnetic field. This effect of the displacement was quantified by measuring the homogeneity of the magnetic field using a Hall probe, Figure 5.10. The field gradient across the crystal was estimated by fitting a parabola to the magnetic field data. From the fit, the magnetic field at the edges of the crystal was 99.95% and

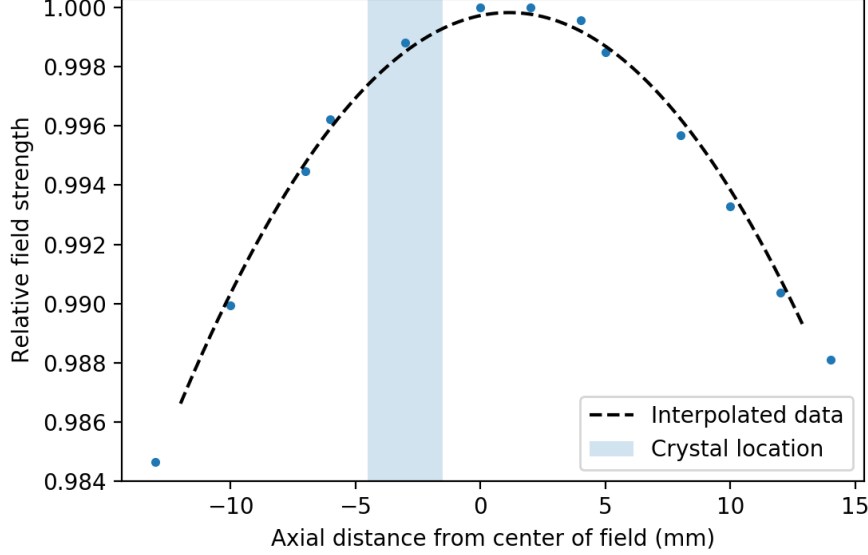


Figure 5.10: Data taken by Kieran Smith. Measurements of magnetic field strength in the sample space using a Hall probe. The highlighted region shows the location of the crystal.

99.75% relative to the center of the field. At our operating field of 6 T this gives an 11.4 mT field gradient. From the hyperfine splittings, tabulated in Section 3.8.1 (Table 3.1) we can calculate the hyperfine splitting gradient across the crystal. For the  $|+\frac{7}{2}\rangle_g$  inverted-four-level echo, the atoms were shelved in the  $|+\frac{5}{2}\rangle_g$  and  $|+\frac{3}{2}\rangle_g$  hyperfine levels. From the values in Table 3.1 we calculate the hyperfine splitting between these levels changes at a rate of 2.1 MHz/T. Assuming a linear gradient, this would result in a splitting of 23.9 kHz between the two hyperfine levels across our crystal.

This means that the ions in the ensemble will dephase at different rates depending on where the ions are in the crystal. In effect, this creates another dephasing mechanism with a tophat line shape, thus, the decay curve will be modulated by the Fourier transform of this lineshape, a sinc function. The first lobe of the sinc function should peak at a time  $t = \frac{\pi}{23.9\text{kHz}} \sim 130 \mu\text{s}$ . This matches the modulation pattern seen on Figure 5.6. If we were to move the crystal to the center of the magnetic field, the field gradient should drop to 3 mT, and the modulation effect will decrease.

#### 5.2.4 Transition choice

So far, two level configurations for the inverted-four-level echo have been shown. In almost every metric, the  $|+\frac{7}{2}\rangle_g$  configuration has shown itself

to be superior. The  $|\frac{7}{2}\rangle_g$  configuration has longer coherence times (less hyperfine broadening), higher rephasing efficiency, and greater optical gain. The downside in the  $|\frac{7}{2}\rangle_g$  configuration comes from the oscillator strengths of the  $\Delta m_I = 1$  transitions and splittings between the optical levels. It was already briefly mentioned that the oscillator strength for the rephasing  $\pi$ -pulses are, on average, 3 times weaker in this configuration, along with this the oscillator strength for the inversion  $\pi$ -pulse is 10 times weaker. The main consequence of this is increased  $\pi$ -pulse duration. As we have seen already, long  $\pi$ -pulses can lead to inefficient echoes if the  $\pi$ -pulse duration is comparable to the coherence time of the inverted-four-level echo. Other factors include limited bandwidth, as the bandwidth of the echo is set by the longest  $\pi$ -pulse (or the  $\pi$ -pulse with the narrowest bandwidth). However, the issue of low Rabi frequency can be solved by amplification of the laser using an EDFA. Indeed, the data shown using the  $|\frac{7}{2}\rangle_g$  configuration was gathered using an EDFA, after the  $|\frac{7}{2}\rangle_g$  configuration data was collected. The complications of adding an EDFA to the experimental setup are detailed in Section 5.3.

Not yet mentioned are the optical transition frequencies for the inverted-four-level echo schemes. The optical transitions for the input pulse and echo are detuned by 96 MHz for the  $|\frac{7}{2}\rangle_g$  scheme, while the  $|\frac{7}{2}\rangle_g$  are only detuned by 34 MHz, although, this only increases the difficulty of data collection in the experiment. Our detectors had a bandwidth of 30 MHz. In the experiments detailed in this chapter, the local oscillator was set to a frequency in between the two input pulse and echo transitions. The heterodyne beat frequencies were 47.0 MHz (input pulse), 48.8 MHz (echo) for the  $|\frac{7}{2}\rangle_g$  scheme and 15.5 MHz (input pulse), 18.6 MHz (echo) for the  $|\frac{7}{2}\rangle_g$  scheme. This means that the  $|\frac{7}{2}\rangle_g$  signals were beyond the bandwidth of our detectors, reducing signal recorded by our detectors by a factor of 3 compared to the  $|\frac{7}{2}\rangle_g$  signals. While a substantial loss in signal, the gain in efficiency from the  $|\frac{7}{2}\rangle_g$  scheme alone makes up for this difference. The RASE experiment chapter will use the  $|\frac{7}{2}\rangle_g$  level configuration. In the RASE experiments, fast local oscillator switching will be used to coherently switch the frequency of the local oscillator during the rephasing  $\pi$ -pulses. This means the ASE and RASE heterodyne beat frequencies can be set arbitrarily, most importantly, they can be set to optimal frequencies for the heterodyne detectors.

### 5.3 EDFA implementation

From the results discussed in Section 5.2.2, we have seen that the optimal level scheme for RASE uses  $\pi$ -pulses on transitions with very weak oscillator strengths. Thus, we require a lot of optical power to achieve the high

Rabi frequencies that we need in the experiment. We need the high Rabi frequencies because the duration of  $\pi$ -pulses needs to be much shorter than our coherence times, and higher Rabi frequencies allow higher memory bandwidths (without having to resort to spectral multiplexing). An EDFA will be used to amplify the stabilised laser and allow for much higher Rabi frequencies. Here, I will discuss the experimental changes and difficulties that arise from adding an EDFA into the cryostat beam path, grey rectangle in Figure 5.1.

With all amplifiers, an EDFA amplifies noise as well as the input signal. Amplifiers increase noise more than they increase the signal of interest. In the experiment, the EDFA will add noise by amplifying the shot noise, creating a broadband ASE signal with a terahertz bandwidth. In the experiment detection, the EDFA ASE will appear identical to the shot noise. This is particularly bad in non-classical experiments where shot-noise-limited detection is required.

For RASE experiments the effect of the EDFA ASE is even worse because the EDFA ASE will also be amplified by the gain feature (from  $\pi_{inv}$ ) creating another ‘ASE’ signal that is indistinguishable from ASE. Thus, it is important to characterise the noise added by the EDFA and block the EDFA output during the (R)ASE time windows, with sub-microsecond precision. For this reason, a free space Acousto-Optic Modulator (AOM) was added to the experiment after the EDFA. The AOM acts a gate for the laser with sub-microsecond gating times. A free-space AOM was used as they can withstand the full output of the EDFA ( $>100$  mW), as opposed to fibre based AOM’s which are usually limited to  $<100$  mW.

To test the AOM gating, the EDFA was turned on and left to run with no input, which allowed the EDFA to produce ASE. The heterodyne detectors then measured the intensity of the ASE under three conditions: with the EDFA unblocked, with the EDFA gated by the AOM, and with the EDFA blocked by a shutter. Figure 5.11 (left) shows the time traces (top graph) and spectra (bottom graph) of the noise on the heterodyne detectors with and without the EDFA gated by the AOM. The increase in noise level is obvious in the time trace, and the spectra reveals a near 20 dB increase in noise that mimics the spectral shape of the shot noise. Figure 5.11 (right) shows two spectra on the heterodyne detectors. One spectrum shows the AOM gating the EDFA, the other spectrum shows a shutter blocking the EDFA. The intensity of the shot noise agrees between both data set to  $<1\%$  and within experimental uncertainty. The peaks at 15 and 28 MHz are electrical noise on the oscilloscope/detector electronics. From these measurements, we can conclude that the AOM can attenuate the EDFA ASE to  $<1\%$  of the heterodyne detector shot noise level (at least 40 dB suppression).

Beyond the issues of increased shot noise, EDFAs also exhibit interesting non-linear performance due to the excited state lifetime of the erbium ions in the doped fibre. If there is no input to an EDFA, the amount of erbium

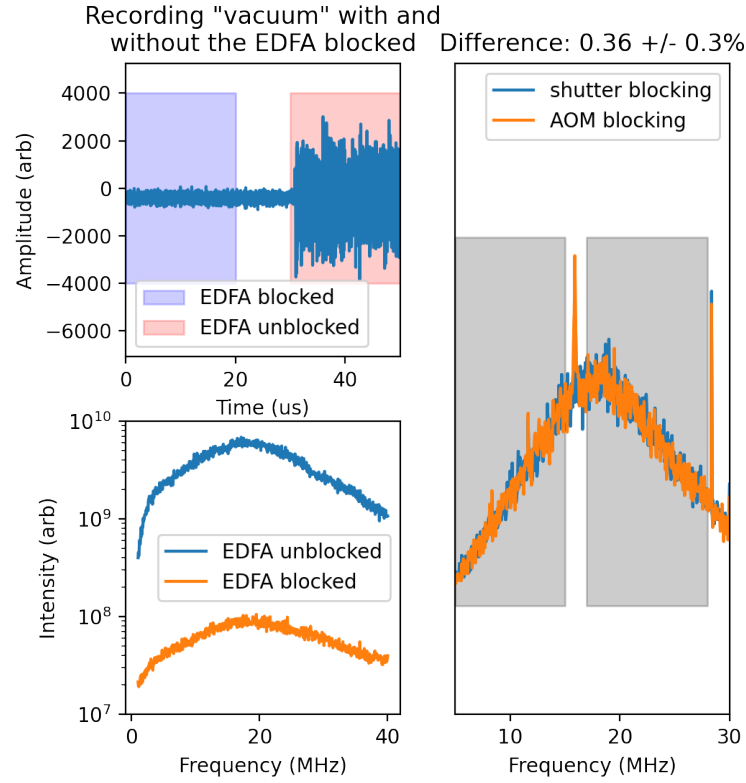


Figure 5.11: Shot noise amplified by the AWG compared to shot noise. Top left shows a time trace of the AWG with no input, the AWG was unblocked at 30  $\mu$ s. Bottom left shows the spectra of the highlighted regions in the top left graph. The right graph shows the spectra of the amplified shot noise blocked by an AOM compared to the amplified shot noise blocked by a shutter, these two spectra are identical to  $< 1\%$ , demonstrating that the AOM's suppression is sufficient for RASE experiments.

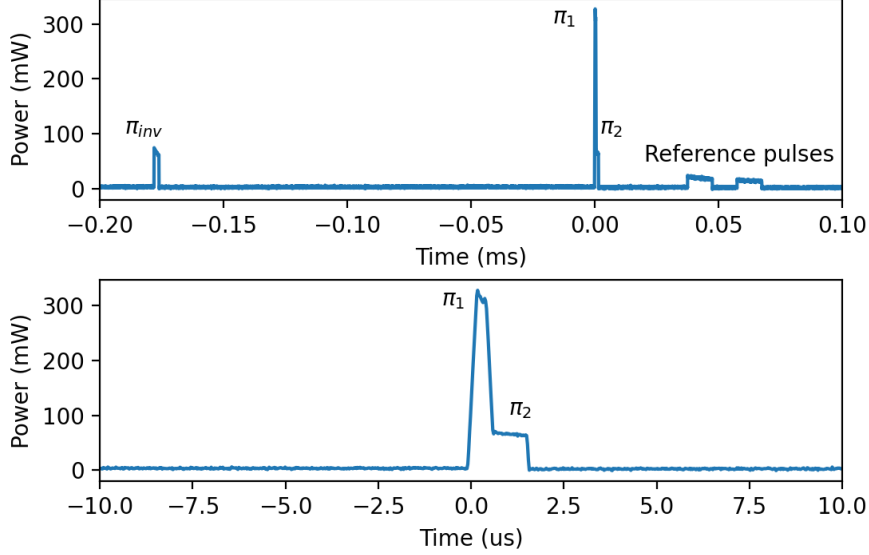


Figure 5.12: Output of the EDFA when the RASE pulse sequence is sent through. The CW output power was 10 mW. We can also see the gain decreases as the intensity of the  $\pi$ -pulses decays across the  $\pi$ -pulse.

ions in the  $I_{13/2}$  level will be greater than when there is a CW signal passing through the EDFA. This is because a CW input will continuously drive population to the ground state. If the EDFA input is pulsed with a pulse time shorter than the lifetime of the erbium ions (10 ms) then the pulsed input can experience gain levels much higher than steady state CW.

Figure 5.12 shows the output of the EDFA when the RASE pulse sequence is sent through the EDFA. For this test, the CW output of the EDFA was 10 mW. The most notable result from this data is that the power spikes to above 300 mW for  $\pi_1$ , 30 times higher than the CW output. Also, the power does decay across the RASE sequence, this is mainly shown in the small decay of power across the reference pulses and  $\pi$ -pulses. More examples of this pulse performance are given in Appendix A. The powers seen here are close to the damage thresholds for optical fibres. Typical optical fibre damage thresholds are quoted at (270 – 800) mW CW and 1 W pulsed for  $1 \mu\text{s}$ <sup>1</sup>. Thus, even when using a relatively weak EDFA (with a max CW power of 50 mW) we can approach the damage threshold for an optical fibre.

<sup>1</sup>[https://www.thorlabs.com/newgrouppage9.cfm?objectgroup\\_id=334](https://www.thorlabs.com/newgrouppage9.cfm?objectgroup_id=334)

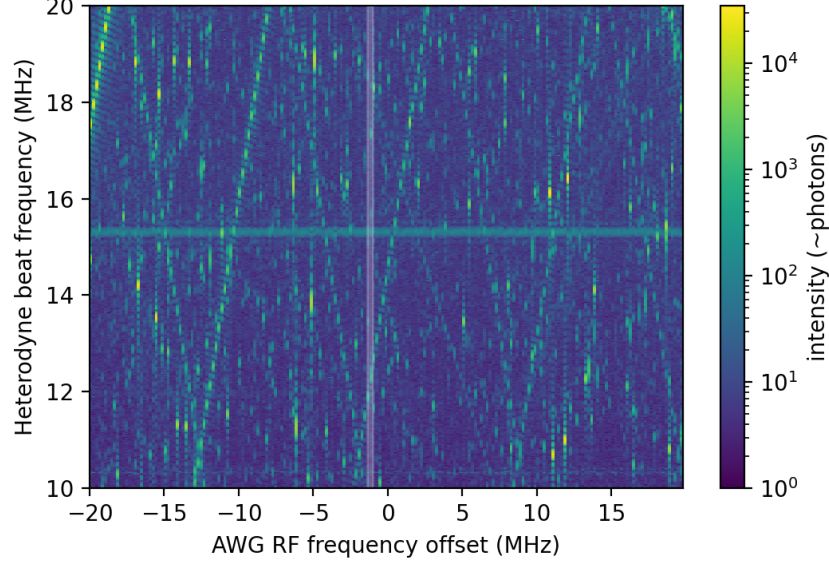


Figure 5.13: Spurious signals recorded during a RASE pulse sequence with no atoms (magnetic field turned off). Varying the frequency of the AWG causes a drastic change in the spectra of the spurs. An offset of  $-1.2$  MHz is highlighted as it gives a clean window about the ASE frequency (15 MHz) while staying close to the original AWG frequency (offset 0 MHz).

## 5.4 AWG spurious signals

As mentioned in Section 3.8, the stable laser was used to prepare optical features and perform pulse sequences on those optical features. Specifically, a sideband of the laser was controlled via an AM-Electro-Optic Modulator (EOM) using an Arbitrary Waveform Generator (AWG). An AWG used a direct digital synthesizer and a digital-to-analog converted to read a user defined waveform from memory and convert it directly into an RF waveform. These devices are extremely flexible and can play any user defined waveform. However, AWGs are also prone to noise, such as spurious signals. These spurs are not present with analogue RF sources.

The source of the AWG spurs, strength of the spurs and several techniques used to minimise the spurs are discussed in Appendix B. Here I will mention that these spurs can be much larger than the ASE and RASE signals we are interested in.

Figure 5.13 shows a spectrogram of the heterodyne signal about the ASE frequency (centered at 15 MHz) during a RASE pulse sequence. The x-axis shows a small offset applied to the AWG RF frequency, this offset changes the frequency of the RASE sequence pulses, and the preparation sequence.

Essentially, this offset changes where in the atomic line the RASE sequence is performed. The local oscillator frequency was also adjusted by this offset so that the ASE frequency would always be recorded at 15 MHz, by the heterodyne detectors. As the AWG signal frequency changed, the frequency of the spurs also changed. Figure 5.13 shows how drastically the spur's spectrum can change with small changes in the AWG frequency. The intensity of these spurs were between 1 – 20,000 photons. Some of the strongest spurs show a linear relationship between frequency and AWG RF offset, while some weaker spurs show an anti-linear relationship or a more chaotic relationship. A region about offset of  $-1.2$  MHz is highlighted, as this gave the cleanest window about the ASE frequency window, this offset was used in the following experiments to minimise the effect of the spurs.

## 5.5 Amplified Spontaneous Emission

This section details the measurement and characterisation of ASE, including gain measurements, in the lead up to the RASE experiments. All the experiments in this section were performed on an anti-polarised featured, using the preparation techniques described in Section 3.8. The anti-hole was prepared into the  $|- \frac{7}{2} \rangle_g$  hyperfine level and were  $> 1$  MHz wide. From here, an inversion pulse ( $\pi_{inv}$ ) drove the  $|- \frac{7}{2} \rangle_g$  ions to the excited state. Then next step differs between the gain and ASE experiments. For ASE measurements, the ions were allowed to spontaneously emit. The heterodyne detectors then recorded emission on the ASE transition ( $|- \frac{5}{2} \rangle_g \rightarrow |- \frac{5}{2} \rangle_e$ ). This was achieved by detuning the local oscillator 15 MHz from the ASE transition frequency. For gain measurements, a short  $0.2 \mu\text{s}$  Gaussian probe stimulated the ASE transition. The probe was then recorded by the heterodyne detectors.

The intensity of the ASE signal was directly related to the gain on the ASE transition. Stimulating the ASE transition with a weak, coherent pulse allowed us to measure the gain on the ASE transition with signals that can be orders of magnitude larger than ASE. The gain was calculated by comparing the intensities of two identical pulses, with one of the pulses amplified by the gain feature, while the other pulse was not amplified (sent through the crystal before  $\pi_{inv}$ ).

The gain will be maximum when all the atoms are driven into the excited state, which was when  $\pi_{inv}$  is a perfect  $\pi$ -pulse. However,  $\pi_{inv}$  does not have to be a  $\pi$ -pulse. We can control the gain on the ASE transition by reducing the energy of  $\pi_{inv}$ . In these experiments, we control the energy in  $\pi_{inv}$  by changing the duration of the pulse.



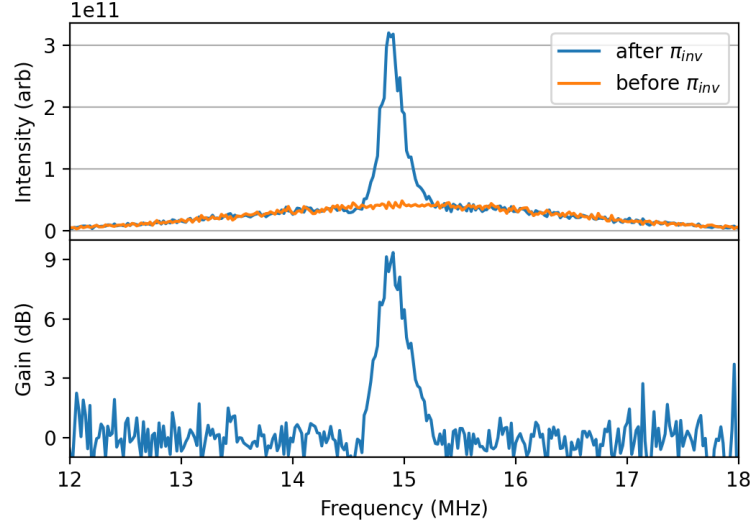


Figure 5.14: Probing the gain feature on the ASE transition,  $|-5/2\rangle_g \rightarrow |-5/2\rangle_e$ . The top graph shows the spectra of a weak probe sent through the crystal before and after  $\pi_{inv}$  inverted population creating the gain feature. The bottom graph is the two spectra on the top graph divided by each other (after / before) converted into dB.

### 5.5.1 Gain

Figure 5.14 top shows the Fourier transform of the two gain probes. This graph shows the spectra of the two weak probes, ‘before  $\pi_{inv}$ ’ in orange and ‘after  $\pi_{inv}$ ’ in blue, with the gain feature centered at 14.8 MHz. The gain was then calculated by dividing the intensity of the after spectra with the before spectra, and then converting to a dB scale. This particular spectra showed a gain of 9 dB at the center of the ASE transition.

In Figure 5.15 the gain measurements were repeated for different inversion pulse durations. Where the optimal duration for  $\pi_{inv} = 3 \mu\text{s}$ . We can model the gain on the ASE transition by the following equation,

$$g = g_{max}(1 - \cos(\Omega t))/2. \quad (5.1)$$

Where  $g_{max}$  is the maximum gain on the ASE transition and  $\Omega$  Rabi frequency. The model was derived geometrically using the Bloch sphere, Section 2.5.1. We can relate the duration of the inversion pulse to the amount of population driven to the excited state. Recall that a coherent pulse will drive the Bloch vector around the Bloch sphere rotating about the y-axis. Thus, a pulse of duration  $t$  will drive the Bloch vector about an angle  $\theta = \Omega t$ . The  $\hat{z}$  component of the Bloch vector is simply  $-\cos\theta$ . The percentage of atoms in the excited state ( $p$ ) is then  $p = (z + 1)/2 = (1 - \cos\theta)/2$ , the gain

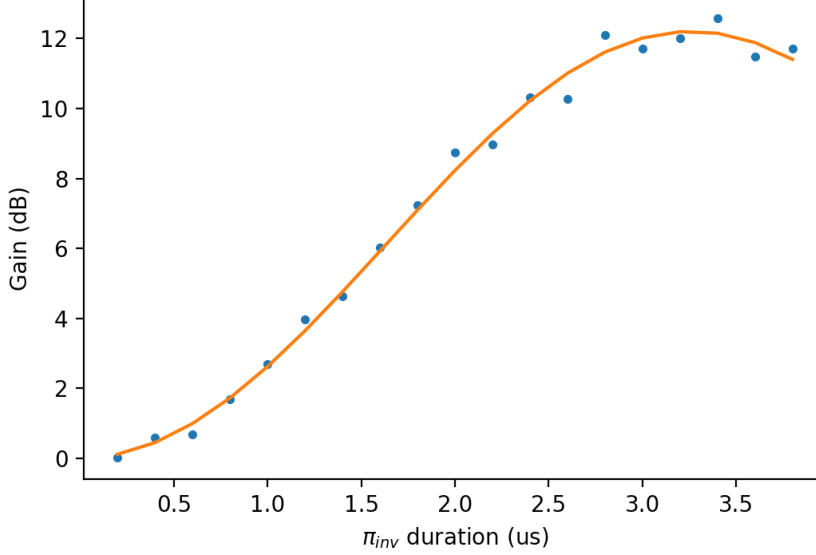


Figure 5.15: Measuring the gain on the ASE transition as the duration of the  $\pi$ -pulse was varied. Gain peaks at 12 dB for a  $\pi$ -pulse duration of 3.1  $\mu$ s. The solid line was a fitted to the data using Equation (5.1).

(in dB) is also proportional to  $p$ . However, this logic only holds true if the  $\pi$ -pulse is not distorted by the atoms as it travels through the crystal, i.e. if optical depth is low. Given we are following the level schemes outlined in Section 5.2.2, the inversion pulse is performed on the  $\Delta m_I = \pm 1$  transitions, while the gain is measured on the  $\Delta m_I = 0$ . This means that the absorption on the inversion pulse transition is much lower than gain we measure (3% when using the  $|+\frac{7}{2}\rangle_g$  level scheme). Thus, even if we measure high gain on the  $\Delta m_I = 0$  transition the  $\pi$ -pulse driving a  $\Delta m_I = \pm 1$  transition can still operate in a low absorption regime.

### 5.5.2 ASE measurements

Here, the ASE was measured and characterised. The ensemble preparation was identical to the gain measurements, however, in this case no probes were sent into the crystal. Instead, the erbium ions were allowed to decay spontaneously, amplifying the vacuum state. As a result, the signal detected here was substantially weaker than the gain measurements. The intensity of the ASE was near the single photon level, thus, many shots were averaged to achieve a high signal-to-noise ratio. For each ASE measurement, 2 ms long shots were recorded 20 times.

Figure 5.16 shows the spectra of a single ASE data set, note this data set

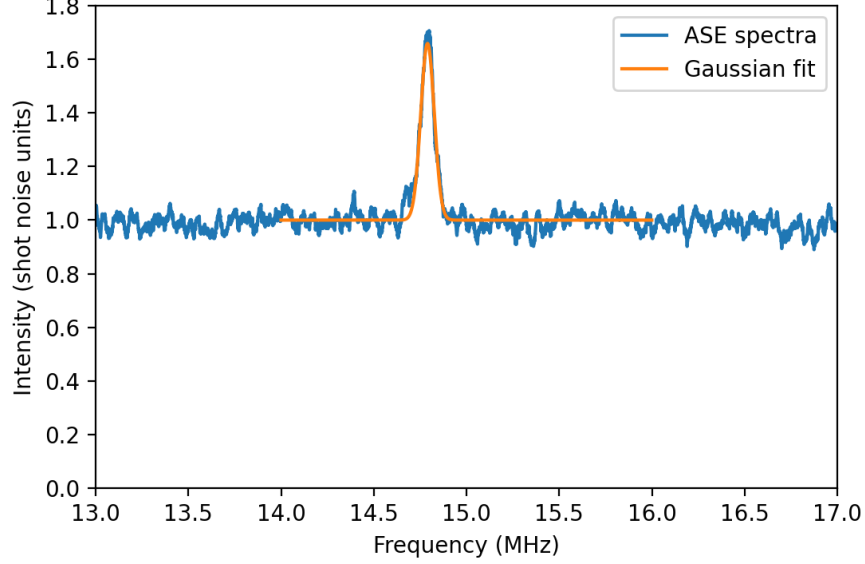


Figure 5.16: Spectrum of an ASE data set. The spectrum was normalised by the shot noise. The ASE signal, centered on 14.8 MHz, has been fitted with a Gaussian with a full-width-half-maximum of 107 kHz.

was taken without the EDFA, thus the  $\pi_{inv}$  are much longer than some gain measurements. Finally, as with the gain measurements, ASE was recorded using an array of input pulse durations. Figure 5.17 shows a colour plot of the ASE spectra as a function of  $\pi_{inv}$  time, where the ASE signal can clearly be seen emerging from the surrounding shot noise. The bottom figure shows the intensity of the ASE peak, as calculated by fitting a Gaussian to the ASE spectra. Fitted to this data was a model based on the gain model used in Section 5.5.1. The variance of the ASE signal (intensity of the ASE compared to the shot noise) at the crystal is given as  $2G - 1$ , from Ferguson's thesis [29], where  $G$  is the linear gain of the ASE transition (as opposed to the gain in dB). The ASE variance as recorded on our detectors then depends on the loss of our detection system. Following from Ferguson's thesis, we model the attenuation of our signal as a beam splitter with the second port open to vacuum. For 50% loss (a 50:50 beam splitter) this would resemble our signal being mixed with 1 part of shot noise, thus our variance decreases to  $\frac{var+1}{2}$ . Our detection system had 82% loss and our heterodyne detection effectively has an additional 50% loss, totalling in 91% loss. This is approximately 11/12, thus, the ASE variance decreases to  $\frac{var+11}{12}$ . In Figure 5.17, the model agrees with the data until the peak, but then decays more quickly than the data. The following equations describe the ASE variance, starting from equation (5.1),

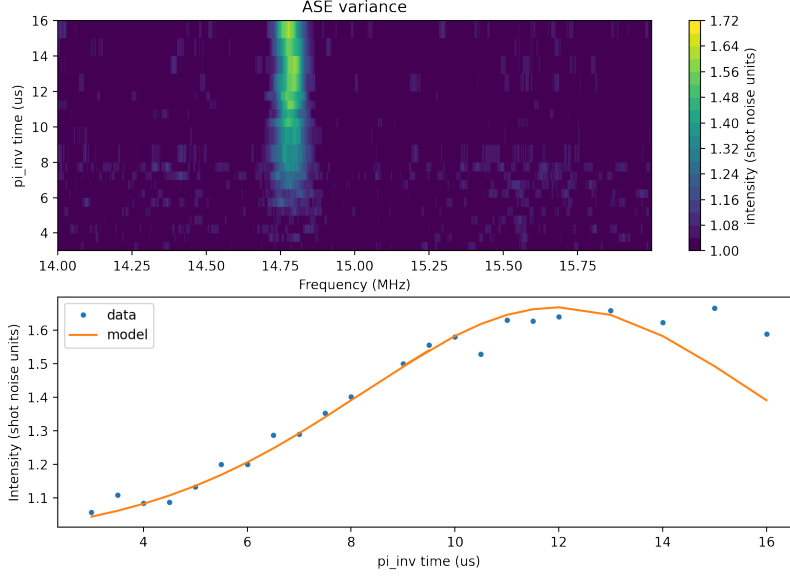


Figure 5.17: ASE variance with varying  $\pi_{inv}$  times. The top graph shows a 2D colour plot of the ASE spectras. The bottom graph shows the peak of the ASE variance from the 2D colour graph, fitting with Equation (5.5).

$$g = g_{max}(1 - \cos(\Omega t))/2, \quad (5.2)$$

$$g_{lin} = 10^{0.1g}, \quad (5.3)$$

$$A_{var} = 2G - 1, \quad (5.4)$$

$$A_{vd} = \frac{A_{var} + 11}{12}, \quad (5.5)$$

where  $A_{var}$  is the variance of the ASE signal directly after the crystal.  $A_{vd}$  is the variance of the ASE signal as recorded by our detectors, with 91% loss.

### 5.5.3 ASE signal decay

The data in Figure 5.17 was taken by integrating signals over a time window of 2 ms. If we instead break this data into several time windows, we can see the ASE signal decay as a function of time. In the low gain regime, this decay time will be the excited state lifetime (9.8 ms [9]). However, if the gain is high enough, the excited state population can decay faster than the excited state lifetime. This is because a large gain will allow the spontaneous emission of one photon to cause the decay of many atoms. Figure 5.18 shows

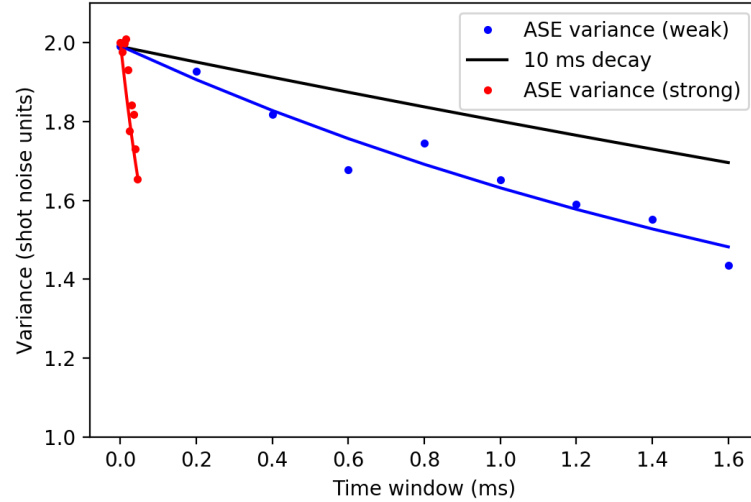


Figure 5.18: The decay of an ASE signal for two data sets. Blue, the data set used in the above section with a decay time of 2.2 ms. Red, ASE data taken from a RASE data set with much higher optical gain. The ASE variance here peaked at 70 shot noise units and has been scaled onto this graph. The red decay time was 120  $\mu$ s. Black shows a decay time of 9.8 ms, a reference to the excited state lifetime.

two different ASE data sets, with exponential decay curves fitted to the data. Also shown is the 9.8 ms excited state lifetime. The blue data is the same data set shown in Figures 5.16 and 5.18 and has a decay time of 2.2 ms. This is already significantly shorter than the excited state lifetime. The red data is the ASE variance taken from a RASE set with very high gain ( $>20$  dB) and the ASE variances measured at 70 shot noise units. In the RASE experiments, the ASE time window is only 50  $\mu$ s long. Even with this small recording time window, a clear decay in the ASE data can be seen. A decay time of 120  $\mu$ s was measured across the 50  $\mu$ s window.

From these results, the ASE signal has an intensity near the single photon level, with a bandwidth of 100 kHz, depending on the gain and bandwidth from the inversion pulse,  $\pi_{inv}$ . The RASE signal should have similar bandwidths to the ASE signal and, from the high rephasing efficiency of the inverted-four-level echo (up to 72%), the intensity should be similar to the ASE signal as well. Finally, the ASE signal can decay much quicker than the excited lifetime in the high gain regime. However, as long as the gain is low enough, the ASE signal will persist for milliseconds.

## 5.6 Summary

The experiments discussed in this chapter lay the groundwork for the following RASE experiment chapter. In this chapter, two types of photon echoes and ASE were investigated. From the photon echoes, the optical coherence time, four-level coherence time, spin-state storage time, and echo efficiency were found. These values will be useful when performing the RASE experiments, as the performance of the RASE should roughly match the performance of the inverted-four-level echo. Also discussed were some experimental details related to the echo experiments, such as: spurious signals from the AWG and the effect of adding an EDFA to the experiment. Finally, ASE was characterised, and gain measurements were performed. From the ASE measurements showed that the lifetime of a gain feature can be significantly shorter than the optical lifetime, up to two orders of magnitude shorter.

## Chapter 6

# RASE Experiments

This chapter describes the first demonstration of the RASE protocol in an erbium doped crystal. The long term goal of this experiment was to develop an entangled photon source for quantum repeater applications in a telecommunications network. Previously, entanglement between the ASE and RASE fields has already been demonstrated using the RASE protocol in Pr:YSO. Pr:YSO was useful for an initial RASE demonstration, however, it was limited by low recall efficiencies and did not inherently work at the telecommunications wavelength. Given erbium inherently works at the telecommunications wavelength, moving to erbium was then a natural next step. The RASE characterisation presented here will also be compared to the inverted-four-level echo characterisation from Chapter 5.

First, the preparation sequence, described in Section 3.8, was optimised for faster repopulation of the atomic ensemble, Section 6.2. Then the RASE performance was characterised, Section 6.3. This leads into the non-classical RASE measurements, Section 6.4, and a discussion into the limitations of the current experiment, with a focus on phase stability, Section 6.5.

### 6.1 RASE experiment outline

The RASE experiments used the same experimental setup detailed in the inverted-four-level echo experiment, Section 5.1. As an overview, a stable laser was coupled into the cryostat to optically access the crystal. Light exiting the cryostat was coupled into a single mode fibre and sent to a pair of heterodyne detectors. The heterodyne detector's local oscillator was generated from an amplified pick off of the stable laser. The frequency of the local oscillator, and thus, the beat frequency of the heterodyne signal, was controlled via an IQ-EOM, Section 3.5.3, operating as a carrier-suppressed single-sideband modulator.

The RASE process was enacted on a 1 MHz wide anti-hole that was created using the anti-polarisation sequence, explained in Section 3.8 and

optimised in Section 6.2. Figure 6.1 diagrammatically shows the RASE pulse sequence using a level diagram and a time plot with all the relevant pulses. This sequence was also described in Section 2.7.4, with the specific energy levels shown in Table 5.1 and Figure 6.1. An anti-hole was created in the  $|+\frac{7}{2}\rangle_g$  hyperfine level from the ensemble preparation. At time  $t = -150 \mu\text{s}$   $\pi_i$  was applied to the  $|+\frac{7}{2}\rangle_g \rightarrow |+\frac{5}{2}\rangle_e$  transition, which created a gain feature in the  $|+\frac{5}{2}\rangle_e$  level. The gain feature then amplified the vacuum state, producing ASE on the  $|+\frac{5}{2}\rangle_g \rightarrow |+\frac{5}{2}\rangle_e$  transition and creating a superposition. At  $t = 50 \mu\text{s}$  the rephasing  $\pi$ -pulses,  $\pi_1$  and  $\pi_2$  were sequentially applied to the optical transitions:  $|+\frac{3}{2}\rangle_g \rightarrow |+\frac{5}{2}\rangle_e$  and  $|+\frac{5}{2}\rangle_g \rightarrow |+\frac{3}{2}\rangle_e$ , respectively. The rephasing  $\pi$ -pulses have transferred the superposition to the  $|+\frac{3}{2}\rangle_e \rightarrow |+\frac{3}{2}\rangle_g$  transition. RASE was produced on the  $|+\frac{3}{2}\rangle_e \rightarrow |+\frac{3}{2}\rangle_g$  transition, time symmetric with ASE about the rephasing  $\pi$ -pulses. Following the RASE time window, 40  $\mu\text{s}$  after the rephasing  $\pi$ -pulses, were three phase correcting reference pulses, each at a distinct frequency: 25, -21, and 11 MHz relative to the local oscillator.

The reference pulses were used to phase correct the RASE data sets for the non-classical demonstrations, as was done in the AFC Chapter, Section 4.6.1. During the experiment ASE was constantly emitted in the timeframe between  $\pi_i$  and  $\pi_1$ . We will set the ASE window to be the last 20  $\mu\text{s}$  of this time period, 30 – 50  $\mu\text{s}$ . The RASE time window was then the first 20  $\mu\text{s}$  after  $\pi_2$ . Recording stopped at  $t = 200 \mu\text{s}$ , any time window between the reference pulses and  $t = 200 \mu\text{s}$  can be used as a reference to vacuum. There will still be a weak ASE signal in this window as the rephasing process was not perfect, and some ions will be left in the excited level. However, the ASE signal in the vacuum window was expected to be very small.

The strongest ASE signals were generated when  $\pi_i$  was a  $\pi$ -pulse, i.e. when gain was maximum. However, we do not always want the strongest possible ASE signal. Particularly for the non-classical experiments, weaker ASE signals were preferable to reduce classical noise. The ASE intensity was controlled by attenuating  $\pi_i$ .

Finally, the heterodyne local oscillator changed between the characterisation (Section 6.3) and non-classical RASE measurements (Section 6.4). In the characterisation measurements, the local oscillator frequency was controlled by CW RF source, a Windfreak SynthNV. In the non-classical experiments, the Windfreak was replaced with one of the Tabor AWG channels, Section 3.6. In the experiments, we wanted the heterodyne beat frequency to be within the bandwidth of the 30 MHz heterodyne detectors. With the current RASE level scheme, the ASE and RASE signals were separated by 96 MHz. Thus, when using a CW RF source for the local oscillator, the beat frequency of the ASE and RASE signals was outside this bandwidth, specifically 48.8 and 47.1 MHz, respectively. By switching the RF source to an AWG, the local oscillator frequency could change quickly ( $\sim \text{ns}$ ) and phase



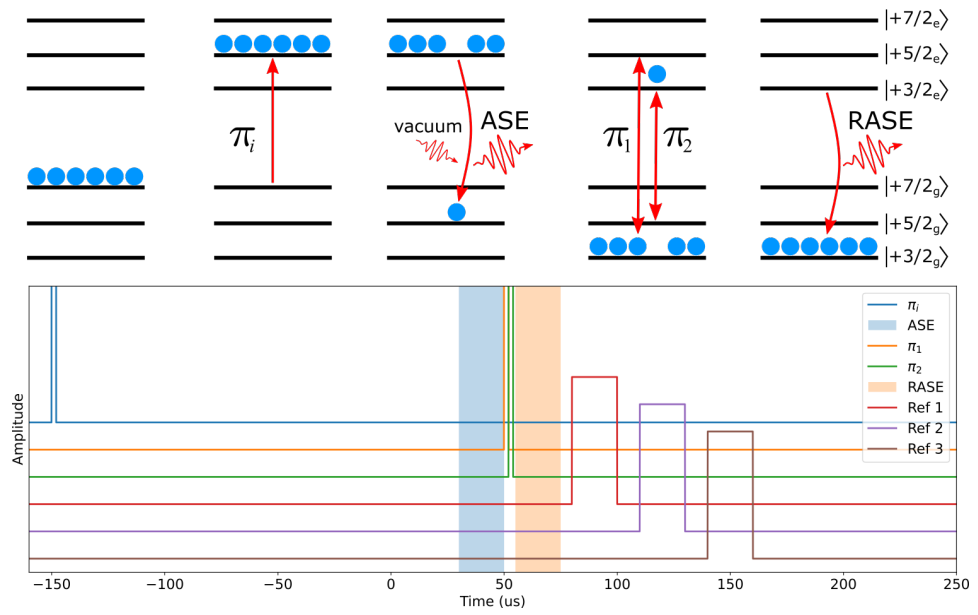


Figure 6.1: Four-level RASE sequence diagram. The top figure shows the ensemble energy level population after each step. The bottom figure shows the amplitude of each pulse in the sequence as a function of time, each line represents one of the pulses in the RASE sequence. The ASE and RASE time windows are highlighted between 30 – 80  $\mu s$ .

coherently. This allowed arbitrary heterodyne beat frequencies for the ASE and RASE signals, specifically I choose, 15.0 and 18.6 MHz, respectively.

## 6.2 RASE preparation sequence

Large RASE data sets will be needed to demonstrate non-classical storage. The reason for this was given in Ferguson et al. [30], essentially, we need to operate in a low gain regime with weak (photon level) RASE signals. Weak signals were needed, as classical noise scales with signal intensity faster than shot noise. Thus, for weak signals, shot noise will dominate the classical noise. In order to accurately measure such weak signals, with high statistical certainty, we need to record large data sets.

To collect large RASE data sets quickly, we need a quick preparation sequence for our ensemble. The 5.4 second long preparation sequence used in the AFC chapter, and the inverted-four-level echo, was too slow (Section 3.8). This was because the preparation sequence needs to run for every single RASE shot. This was not an issue for the inverted-four-level echo because a single shot gives a very large signal. This also was not an issue for the AFC, as 10,000 shots could be recorded in a single preparation sequence. RASE, however, is a ‘destructive’ protocol. ‘Destructive’ because once we prepare the anti-polarised feature, we apply an inverting  $\pi$ -pulse to the feature, followed by rephasing  $\pi$ -pulses. As a result, the ions of the sub-ensemble are distributed over the hyperfine levels used in the RASE sequence ( $|+\frac{7}{2}\rangle_g, |+\frac{5}{2}\rangle_g, |+\frac{3}{2}\rangle_g$ ) and the anti-hole is destroyed. Thus, the sub-ensemble must be re-prepared for every shot. However, the spin polarisation is not affected by the RASE sequence.

Recall that the preparation sequence, outlined in Section 3.8, spin polarises our ensemble into one extremum hyperfine level and then anti-polarises a small ( $< 2$  MHz bandwidth) sub-ensemble into the opposite extremum hyperfine level. This preparation sequence was broken down into two steps, spin polarisation and anti-polarisation. A third step was added, a cleanup step to remove any ions on the ASE and RASE transitions. The cleanup consists of two two-megahertz wide trenches centered on the  $|+\frac{5}{2}\rangle_g \rightarrow |+\frac{7}{2}\rangle_e$  and  $|+\frac{3}{2}\rangle_g \rightarrow |+\frac{1}{2}\rangle_e$  transitions. Spin polarisation takes 5 seconds, while the anti-polarisation and cleanup both take 200 ms. The spin polarisation takes the longest time by far and was not needed after every RASE shot. As mentioned above, this was because the RASE sequence only destroys the anti-polarised feature. Only the anti-polarisation and cleanup needed to be repeated between shots. However, after enough RASE shots the spin polarisation will rethermalise, either through resonant phonons created during anti-polarisation (Section 3.9.3) or through hyperfine cross-relaxation (Section 3.9.1). The ensemble was still mostly spin polarised, and we only needed to spin polarise the few ions that have become unpolarised. Thus, a shorter

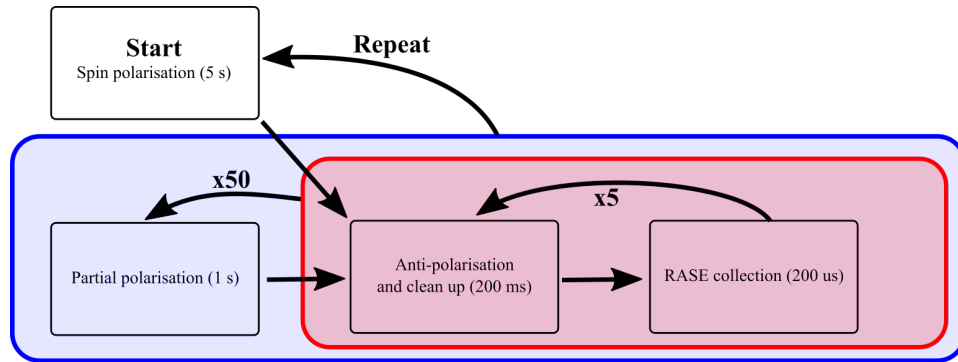


Figure 6.2: RASE preparation and re-pumping sequences. For every RASE shot, the full anti-polarisation sequence was run (red shaded box). Every 5 shots, a quick one-second spin polarisation sequence was run in addition to the anti-polarisation (blue shaded box). Every 250 shots, a full five-second spin pumping sequence was added to the preparation (return to start). Using this preparation gave an average of 1 RASE shot per second, rather than 0.2 shots per second if the full preparation sequence was used for every shot.

spin polarisation can be used.

Figure 6.2 diagrammatically shows the new preparation sequence. Initially, the full 5.4 second preparation sequence was run before the first RASE shot. For the next four shots, only the anti-polarisation and cleanup sequence were run, totalling in a set of 5 shots. After every set of 5 shots, a short one-second spin polarisation was performed to spin polarise the rethermalised ions. This sequence was repeated 50 times, totalling in 250 RASE shots. Now the sequence was repeated and a full 5.4 second preparation sequence was re-run. In-between groups of 250 shots, a set of diagnostic measurements were taken to make sure the experiment was running without issue. The diagnostic measurements are explained in Section 6.2.1. This cycle of 250 RASE shots plus diagnostics takes 4.5 minutes. For reference, 250 RASE shots using the full preparation sequence between each shot would take 22.5 minutes, 5 times slower.

### 6.2.1 Diagnostic measurements

The diagnostic measurements, recorded once every 250 RASE shots, were composed of three measurements: a spectrum of the anti-polarised feature, a gain measurement on the ASE transition after  $\pi_i$ , and 15 inverted-four-level echo shots. During the inverted-four-level echo, only the anti-polarisation and cleanup sequences were run in between each shot. By looking at the inverted-four-level echo diagnostic data, we can test the consistency of the new preparation sequence. Figure 6.3 shows the intensities of the input pulse, echo, and three phase-reference pulses for a series of 15 inverted-four-

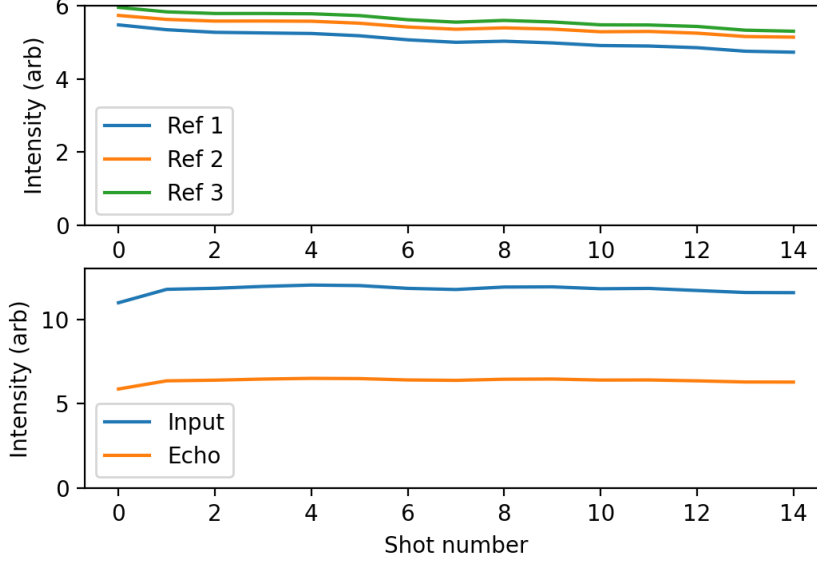


Figure 6.3: Intensities of each pulse in the diagnostic-inverted-four-level echo across 15 shots. Between each shot, only the anti-polarisation and ASE/RASE cleanup are performed.

level echoes. We can see that the intensity of the input and echo remains constant across the 15 shots (within 2 %). The reference pulses' intensities steadily decay by 1% per shot. The decrease in reference pulse intensity is likely from the spin-polarised feature rethermalising, which increases the background absorption at the reference pulses' frequencies. The input and echo were not effected because the cleanup sequence keep these transitions clear of ions. However, the reference pulses were at different frequencies.

After five shots, the reference pulses in Figure 6.3 are attenuated by 5%, 0.2 dB. This corresponds to 1% of the ions rethermalising from the spin polarised ensemble (21 dB optical depth). Five shots of data, with a 400 ms re-preparation sequence between each shot, takes two seconds to record. This level of rethermalisation is consistent with the  $\mathcal{O}(200)$  second lifetime of the spin polarised ensemble, Section 3.9.1. Thus, the attenuation of the reference pulses is most likely due to hyperfine cross relaxation. To keep the ensemble spin-polarised with  $<1\%$  of the ions in the experiment hyperfine levels ( $|+\frac{7}{2}\rangle_g, |+\frac{5}{2}\rangle_g, |+\frac{3}{2}\rangle_g$ ), the quick spin pumping sequence was performed every five shots. The consistency of the input pulse and echo intensities shows that the preparation sequence can consistently re-prepare an anti-hole for the RASE experiment. In total, the new preparation sequence reduces data collection time by a factor of five, allowing large data sets to be collected much quicker than the original preparation.

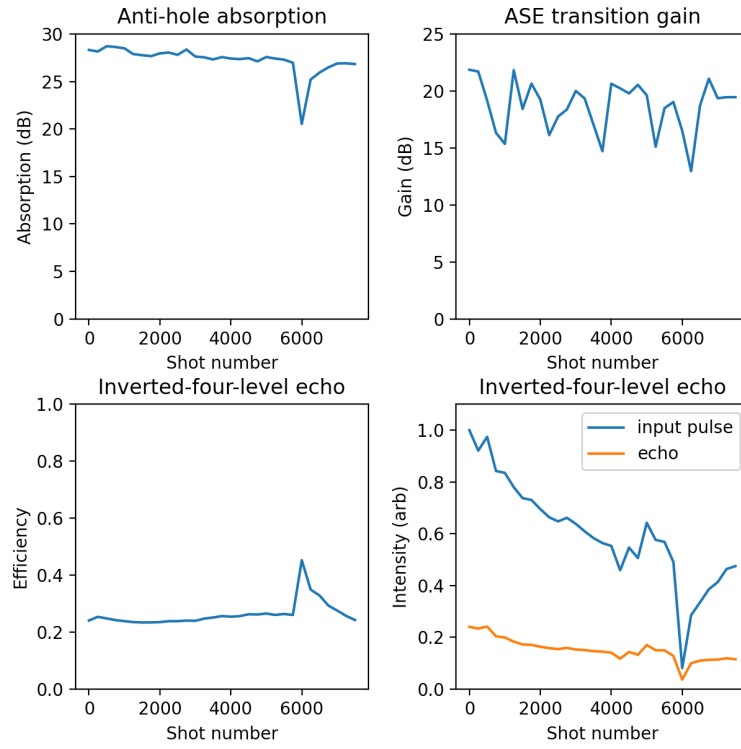


Figure 6.4: RASE diagnostics over a 7,500 shot data series. Top left shows the absorption of the anti-polarised feature, prepared into the  $|+\frac{7}{2}\rangle_g$  hyper-fine level. Top right shows the gain on the ASE transition, after  $\pi_i$  has been applied to the feature prepared in the top left graph. The bottom graphs show the efficiency of the inverted-four-level echo and the intensity of the input pulse and echo.

During a RASE experiment, hundreds or thousands of RASE shots are recorded over timescales of multiple hours. The diagnostic measurements were also used to monitor the consistency of the experiment throughout data collection. Figure 6.4 shows the diagnostics recorded over a fairly long 7,500 shot RASE data series, where data collection took 3 hours and 17 minutes. The anti-hole absorption, shown in the top left, decays by 2 dB across the entire data series, with an anomaly at shot 6,000. The gain on the ASE transition (top right) should follow this, although the probing method was less accurate at high gain, so the uncertainty was higher. An inverted-four-level echo also measures the rephasing efficiency of the RASE sequence. The time delay for this echo was relatively long, so the inverted-four-level echo rephasing efficiency is low, relative to the peak efficiencies mentioned in Section 5.2.2. These measurements inform us of when something fails in the experiment, i.e. the sample space runs out of helium or if equipment malfunctions.

### 6.3 Characterisation of RASE

In this section, we look at the performance of the RASE sequence by measuring the intensity of the (R)ASE fields. In particular, the rephasing efficiency, hyperfine storage time, and (R)ASE window times were measured. These results were used to determine the mode storage capacity and storage time of the memory, two very important parameters when considering quantum repeater applications.

Figure 6.5 shows the RASE efficiency as a function of gain on the ASE transition. The efficiency of the inverted-four-level echo (Figure 5.8) and the theoretical efficiency from Ledingham et al.’s model [49, 29], are also shown. Figure 6.6 shows the power spectrum of the (R)ASE windows from the most efficient RASE data set, the ASE and RASE heterodyne beat frequencies were 48.8 and 47 MHz, respectively (Section 5.2.4 explains why the heterodyne beats were at these frequencies). The gain was determined from the diagnostic measurements, and the efficiency was the ratio of the (R)ASE intensities.

In Figure 6.7, RASE was recorded with different time delays between the two rephasing  $\pi$ -pulses,  $\pi_1$  and  $\pi_2$ . The time delays varied from 0.1 – 30  $\mu\text{s}$ . An exponential fit to the data gives a storage time of  $27 \pm 4 \mu\text{s}$ .

Finally, the 20  $\mu\text{s}$  (R)ASE time windows, from the data set in Figure 6.6, were subdivided into smaller 4  $\mu\text{s}$  windows to measure the (R)ASE intensity for increasing delay times between the (R)ASE windows and the rephasing  $\pi$ -pulses. This is analogous to the four-level coherence time from Section 5.2.2. Figure 6.8 shows the intensity of the (R)ASE windows as a function of time between the (R)ASE windows. The ASE intensity stays constant, with no noticeable trend, while the RASE intensity steadily decays. An

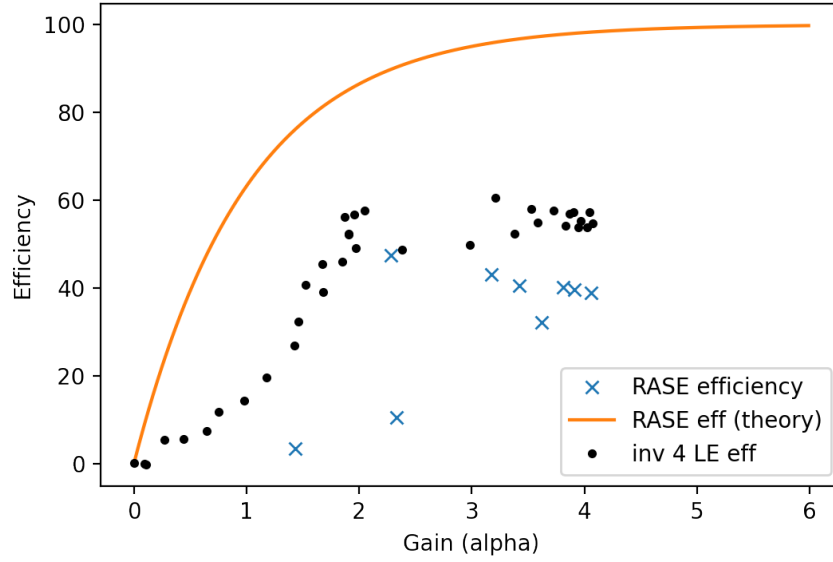


Figure 6.5: Efficiency of the inverted-four-level echo and RASE sequence as a function of the gain on the ASE/input transition. The solid line shows the theoretical curve, given by Ledingham et al.'s model [49, 29].

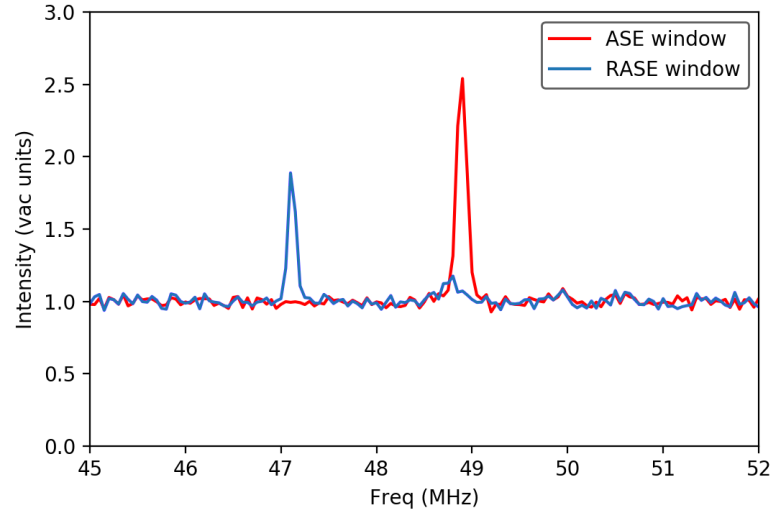


Figure 6.6: Spectra of a highly efficient RASE data set. The data set comprises 2000 RASE shots. The vacuum window was taken as the last 20  $\mu$ s of each RASE shot.

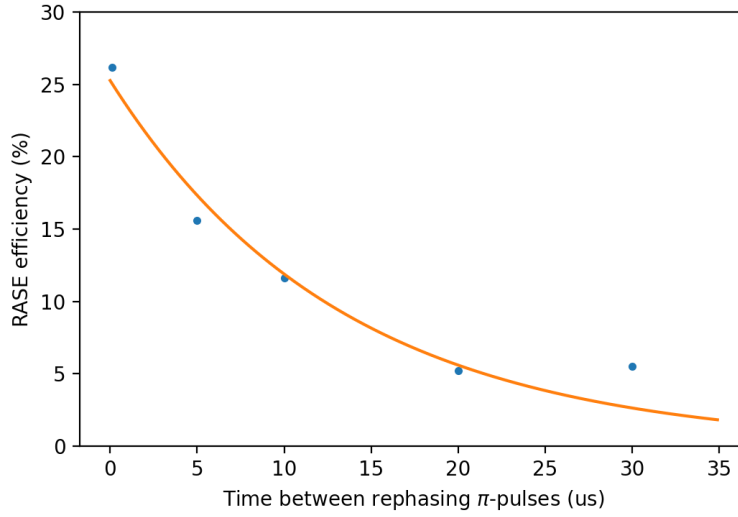


Figure 6.7: Each data point shows the efficiency of a 2000 shot RASE data set with a different time delay between the rephasing  $\pi$ -pulses. An exponential decay is fitted (orange) and shows a spin-state storage time of  $27 \pm 4 \mu\text{s}$ . Very similar to the spin-state storage time of the inverted-four-level echo.

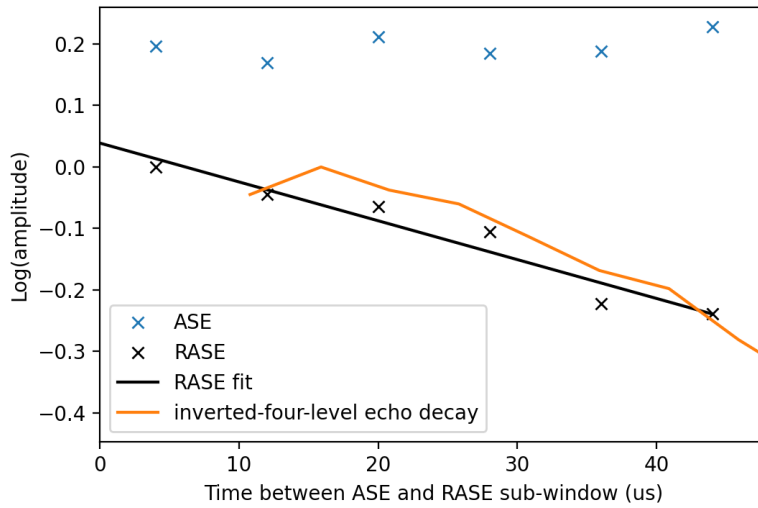


Figure 6.8: Intensity of the (R)ASE signals for temporal windows separated by some time,  $t$ . The decay of the RASE signal has been fitted, giving a decay time of  $160 \pm 20 \mu\text{s}$ . The orange line shows the start of the inverted-four-level echo decay, from Figure 5.6.



exponential decay has been fitted to the data, revealing a  $160 \pm 20$   $\mu\text{s}$  decay time. Also shown is the inverted-four-level echo decay from Figure 5.6.

The RASE efficiency measurements, from Figure 6.5, show that both the inverted-four-level echo and RASE sequence have much lower efficiencies than theory predicts. Ledingham et al.'s model [49, 29] assumes that the rephasing  $\pi$ -pulses have unitary efficiency. The non-unitary rephasing efficiency may account for some difference between data and theory. However, at lower gain, the general shape of the data does not match the shape of the theory curve. This does suggest there was some gain dependant mechanism. One reason for this could be that the rephasing  $\pi$ -pulses were optimised for a high gain regime. In the high gain regime, the rephasing  $\pi$ -pulses were absorbed by the high optical depth on the rephasing transitions. To counteract the absorption, the  $\pi$ -pulses were over driving the transition. In the low gain regime, the rephasing  $\pi$ -pulses were not absorbed and over driving the transition lead to a lower rephasing efficiency.

The RASE efficiency peaks at medium gain and decreases towards higher gain. Also, there are two data points, both at a gain of 2.3, which have wildly different efficiencies, 47% (data from Figure 6.6) and 15%. Currently, the data suggests some unknown process that affects the efficiency, either in the preparation or RASE pulse sequence. However, we cannot concretely conclude anything for gain less than three, given the lack of data, more experiments are needed in the lower gain regime.

The efficiencies shown here are much higher than the Pr:YSO demonstrations, 14% [26] and 3% (non-classical) [30]. The efficiency of Pr:YSO was limited by the rephasing  $\pi$ -pulses, as they were distorted by the optically thick gain feature [30]. We can achieve higher rephasing efficiencies because of the relative oscillator strengths of the transitions used in the RASE sequence. The (R)ASE transitions were set to both be on the  $\Delta m_I = 0$  transitions, while the three  $\pi$ -pulses were on the  $\Delta m_I = \pm 1$  transitions. Because of this particular level configuration, the  $\pi$ -pulses experienced absorption/gain 2 – 5% of the (R)ASE transitions. Thus, the optical gain of ASE could remain high, up to 23 dB, while the rephasing  $\pi$ -pulses were only distorted by weak  $\sim 1$  dB optical features. These oscillator strengths are small enough that efficient rephasing is possible in a fairly high gain regime, 15 dB, but still large enough that  $\pi$ -pulse distortion can decrease the rephasing efficiency in the higher gain regions (gain above 3,  $\sim 15$  dB), Figure 6.5.

While the efficiency of the rephasing was indeed high, it was still less than the inverted-four-level echo efficiency, 72%. There are a few potential reasons for this. One reason for this might be that the inverted-four-level echo pulses have a different spatial mode to their ASE and RASE counterparts. The output of the cryostat was coupled into a single mode fibre, the coupling was optimised for the spatial mode of the input laser. The spatial profile of ASE was defined by the gain spatial profile, determined by  $\pi_i$ . The spatial

profile for RASE was then the spatial profile of the ASE convoluted with the rephasing  $\pi$ -pulses,  $\pi_1, \pi_2$ . If the collection efficiency for RASE was lower than ASE, then it would appear as if the RASE had a lower rephasing efficiency. Furthermore, as the gain becomes stronger, pulses sent through the crystal will become more distorted. A large peak gain could create a spatially dependent change in refractive index [26], effectively creating a gradient index (GRIN) lens. Distorting the spatial mode of our (R)ASE signals was probable and can offer a reason why the inverted-four-level echo efficiency and RASE efficiency are different.

Figure 6.7 shows a storage time of  $27 \pm 4 \mu\text{s}$ . This storage time was slightly longer than the inverted-four-level echo storage time,  $20 \mu\text{s}$ , Section 5.2.2. There was no obvious reason why these two storage times would be different. The uncertainty in the RASE storage time might account for the storage time difference, as the two storage times disagreed by only  $2\sigma$ .

The intensity of the RASE signal in the RASE time windows decreased with a time constant of  $160 \pm 20 \mu\text{s}$ , Figure 6.8. This result seems surprising, as the inverted-four-level echo coherence time was almost a quarter of this,  $46 \mu\text{s}$  from Section 5.2.2, due to a magnetic field gradient, Section 5.2.3. However, when we compare the RASE data to the inverted-four-level echo coherence time data, we saw that the RASE and echo data roughly match. Thus, the RASE windows were not long enough to experience the effects of the magnetic field gradient. If RASE data were collected with longer (R)ASE windows, we would expect to see the same modulated decay curve from Figure 5.6.

This data also suggests that removing the magnetic field gradient could improve the window time to at least  $160 \mu\text{s}$ . The bandwidth of RASE was  $250 \text{ kHz}$ , from Figure 6.6, the  $46 \mu\text{s}$  inverted-four-level echo coherence time gives a time-bandwidth product of  $46 \mu\text{s} \times 250 \text{ kHz} = 11$ . If the magnetic field gradient is removed, then the time-bandwidth product could increase to 40, which means 40 temporal modes can be stored in our memory.

We have shown high storage efficiencies using the RASE protocol. The reason for these high efficiencies comes from the oscillator strengths of our particular level scheme. We have also shown a spin-state storage time of  $27 \mu\text{s}$  and a  $160 \mu\text{s}$  RASE window time, if the magnetic field gradient is removed. This allows 40 temporal modes to be stored in the memory. Next we will look at the correlations between our (R)ASE signals. The correlation measurements provide a way to determine if the ASE and RASE are phase coherent and if the ASE is purely an amplified vacuum state or if the ASE is derived from the laser (amplified stimulated emission).

## 6.4 Non-classical RASE measurements

The following results focus on the correlation between the (R)ASE time windows. The preparation and general setup of the experiment was the same as the above classical measurements section, with a few changes to the fibre laser. The main differences between this experiment and the previous characterisation measurements was that the fibre laser was locked to an external reference cavity and that fast local oscillator switching was used to keep the heterodyne beat frequencies of the (R)ASE windows within the bandwidth of the heterodyne detectors, Section 6.1.

A fibre-coupled AOM was used to lock the fibre laser to an external reference cavity, locking details are in Section 3.4. The fibre-coupled AOM had a coupling efficiency of 50%. A consequence of locking the fibre laser to a stable reference cavity meant that the power of the local oscillator dropped from 2 mW to 0.5–0.8 mW. As a result, our heterodyne detection system has less clearance over the electrical noise. The power of the probe sent through the cryostat was also reduced, but this was counteracted by increasing the gain of the EDFA.

### 6.4.1 Characterising the electrical noise

Figure 6.9 shows the noise floor of the heterodyne detection with and without the local oscillator. When the local oscillator was turned off, we were measuring the electrical noise of the detection system. The graph shows that the noise floor with the local oscillator on was 3 dB stronger than the electrical noise, between 5 – 25 MHz. This means that the intensity of the electrical noise plus the intensity of the shot noise was twice the intensity of the electrical noise. Thus, the electrical noise is effectively the same size as the shot noise.

The local oscillator power lost from locking the fibre laser to the external reference cavity meant that the heterodyne electrical noise clearance dropped from >6 dB clearance to around 3 dB clearance (frequency dependant). This poses an issue for non-classical measurements. In non-classical experiments, having an accurate measurement of the shot noise was a requirement. The previous sections have shown the FFT of the ASE and RASE windows normalised to a chosen vacuum window, Figure 6.6. If our detection was shot-noise-limited, then the vacuum window was a good reference to shot noise. However, this assumption only holds true if the shot noise was much larger than any other noise in our detection.

For the following RASE experiments, this means that we cannot assume the shot noise is the dominant source of noise in the detection path. Thus, to measure the shot noise accurately, we must account for the electrical noise. We can use the electrical noise clearance to convert the vacuum window noise into shot noise using the following logic. First, we define the electrical noise

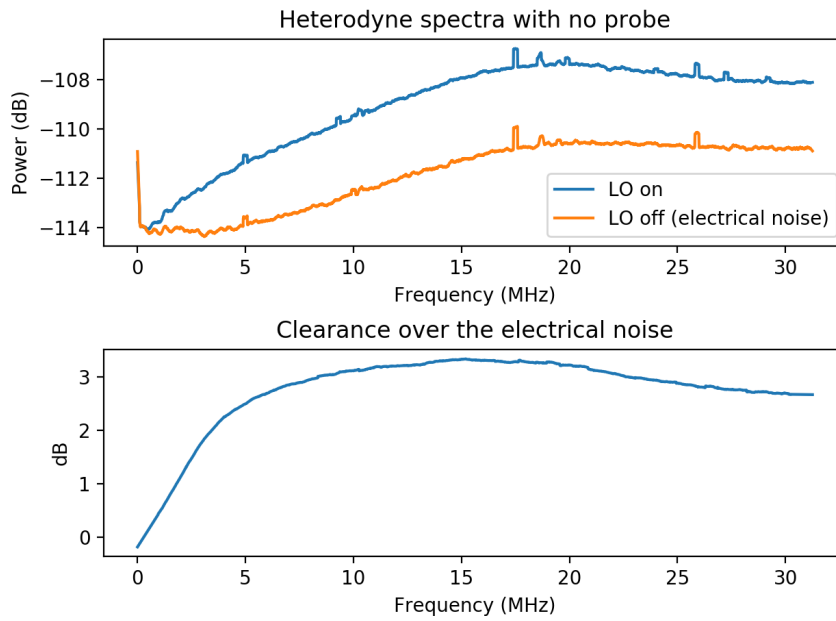


Figure 6.9: The top figure shows the noise floor of the heterodyne detection with and without the local oscillator. Where the trace without the local oscillator is the electrical noise floor. The bottom figure is the difference of the two traces from the top figure. In the bottom figure, a clearance of 3 dB indicates that the electrical noise and shot noise have equal intensity.

clearance ( $c(f)$ ) and vacuum noise ( $v(f)$ ) as,

$$c(f) = \frac{s(f) + e(f)}{e(f)}, \quad (6.1)$$

$$v(f) = s(f) + e(f), \quad (6.2)$$

as a function of frequency,  $f$ .  $e(f)$  is the electrical noise, and  $s(f)$  is the shot noise. We wish to find some function  $g(f)$  such that  $g(f) \cdot v(f) = s(f)$ . Then we can find  $g(f)$  in terms of  $c(f)$ ,

$$g(f) = \frac{s(f)}{v(f)} \quad (6.3)$$

$$= 1 + \frac{1}{c(f) - 1}. \quad (6.4)$$

Thus, we can convert the background noise in our vacuum window to shot noise. Figure 6.10 shows the FFT of a RASE data set before and after correcting for the electrical noise. Because the clearance over the shot noise was at most 3.3 dB, the background noise floor is almost 2 shot noise units. The noise also drastically increases below 5 MHz due to a 1 MHz high pass filter between the heterodyne detectors and the oscilloscope.

#### 6.4.2 Correlation measurements

So far we have shown a high rephasing efficiency between the ASE and RASE windows, and we have shown that the storage time can be extended out to 27  $\mu$ s, without hyperfine rephasing. However, we need to show that the ASE and RASE fields are non-classically correlated. We also want to demonstrate that the ASE signal derives from the vacuum state, as opposed to the ASE being stimulated by our laser. Entanglement can be demonstrated by analysing the correlation between the two (R)ASE time windows. We can measure correlation by taking the convolution of said windows, this was shown in Section 2.7.5.

Each shot of RASE data was phase corrected using the same techniques outlined in the AFC chapter, Section 4.6. However, in the RASE experiments, three phase-correcting reference pulses were used. Two reference pulses were enough to correct for arbitrary global phase shifts and oscilloscope triggering delays. The third reference pulse allows us to quantify the accuracy of the phase correction. Using the three reference pulses, we determined the phase correction was accurate to within 40 mrad, Appendix D.

After the phase correction, the ASE and RASE signals were windowed (with 20  $\mu$ s windows). The ASE and RASE windows were digitally beaten

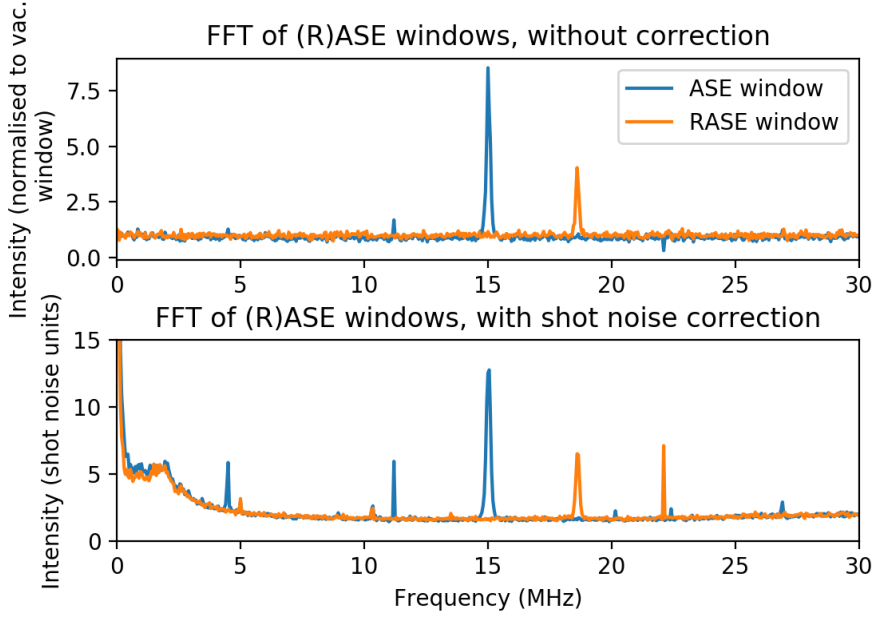


Figure 6.10: Top: FFT of the ASE and RASE windows referenced to a vacuum window. Bottom: The same data corrected to shot noise units using the electrical clearance data.

down to DC and filtered 1 MHz about DC. In effect, this shifted the ASE and RASE windows to the same frequency, which made analysing the correlations between the two windows easier. Then the correlation between the two windows is simply,

$$\rho_{AR} \propto \int A(\tau) \cdot R(\tau - t) d\tau. \quad (6.5)$$

Figure 6.11 shows the auto-correlation of the ASE window (the convolution of the ASE window with itself), the auto-correlation of the RASE window, and the correlation of the ASE shots with the succeeding ASE shots. The (R)ASE auto-correlations show a double-Gaussian-like structure centered at 0  $\mu\text{s}$ . In these two traces we see the auto-correlation of the (R)ASE, the broader  $\sim 4 \mu\text{s}$  peak, and the auto-correlation of the vacuum, the narrower 1  $\mu\text{s}$  peak. Both the (R)ASE and the vacuum will only be correlated when the two windows are perfectly overlapped (when  $t=0$ ). The vacuum auto-correlation decays over 1  $\mu\text{s}$  as the data was digitally filtered in a 1 MHz window. The (R)ASE correlation decays over 4  $\mu\text{s}$  due to the 250 kHz bandwidth of the (R)ASE feature, seen in Figure 6.10. Finally, the correlation between the ASE and ‘ASE next shot’ is noise with no clear structure, indicating that the (R)ASE was derived from the vacuum and not stimulated by the laser. This confirms that there was no laser light leaked

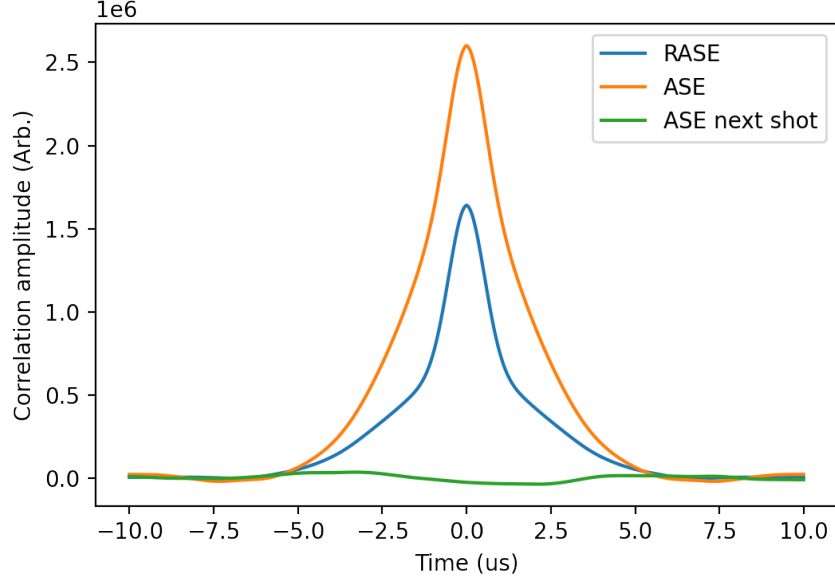


Figure 6.11: The auto-correlations of the ASE and RASE windows, and the correlation between an ASE shot and the succeeding ASE shot.

into the experiment during the (R)ASE windows.

Figure 6.12 shows the cross-correlation between the ASE and RASE windows. The cross-correlation here had a non-zero imaginary component. This means that the two (R)ASE windows were correlated, however, there was a phase offset between the two windows. This was to be expected because there was a  $9.1 \mu\text{s}$  time gap between the two windows. The time gap means that the phase of the local oscillator was different between the two (R)ASE windows, which results in the phase shift on the cross-correlation measurement. There was also no vacuum self correlation in this data because the two windows were time separated with no overlap.

We can also use the auto-correlation measurements to predict the strength of the RASE cross-correlation. If the ASE and RASE windows were perfectly correlated, then we can write the RASE window as a time reversal of the ASE window with some phase shift,  $\theta$ , and rephasing efficiency,  $\eta$ .

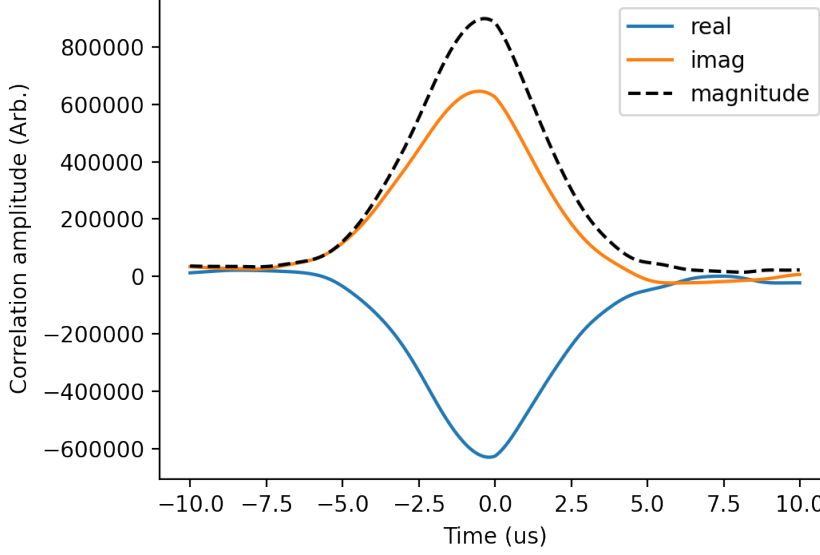


Figure 6.12: Cross-correlation graph between the two ASE and RASE windows.

$$R(t) = \sqrt{\eta}A(-t) \cdot e^{i\theta} \quad (6.6)$$

$$\rho_{AA} \propto \int A(\tau) \cdot R(\tau - t) d\tau \quad (6.7)$$

$$\rho_{AR} \propto \int A(\tau) \cdot \sqrt{\eta}A(\tau - t)e^{i\theta} d\tau \quad (6.8)$$

$$= \rho_{AA} \cdot \sqrt{\eta}e^{i\theta} \quad (6.9)$$

For a rephasing efficiency  $\eta$ , the magnitude of the RASE cross-correlation should be the magnitude of the ASE auto-correlation multiplied by  $\sqrt{\eta}$ .

To find the strength of the ASE auto-correlation, we have to subtract off the vacuum auto-correlation. Figure 6.13 shows the RASE auto-correlation fitted with a double Gaussian. The vacuum auto-correlation was then the narrower of the two fitted Gaussian's. The vacuum auto-correlation was removed by subtracting the narrower Gaussian.

Figure 6.14 shows the ASE and RASE auto-correlations with the vacuum auto-correlation subtracted and the RASE cross-correlation. There was a small artefact in the subtracted auto-correlations, at  $t = 0 \mu\text{s}$ , this shows that the double Gaussian fit in Figure 6.13 was not perfect. However, this should give a close approximation to the (R)ASE auto-correlation. The amplitude of the (R)ASE auto-correlation and the RASE cross-correlation



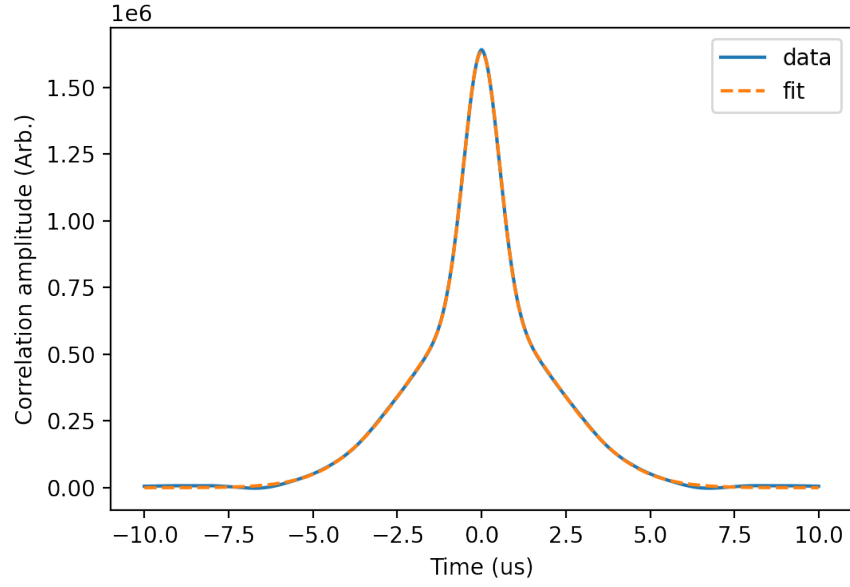


Figure 6.13: ASE auto-correlation with a double Gaussian fit.

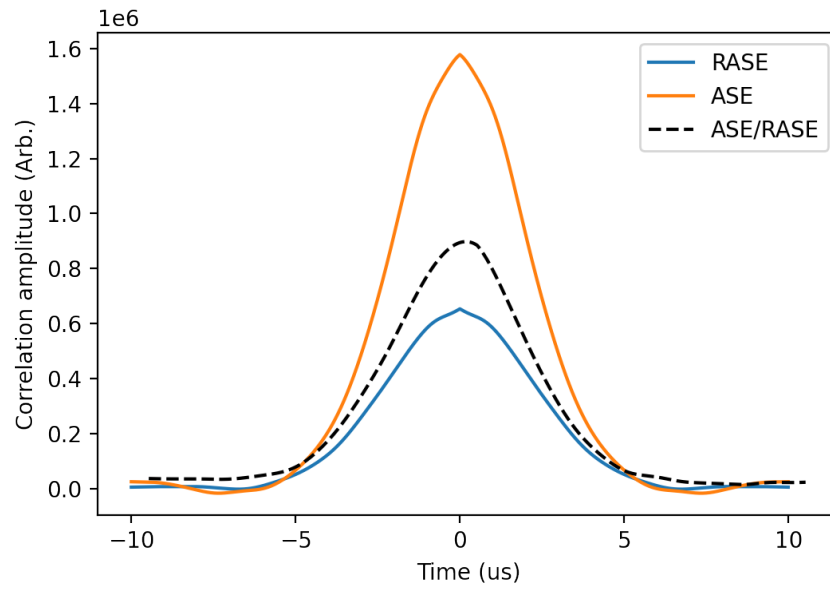


Figure 6.14: (R)ASE auto-correlations with the vacuum auto-correlation subtracted and the RASE cross-correlation (labelled as ASE/RASE).

was then found by integrating the correlation graph. The ratio of the (R)ASE auto-correlations gave an efficiency of 47.6%, thus, we expect the RASE cross-correlation to be  $\sqrt{0.467} = 68.3\%$  of the ASE auto-correlation. We found that the RASE cross-correlation was actually 61% of the ASE auto-correlation, 88% of the expected value. The discrepancy suggests there was some classical noise in our ASE or RASE windows, and later we will see (Section 6.5) that this discrepancy could be attributed to phase noise between the ASE and RASE windows.

We can see that there was a very clear correlation between our ASE and RASE windows, and that there was no correlation between the ASE and our laser. To determine whether there is a non-classical correlation between the (R)ASE fields, we use the inseparability criterion [23, 48, 30], introduced in Section 2.7.5.

### 6.4.3 Inseparability criterion

Recall that the inseparability criterion (Section 2.7.5) introduced two entangled operators that were weighted sums of the quadratures from our ASE and RASE windows.

$$\hat{u} = \sqrt{b}I_A + \sqrt{1-b}I_R \quad (6.10)$$

$$\hat{v} = \sqrt{b}Q_A + \sqrt{1-b}Q_R \quad (6.11)$$

Where  $b$  was a weighting parameter between the ASE and RASE windows. The sum of the variances of these operators was  $\geq 2$  for a separable quantum state, assuming shot-noise-limited detection. However, our detection system was not shot-noise-limited, so we had to account for the heterodyne detector's electrical noise. If we assume that the electrical noise was not correlated with the light fields, then we can sum the shot noise and electrical noise. This changes the inequality to,

$$\sigma_u^2 + \sigma_v^2 \geq 2 + 2e, \quad (6.12)$$

where  $e$  was the electrical noise, equal to 0.66 vac units for the electrical noise clearance at the (R)ASE frequencies. Then the variance of the two operators,  $\hat{u}, \hat{v}$  can be written purely as the variance and co-variance of the ASE and RASE windows.

$$\langle \hat{u}^2 \rangle = b \langle I_A^2 \rangle + (1-b) \langle I_R^2 \rangle + 2\sqrt{b(1-b)} \langle I_A I_R \rangle \quad (6.13)$$

$$\langle \hat{v}^2 \rangle = b \langle Q_A^2 \rangle + (1-b) \langle Q_R^2 \rangle + 2\sqrt{b(1-b)} \langle -Q_A Q_R \rangle \quad (6.14)$$

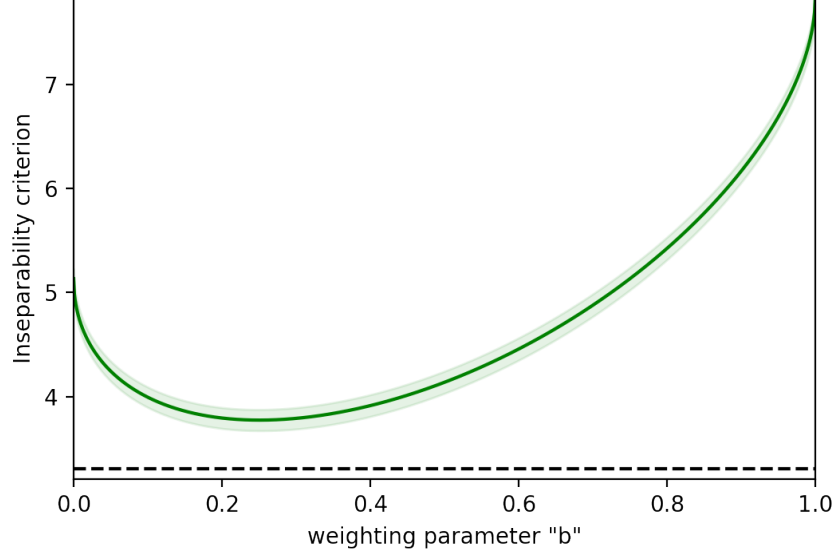


Figure 6.15: Inseparability line for the RASE data set, corrected for electrical noise. The effect of the electrical noise pushes the classical boundary to  $y = 3.31$  and the minimum for a maximally entangled state to 1.31 (from 0).

The co-variance matrix for each RASE shot can easily be found and is given in the form,

$$\text{CovMat} = \begin{bmatrix} \sigma_A^2 & \sigma_{AR} \cdot e^{i\theta} \\ \bar{\sigma}_{AR} \cdot e^{-i\theta} & \sigma_R^2 \end{bmatrix}. \quad (6.15)$$

The diagonal of this matrix was the variance of the ASE and RASE respectively.  $\sigma_{AR}$  was the magnitude of co-variance between the ASE and RASE windows, the  $e^{i\theta}$  term accounts for the phase difference between the ASE and RASE windows (and also appeared in Equation (6.6)). We apply a rotation correction factor to ensure the co-variance term was strictly real-negative, this accounts for the phase difference between the ASE and RASE windows.

We then calculate the inseparability criterion for a series of weighting values,  $b$ . Figure 6.15 shows the inseparability line and the classical boundary at 3.31. With an optimal  $b$  parameter of 0.24 and minimum dip of 3.78. Clearly, the inseparability line does not pass through the classical boundary. Indicating that the (R)ASE windows must have some uncorrelated classical noise. The evidence of classical noise was also given in the correlation measurements, Section 6.4.2, where the amplitude of the RASE correlation was 12% weaker than expected.

## 6.5 Characterising the classical noise

In this section, I determine the main source of classical noise in the RASE experiment. The magnitudes of these noise sources were measured to determine whether the noise sources could account for the lack of a non-classical correlation. The RASE protocol can demonstrate non-classicality because, previously, a non-classical correlation was shown between the ASE and RASE fields [30], in Pr:YSO, with a very stable experimental setup (outlined in Ferguson’s PhD thesis [29]).

I will examine the classical noise in the experiment under the two categories, phase and intensity noise. Intensity noise manifests in the experiment from laser intensity fluctuations, however, further intensity fluctuations can be introduced onto the laser by the various modulators in the experiment. The diagnostic measurements, from Section 6.2.1, were used to calculate the intensity noise at the heterodyne detectors, as well as the gain fluctuations on the ASE transition. In particular, the input pulse and reference pulses from the inverted-four-level echo data were examined. Phase noise can manifest in the experiment in three different ways: laser phase noise, atom phase noise (from fluctuating magnetic fields), and interferometer phase noise from mechanical vibrations in the experimental beam path. To measure the mechanical stability of the experiment, a homodyne interferometer was set up between the experiment and local oscillator beam paths. Interferometer measurements were repeated with the cryostat bypassed to determine the mechanical stability of the crystal in the magnetic field. Finally, the phase stability between the atoms and the laser was measured by recording a long free induction decay.

The top graph of Figure 6.16 shows the intensity of each reference pulse and the input pulse from the inverted-four-level echo. The bottom graph of Figure 6.16 shows the gain of the inverted-four-level, calculated from the intensity of the input pulse. In Section 6.2.1, we saw that the intensity of the reference pulses decreases across a set of 15 shots due to ensemble rethermalisation. To avoid this, only the first shot from each data set was analysed.

The top graph of Figure 6.16 shows that there was a significant amount of noise on the laser intensity recorded by the heterodyne detectors, 10s of percent across the data set. However, the gain of the inverted-four-level echo, which was also the ASE transition gain, stays consistent across the RASE shot,  $18.7 \pm 0.19$  dB. The gain only varied by 1% over the data set, and the intensity of the (R)ASE fields should only change by 0.19 dB (4.7%).

Figure 6.17 shows a histogram of phase drifts in the homodyne interferometer, recorded over a 200  $\mu$ s time period, for many shots. The orange and blue histograms show the phase noise with and without the cryostat bypassed, respectively. Clearly, the cryostat has mechanical instabilities, but the mechanical motion only equates to a phase drift of 0.03 radians over 200

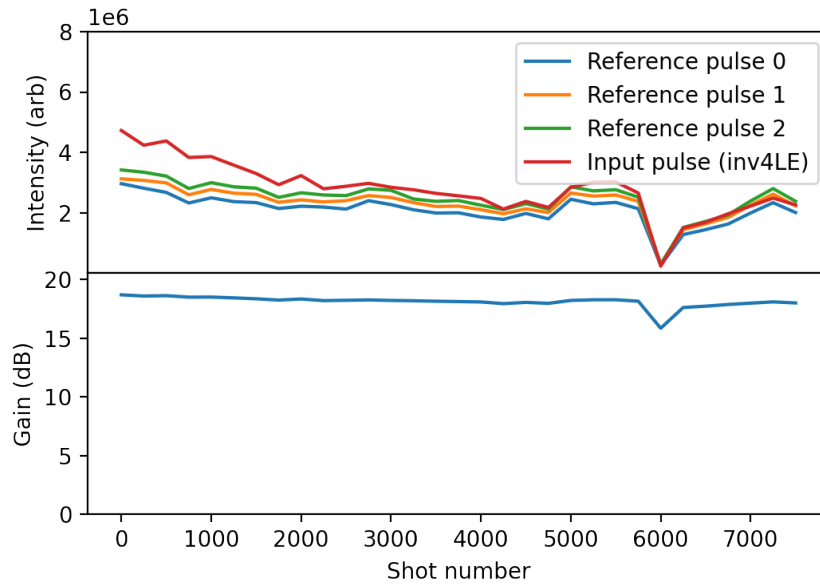


Figure 6.16: Intensity stability of the experiment during the non-classical RASE data set. The top graph shows the intensities of the three reference pulses along with the intensity of the input pulse (scaled by a factor of 0.1 to roughly match the reference pulse intensity). The bottom graph shows the gain on the inverted-four-level echo. Both graphs show the dip at shot 6,000 which also appears in the diagnostic measurements, Figure 6.4. Ignoring the outlier at shot 6,000, the gain is consistent across the data set,  $18.7 \pm 0.19$  dB, varying by only 1%.

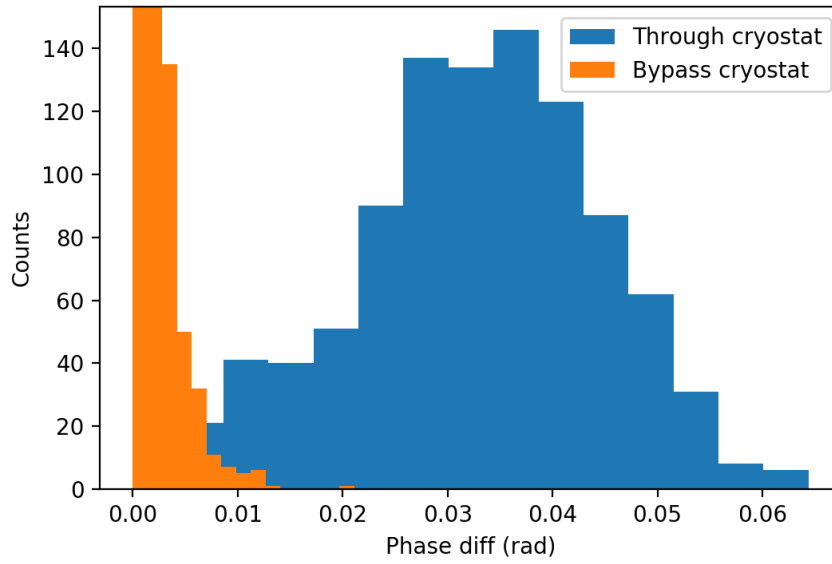


Figure 6.17: Data taken by Kieran Smith. Histogram of phase drift measurements over  $200\ \mu\text{s}$  time scales. Blue shows the phase drift when the probe was sent through the cryostat while orange shows the probe bypassing the cryostat.

$\mu\text{s}$ . The phase noise from the rest of the experimental beam path is much smaller, 0.002 radians over 200  $\mu\text{s}$ .

Figure 6.18 shows a 50  $\mu\text{s}$  long pulse resonant with the  $|+\frac{7}{2}\rangle_g \rightarrow |+\frac{7}{2}\rangle_e$  optical transition. The data was recorded with the heterodyne detectors and digitally beaten down to homodyne. The top graph of Figure 6.18 shows the quadrature values of the long probe sent through the crystal (from 40 – 90  $\mu\text{s}$ ). The free induction decay from this probe can be seen from 90 – 170  $\mu\text{s}$ . The middle graph shows the phase of the free induction decay, which clearly shows a phase modulation with an amplitude of 0.6 radians and a time period of 30  $\mu\text{s}$ . The bottom graph of Figure 6.18 shows the phase of another free induction decay where the laser frequency feedback gain was increased by 10 dB. This result indicates that the phase noise was injected onto the laser by the frequency feedback loop, which would mean that the 30  $\mu\text{s}$  phase modulation was not from the atoms.

We have seen that the ASE gain changes by 1% across the RASE data set. Exactly how intensity fluctuations affect the inseparability line is subtle. From equations (6.13) and (6.14), we know that the inseparability line is effected by the (R)ASE variances and the covariance. The ASE variance scales with gain, the RASE variance and covariance both scale with gain and the efficiency. As the (R)ASE variances increase, the inseparability line is shifted upwards, however, the covariance also increases, increasing the inseparability dip. These changes cancel each other, and the inseparability minimum does not change. Thus, the inseparability line is insensitive to intensity fluctuations, as long as the RASE efficiency does not change. However, if the RASE efficiency changes, then the optimal  $b$  value for the inseparability dip will also change. A RASE data set is averaged over many shots, efficiency fluctuations in the data set will cause the inseparability dip to be smoothed, which will increase the minimum of the inseparability line. From the intensity measurements, we will estimate how much the RASE efficiency should change across our data set. The intensity noise measurements show that the ASE gain only changes by 0.19 dB, 1% of the average ASE gain. We will assume that the rephasing  $\pi$ -pulses are affected similarly, thus the rephasing efficiency of the  $\pi$ -pulses should only change by 1% each. In the non-classical data set, the RASE efficiency was 47.6%, calculated from the correlation graphs in Section 6.4.2. Thus, the rephasing efficiency should change by 1%. RASE efficiency is also affected by the gain of the ASE transition, from Ledingham et al.'s model [49, 29]. Ledingham et al.'s model predicts the efficiency should change by 0.1% if the gain changes by 0.19 dB. Such small changes in efficiency will have very little effect on the inseparability line, especially compared to the measured phase noise. We can conclude that the classical noise is predominately phase noise.

From the phase noise measurements, there are three sources of phase noise. The phase stability of the experiment beam paths without the cryostat, which had  $< 0.01$  radians of phase noise over 200  $\mu\text{s}$  timescales. The

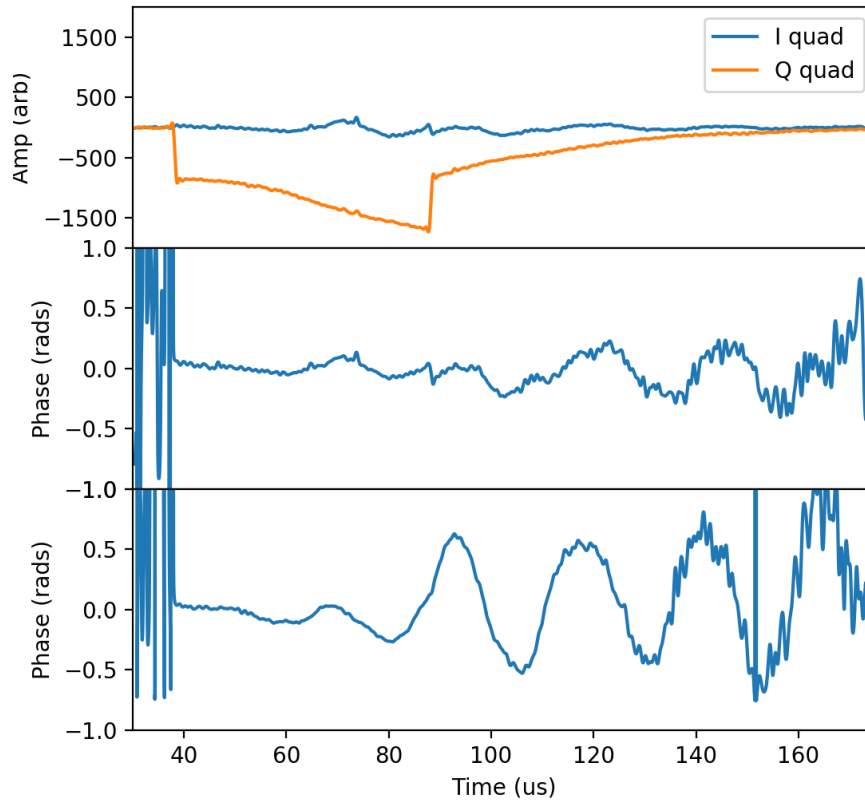


Figure 6.18: Phase stability of a free induction decay. The top figure shows the two quadratures of a free induction decay measurement. The middle figure shows the phase of the top figure. The bottom figure shows the phase of a free induction decay with the gain of the laser frequency feedback increased by 10 dB. The oscillation had a frequency of 30 kHz.



mechanical stability of the crystal inside the cryostat, which added 0.035 more radians of phase noise (over 200  $\mu\text{s}$ ) to the experiment. Recall that the (R)ASE time windows were separated by 9 – 49  $\mu\text{s}$ , which averages to 29  $\mu\text{s}$  (seen in Figure 6.1). The mechanical instabilities add 5 mrad of phase noise to the experiment during the RASE rephasing. This phase shift came from the crystal (and mirror mounted above the crystal) moving inside the cryostat. However, we must also consider that the crystal was moving in a magnetic field, which Zeeman shifts the atomic ensemble. Zeeman shifting will cause the ions to accumulate phase over the RASE storage. We can estimate the accumulated phase given the wavelength of the laser ( $\sim 1538$  nm), the Zeeman splitting of our ions (216 GHz/T, Table 2.3), and the 11.4 mT field gradient across the 3 mm long crystal (Section 5.2.3). The Zeeman splitting gives the frequency splitting of the upper Zeeman level, relative to the lower Zeeman level, thus, the Zeeman shift of one of these levels is 108 GHz/T. The Zeeman shift from the mechanical instabilities can be calculated as 500 Hz over 29  $\mu\text{s}$ . If we pessimistically assume that this 500 Hz shift occurs instantly after the ASE field is emitted, then the ions would accumulate 0.09 radians of phase noise over the 29  $\mu\text{s}$  storage time. In total, the mechanical instabilities have added  $0.095 \approx 0.1$  radians of phase noise to the experiment. Finally, the free induction decay shows a total phase noise of 0.6 radians over a 30  $\mu\text{s}$  time period. If we assume that 0.1 radians comes from the mechanical instabilities, then we also assume that the remaining 0.5 radians is injected into the laser from the laser locking frequency feedback. We are confident that most of the 30 kHz phase noise come from the laser locking feedback because when the locking gain was increased the phase noise also increased.

We have calculated that the majority of the classical noise is from laser phase noise (80%) and the remainder is from mechanical instabilities inside the cryostat. Next, I will model the inseparability criterion to see how much of an effect this noise had on the inseparability line.

### 6.5.1 Inseparability criterion modelling

I have extended Ferguson’s inseparability criterion model [29] to account for phase noise between the ASE and RASE windows. Ferguson’s model uses the ASE variance, rephasing efficiency, and light collection efficiency (from crystal to detector) to simulate the inseparability line. The inseparability line is calculated from the averaged variance of the ASE and RASE windows, along with the averaged covariance, across a RASE data set. The covariance of each RASE shot is a complex number,  $\sigma_{AR} = re^{i\theta}$ , where  $\theta$  is the phase between the ASE and RASE windows. Phase noise,  $\phi$ , in the experiment, will change the phase of the covariance to be  $\sigma_{AR}(n) = re^{i(\theta+\phi_n)}$ , for each shot in  $n$  shots of RASE data. Thus, the averaged magnitude of the covariance will decrease as a result of the phase noise. In the inseparability line,

the inseparability dip is governed by the covariance, thus, if the covariance decreases then the inseparability line minimum will increase.

A phase noise amplitude of 0.6 radians was used, from the FID measurements in Figure 6.18. Given the RASE time delay ( $9 - 49 \mu\text{s}$ ) was similar to the phase noise time period ( $30 \mu\text{s}$ ), we will assume that the phase noise has a Gaussian distribution. For simplicity, we will state that the ASE and RASE fields are in-phase, this will not change the magnitude of the covariance but will make the following equations simpler. The covariance for a single RASE shot is given by Equation (2.30) as,

$$\sigma_{AR} \propto A(\tau) * R(\tau - t).$$

Then the average covariance for  $n$  RASE shots with phase noise  $\phi$  will be,

$$\langle \sigma_{AR} \rangle = \frac{1}{n} \sum_{m=1}^n A(\tau) * R(\tau - t) e^{i\phi_m} \quad (6.16)$$

$$\langle \sigma_{AR} \rangle = \sigma_{AR} \cdot \frac{1}{n} \sum_{m=1}^n e^{i\phi_m}. \quad (6.17)$$

This means that the covariance is simply scaled by the average of  $e^{i\phi}$ , remember that  $\phi$  has a Gaussian distribution. The approximate scaling factor was numerically found for a phase noise of 0.6 radians as 0.835, in the separability criterion model the diagonal terms,  $\langle I_A I_R \rangle$  and  $\langle -Q_A Q_R \rangle$ , were scaled by this factor.

Figure 6.19 shows the inseparability line data from Figure 6.15 along with the modelled inseparability line. The blue line shows the expected inseparability line if there was no phase noise, clearly below the classical boundary. The shaded line shows the inseparability line with phase noise, I have used a shaded line because the phase noise can change depending on the laser locking settings. The laser locking settings were optimised on a day-to-day basis, thus, the phase noise can change from day to day. The black line shows the maximum phase noise that still gives a non-classical result, 0.39 radians. Finally, the red line shows the inseparability dip if the laser phase noise is completely removed, leaving the 0.1 radians of phase noise from the mechanical instabilities in the experiment. In theory, decreasing the phase noise by a factor of two, to 0.39 radians, would be enough to give a non-classical result, however, this assumes that there are no other unaccounted sources of classical noise. If the laser phase noise was completely removed then, by current measurements, the next largest source of phase noise is the 0.1 radians from mechanical instabilities in the cryostat, Figure 6.17. By lowering the phase noise to this level the inseparability dip would match the no phase noise, blue line, dip to within a few percent.

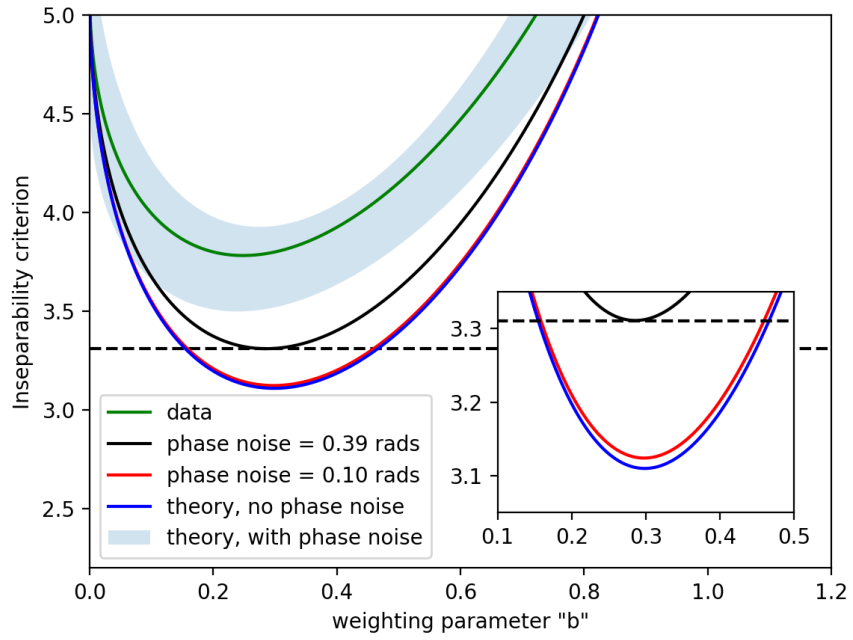


Figure 6.19: Modelling the inseparability criterion for the RASE experiments. Collection efficiency: 10.5% (includes fibre coupling, cryostat window reflection, and detector quantum efficiency), rephasing efficiency: 40%, ASE variance: 13 shot noise units, and phase noise of 0.6 radians. The green line shows the inseparability line data from Figure 6.15, the shaded line shows the predicted inseparability line give the measured phase noise. The inset zooms on the red and blue lines, so that the red line can be seen. The classical boundary is shown at  $y = 3.31$ .

From the data, and modelling, shown here, it is fairly conclusive that the classical noise seen on the RASE data is due to phase instabilities between the erbium ions and the laser. More specifically, the phase instability is derived from an oscillation in our laser-locking frequency feedback loop. The phase instability on the free induction decay also has the same amplitude and time period that we expect from the classical noise seen on the RASE data. Unfortunately, we cannot simply turn down the gain on the laser frequency feedback, as we need the high gain to null low frequency noise. The proposed solution is to add a second stage of frequency feedback to suppress the higher frequency oscillations. This will be achieved by adding a phase modulator (EOM) into the feedback. If the laser locking is improved, removing 0.5 radian phase noise, then we expect to see a non-classical result. Non-classical RASE has been shown previously, in Ferguson et al. [30], so we know that non-classical RASE is achievable. Furthermore, Ferguson's RASE demonstration was limited to an efficiency of 3%, given we can achieve an efficiency that is an order of magnitude higher, we expect to show a greater dip below the non-classical line.

As a final note, the AFC experiment was able to demonstrate a non-classical result, while the RASE experiment could not. The two main differences between the AFC data and the RASE data comes from the storage times and intensity of the signals. The RASE experiment has a storage time of 9 - 40  $\mu\text{s}$ , relative to the 0.66  $\mu\text{s}$  for the AFC. The pulse stored in the AFC experiments was 0.8 photons, relative to the 12 photon ASE signal. The difference in storage times means that the RASE experiment is 40 times more sensitive to phase noise, and the difference in signal intensity means that any classical noise in the RASE experiment will be over 10 times larger. Thus, the classical noise in the RASE experiment will be almost 400 times larger than the AFC experiment. For this reason, the AFC experiment can show a non-classical result, while the RASE experiment did not.

## 6.6 Summary

To summarise, a series of RASE experiments have been shown. The classical results are very promising with very high rephasing efficiency, 47%, a spin state storage time of 27  $\mu\text{s}$ , and the ability to store 40 temporal modes. Currently, this is the second-highest efficiency in a free space solid-state memory, beaten by Hedges et al. [57] at 69%, but this demonstration is also the most efficient memory using spin-state storage in a solid-state memory. Other high efficiency free space memories are AFC demonstrations, 35% efficiency [4, 17], and ROSE demonstrations, 40% efficiency [18]. The correlations between the ASE and RASE fields are strong, and the lack of correlation between subsequent shots of data indicated that the ASE and RASE fields are derived from an amplified vacuum state. However, non-classical storage

has yet to be shown. The current limitation here is phase noise on our laser from the frequency feedback loop. This is not a physical limitation of the experiment and can be removed. As such, the experiment can be improved, reducing the phase noise. If these experimental changes can be implemented, we should have the most efficient non-classical memory in rare earth ions, with spin state storage and compatibility with the telecommunications infrastructure.



## Chapter 7

# Conclusion

The goal of this thesis was to determine whether  $^{167}\text{Er}^{3+}:\text{Y}_2\text{SiO}_5$  can be used to create a quantum memory appropriate for quantum repeater demonstrations. In this thesis, I have shown a new spectral preparation technique that creates optical features for a quantum memory using  $^{167}\text{Er}^{3+}:\text{Y}_2\text{SiO}_5$ . Using this preparation technique, two quantum memory protocols were demonstrated, the Atomic Frequency Comb (AFC) and Rephased Amplified Spontaneous Emission (RASE).

In the AFC experiments, non-classical storage was demonstrated, with an efficiency of 22% and a storage time of 0.66  $\mu\text{s}$  (Section 4.5). This efficiency was an order of magnitude larger than previous erbium based memory demonstrations [61, 47]. The higher memory efficiency was a result of the preparation process, which prepared an AFC with an absorption contrast of 40:1. However, the AFC efficiency was still limited by background absorption in the AFC, due to  $^{167}\text{Er}$  ions. Further improvements to the preparation sequence could remove the  $^{167}\text{Er}$  ions. This would make background absorption due to the isotopic impurities the limiting factor for the AFC efficiency. Implementing an optimised preparation sequence would increase the AFC efficiency to 35% (Section 4.5.3). Cavity enhancement will be needed to further improve the efficiency. Section 4.7 showed that an efficiency of 96.6% is theoretically possible with an impedance matched cavity.

In the RASE experiments, an efficiency of 47% was shown with storage times up to 27  $\mu\text{s}$  (Section 6.3). The RASE chapter also showed that 40 temporal modes could be stored in the memory (Section 6.3). However, the RASE experiments were not non-classical due to phase noise on the laser (Section 6.5). We are confident that removing this phase noise from the laser will lead to a non-classical demonstration, as a non-classical demonstration has already been demonstrated in Pr:YSO [30].

From the AFC chapter discussion, an efficiency of 88% and 96% could be achieved through cavity enhancement with a modest finesse of 11 and 38, respectively, Section 4.7.2. These finesse values are quite low and easy

to engineer. We can calculate the size of our cavity as well if we know the desired bandwidth of the cavity. The splitting between (R)ASE fields would limit the bandwidth to 96 MHz, but we will round to 100 MHz. The bandwidth of our cavity would need to be 200 MHz, 100 MHz bandwidth for both the ASE and RASE fields. This gives a Free Spectral Range (FSR) of 2 – 8 GHz, depending on the exact finesse of the cavity. The length of this cavity would be 15 – 3.7 cm, in free space. This is reasonable as the larger cavity length could fit in our cryostat’s sample space and the smaller cavity length is still larger than our 3 mm wide crystal. These finesse values were calculated for a cavity-enhanced AFC, the finesse for cavity-enhanced RASE would be different, the values used here were only used to estimate the size and FSR of the cavity and show that such a cavity would work in the current experiment.

Another requirement of cavity enhancement is that the cavity must not affect the inversion or rephasing  $\pi$ -pulses. Historically, cavity enhanced storage demonstrations have solved this problem by spatially separating the control pulses from the cavity spatial mode [45, 69, 70, 13, 44]. There are other options, such as: using a polarisation dependant cavity and setting the control pulses to an orthogonal polarisation [39], Q-switching the cavity during the control pulses, or using narrow bandwidth mirrors like fibre-Bragg gratings. One proposed cavity design uses all-in fibre components. The all-in fibre design would use Bragg grating reflectors as the cavity mirrors and gradient refractive index (GRIN) lens to control the beam focus through the crystal. Two of these fibres will be glued to either side of the crystal, the light exiting one fibre will focus in the center of the crystal and then couple directly into the second fibre. There are several reasons to use a fibre cavity of this design.

- High collection efficiency. Currently, the collection efficiency of the experiment, from crystal to detector, is 10%, Section 6.5.1. The main losses in the light collection are from reflections off of the three cryostat windows and coupling back into a single mode fibre. A fibre cavity would couple light directly in and out of the crystal, bypassing all the free space optics in the experiment. Such a cavity could increase the collection efficiency to  $> 90\%$ .
- Reduced magnetic field gradient, from using a thin crystal. Cavity enhancement uses thin crystals to lower the optical depth of the ensemble [60]. In the inverted-four-level echo experiments, evidence of a magnetic field gradient was observed in the four-level coherence time, Section 5.2.2. Using a thinner crystal will also reduce the effects of magnetic field gradients, which should increase the four-level coherence time.
- No optical alignment needed. An all in fibre design requires no optical



alignment. However, a cavity placed in a cryostat will contract as the cavity is cooled, causing the cavity to misalign. The cavity will have to be purposely misaligned at room temperature such that the cavity aligns once cooled to 1.4 K.

- Reduced distortion on the inverse and rephasing  $\pi$ -pulses (for RASE). In the RASE and inverted-four-level echo experiments, the rephasing efficiency decreased above a gain of  $\alpha L = 3$ , Section 6.3. This was attributed to the large optical depth distorting the rephasing  $\pi$ -pulses. A lower optical depth means that  $\pi$ -pulses distortion will be reduced. This will increase the efficiency of each  $\pi$ -pulse, which will also increase the total rephasing efficiency.

Finally, the storage time can be increased by implementing hyperfine rephasing. Hyperfine rephasing has already been demonstrated in this crystal by Rančić et al. [59], with a coherence time of 1.3 seconds. In Rančić's demonstration, Raman echoes were demonstrated with optical pulses. In future experiments, the hyperfine levels will be driven directly using a resonant RF coil.

In summary, this thesis presents an ensemble preparation technique that has been used to show two initial quantum memory demonstrations. The initial results present a moderate efficiency, storage time, and mode capacity. There is also a pathway to an optimised experiment that uses cavity-enhancement and RF rephasing that could achieve efficiencies of 96% with 1.3 second storage times. A memory of this design could be used in an initial quantum repeater demonstration.



# Appendices



## Appendix A

### EDFA pulsed gain

An erbium doped fibre amplifier (EDFA) is a device containing an erbium doped fibre and a pump laser resonant with the 980 nm erbium transition,  $I_{15/2} \rightarrow I_{11/2}$ . The pump laser drives erbium ions into the  $I_{11/2}$  level where they then decay, non-radiatively, to the  $I_{13/2}$ . This process creates an inverted population centered on the telecommunications wavelength, 1550 nm, with a very broad bandwidth due to the extremely broad linewidth ( $\sim$  THz / 10s of nm) of room temperature erbium ions. Light coupled into the erbium doped fibre that is resonant with the  $I_{15/2} \rightarrow I_{13/2}$  transition is then amplified by the inverted population. The amplification can be directly controlled by the current of the pump laser. Finally, the 980 nm pump is filtered on the output of the EDFA.

EDFA's also exhibit interesting non-linear performance due to the excited state lifetime of the erbium ions in the doped fibre. If there is no input to an EDFA, the amount of erbium ions in the  $I_{13/2}$ 's level will be greater than when there is a CW signal passing through the EDFA, driving the population to the ground state. The gain of an EDFA can be much higher for pulsed light, than for CW light, because of this. This will be true as long as the time between pulses is long compared to erbium's excited state lifetime.

Figure A.1 shows the output of an EDFA for 1 ms long pulses. The output of the EDFA was 1 mW when the laser was not pulsed. By gating this signal for times comparable to the  $I_{13/2}$ 's lifetime (10 ms), the initial output power can exceed 5 mW, the intensity then decays down to the steady state level of 1 mW.

Figures A.2 and A.3 show the output of an EDFA when the RASE pulse sequence was sent through, each graph shows two different steady state output power levels, 2.5 and 10 mW, respectively. From these two graphs, we see that the peak power can spike to extremes, 50 mW for a 2.5 mW CW output and 300 mW for a 10 mW CW output. This is of particular importance as CW output powers can be safe, but fast pulses can reach damage thresholds

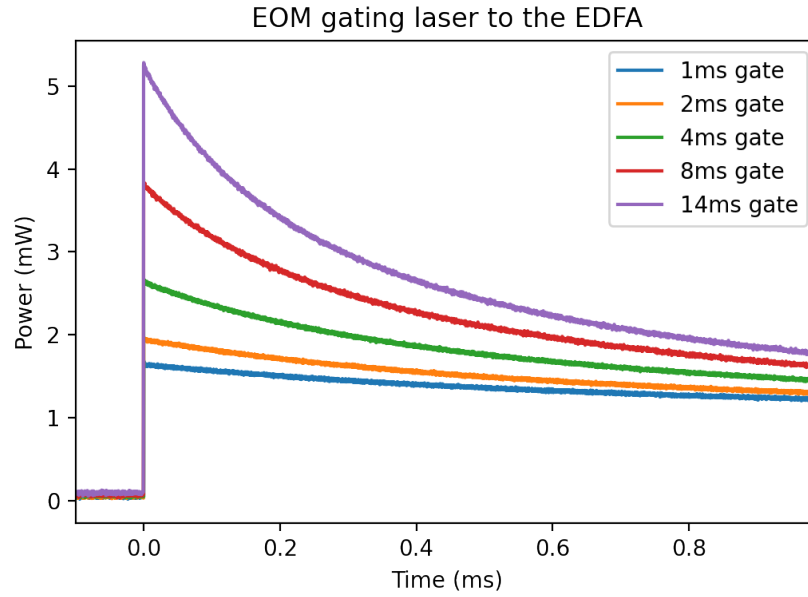


Figure A.1: Output of an EDFA with the laser gated by an AM-EOM. Steady state output power was 1 mW. The instantaneous gain of the EDFA increases, up to a maximum of 5 mW.

for optical fibres. The intensity ratio of  $\pi_1$  and  $\pi_2$  changes between the 2.5 and 10 mW graphs. This means that any optimisations, such as  $\pi$ -pulse duration, will not scale linearly between low and high EDFA powers.

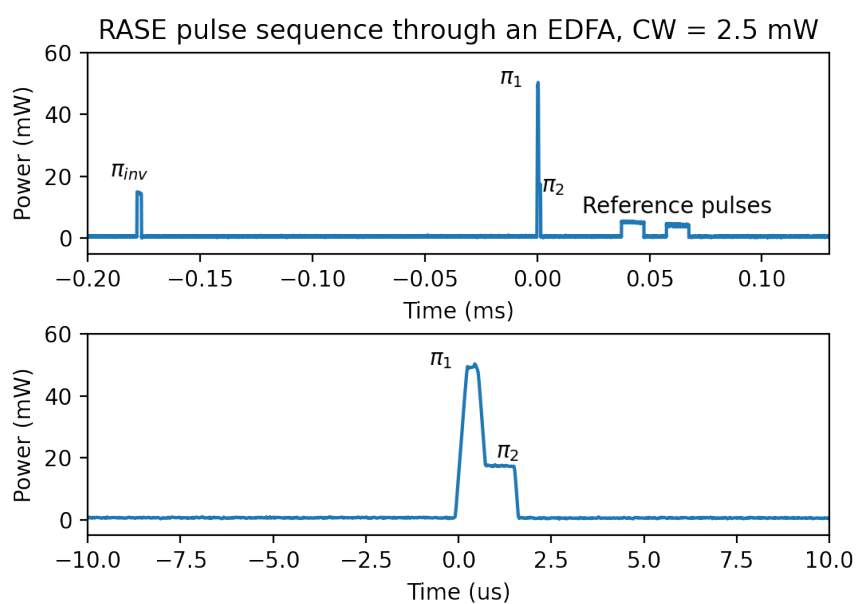


Figure A.2: Output of the EDFA when the RASE pulse sequence is sent through, the CW output power was 2.5 mW. The EDFA was allowed to reach maximum gain (no light input for many erbium lifetimes) before the RASE sequence was sent through.

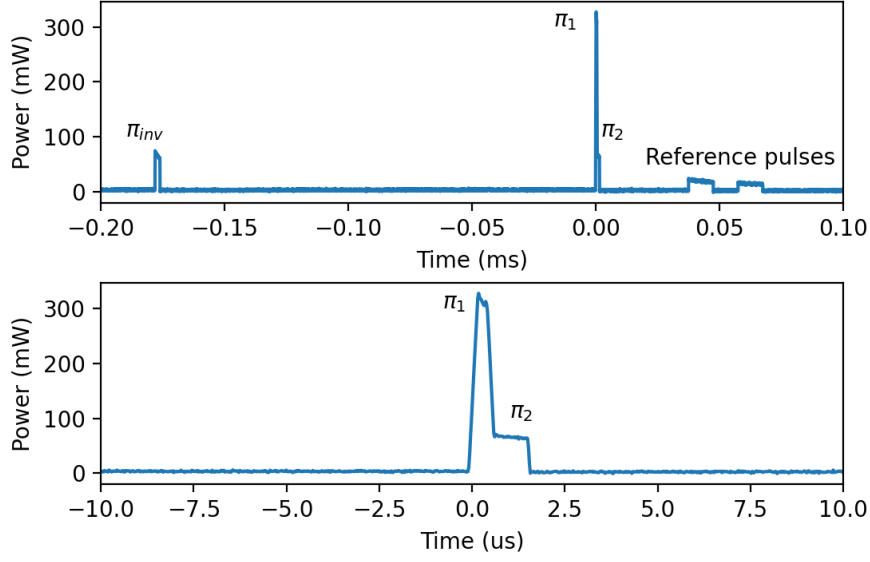


Figure A.3: Output of the EDFA when the RASE pulse sequence is sent through, this time with a CW output power of 10 mW. This graph really indicates the non-linearity of the EDFA pulse gain, as the ratio between the power of  $\pi_1$  and  $\pi_2$  is much larger than in Figure A.2. We can also see the gain depopulates much fast with the higher CW power as the intensity of the  $\pi$ -pulses decays across the  $\pi$ -pulse.



## Appendix B

# AWG spurious signals

As mentioned in Section 3.8, the stable laser was used to prepare optical features and then performs pulse sequences on those optical features. A side-band of the laser was controlled via an AM-EOM using an AWG. An AWG uses a direct digital synthesizer and a digital-to-analog converted (DAC) to read a user defined waveform from memory and convert it directly into an RF waveform. The waveform is played at a rate defined by the clock rate of the AWG. These devices are extremely flexible and can allow any waveform to be played, so long as the frequency of the waveform is lower than half the clock rate of the AWG (the Nyquist frequency) (there are techniques that allow you to play frequencies above this, but that is not important here). There are several issues that can arise from using an AWG, typically in the form of noise or extra harmonics beyond a typical analog RF source.

In Section 5.2 coherence measurements were recorded using relatively strong input pulses. The large signals recorded meant that the noise levels of the AWG were not noticeable. In the ASE and RASE sections (Sections 5.5 and 6.3), the intensities of the ASE and RASE signals were much weaker, near the single photon level. Here, the noise and harmonic signals of the AWG were an issue. I have documented some of these spurious signals and solutions to minimise spurious signals for the RASE experiments.

The main issue with the AWG is that the signal is produced digitally, with a vertical resolution of 8-bits. This means that the waveform produced by the AWG is segmented into 255 voltage levels. Spurious signals can be produced due to non-linear interactions between electrical components in the AWG, (DACs, mixers, and amplifiers) and the amplitude of these spurious signals scales with the vertical resolution of the AWG. The intensity of spurious signals can be up to  $(1/2^{\text{bits} \times 2})^{\text{th}}$  the intensity of the waveform.

We use this to estimate the intensity of the spurious signals in our experiment. Typically,  $\pi$ -pulses are  $\mathcal{O}(1)$   $\mu\text{s}$  at  $\mathcal{O}(1)$  mW of optical power, which translates to  $10^{10}$  photons per  $\pi$ -pulse. Then, for an 8-bit AWG, the RF spurs created during a  $\pi$ -pulse will be  $\leq 10^{10}/2^{2 \times 8} (\approx 100,000)$  photons.

While the strongest spurs will be  $\mathcal{O}(100,000)$  photons, there is also a discrete spectrum of weaker spurs. If any of these spurs overlap with our ASE or RASE spectra, then this can cause false positives with ASE / RASE detections. However, because the spurs are created by a non-linear interaction in the AWG, a small change in frequency can cause a chaotic change in the spectra of the spurs.

For future experiments, an AWG with higher vertical resolution can be used. A technical document written by Tabor [50] shows that for our AWG, a vertical resolution of 14-bits gives spurious noise levels comparable to thermal noise when operating at 25°C. At this level, the spurious signals would be  $10^{10}/2^{28} \leq 10 - 100$  photons. While this is still not perfect, suppressing the spurs by 3 orders of magnitude will remove most of the spurs shown in Figure 5.13.

There are also several techniques that can be employed to limit the intensity of these spurs.

1. Digitise the frequency of the waveforms. Let us create a simple sine wave waveform that is 1 ms long. If the sine wave has a frequency that is not an integer multiple of 1 kHz, then there will be a discontinuity between the end and start of the waveform. In this case, ensuring that the frequencies used in the waveform are multiples of 1 kHz will reduce spurs.
2. Using long waveforms. A waveform that is a simple 1 MHz sine wave can be as short as 1  $\mu$ s. Using long waveforms, e.g. 1 ms long, with many oscillations also reduces the intensity of spurs. However, this technique cannot always be employed, as sometimes waveforms are required to be a certain duration.
3. Use prime numbers of oscillations. This technique was not used in these experiments, but the Tabor technical document [50] does state that using long waveforms with prime number oscillations will also reduce the intensity of spurs.
4. Avoiding aliasing. While the maximum frequency of an AWG is the Nyquist frequency, as you approach the Nyquist frequency, aliasing becomes a bigger issue. In the frequency domain, you see signals appearing symmetric about the Nyquist frequency. e.g. If the Nyquist frequency is 5 GHz and a waveform of 4.5 GHz is played, then a second signal at 5.5 GHz will also be present. Included with this, spurs can also appear at  $>5$  GHz. To avoid this, an AWG can be played at a lower frequency and mixed up to a higher frequency. Some AWG's include NCO's (Numerically Controlled Oscillators) which will digitally

mixed and upscale the AWG frequency. This technique was employed with the ADS7-V2 AWG in the AFC experiments, as this AWG had a lower Nyquist frequency (2.5 GHz).



## Appendix C

# Erbium holeburning simulation

This section details a simulation that was developed in python to simulate the lineshape and spectral holeburning of  $^{167}\text{Er}^{3+}:\text{Y}_2\text{SiO}_5$ . The modelling of the erbium lineshape is built upon data collected by myself and Rančić [58]. This simulation uses oscillator strengths measurements (at 7 T), hyperfine splitting measurements (at 6 and 7 T) to numerically solve rate equations that simulate the populations of hyperfine levels given a perturbing laser. This simulation has been used to simulate spin polarisation, spectral holeburning, and the selective anti-polarisation technique. It can also approximate the splittings of optical transitions at fields beyond 6 or 7 T by linearly interpolating the 6, 7 T hyperfine splitting data.

### C.1 Data used in the simulation

nuclear spin	ground level (MHz)	excited level (MHz)
$-\frac{7}{2}\rangle$	0	0
$-\frac{5}{2}\rangle$	997.1	993.1
$-\frac{3}{2}\rangle$	1942.2	1965.2
$-\frac{1}{2}\rangle$	2841.3	2917.9
$+\frac{1}{2}\rangle$	3701.6	3852.5
$+\frac{3}{2}\rangle$	4531.1	4770.7
$+\frac{5}{2}\rangle$	5338.9	5673.8
$+\frac{7}{2}\rangle$	6134.4	6562.6

Table C.1: Hyperfine energy levels for both the ground and excited levels, relative to the  $|\frac{7}{2}\rangle$ , 7 T.

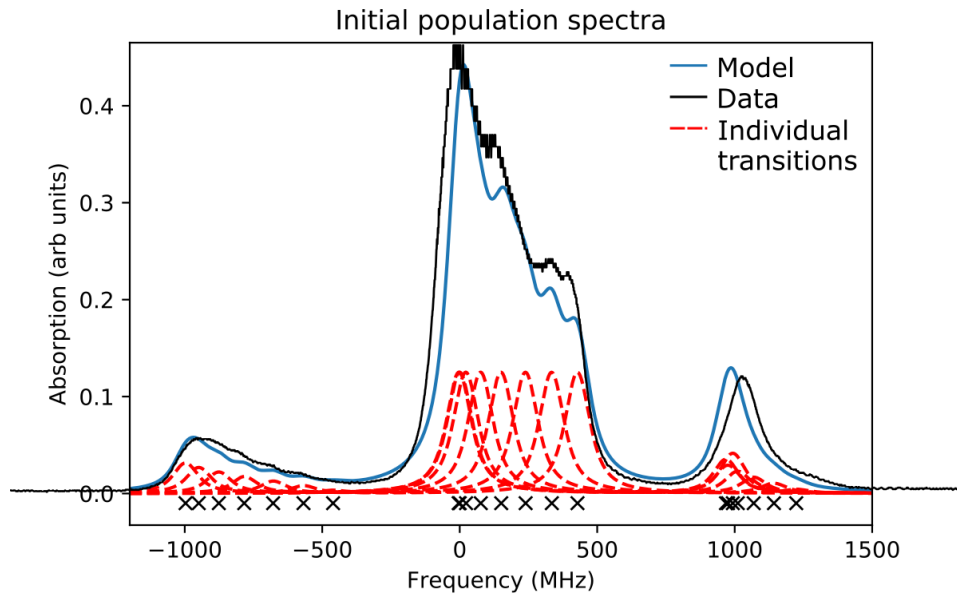


Figure C.1: Comparing the spectra generated from the model with all hyperfine levels equally populated to data taken by Milos at 7 T. The red dashes show the individual optical transitions. The level structure looks slightly different, however all the peaks seem to align fairly well.

nuclear spin	ground level (MHz)	excited level (MHz)
$-\frac{7}{2}g$	0	0
$-\frac{5}{2}g$	985.2	990.0
$-\frac{3}{2}g$	1920.6	1959.5
$-\frac{1}{2}g$	2812.2	2909.9
$+\frac{1}{2}g$	3667.0	3842.8
$+\frac{3}{2}g$	4493.0	4759.6
$+\frac{5}{2}g$	5298.7	5661.1
$+\frac{7}{2}g$	6093.0	6548.9

Table C.2: Hyperfine energy levels for both the ground and excited levels, relative to the  $-\frac{7}{2}$ , 6 T.

state:	$-\frac{7}{2}e$	$-\frac{5}{2}e$	$-\frac{3}{2}e$	$-\frac{1}{2}e$	$+\frac{1}{2}e$	$+\frac{3}{2}e$	$+\frac{5}{2}e$	$+\frac{7}{2}e$
$-\frac{7}{2}g$	0.752	0.248						
$-\frac{5}{2}g$	0.163	0.653	0.183					
$-\frac{3}{2}g$		0.147	0.693	0.160				
$-\frac{1}{2}g$			0.129	0.737	0.134			
$+\frac{1}{2}g$				0.108	0.788	0.104		
$+\frac{3}{2}g$					0.085	0.846	0.07	
$+\frac{5}{2}g$						0.057	0.913	0.03
$+\frac{7}{2}g$							0.024	0.976

Table C.3: 8 x 8 matrix of known relative oscillator strengths. These values were initially published in Rančić's thesis [58] with the diagonal values as 1. Here, I have normalised them such that each hyperfine level's oscillator strengths will sum to 1.

## C.2 Simulating the level structure

Figure C.1 shows the spectrum generated from the above energy level and oscillator strength data, with a recorded spectrum overlaid. The lineshape used in this model is the same used in Milos's thesis, a Voigt profile with a Gaussian width of 45 MHz and a Lorentzian width of 45 MHz. The model takes in a  $1 \times 8$  array for the initial population of each hyperfine level. When the initial population array is an array of ones, the spectra shown in Figure C.1 is generated (the thermal spectrum). From here a laser (l) can hole burn the spectra, this laser has parameters for the center frequency, linewidth, intensity, and line shape. When a laser interacts with the spectrum atoms are driven to the excited state. The atoms can relax back to a ground state. The branching ratios for optical decay were assumed to be the same as the optical transitions relative oscillator strengths. Every atom that relaxes back to the ground state has a probability to create a resonant phonon. This

phonon will cause a random  $\pm 1$  nuclear spin flip. Currently, there is no hyperfine cross-relaxation in the model, as the hyperfine levels have a much longer lifetime ( $>100$  s) than typical holeburning simulations ( $\sim 100$  ms).

When simulating spectral hole burning, the model steps through every possible optical transition (all 64 of them) if the oscillator strength is not known ( $|\Delta m_I| \geq 2$ ) the transition is skipped. For all other transitions ( $\Delta m_I = -1, 0, 1$ ) the following dynamic equations are used:

$$\begin{aligned}\Delta g(f, h) &= \sigma(h) \cdot l(f) \cdot g(f, h, t) \cdot \Delta t, \\ \Delta e(f, h) &= (1 - e^{\Delta t/t_0}) \cdot e(f, h, t), \\ g(f, h, t+1) &= g(f, h, t) - \Delta g(f, h) + \sum_{h_i} \Delta e(f, h_i, t) \cdot \sigma(h_i), \\ e(f, h, t+1) &= e(f, h, t) - \Delta e(f, h) + \sum_{h_i} \Delta g(f, h_i, t).\end{aligned}$$

These equations follow a basic population growth rate equation with multiple paths of populations to enter/ leave a given hyperfine level, where  $f$  is frequency,  $h$  is the hyperfine level, and  $t$  is time.  $\Delta g$  is the population leaving the ground state due to the laser and is the product of the laser intensity ( $l$ ), the amount of population initially in the ground state  $g$ , and the oscillator strength ( $\sigma$ ) of the optical transition.  $\Delta e$  is the population leaving the excited state due to spontaneous decay and is only governed by the decay rate  $t_0$ . Then the change in population of a ground state hyperfine level ( $g$ ) between two time steps is governed by the amount of population leaving said level due to the perturbing laser ( $\Delta g$ ), and the population entering from a given excited state level (summed over all excited state levels). Similarly, the change in excited state population is governed by the amount of population decaying from that excited state and the population entering all possible ground states.

### C.3 Other simulations



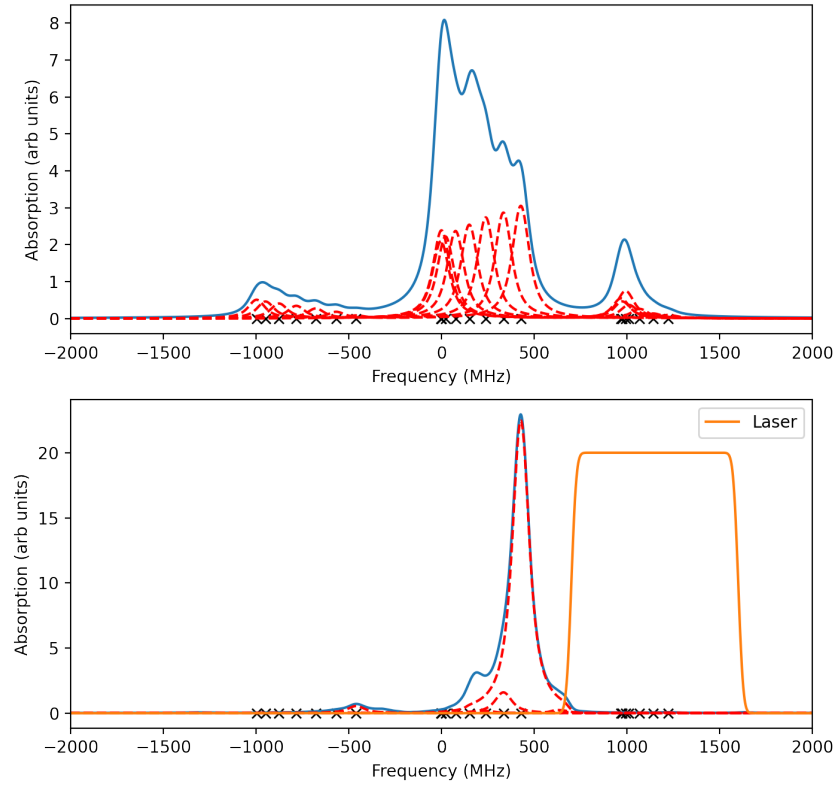


Figure C.2: Simulation example, spin polarisation. Top: Thermal spectra. Bottom: Spin polarised spectra. This example used a wide laser covering the entire  $\Delta m_I = 1$  feature, as expected the majority of the atoms have been driven into the  $|+\frac{7}{2}\rangle_g$  hyperfine level.

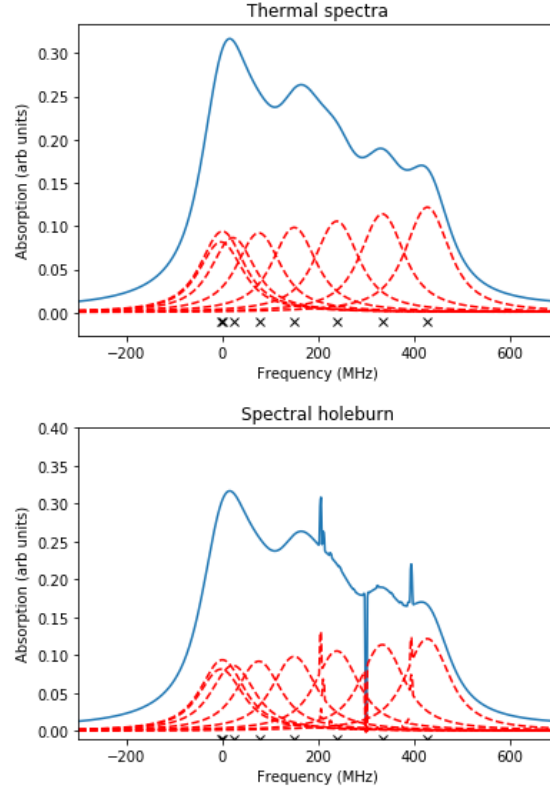


Figure C.3: Simulation example, spectral hole burning. Top: Thermal spectra. Bottom: hole burnt spectra. This example used a two MHz wide laser to burn a hole at 300 MHz, roughly in between the  $|+\frac{5}{2}\rangle_g$  and  $|+\frac{3}{2}\rangle_g$  hyperfine levels of the  $\Delta m_I = 0$ . We can also see the interesting anti-hole structure surrounding the spectral hole.

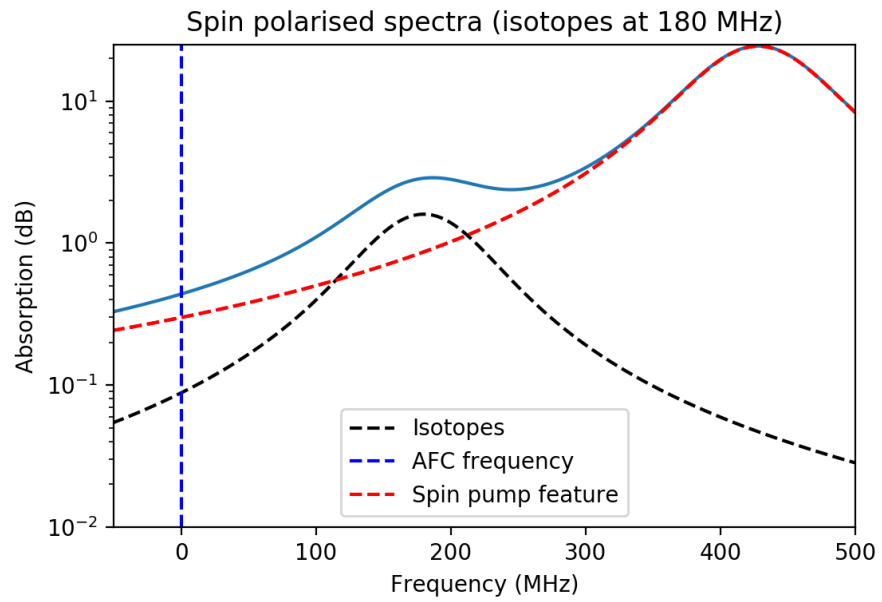


Figure C.4: Simulating the spin pumping background absorption for the AFC, Section 4.5. Spin pump line: 0.3 dB, Isotope line: 0.08 dB at zero MHz, the AFC frequency.



## Appendix D

### Phase correction accuracy

In both the AFC and RASE non-classical experiments, sets of reference pulses are used to correct for time delays between the probe and local oscillator for our heterodyne beam paths and ‘clock jitter’ from desynchronised RF clocks in our experiment, Section 4.6.1. Time delays between probe and local oscillator manifest as phase delays in our data, while clock jitter manifests as a time delay. To measure and correct for both time and phase delays, we require at least two reference pulses at distinct frequencies, as was used in the AFC experiment, Section 4.6. However, if three reference pulses are used, then the accuracy of this correction can be measured. This was mentioned but not discussed in the RASE experiment chapter, Section 6.4.2. We check the accuracy of the phase correction by applying the correction algorithm to a data set using only two of the reference pulses and then measuring the phase of the third reference pulse. If the correction algorithm was perfect then in every shot of our data set the third reference pulse will have identical phases, i.e. the correction algorithm will have perfectly corrected an unknown signal. Below, I show the correction accuracy from a RASE data set.

I take the first 500 shots from a RASE data set. Each shot of RASE data contains three reference pulses, Figure D.1, with frequencies of 25,  $-21$ , and 11 MHz at times 90, 110, and 130  $\mu\text{s}$  respectively. Then I run the correction algorithm three times, each time using different pairs of the three reference pulses. Finally, the phase of the unused reference pulse is calculated using the methods discussed in Section 4.6.1.

Figure D.2 shows the results of the three phase corrections. The top, middle, and bottom graphs all show the distribution of phases for each of the reference pulses (25,  $-21$ , and 11) MHz, where the phase correction algorithm was run using the ( $[-21, 11]$ ,  $[25, 11]$ ,  $[25, -21]$ ) MHz reference pulses. Blue shows the phases of the uncorrected reference pulse which is evenly, and randomly, distributed about  $2\pi$  radians. Orange shows the phases of the corrected reference pulse which, on this scale, is almost a single bar

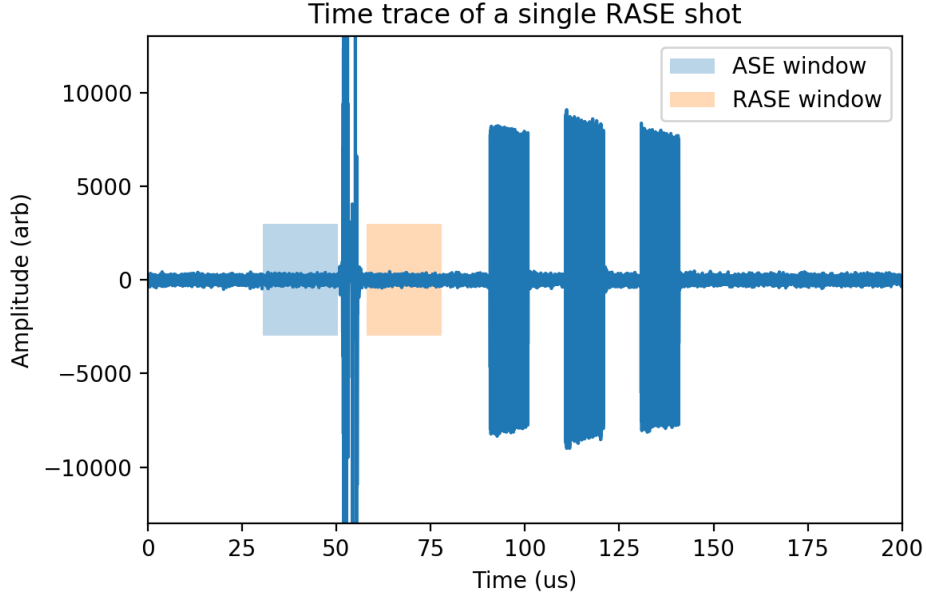


Figure D.1: Time trace of a RASE data set. Each RASE shot contains three reference pulses with frequencies: 25,  $-21$ , and 11 MHz at times: 95, 115, 135  $\mu\text{s}$ .

wide. Note that the reference pulses, by chance, happen to have phases near 0, the reference pulses can have any arbitrary phase.

Figure D.3 shows the bottom bar graph of Figure D.2 zoomed with a Gaussian fitted to the corrected phase data. I choose the bottom graph as it appeared to have the widest distribution of the graphs from the above figure, thus this should underestimate the accuracy of the phase correction. The fitted Gaussian has a FWHM of 38 mrad (roughly  $2^\circ$ ).

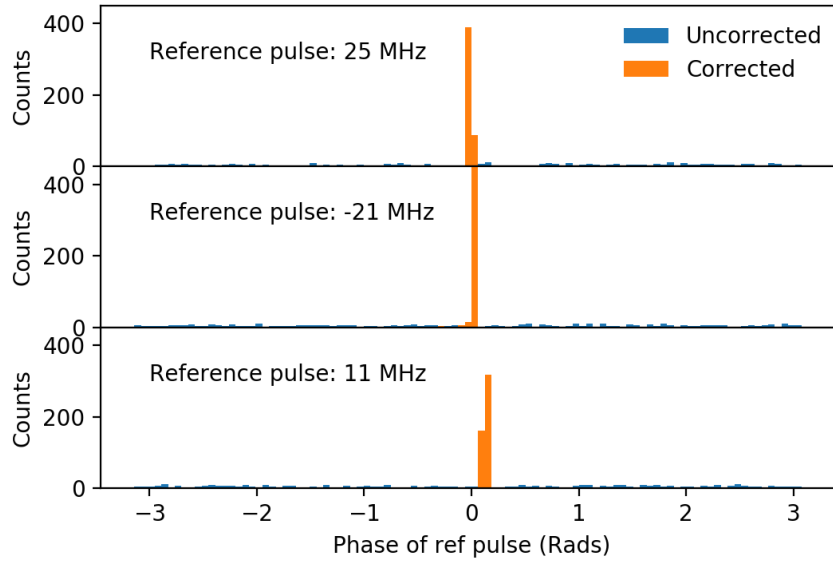


Figure D.2: Bar graphs showing the phases of a reference pulse pre- and post-phase correction, given that the correction algorithm was run using the two other reference pulses. The data set used here was the first 500 shots from the RASE data set used in the RASE correlation section, Section 6.4.2.

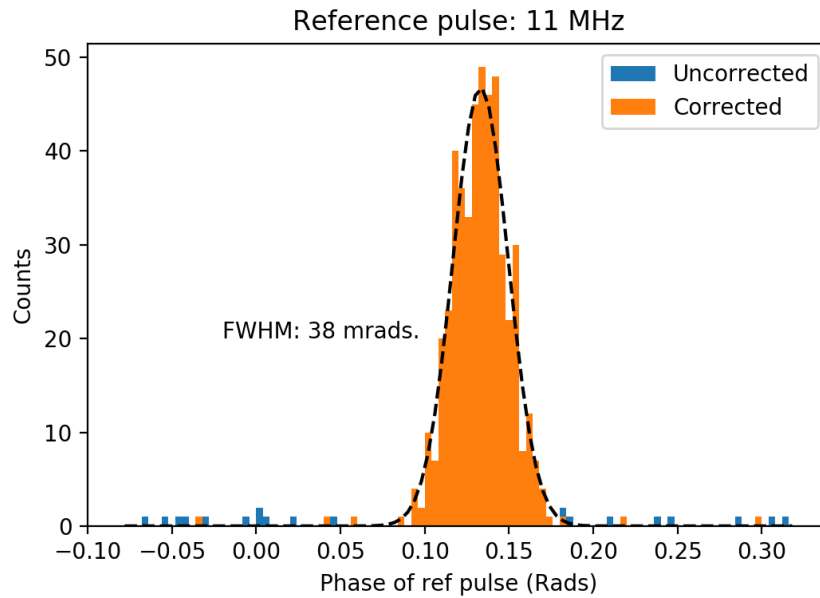


Figure D.3: Zooming in on the bottom bar graph from Figure D.2. The bottom graph was chosen as it had the widest phase distribution.





# Bibliography

1. M. Afzelius and C. Simon. Impedance-matched cavity quantum memory. *Phys. Rev. A*, 82:022310, Aug 2010. 5, 17, 34, 105
2. M. Afzelius, C. Simon, H. de Riedmatten, and N. Gisin. Multimode quantum memory based on atomic frequency combs. *Phys. Rev. A*, 79:052329, May 2009. 31, 34, 87, 103
3. A. L. Alexander, J. J. Longdell, M. J. Sellars, and N. B. Manson. Photon echoes produced by switching electric fields. *Phys. Rev. Lett.*, 96:043602, Feb 2006. 87
4. A. Amari, A. Walther, M. Sabooni, M. Huang, S. Kröll, M. Afzelius, I. Usmani, B. Lauritzen, N. Sangouard, H. de Riedmatten, and N. Gisin. Towards an efficient atomic frequency comb quantum memory. *Journal of Luminescence*, 130(9):1579–1585, 2010. Special Issue based on the Proceedings of the Tenth International Meeting on Hole Burning, Single Molecule, and Related Spectroscopies: Science and Applications (HBSM 2009) - Issue dedicated to Ivan Lorgere and Oliver Guillot-Noel. 87, 164
5. F. Arute et al. Quantum supremacy using a programmable superconducting processor. *Nature*, 574:505–510, 2019. 1
6. S. E. Beavan, M. P. Hedges, and M. J. Sellars. Demonstration of photon-echo rephasing of spontaneous emission. *Phys. Rev. Lett.*, 109:093603, Aug 2012. 4, 37, 67
7. S. E. Beavan, P. M. Ledingham, J. J. Longdell, and M. J. Sellars. Photon echo without a free induction decay in a double- $\lambda$  system. *Opt. Lett.*, 36(7):1272–1274, Apr 2011. 27
8. E. D. Black. An introduction to pound–drever–hall laser frequency stabilization. *American Journal of Physics*, 69(1):79–87, 2001. 49
9. T. Boettger, Y. Sun, C. W. Thiel, and R. L. Cone. Material optimization of  $\text{Er}^{3+}:\text{Y}_2\text{SiO}_5$  at 1.5  $\mu\text{m}$  for optical processing, memory, and laser frequency stabilization applications. In H. J. Coufal, A. E. Craig, and Z. U. Hasan, editors, *Advanced Optical Data Storage*, volume 4988, pages

- 51 – 61. International Society for Optics and Photonics, SPIE, 2003. 8, 16, 110, 114, 132
10. T. Bottger. *Laser frequency stabilization to spectral hole burning frequency references in erbium -doped crystals: Material and device optimization*. PhD thesis, University of San Francisco, 2002. 16
11. H.-J. Briegel, W. Dür, J. I. Cirac, and P. Zoller. Quantum repeaters: The role of imperfect local operations in quantum communication. *Phys. Rev. Lett.*, 81:5932–5935, Dec 1998. 2
12. R. P. Budoyo, K. Kakuyanagi, H. Toida, Y. Matsuzaki, W. J. Munro, H. Yamaguchi, and S. Saito. Phonon-bottlenecked spin relaxation of  $\text{er}^{3+}:\text{Y}_2\text{SiO}_5$  at sub-kelvin temperatures. *Applied Physics Express*, 11(4):043002, 2018. 84
13. M. Businger, A. Tiranov, K. T. Kaczmarek, S. Welinski, Z. Zhang, A. Ferrier, P. Goldner, and M. Afzelius. Optical spin-wave storage in a solid-state hybridized electron-nuclear spin ensemble. *Phys. Rev. Lett.*, 124:053606, Feb 2020. 87, 168
14. B. Casabone, C. Deshmukh, S. Liu, D. Serrano, A. Ferrier, T. Hümmer, P. Goldner, D. Hunger, and H. de Riedmatten. Dynamic control of purcell enhanced emission of erbium ions in nanoparticles. *Nature Communications*, 12(1):3570, Jun 2021. 42
15. T. Chanelière, J. Ruggiero, M. Bonarota, M. Afzelius, and J.-L. L. Gouët. Efficient light storage in a crystal using an atomic frequency comb. *New Journal of Physics*, 12(2):023025, feb 2010. 87
16. S. Cotton. *Introduction to the Lanthanides*, chapter 1, pages 1–7. John Wiley & Sons, Ltd, 2006. 8
17. E. Z. Cruzeiro, A. Tiranov, J. Lavoie, A. Ferrier, P. Goldner, N. Gisin, and M. Afzelius. Efficient optical pumping using hyperfine levels in  $^{145}\text{Nd}^{3+}:\text{Y}_2\text{SiO}_5$  and its application to optical storage. *New Journal of Physics*, 20(5):053013, may 2018. 5, 87, 164
18. J. Dajczgewand, J.-L. L. Gouët, A. Louchet-Chauvet, and T. Chanelière. Large efficiency at telecom wavelength for optical quantum memories. *Opt. Lett.*, 39(9):2711–2714, May 2014. 164
19. V. Damon, M. Bonarota, A. Louchet-Chauvet, T. Chanelière, and J. Gouët. Revival of silenced echo and quantum memory for light. *New Journal of Physics*, 13:093031, 2011. 29, 87
20. G. H. Dieke, H. M. Crosswhite, and H. Crosswhite. *Spectra and energy levels of rare earth ions in crystals*. Interscience Publishers, New York, 1968. 10, 11

21. A. R. Dixon, J. F. Dynes, Z. L. Yuan, A. W. Sharpe, A. J. Bennett, and A. J. Shields. Ultrashort dead time of photon-counting ingaas avalanche photodiodes. *Applied Physics Letters*, 94(23):231113, 2009. 67
22. R. W. P. Drever, J. L. Hall, F. V. Kowalski, J. Hough, G. M. Ford, A. J. Munley, and H. Ward. Laser phase and frequency stabilization using an optical resonator. *Applied Physics B*, 31(2):97–105, 1983. 49
23. L.-M. Duan, G. Giedke, J. I. Cirac, and P. Zoller. Inseparability criterion for continuous variable systems. *Phys. Rev. Lett.*, 84:2722–2725, Mar 2000. 40, 154
24. L.-M. Duan, M. D. Lukin, J. I. Cirac, and P. Zoller. Long-distance quantum communication with atomic ensembles and linear optics. *Nature*, 414(6862):413–418, Nov. 2001. 3
25. C. Duda. Characterizing a quantum memory incorporating an entangled light source. Master’s thesis, Research School of Physics, ANU College of Science, The Australian National University, 2020. 28
26. C. K. Duda, K. R. Ferguson, R. L. Ahlefeldt, M. P. Hedges, and M. J. Sellars. Optimising the efficiency of a quantum memory based on rephased amplified spontaneous emission, 2022. 145, 146
27. R. W. Equall, R. L. Cone, and R. M. Macfarlane. Homogeneous broadening and hyperfine structure of optical transitions in  $\text{pr}^{3+}:\text{y}_2\text{siO}_5$ . *Phys. Rev. B*, 52:3963–3969, Aug 1995. 42
28. R. W. Equall, Y. Sun, R. L. Cone, and R. M. Macfarlane. Ultraslow optical dephasing in  $\text{eu}^{3+}:\text{y}_2\text{siO}_5$ . *Phys. Rev. Lett.*, 72:2179–2182, Apr 1994. 42
29. K. R. Ferguson. *Generation and storage of optical entanglement in a solid state spin-wave quantum memory*. PhD thesis, Laser Physics Centre, Research School of Physics and Engineering, College of Physical and Mathematical Sciences, 2016. 2, 120, 131, 142, 143, 145, 156, 159, 161
30. K. R. Ferguson, S. E. Beavan, J. J. Longdell, and M. J. Sellars. Generation of light with multimode time-delayed entanglement using storage in a solid-state spin-wave quantum memory. *Phys. Rev. Lett.*, 117:020501, Jul 2016. 4, 5, 37, 67, 138, 145, 154, 156, 164, 167
31. R. P. Feynman. Simulating physics with computers. *International journal of theoretical physics*, 21(6-7):467–488, 1982. 1
32. A. J. Freeman and R. E. Watson. Theoretical investigation of some magnetic and spectroscopic properties of rare-earth ions. *Phys. Rev.*, 127:2058–2075, Sep 1962. 8

33. A. V. Gorshkov, A. André, M. D. Lukin, and A. S. Sørensen. Photon storage in  $\Lambda$ -type optically dense atomic media. ii. free-space model. *Phys. Rev. A*, 76:033805, Sep 2007. 32
34. L. K. Grover. A fast quantum mechanical algorithm for database search. In *Proceedings of the Twenty-Eighth Annual ACM Symposium on Theory of Computing*, STOC '96, page 212–219, New York, NY, USA, 1996. Association for Computing Machinery. 1
35. E. L. Hahn. Spin echoes. *Phys. Rev.*, 80:580–594, Nov 1950. 4, 24
36. S. R. Hastings-Simon, B. Lauritzen, M. U. Staudt, J. L. M. van Mechele, C. Simon, H. de Riedmatten, M. Afzelius, and N. Gisin. Zeeman-level lifetimes in  $\text{er}^{3+} : \text{y}_2\text{siO}_5$ . *Phys. Rev. B*, 78:085410, Aug 2008. 17
37. S. R. Hastings-Simon, B. Lauritzen, M. U. Staudt, J. L. M. van Mechele, C. Simon, H. de Riedmatten, M. Afzelius, and N. Gisin. Zeeman-level lifetimes in  $\text{er}^{3+} : \text{y}_2\text{siO}_5$ . *Phys. Rev. B*, 78:085410, Aug 2008. 88
38. M. Hedges et al. *High performance solid state quantum memory*. PhD thesis, Laser Physics Centre, Research School of Physics and Engineering, The Australian National University, 2011. 14
39. L. Heller, P. Farrera, G. Heinze, and H. de Riedmatten. Cold-atom temporally multiplexed quantum memory with cavity-enhanced noise suppression. *Phys. Rev. Lett.*, 124:210504, May 2020. 168
40. M. Hosseini, B. M. Sparkes, G. Campbell, P. K. Lam, and B. C. Buchler. High efficiency coherent optical memory with warm rubidium vapour. *Nature Communications*, 2011. 30
41. R. Hull, J. Parisi, R. Osgood, H. Warlimont, G. Liu, and B. Jacquier. *Spectroscopic Properties of Rare Earth in Optical Materials*, volume 83. Springer, 01 2005. 9, 14
42. M. Żukowski, A. Zeilinger, M. A. Horne, and A. K. Ekert. “event-ready-detectors” bell experiment via entanglement swapping. *Phys. Rev. Lett.*, 71:4287–4290, Dec 1993. 2
43. J. D. Jackson. *Classical electrodynamics*, 1999. 60
44. P. Jobez, N. Timoney, C. Laplane, J. Etesse, A. Ferrier, P. Goldner, N. Gisin, and M. Afzelius. Towards highly multimode optical quantum memory for quantum repeaters. *Phys. Rev. A*, 93:032327, Mar 2016. 168
45. P. Jobez, I. Usmani, N. Timoney, C. Laplane, N. Gisin, and M. Afzelius. Cavity-enhanced storage in an optical spin-wave memory. *New J. Phys.*, 16(8):083005, aug 2014. 105, 168

46. N. A. Kurnit, I. D. Abella, and S. R. Hartmann. Observation of a photon echo. *Phys. Rev. Lett.*, 13:567–568, Nov 1964. 25
47. B. Lauritzen, J. c. v. Minář, H. de Riedmatten, M. Afzelius, N. Sangouard, C. Simon, and N. Gisin. Telecommunication-wavelength solid-state memory at the single photon level. *Phys. Rev. Lett.*, 104:080502, Feb 2010. 17, 88, 96, 167
48. P. M. Ledingham, W. R. Naylor, and J. J. Longdell. Experimental realization of light with time-separated correlations by rephasing amplified spontaneous emission. *Phys. Rev. Lett.*, 109:093602, Aug 2012. 4, 5, 67, 154
49. P. M. Ledingham, W. R. Naylor, J. J. Longdell, S. E. Beavan, and M. J. Sellars. Nonclassical photon streams using rephased amplified spontaneous emission. *Phys. Rev. A*, 81:012301, Jan 2010. 4, 35, 87, 120, 142, 143, 145, 159
50. T. E. LTD. Effective number of bits for arbitrary waveform generators. [https://www.taborelec.com/Files/Effective%20Number%20of%20Bits\\_for%20Arbitrary%20Waveform%20Generators%20full%20White%20paper.pdf](https://www.taborelec.com/Files/Effective%20Number%20of%20Bits_for%20Arbitrary%20Waveform%20Generators%20full%20White%20paper.pdf). 178
51. E. Lucero, R. Barends, Y. Chen, J. Kelly, M. Mariani, A. Megrant, P. O'Malley, D. Sank, A. Vainsencher, J. Wenner, T. White, Y. Yin, A. N. Cleland, and J. M. Martinis. Computing prime factors with a Josephson phase qubit quantum processor. *Nature Physics*, 8(10):719–723, 2012. 1
52. R. M. Macfarlane, A. Cassanho, and R. S. Meltzer. Inhomogeneous broadening by nuclear spin fields: A new limit for optical transitions in solids. *Phys. Rev. Lett.*, 69:542–545, Jul 1992. 70, 93
53. D. L. McAuslan, P. M. Ledingham, W. R. Naylor, S. E. Beavan, M. P. Hedges, M. J. Sellars, and J. J. Longdell. Photon-echo quantum memories in inhomogeneously broadened two-level atoms. *Phys. Rev. A*, 84:022309, Aug 2011. 30
54. B. Merkel, A. Ulanowski, and A. Reiserer. Coherent and purcell-enhanced emission from erbium dopants in a cryogenic high- $q$  resonator. *Phys. Rev. X*, 10:041025, Nov 2020. 42
55. W. B. Mims. Phase memory in electron spin echoes, lattice relaxation effects in  $\text{CaWO}_4$ : Er, Ce, Mn. *Phys. Rev.*, 168:370–389, Apr 1968. 118
56. S. A. Moiseev and S. Kröll. Complete reconstruction of the quantum state of a single-photon wave packet absorbed by a doppler-broadened transition. *Phys. Rev. Lett.*, 87:173601, Oct 2001. 103

57. Y. L. . M. J. S. Morgan P. Hedges, Jevon J. Longdell. Efficient quantum memory for light. *Nature*, 465(7301):1052–1056, jun 2010. 5, 17, 30, 34, 164
58. M. Rancic. *High Resolution Spectroscopy of Erbium Doped Solids*. PhD thesis, Laser Physics Centre, Research School of Physics and Engineering, The Australian National University, 2017. 2, 16, 69, 70, 72, 91, 110, 181, 183
59. M. Rančić, M. P. Hedges, R. L. Ahlefeldt, and M. J. Sellars. Coherence time of over a second in a telecom-compatible quantum memory storage material. *Nat. Phys.*, 14(1):50–54, 2018. 5, 8, 13, 17, 28, 46, 71, 75, 78, 88, 106, 110, 121, 169
60. M. Sabooni, Q. Li, S. Kröll, and L. Rippe. Efficient quantum memory using a weakly absorbing sample. *Phys. Rev. Lett.*, 110:133604, Mar 2013. 168
61. E. Saglamyurek, J. Jin, V. B. Verma, M. D. Shaw, F. Marsili, S. W. Nam, D. Oblak, and W. Tittel. Quantum storage of entangled telecom-wavelength photons in an erbium-doped optical fibre. *Nat. Photonics*, 9(2):83–87, jan 2015. 5, 88, 95, 96, 167
62. N. Sangouard, C. Simon, M. Afzelius, and N. Gisin. Analysis of a quantum memory for photons based on controlled reversible inhomogeneous broadening. *Phys. Rev. A*, 75:032327, Mar 2007. 30, 32, 103
63. A. Schmidt. *Investigating Excitation-Induced Phonons in an Erbium Quantum Memory Crystal*. PhD thesis, Laser Physics Centre, Research School of Physics and Engineering, The Australian National University, 2020. 81
64. M. J. Sellars. *Ultra-high resolution laser spectroscopy of rare earth doped solids*. PhD thesis, Laser Physics Centre, Research School of Physics and Engineering, The Australian National University, 1996. 49
65. R. Shannon and C. Prewitt. Effective ionic radii in oxides and fluorides. *Acta Crystallographica Section B Structural Crystallography and Crystal Chemistry*, 25:925–946, 05 1969. 13
66. P. W. Shor. Polynomial-time algorithms for prime factorization and discrete logarithms on a quantum computer. *SIAM Review*, 41(2):303–332, 1999. 1
67. Y. Sun, T. Böttger, C. W. Thiel, and R. L. Cone. Magnetic g tensors for the  $4f^{15}6s^2$  and  $4f^{13}6s^2$  states of  $\text{Er}^{3+} : \text{Y}_2\text{SiO}_5$ . *Phys. Rev. B*, 2008. 16

68. C. Thiel, T. Böttger, and R. Cone. Rare-earth-doped materials for applications in quantum information storage and signal processing. *Journal of Luminescence*, 131(3):353–361, 2011. Selected papers from DPC’10. 70
69. N. Timoney, B. Lauritzen, I. Usmani, M. Afzelius, and N. Gisin. Atomic frequency comb memory with spin-wave storage in  $153\text{eu}^{3+}:\text{y}_2\text{sio}_5$ . *Journal of Physics B: Atomic, Molecular and Optical Physics*, 45(12):124001, jun 2012. 87, 168
70. N. Timoney, I. Usmani, P. Jobez, M. Afzelius, and N. Gisin. Single-photon-level optical storage in a solid-state spin-wave memory. *Phys. Rev. A*, 88:022324, Aug 2013. 168
71. W. Tittel, M. Afzelius, T. Chanelière, R. Cone, S. Kröll, S. Moiseev, and M. Sellars. Photon-echo quantum memory in solid state systems. *Laser Photonics Rev.*, 4(2):244–267, 2 2010. 2
72. H. Varian. Bootstrap tutorial. *Mathematica Journal*, 9(4):768–775, 2005. 101
73. S. Weigert. *No-Cloning Theorem*, pages 404–405. Springer Berlin Heidelberg, Berlin, Heidelberg, 2009. 2
74. Y. Wu et al. Strong quantum computational advantage using a superconducting quantum processor. *Phys. Rev. Lett.*, 127:180501, Oct 2021. 1
75. N. Xu, J. Zhu, D. Lu, X. Zhou, X. Peng, and J. Du. Quantum factorization of 143 on a dipolar-coupling nuclear magnetic resonance system. *Phys. Rev. Lett.*, 108:130501, Mar 2012. 1
76. B. Yang, R. Raymond, H. Imai, H. Chang, and H. Hiraishi. Testing scalable bell inequalities for quantum graph states on ibm quantum devices, 2021. 1
77. B. C. Young, F. C. Cruz, W. M. Itano, and J. C. Bergquist. Visible lasers with subhertz linewidths. *Phys. Rev. Lett.*, 82:3799–3802, May 1999. 49
78. M. Zhong, M. P. Hedges, R. L. Ahlefeldt, J. G. Bartholomew, S. E. Beavan, S. M. Wittig, J. J. Longdell, and M. J. Sellars. Optically addressable nuclear spins in a solid with a six-hour coherence time. *Nature*, 517, 2014. 5, 8, 17, 28